

AN INVESTIGATION OF DUCTILE FRACTURE CRITERIA  
FOR SHEET METAL FORMING

A THESIS SUBMITTED TO  
THE GRADUATE SCHOOL OF NATURAL AND APPLIED SCIENCES  
OF  
MIDDLE EAST TECHNICAL UNIVERSITY

BY

SHAHRAM ABBASNEJAD DIZAJI

IN PARTIAL FULFILLMENT OF THE REQUIREMENTS  
FOR  
THE DEGREE OF DOCTOR OF PHILOSOPHY  
IN  
MECHANICAL ENGINEERING

DECEMBER 2014



**AN INVESTIGATION OF DUCTILE FRACTURE CRITERIA  
FOR SHEET METAL FORMING**

Submitted by **Shahram ABBASNEJAD DIZAJI** in partial fulfillment of the requirements for the degree of **Doctor of philosophy in Mechanical Engineering Department, Middle East Technical University** by,

Prof. Dr. Gülbin Dural Ünver  
Dean, Graduate School of **Natural and Applied Sciences**

\_\_\_\_\_

Prof. Dr. R. Tuna Balkan  
Head of Department, **Mechanical Engineering**

\_\_\_\_\_

Prof. Dr. Haluk Darendeliler  
Supervisor, **Mechanical Engineering Dept., METU**

\_\_\_\_\_

Prof. Dr. Bilgin Kaftanoğlu  
Co-Supervisor, **Manufacturing Dept., Atılım University**

\_\_\_\_\_

**Examining Committee Members:**

Prof. Dr. Mustafa İlhan Gökler  
Mechanical Engineering Dept., METU

\_\_\_\_\_

Prof. Dr. Haluk Darendeliler  
Mechanical Engineering Dept., METU

\_\_\_\_\_

Prof. Dr. Mehmet Utku  
Civil Engineering Dept., METU

\_\_\_\_\_

Prof. Dr. F. Suat Kadioğlu  
Mechanical Engineering Dept., METU

\_\_\_\_\_

Prof. Dr. Can Çoğun  
Mechanical Engineering Dept., Çankaya University

\_\_\_\_\_

**Date:** 29.12.2014

**I hereby declare that all information in this document has been obtained and presented in accordance with academic rules and ethical conduct. I also declare that, as required by these rules and conduct, I have fully cited and referenced all material and results that are not original to this work.**

Name, Last name: Shahram Abbasnejad Dizaji

Signature:

## ABSTRACT

### AN INVESTIGATION OF DUCTILE FRACTURE CRITERIA FOR SHEET METAL FORMING

Abbasnejad Dizaji, Shahram  
PhD, Department of Mechanical Engineering  
Supervisor : Prof. Dr. Haluk Darendeliler  
Co-Supervisor: Prof. Dr. Bilgin Kaftanoglu

December 2014, 174 pages

Deep drawing is a sheet metal forming process in which a sheet metal stock, commonly referred to as a blank, is drawn into a die by a punch. Forming limit diagram (FLD), a representation of the critical combination of the principal surface strains, is an important concept utilized for the evaluation of the formability of sheet metals. Most of the theoretical methods for determining FLDs are strain-path dependent and cannot exactly clarify the location of necking or fracture. Using stress-based forming limits (FLSD) can resolve this problem, but numerical implementations of the FLSDs are difficult and sometimes not reliable. Another way to determine the limits of formability is to apply a ductile fracture criterion (DFC). The main goal of ductile fracture criteria is to predict the location of the fracture in the sheet metals and overcome the deficiency of strain path dependency of FLDs. The objective of the present thesis work is to develop a robust DFC for sheets. The algorithm of proposed criterion is implemented into a commercial explicit finite element code by using user-defined material subroutines. Recently developed constitutive models are used with appropriate hardening rules in the explicit code. The results of numerical implementations are compared with the results of the other known criteria and the experimental tests to validate the newly developed criterion. It is observed that the newly developed ductile fracture criterion can be used efficiently for different materials and predicts the fracture initiation better than the existing DFCs.

Keywords: Sheet metal forming, ductile fracture, constitutive equations, numerical methods

## ÖZ

### SAC ŞEKİLLENDİRME İŞLEMİ İÇİN SÜNEK KIRILMA KRİTERİLERİNİN ARAŞTIRILMASI

Abbasnejad Dizaji, Shahram  
PhD, Makina Mühendisliği Bölümü  
Danışman : Prof. Dr. Haluk Darendeliler  
Eş Danışman : Prof. Dr. Bilgin Kaftanoğlu

Aralık 2014, 174 sayfa

Derin çekme, metal levhaların zımba yardımıyla kalıp içinde şekillendirildiği bir sac şekillendirme işlemidir. Asal yüzey gerinimlerinin kritik sınırlarını gösteren şekillendirilebilirlik şeması sacın şekillendirilebilirliğinin değerlendirilmesinde kullanılan önemli bir yaklaşımdır. Şekillendirilebilirlik şemasının hesaplanmasında kullanılan teorik yöntemlerin çoğu gerinim yoluna bağlıdır ve boyun yapma veya kırılmanın nerede olacağına açıklık getirememektedir. Bu sorun gerilmeye dayanan şekillendirilebilirlik sınırları kullanılarak çözülebilmektedir, ancak bu yöntemin sayısal uygulaması zordur ve bazı durumlarda güvenilir sonuçlar vermemektedir. Bu konu ile ilgili diğer bir yaklaşım da sünek kırılma kriterlerinin kullanılmasıdır. Sünek kırılma kriterlerinin amacı sac şekillendirme işlemlerinde kopmanın nerede olacağını belirlemek ve şekillendirme şemalarının gerinim yoluna bağlı olmasından kaynaklanan prolemleri ortadan kaldırmaktır. Bu tezin amacı sünek sac şekillendirme işlemlerinde kopmanın öngörülmesini sağlayacak bir sünek kırılma kriterinin geliştirilmesidir. Önerilen kriterin algoritması, kullanıcı-tanımlı malzeme altprogramları vasıtasıyla, ticari bir açık sonlu elamanlar programına uygulanmıştır. Yeni geliştirilmiş olan yapısal modeller uygun pekleşme bağlantıları ile birlikte programda kullanılmıştır. Sayısal analizlerin sonuçları bilinen diğer kriterler ile karşılaştırılmıştır. Yeni geliştirilen sünek kopma kriteri kullanılarak elde edilen sonuçları doğrulamak amacıyla deneyler yapılmıştır. Karşılaştırmalar sonucunda, yeni geliştirilen sünek kırılma kriterinin etkili bir şekilde kullanılabileceği ve kopma başlangıcını var olan diğer kriterlere göre daha iyi belirlediği görülmüştür.

Anahtar kelimeler: sac şekillendirme, sünek kırılma, bünye denklemleri, sayısal yöntemler

*To My family who always supported me*

## ACKNOWLEDGEMENTS

I would like to express my sincere and gratitude to my supervisor, Prof. Dr. Haluk Darendeliler, for his gentleness and appreciate his treasured advices.

Further, I thank Prof. Dr. Bilgin Kaftanođlu as my co-supervisor for his valuable comments and oportune recommendations in the thesis.

I also appreciate Prof. Dr. Mustafa I. Gökler and Prof. Dr. Mehmet Utku for their kindly guidance in the different stages of the thesis.

I moreover thank the Middle East Technical University for providing the necessary equipment for experimental tests. My especial thanks is for the staff Solid Mechanics Laboratory of Mechanical Engineering Department for their assistance during the tests.

Furthurmore, I want to appreciate METU-BILTIR Center for providing some requiered facilities during the experimental tests.

The Author is delighted to thank TÜBİTAK (The Scientific and Technological Research Council of Turkey) for supporting this thesis under the graduate scholarship program for international students (Grant No: 2215).



## TABLE OF CONTENTS

ABSTRACT .....	v
ÖZ .....	vi
ACKNOWLEDGEMENTS .....	viii
TABLE OF CONTENTS .....	ix
LIST OF TABLES .....	xii
LIST OF FIGURES .....	xiii
LIST OF SYMBOLS .....	xix
CHAPTERS	
1. INTRODUCTION .....	1
1.1 Motivation .....	1
1.2 Background .....	1
1.2.1 Deep drawing Process .....	2
1.2.1.1 Important factors in deep drawing .....	3
1.2.1.2 Instability in deep drawing .....	4
1.2.2 Yield criterion and Hardening rules .....	6
1.2.3 Forming Limit Diagram (FLD) .....	8
1.2.4 Ductile Fracture .....	9
1.3 Research objectives .....	10
1.4 Outline of the thesis .....	12
2. LITERATURE SURVEY .....	13
3. SCOPE OF THE THESIS .....	31
4. FINITE ELEMENT METHOD .....	35
4.1 Introduction .....	35
4.2 Finite Element Method .....	35
4.2.1 Virtual Work Principle .....	36
4.2.2 Shape Functions .....	36
4.2.3 Equations of Finite Elements .....	37
4.3 Finite Element Solvers .....	38
4.3.1 Implicit and Explicit Methods .....	39

4.3.2 Dynamic Explicit Method .....	41
4.3.3 Explicit time integration.....	42
4.3.4 Speeding up methods in the explicit solvers .....	44
4.4 Subroutines in the commercial ABAQUS software.....	45
4.5 Finite element model specifications.....	47
5. CONSTITUTIVE EQUATIONS AND DUCTILE FRACTURE CRITERIA .51	
5.1 Yield Criterion .....	51
5.1.1 Von-Mises yield criterion.....	52
5.1.2 Hill'48 Yield Criterion .....	52
5.1.3 Aretz's Yld2003 Criterion.....	55
5.1.4 BBC2008 yield criterion .....	68
5.2 Hardening rules .....	77
5.2.1 Implementation of the isotropic hardening rule .....	78
5.2.1.1 Hollomon (power law) model.....	79
5.2.1.2 Piecewise linear model .....	79
5.2.2 Implementation of the kinematic hardening.....	79
5.2.3 Implementation of the combined hardening model.....	81
5.3 Forming Limit Diagrams.....	82
5.4 Fracture in sheet metal .....	83
5.4.1 Uncoupled ductile fracture criteria.....	83
5.4.2 Coupled ductile fracture criteria.....	86
6. THE NEW DUCTILE FRACTURE CRITERION .....	89
6.1 The objectives of the new criterion .....	89
6.2 Parameters affecting the criterion .....	91
6.3 The new ductile fracture criterion .....	96
6.3.1 Calculating the criterion constants .....	96
6.3.2 Implementation of the new criterion .....	97
6.3.3 Verification of the new criterion .....	99
7. EXPERIMENTAL TESTS.....	103
7.1 Uniaxial tension test of the sheet metals .....	103
7.2 Erichsen test .....	107
7.3 Nakazima test.....	109

7.4 Deep drawing test .....	110
8. VERIFICATION, RESULTS AND DISCUSSION .....	115
8.1 Verification of the numerical approach .....	115
8.2 Verification and validation of the new criterion .....	126
8.3 Predictions with new DFC .....	127
8.3.1 Effect of yielding functions on the DFCs .....	128
8.3.2 Effect of hardening models on the DFCs.....	137
8.3.3 Case studies.....	143
9. CONCLUSIONS AND FUTURE WORKS .....	153
9.1 Conclusions.....	154
9.2 Future works .....	155
REFERENCES.....	157
APPENDICES	
A. REQUIRED TOOLS TO WRITE A SUBROUTINE.....	165
B. DETERMINATION OF THE CRITERION UNKNOWN.....	169
C. IMPLEMENTATION OF THE NEW DFC.....	171
VITA.....	173

## LIST OF TABLES

### TABLES

Table 5.1 The material parameters of DKP6112 used to calculate the YLD2003 yield criterion constants .....	59
Table 5.2. YLD2003 anisotropy constants obtained using the optimization methods for DKP6112 steel material .....	67
Table 5.3. BBC2008 constants obtained using the optimization methods for DKP6112 steel material .....	76
Table 6.1 Different materials utilized to determine the material parameters effects on the forming limit curves at fracture.....	92
Table 7.1 Material parameters of DKP 6112 (DIN EN 10130-1999) steel obtained by uniaxial tension tests (UTT).....	106
Table 7.2 Material parameters of SS304 steel obtained by UTT.....	106
Table 7.3 Material parameters of AA5450, aluminum alloy, obtained by UTT.....	107
Table 7.4. The material parameters obtained Erichsen test .....	108
Table 7.5 Tooling dimensions in the cylindrical cup drawing.....	112
Table 8.1. DFC constants for DKP 6112 and SS304 materials .....	137

## LIST OF FIGURES

### FIGURES

Figure 1.1. Different types of the fracture in the cup drawing.....	6
Figure 1.2. The effect of planar anisotropy in sheet metal Earing.....	7
Figure 1.3. Schematic of the forming limit curve (FLC) .....	8
Figure 4.1. VUMAT operational flowchart .....	46
Figure 5.1. Schematic view of hardening rules.....	77
Figure 5.2. Scheme of the M-K model, a) unreformed, b) deformed .....	83
Figure 6.1. Comparison of various uncoupled criteria in determination of FLCF for DKP6112 steel .....	90
Figure 6.2. Effect of initial sheet thickness on the shape of FLCFs in St14 steel sheets [54].....	93
Figure 6.3. Effect of hardening index ( $n$ ) and normal anisotropy ( $r$ ) considering three materials with the same thicknesses.....	94
Figure 6.4. Effect of strength coefficient ( $K$ ) on the height of the FLCFs .....	95
Figure 6.5. Effect of thickness and strain hardening parameters on the FLCFs of the materials with almost identical $K$ and $r$ -values .....	95
Figure 6.6. Simulation snapshot of the uniaxial tensile test showing the fracture initiation phenomenon.....	98
Figure 6.7. Simulation of the necking phenomenon in the uniaxial tension test using ABAQUS/Explicit .....	99
Figure 6.8. A flowchart to determine the fracture point in any desired test .....	100
Figure 7.1. Uniaxial tension test equipment .....	104

Figure 7.2. Schematic of the UTT specimen and its dimensions.....	104
Figure 7.3. The DKP6112 specimens after UTT test.....	105
Figure 7.4. Measuring the thickness and width of the specimen (SS304) using high accuracy optical microscope .....	106
Figure 7.5. Marked specimens a) specimen for cylindrical cup drawing test b) specimen for squared-cup drawing c) specimen for Erichsen test.....	108
Figure 7.6. Various specimens with different heights deformed in the Erichsen test for SS304 material .....	108
Figure 7.7. Deformed specimens by the Nakazima test for DKP 6112 steel.....	110
Figure 7.8. The schematic of the Nakazima test tooling.....	110
Figure 7.9. Experimentally obtained FLCN and FLCF curves for three materials..	111
Figure 7.10. The deep drawing machine .....	111
Figure 7.11. Cylindrical cup drawing of DKP6112 .....	112
Figure 7.12. The fractured specimens in the 18 and 12 mm punch travels for DKP6112 material.....	113
Figure 7.13. The fractured cup in 14.5 mm of punch travel for AA5450 material ..	113
Figure 7.14. Squared cup drawing, tools dimensions .....	114
Figure 7.15. Squared cup drawing of SS304 steel .....	114
Figure 7.16. The fractured part in the square cup drawing of DKP6112 material...	114
Figure 8.1. Internal and kinetic energy diagrams in the deep drawing process of the DKP6112 material.....	116
Figure 8.2. Punch force-punch displacement diagram of DKP6112 material in the cylindrical cup drawing process.....	116
Figure 8.3. Thickness distribution-distance diagram of DKP6112 in the cylindrical cup drawing at 15 mm punch travel implementing Von-Mises yield criterion .....	117
Figure 8.4. Thickness distribution-distance diagram of DKP6112 in the cylindrical cup drawing at 25 mm punch travel implementing Von-Mises yield criterion .....	117

Figure 8.5. Thickness distribution-distance diagram of DKP6112 in the cylindrical cup drawing at 35 mm punch travel implementing Von-Mises yield criterion .....	118
Figure 8.6. Thickness distribution-distance diagram of DKP6112 in the cylindrical cup drawing at 45 mm punch travel implementing Von-Mises yield criterion .....	118
Figure 8.7. Thickness distribution-distance diagram of DKP6112 in the cylindrical cup drawing at 15 mm punch travel implementing Hill48 yield criterion.....	119
Figure 8.8. Thickness distribution-distance diagram of DKP6112 in the cylindrical cup drawing at 25 mm punch travel implementing Hill48 yield criterion.....	119
Figure 8.9. Thickness distribution-distance diagram of DKP6112 in the cylindrical cup drawing at 35 mm punch travel implementing Hill48 yield criterion.....	119
Figure 8.10. Thickness distribution-distance diagram of DKP6112 in the cylindrical cup drawing at 45 mm punch travel implementing Hill48 yield criterion.....	120
Figure 8.11. Thickness distribution-distance diagram of DKP6112 in the cylindrical cup drawing at 15 mm punch travel implementing YLD2003 yield criterion.....	120
Figure 8.12. Thickness distribution-distance diagram of DKP6112 in the cylindrical cup drawing at 25 mm punch travel implementing YLD2003 yield criterion.....	121
Figure 8.13. Thickness distribution-distance diagram of DKP6112 in the cylindrical cup drawing at 35 mm punch travel implementing YLD2003 yield criterion.....	121
Figure 8.14. Thickness distribution-distance diagram of DKP6112 in the cylindrical cup drawing at 45 mm punch travel implementing YLD2003 yield criterion.....	121
Figure 8.15. Thickness distribution-distance diagram of DKP6112 in the cylindrical cup drawing at 15 mm punch travel implementing BBC2008 yield criterion.....	122
Figure 8.16. Thickness distribution-distance diagram of DKP6112 in the cylindrical cup drawing at 25 mm punch travel implementing BBC2008 yield criterion.....	122
Figure 8.17. Thickness distribution-distance diagram of DKP6112 in the cylindrical cup drawing at 35 mm punch travel implementing BBC2008 yield criterion.....	123
Figure 8.18. Thickness distribution-distance diagram of DKP6112 in the cylindrical cup drawing at 45 mm punch travel implementing BBC2008 yield criterion.....	123
Figure 8.19. Thickness strain variations of DKP6112 in the different punch heights (15, 25, 35, 45 mm) implementing Hill48 yield criterion .....	124

Figure 8.20. Successfully predicted ears in the drawn cup for SS304 material at 49 mm punch travel implementing Hill48 yield criterion .....	124
Figure 8.21. Thickness distribution of SS304 at the 49 mm punch travel in the rolling direction implementing various yield criteria .....	125
Figure 8.22. Successfully drawn cup for AA5450 material at 29 mm punch travel implementing Hill48 yield criterion .....	126
Figure 8.23. Thickness distribution of AA5450 at the 29 mm punch travel in the rolling direction implementing various yield criteria .....	126
Figure 8.24. Comparison of the numerical and experimental FLCFs for four cases after fitting process .....	127
Figure 8.25. Comparison of the new DFC and experimental FLCFs for three different materials .....	128
Figure. 8.26 FLCFs of various DFCs implementing Von-Mises constitutive equation for DKP6112 material .....	129
Figure. 8.27 FLCFs of various DFCs implementing Hill48 constitutive equation for DKP6112 material.....	129
Figure 8.28. FLCFs of various DFCs implementing BBC2008 constitutive equation for DKP6112 material .....	130
Figure 8.29. FLCFs of various DFCs implementing YLD2003 constitutive equation for DKP6112 material .....	130
Figure 8.30. FLCFs of various DFCs implementing Von-Mises equation for SS304 .....	131
Figure 8.31. FLCFs of various DFCs implementing Hill48 equation for SS304 ....	131
Figure 8.32 FLCFs of various DFCs implementing BBC2008 equation for SS304	132
Figure 8.33. FLCFs of various DFCs implementing YLD2003 equation for SS304 .....	132
Figure. 8.35. FLCFs of various DFCs implementing Hill48 constitutive equation for AA5450 material .....	133
Figure 8.36. FLCFs of various DFCs implementing BBC2008 constitutive equation for AA5450 material .....	134



Figure 8.37. FLCFs of various DFCs implementing YLD2003 constitutive equation for AA5450 material .....	134
Figure. 8.38. FLCFs of the new DFC implementing various constitutive models for DKP6112 material.....	135
Figure. 8.39. FLCFs of the new DFC implementing various constitutive models for SS304 material .....	136
Figure. 8.40. FLCFs of the new DFC implementing various constitutive models for AA5450 material.....	136
Figure 8.41. Nakazima test results for isotropic hardening rule that uses Hollomon hardening equation for DKP6112 .....	138
Figure. 8.42. Nakazima test results for kinematic hardening that uses Zeigler-Prager equation for DKP6112 .....	138
Figure. 8.43. Nakazima test results for combined hardening that uses Chaboche-Zeigler equation for DKP6112.....	139
Figure. 8.44. FLCFs of the New DFC that uses four different hardening equations for DKP6112 material.....	140
Figure. 8.45. Nakazima test results for kinematic hardening that uses Zeigler-Prager equation for SS304 material.....	141
Figure. 8.46. Nakazima test results for combined hardening that uses Chaboche-Zeigler equation for SS304 material .....	141
Figure. 8.47. FLCFs of the new DFC using three different hardening models for SS304 material.....	142
Figure. 8.48. Distribution of the DFC constant (SDV2) at 24 mm of the punch travel for DKP6112 material .....	143
Figure. 8.49. Comparison of different DFCs for square cup drawing of DKP6112 at 24.6 mm of punch travel using Von-Mises constitutive model .....	144
Figure. 8.50. Comparison of different DFC results for square cup drawing of SS304 at 23.2 mm of punch travel using Von-Mises constitutive model .....	145
Figure. 8.51. Comparison of the different yield criteria in the prediction of the fracture at 24.6 mm of punch travel for squared cup of DKP6112.....	146

Figure. 8.52. Comparison of the different yield criteria in the prediction of the fracture at 23.2 mm of punch travel for squared cup of SS304 .....	146
Figure. 8.53. Distribution of the <i>FIP</i> at 17.9 mm of the punch travel for DKP6112 using BBC2008 yield criterion .....	147
Figure. 8.54. Distribution of the <i>FIP</i> at 11.7 mm of the punch travel for DKP6112 using BBC2008 yield criterion .....	148
Figure. 8.55. Comparison of the different DFCs using BBC2008 yield criterion in the prediction of the fracture at 18 mm for cylindrical cup of DKP6112 .....	149
Figure. 8.56. Comparison of the different DFCs using BBC2008 yield criterion in the prediction of the fracture at 12 mm for cylindrical cup of DKP6112 .....	149
Figure. 8.57. Comparison of the different constitutive models in the prediction of the fracture using the new DFC at 18 mm of punch travel for DKP6112 .....	150
Figure. 8.58. Comparison of the different constitutive models in the prediction of the fracture using the new DFC at 12 mm of punch travel for DKP6112 .....	150
Figure. 8.59. Comparison of the different constitutive models in the prediction of the fracture using the new DFC at 19 mm of punch travel for SS304 .....	151
Figure. 8.60. Comparison of the different constitutive models in the prediction of the fracture using the new DFC at 14.5 mm of punch travel for AA5450 .....	152
Figure A.1. ABAQUS CAE post processing environment .....	165
Figure A.2. An example of the generated model file .....	166
Figure A.3. Visual FORTRAN environment linked with Microsoft Visual studio. ....	166
Figure A.4. Intel Fortran build environment .....	167
Figure B.1. A flowchart to determine the criterion unknown <i>B</i> .....	169
Figure C.1. Flowchart showing the implementation of the new DFC .....	171

## LIST OF SYMBOLS

Symbol	Explanation	Symbol	Explanation
$D$	Damage parameter	$\Delta r$	Planar anisotropy parameter
$E$	Modulus of elasticity	$\varepsilon_1$	In-plane major strain
$F(\sigma, Y)$	Yield function	$\varepsilon_2$	In-plane minor strain
$FIP$	Fracture indicator parameter	$\bar{\varepsilon}$	Equivalent strain
$FLCF$	Forming limit curve at fracture	$\tau_{max}$	Maximum shear stress
$FLCN$	Forming limit curve at necking	$\bar{\varepsilon}_f$	Equivalent strain at fracture
$g(C_i, \rho)$	Material parameters dependent function	$\bar{\varepsilon}^p$	Equivalent plastic strain
$G$	Modulus of shear	$d\lambda$	Plastic multiplier
$H$	Hardening parameter	$\nu$	Poisson's ratio
$K$	Strength coefficient	$\rho$	Strain ratio
$n$	Hardening index	$\sigma_m$	Hydrostatic stress
$r$	Normal anisotropy parameter	$\sigma_y$	Yield stress
$r_\theta$	Anisotropy factor in the $\theta$ direction from RD	$\sigma_\theta$	stress value in the $\theta$ direction from RD
RD	Rolling direction of a sheet	$\sigma_{max}$	Maximum principal stress
$S_{ij}$	Deviatoric stress	$\bar{\sigma}$	Equivalent stress
$SDV$	State dependent variable	$\omega_{max}$	Highest frequency in the system
$t$	Blank thickness		
TD	Transverse direction		
$Y_{ref}$	Reference yield stress		
$\alpha_{ij}$	Back stress parameter		



## **CHAPTER 1**

### **INTRODUCTION**

#### **1.1 Motivation**

Everybody in his environment has experienced fracture phenomenon somehow. It can be a dish fallen from your hand and broken to pieces or a breakdown in the car crankshaft which leaves a big harm on the vehicle motor or a collapse in the columns of a big bridge which will carve irreparable and undesirable damages in the memories.

Human being instinctively explores the nature of the phenomena. This curiosity has helped them to find a way to improve their life styles throughout the history. With the industrial revolutions, the scientists have tried to enhance the processes and decrease the cost of the production. Fracture phenomenon is one of those problems that always have been investigated by many to find the mechanisms and avoid the upcoming damages.

The formability and the ductility of the materials may categorize the fracture phenomenon to ductile and brittle but the truth is that when a material reaches beyond a limit, it fails. The failure mechanism is believed to be related with the material parameters by mechanical and material engineers. Two points of views have been extended; a view which relates the fracture with the physical and atomic parameters and the other one is relating the fracture with the phenomenological parameters of the materials. Both of the theories are used to solve the fracture based issues in the industrial processes like sheet metal forming nowadays.

#### **1.2 Background**

Metal forming process, is the series of operations during which a given material of a simple geometry, is transformed into a desired part having a complex geometry with well-defined shape, size and accuracy. Metal forming generally is classified into sheet forming and bulk forming processes. Bulk forming is the process where the work piece

is subjected to triaxial stresses like forging, rolling, extrusion, and drawing. However, in sheet metal forming because of the low thickness values, the blank is in the plane stress conditions. Sheet metal forming plays an important role in the manufacturing world. Over the last decade, due to innovations and developments of the new materials and their superior functionalities, sheet metal forming becomes more and more popular, its application areas getting wider and it is turning out to be one of the most desirable manufacturing processes throughout the world. It's applications in appliances, automotive industry, aerospace industry, food and drink packing, building materials etc. seem impossible to be replaced by any other manufacturing process.

Despite its wide use, the development of sheet metal forming processes is limited with long lead times, which originated from much iteration of tryouts on expensive prototype tooling. Furthermore, the sheet metal forming process is very sophisticated and can only be understood through a considerable amount experience. Sheet metal formability is affected by a large number of parameters such as die and press design, material properties, blank configurations and the complex interaction between the blank and tooling.

There are many types of sheet metal fabrication for engineers to choose from. Deep drawing, blanking, piercing, notching, slitting, trimming, flanging, ironing, bending, spinning, stretch forming, rubber forming, hydroforming, and high-energy-rate forming (HERF) etc. are all different methods used for creating desired shapes out of a sheet metal.

### **1.2.1 Deep drawing Process**

Deep drawing is the forming of sheet metal stock, commonly referred to as a blank, around a punch. The edges of the metal blank are restrained by rings and the punch is deep drawn into a die cavity to achieve the end shape that is desired. Regardless of the many factors involved affecting the draw quality, the most important element to a successful sheet metal deep drawing operation is the smoothness of sheet metal flow. There are many shapes that can be made through deep drawing and stamping such as cups, pans, cylinders, domes and hemispheres, as well as irregular shaped products. Automotive and aerospace industries are using deep drawing process very extensively in manufacturing of their products. Appliances, auxiliary parts and building industry

are the other areas where deep drawing is used and cannot be replaced by any other manufacturing process at least in the near coming years.

### **1.2.1.1 Important factors in deep drawing**

*Limiting drawing ratio (LDR), tooling geometry and material parameters* are some of the important parameters which are affecting the deep drawing process. The drawability of sheet metal which is commonly expressed with limiting drawing ratio (LDR) is defined as the ratio of the largest blank that can be drawn without tearing to the punch diameter in cup drawing. It can provide useful information for tool design before dealing with the expensive tryout procedures. Punch's profile, shape and radius, die radius and clearance between punch and die are some important geometry parameters that affect the process commonly.

Punch nose radius is an important factor, the sharper the die radius, the greater the maximum load exerting by the press due to increasing in the work done as plastic bending; consequently the limiting drawing ratio (LDR) will be limited. With a generous punch radius, the failure location moves away from the punch radius where the wall has been strengthened by more work hardening.

Die radius named also as draw radius is the radius on the draw die where the material flows through. The draw radius should be approximately four to six times the metal thickness for most applications. The draw radius has a large effect on the punch force required to pull the metal into the draw cavity. As the metal passes over the radius it is bent and then straightened to form the sidewall of the drawn cup. Too small a radius can lead to fracture because more force is required to pull the metal over a small radius than a larger one. In addition, too small a radius will more severely strain the metal increasing work hardening. The greater the draw radius, the larger the LDR will be if the probable small defects are neglected.

Draw bead height and shape controls the material flow during the process and is used when the general blank holding operations cannot satisfy the desired part drawing. Draw beads can control the thickness variations and circumferential compressive stresses in the flange area which can prevent the blank from buckling in this region and will improve the LDR.

Clearance between die and punch is another determinative factor in deep drawing. Greater clearance will lead to puckering tapering and bell mouth but will increase the LDR. A net clearance should be larger than blank thickness clearly and the amount of 30% is suitable most of the times.

Strain hardening index ( $n$ ), anisotropy ( $r$ ), strength coefficient ( $K$ ) and sheet thickness ( $t$ ) are the most important material parameters which affect the blank forming and should be considered in all investigations related to sheet metal forming processes. Briefly higher strain hardening and normal anisotropy factors will improve forming process and lower sheet thickness will restrict the deformation where the effect of strength coefficient is complicated and should be considered in combination with the other parameters.

Process parameters like sufficient pressing speed allow the materials to flow through the tool. During deep drawing, if the process is too fast, the corners will begin to crack. For example in the tensile test, rate sensitivity does not affect the strain at which the tension stress reaches a maximum, but it influences the rate of growth of a neck. However, in biaxial tension test, rate sensitivity delays growth of neck.

Lubrication has two opposing effects in deep drawing. Lubrication of the flange and die lip reduces the frictional work and helps the LDR to increase. However, high friction between the cup and the punch causes the potential failure location move away from the punch radius toward the material which has been work hardened more and consequently it increases the LDR.

### **1.2.1.2 Instability in deep drawing**

Sheet metal specimens may fail due to different conditions but there are three basic failure types; wrinkling caused by compressive instability, surface defects and rupture or tearing due to exceeding the material capabilities (tensile instability).

Most of the tests to evaluate the formability of sheet metals in sheet forming processes and particularly in deep drawing focus on the fracture failure mode. Fracture usually follows a necking, i. e. a localized thinning of the metal. Therefore, necking is usually considered as a failure mode as well.

*Wrinkling* is a phenomenon which causes the process to fail due to compression stresses and so it must be prevented. There are two general methods to avoid wrinkling:



choosing the appropriate blank holding force and using draw beads. Two types of blank holding applications exist: clearance type blank holders and pressure type blank holders. In the first one, the clearance between the blank holder and the die is kept constant. This type can be assumed as a plane strain conditions. In the second type, blank holder can move freely which will give necessary space to the material to get thicken. The force required to prevent wrinkling should be applied directly to the blank holder after calculations. Since controlling the blank holding force is a sophisticated operation which needs so complicated control algorithms, the constant blank holding force is utilized most of the times.

Drawbeads are the other method to avoid the wrinkling formation. In this method, material is held tightly between a groove and the male of the groove and forced to flow on the blank holder which will reduce the circumferential compressive stresses and prevent the wrinkling. There should be very accurate calculations regarding to these drawbeeds.

*Surface defects* can affect the appearance of the sheet metals and will occur because of the inappropriate friction between tooling components, material parameters and geometrical characteristics of the blank; hence, to obtain a good appearance, special attention should be made in the design steps.

*Necking* is one of the most complicated and challenging phenomena in sheet metal drawing. Being familiar enough to necking phenomena will lead to well-designed tools and processes with minimum tryouts which is one of the most time consuming and costly processes in sheet forming.

*Tearing* in deep drawing occasionally takes place along the punch radius, but it can also be observed in wall or in die profile depending on the friction and loading conditions (Figure 1.1).

Generally, the main reason for fractures in the deep drawing process is a too large tensile stress in the cup wall. If the forces on a blank in the flange area is too high or is not capable enough to tolerate the stresses on the wall, the fracture process will initiate.



Figure 1.1. Different types of the fracture in the cup drawing

### 1.2.2 Yield criterion and Hardening rules

A yield criterion is an important concept in plasticity which is a term defining the limit of elasticity in a material and the onset of plastic deformation under any possible combination of stresses. It is used together with a stress-strain curve as the material input for numerical simulations of the forming processes. The coupling of the yield surface and hardening law in a numerical framework can be used as a tool to evaluate the formability of the material. Yield criteria can be isotropic or anisotropic according to the material behavior. Isotropic yielding formulations are used in the sheets where the material is homogenous enough, but for most of the processes, the material is not showing the same behavior in the different directions and is known as anisotropic material.

In sheet metal working, anisotropy is subdivided into normal and planar anisotropy. Normal anisotropy affects the maximum drawability of sheet and increases the LDR whereas planar anisotropy leads to earing. The anisotropy factor is defined as the ‘resistance to thickness change’ in some texts and is used to model the anisotropic and orthotropic yield criteria:

$$r = \frac{\varepsilon_w}{\varepsilon_t} \quad (1.1)$$

where  $\varepsilon_w$  and  $\varepsilon_t$  are the strains in the width and thickness directions respectively. For the isotropic conditions,  $r = 1$ . A high  $r$ -value suggests that there is a high resistance to thinning and therefore a high strength in biaxial tension in the plane of the sheet and in through-thickness compression.

Although the  $r$ -value is defined as the width to thickness strains ratio, the thickness strain of a sheet cannot be measured accurately. Instead the thickness strain is found from the width and length strains ( $\varepsilon_t = -(\varepsilon_w + \varepsilon_l)$ ). The  $r$ -values vary with the test direction in the plane of the sheet. In orthogonal anisotropy three  $r$ -values are

determined; along the rolling direction (RD), along 45° to RD and in the transverse direction (TD). These values are denoted as  $r_0$ ,  $r_{45}$  and  $r_{90}$  respectively. It is customary to define an average value as:

$$\bar{r} = \frac{r_0 + 2r_{45} + r_{90}}{4} \quad (1.2)$$

The height of the walls of drawn cups usually has peaks and valleys. This phenomenon is known as *earing* in deep drawing. It is one of the defects which is caused by anisotropic properties of the sheet known as planar anisotropy.

There are commonly four or eight ears, but four ears are most usual. The ear height and angular position correlate well with the angular variation of r-value. For four ears, earing is described by the parameter as:

$$\Delta r = \frac{r_0 - 2r_{45} + r_{90}}{4} \quad (1.3)$$

If  $\Delta r > 0$ , there are ears at 0° and 90°, and if  $\Delta r < 0$ , ears are at 45° (Figure 1.2). For instance, steels usually have positive  $\Delta r$ .

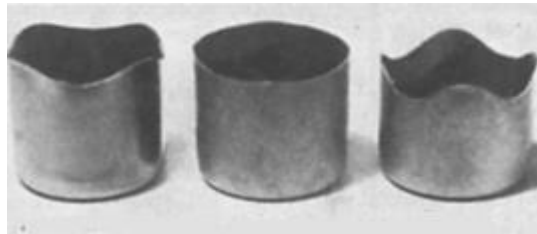


Figure 1.2. The effect of planar anisotropy in sheet metal Earing

To model a sheet metal process correctly, implementing the correct yielding locus is inevitable; otherwise, the obtained numerical solutions will not represent the actual deformation history in the material. Anisotropic and orthotropic yield criteria use the anisotropy coefficients,  $r_0$ ,  $r_{45}$  and  $r_{90}$  to model the material behavior correctly and precisely.

The other important issue here is to select the appropriate hardening model based on the nature of the sheet forming process. Normally the isotropic hardening models are used widely in most of the processes. In the processes where bending and unbending deformations take place, to better model the material constitutive behavior, kinematic and combined hardening models are used. Deep drawing is a process where bending

on the die shoulder and unbending on the punch shoulder may affect the process and hence these types of the hardening models can be more helpful.

**1.2.3 Forming Limit Diagram (FLD)**

The forming limit diagram (FLD) is another important concept utilized for the evaluation of the formability of sheet metals. A plot of the combination of strains that lead to failure is called a forming limit diagram or FLD. Using these curves, the onset of failure due to local necking or potential failure points on the deformed part under different loading histories may be predicted and studied.

The in-plane strains can experimentally be observed for a wide range of the loading paths. The commonly used method is to print or etch a grid of small circles on the blank before deformation; then when the sheet is deformed, the circles turn into ellipses. The principal strains can be found by measuring the major and minor diameters after straining with comparing to the initial diameter. These values at the necking or fracture indicate the failure condition, where the strain conditions below these drawn lines are in the safe region (Figure 1.3).

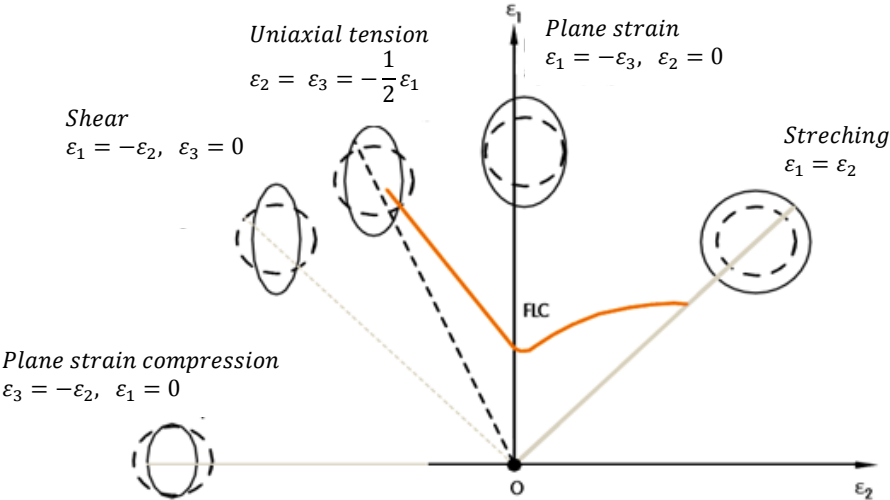


Figure1.3 Schematic of the forming limit curve (FLC)

In the newly developed methods, the deformation history of each dotted point printed on the specimen before deformation is measured by optical equipment. Some of the deformation modes can be explained as:

- Stretching, or biaxial tension: this is accompanied by thinning of the blank and typically occurs using the spherical punches in the deep drawing process.
- Plane strain tension: usually occurs in the vertical walls of the cup, because of the tensile stress due to the pressure employed on the flange region.
- Uniaxial tension: this is the situation happening in the tensile tests and it usually takes place in the transition area between the flange and wall regions in the deep drawing process.
- Shear deformation: this kind of deformation can happen on the blank-holding region if the fixed clearance is used as a blank holding process.

#### **1.2.4 Ductile Fracture**

One of the most important and key concepts in the entire field of materials science and engineering is the fracture. For engineering materials there are only two possible modes of fracture, ductile and brittle. In general, the main difference between brittle and ductile fracture can be attributed to the amount of plastic deformation that the material undergoes before fracture occurs. Ductile materials demonstrate large amounts of plastic deformation while brittle materials show little or no plastic deformation before fracture. Crack initiation and propagation are essential to the fracture. The crack propagation manner through the material gives great insight into the mode of the fracture. In ductile materials (ductile fracture), the crack moves slowly and is accompanied by a large amount of plastic deformation. On the other hand, in dealing with brittle fracture, cracks spread very rapidly with little or no plastic deformation.

The main objective here is to predict when and where the cracks can appear in the workpiece during the deformation process. FLC diagrams are not able to estimate when and where the cracks in the workpiece will appear and they just predict the instability in the specimens.

Ductile fracture criteria (DFCs) are able to consider nonlinear stress and strain loading histories in the plastic deformation which is the biggest weakness of the forming limit curves (FLC). However, the verification process, reliability and applicability of DFCs have been the main problems which limit their industrial applications.

Several criteria can be classified under the categories of ‘uncoupled damage criterion’ and the ‘coupled damage criterion’. In the uncoupled DFC category, damage accumulation process is formulated using empirical or semi-empirical methods implementing the general plasticity relations.

On the other hand coupled DFCs consider damage accumulation parameter as a part of the constitutive equations. In this model the yield locus of the materials are allowed to be modified using the damage parameter. This kind of DFC is very difficult to incorporate into the finite element codes because of the unsatisfactory calculation and computation loads which obstruct the formation of the tangent stiffness matrices. All of the criteria used in deep drawing of sheets are based on stated two categories. Lately some researchers have developed the uncoupled DFCs and changed the general plastic work function to be able to include some material parameters like anisotropy and strain hardening coefficient. In the new DFCs, the formulation constant can be assumed as a function of some material parameters to make the estimation more accurate and usable for different nonlinear strain paths.

### **1.3 Research objectives**

Forming limit curves are very useful tools in the sheet metal forming industry. However, they have some shortcomings which limit their effectiveness in the processes struggling with nonlinear strain paths or fracture phenomena. Due to dependency on strain paths, the instability predictions by forming limit curves are not accurate enough and also in the processes where the prediction of the place and the time of the fracture is needed, the FLC curves are not applicable. Furthermore, most of the times properties of a coming sheet batch in a factory is different from the former one; thus, existing FLC is not valid anymore and the new experimentally determined FLCs are needed which are both complicated and time consuming tests. Therefore there should be a method free from these limitations to be able to precisely model the fracture phenomenon.

Usually the term *ductile fracture* is used for the processes where there is a noticeable plastic deformation prior to the fracture, and is in contrast with the brittle fracture where there is not any distinct plastic deformation before the fracture. Ductile fracture criteria can fulfill all requirements related to the fracture in the metal parts. In the ductile fracture process there are commonly three steps named as nucleation, growth

and coalescence. Most of the ductile fracture criteria are used to indicate the initiation of the fracture by physical or phenomenological relations; while some others are related to the evolution of the initially composed cracks in the parts until the fracture. Different approaches have been used to model the ductile fracture phenomena. Some of them have concentrated on the micro and meso-scale voids and their nucleation, growth and coalescence. Some others has concentrated on the continuum damage mechanics and the damage parameters ( $D$ ) has been considered as a key concept in the fracture. On the other hand energy release rates have been taken so many attentions and there are so many criteria considering general energy function as a basic concept. Macroscopic approaches have gained much interests lately from the industry because of the simplicity in the validation and utilization. Most of the macro-scale approaches are using the general plasticity function somehow to calculate the material energy capacity. Mean stress, maximum tensile stress, triaxiality and some other relations have been used during the last fifty years to better model the total energy in which the material will fail.

To determine which approach is better, three challenges should be considered in the fracture models:

- The model parameters should be easily validated and comfortably calibrated.
- The onset of the fracture and evolution process of the cracks have not been physically measured yet; hence, using the numerical methods are inevitable which have their own difficulties and shortcoming.
- Considering the second challenge, the models should be convenient enough to be implemented to the numerical analyses.

In the present work a robust ductile fracture model based on the general plasticity function has been developed. For this purpose, the theoretical basis of the fracture initiation have been studied extensively and a new ductile fracture has been proposed. This model has been established with some experimental tests and can be used for any sheet metal forming process by doing a simple tensile testing. To verify the reliability of the criterion, many numerical analysis have been conducted and the results have also been compared with the existing ductile fracture criteria.

## 1.4 Outline of the thesis

This work consist of nine chapters, appendices and references. The background and the theory of the new ductile fracture and the used constitutive equations are given in Chapters 1-5. The Chapters 6-8 give the experimental works, the numerical verifications and results. In the Chapter 9 the conclusion of the thesis have been included.

*Chapter 1* is about the motivation, a brief background, objectives and the outline of the current work.

*Chapter 2* gives a brief history of the previous works related to the ductile fracture and constitutive equations.

*Chapter 3* describes the main objectives of this research and the methods which have been used to fulfill these goals.

*Chapter 4* provides a brief summary about the finite element method and the configurations which have been used in this work.

*Chapter 5* describes a theoretical background of the implemented constitutive equations and ductile fracture criteria.

*Chapter 6* gives the theories and basis of the new ductile fracture and the algorithms for calibration and implementation.

*Chapter 7* provides the information about the experimental tests which have been accomplished to establish and validate the new ductile fracture criterion.

*Chapter 8* gives the verification results using the numerical methods and also provides the comparison results for different DFCs.

*Chapter 9* explains all conclusions obtained in this work.



## CHAPTER 2

### LITERATURE SURVEY

Many investigations have been accomplished on the instability of sheet in deep drawing. Study on wrinkling and fracture modes of instability started long time ago and is continuing very extensively in the recent years; therefore, different methods of obtaining forming limit curves and their advantages and disadvantages have been developed.

Finite element method as an undisputed solution method in solving of non-linear problems is used widely comparing with other numerical methods; therefore many researchers have been interested in using finite element methods recently to avoid costly and time consuming experimental tests in sheet metal deep drawing. To get more accurate model, anisotropy conditions of the sheet cannot be neglected; thus, extensive investigations have been implemented on anisotropic yield criteria and related flow rules.

The basic principles of the metal forming and manufacturing processes have been explained clearly by Grote and Antonson [41]. The same subjects mostly focusing on the manufacturing processes have been published by Beddoes and Bibby [2]. These works are the most comprehensive references for those who are dealing with metal fabricating processes.

Semiatin [3] and Hosford et al. [4] have investigated most of the forming processes and their critical parameters. The effect of each parameter in any process has been explained in their works. There are extensive studies in both works about sheet metal production too. Johnson and Mellor [5] have studied the plasticity conditions of metals in the forming processes and have driven the related plasticity formulations.

Siegert and Wagner [6] have studied the deep drawing process and all parameters affecting the sheet forming like limiting drawing ratio, die and punch, shoulder radiuses, friction between the parts etc. have been considered.

They have shown the effects of the friction coefficient and die and punch shoulder radii on the deep drawing processes.

Davis [7] gave an extensive information about the tensile testing methods and the parameters that may affect the results during this test especially in the sheet metals. Different materials were tested and the results were compared to each other to show the strength and weakness of the tensile tests. Also the various methods which can be used to extract the material parameters from uniaxial tension tests have been proposed clearly based on the testing standards and the effect of each material parameter was explained briefly.

El-Sebaie and Mellor [8] developed a theoretical relation for limiting drawing ratio (LDR) of deep drawing using flat headed punch. They showed that two modes of the instability are possible in deep drawing. The first mode in the cup wall occurs under plane strain tension and the second mode is in the flange under uniaxial tension.

Colgan and Monaghan [9] investigated on the determination of the important factors influencing a drawing process, using the design of the experiments and statistical analysis. Based on their study, it seems that the punch and die radii have the greatest effect on the thickness of the deformed mild steel cups compared to the blank-holding force or friction. The smaller is the punch or die radius, the greater is the punch force and shorter is the final draw. It has been also observed that the higher speed of the drawing leads to deeper drawing which is not as expected.

Gavas and Izciler [10] studied on the effect of blank holding gap on deep drawing square cups and showed that this gap is the effective way to control the material flow. Their experimental implementation shows that a reasonable value of the blank holder gap has a great effect on the forming quality of the final part. Some failure modes have been shown and discussed briefly and a suitable blank holder gap for deep drawing of the squared cup for given tooling and material is proposed.

Lang et al. [11] studied the hydrodynamic deep drawing and showed the possible failure modes like wrinkling and fracture modes. They divided the wrinkling modes to two types: wrinkling in the flange area and wrinkling in the wall; and fracture to three types: the initial fracture, the middle fracture and the final fracture according to the deformation characters of the blanks. They also suggested the effective methods to prevent these failures in deep drawing process.

Sanay and Kaftanoglu [12] predicted the necking of the sheets using FEM and theoretical methods. Nakazima test method was simulated by applying the strain propagation criteria to determine the failure of the sheet and compared with the experimental methods and other instability criteria like maximum load instability criterion.

To evaluate the material capabilities in the sheet metal forming processes, some researchers tried to propose a robust tools like forming limit curves (FLC).

Keeler [13] was the first one who plotted the forming limit diagrams in 1961. He mentioned that the values of principal strains  $\varepsilon_1$  and  $\varepsilon_2$  can be determined by measuring the strains at fracture on sheet components using the grids of circles printed or etched before the forming. During the forming process, the circles turn into ellipses and from the minor and major axes of these ellipses, the in-plane principal strains on sheet specimens can be determined. He plotted the maximum principal strain against the minimum principal strain obtained from such ellipses and a curve showing the tolerable ranges of a sheet metal is obtained.

Swift [14] studied the conditions for instability under plane stress for a material. The strain at which instability takes place is found in terms of the stress ratio,  $(\sigma_2/\sigma_1)$ , under different conditions of applied loading. The analysis is also applied to certain cases of non-uniform stress distribution.

Stören and Rice [15] predicted the localized necking over the entire range of FLD by incorporating the  $J_2$  deformation theory of plasticity into the classical bifurcation analysis, which is proposed by Hill. They used a simplified constitutive model of a pointed vertex on subsequent yield loci such that the equations of deformation theory apply for fully-active stress increments.

Marciniak-Kuczynski model [16] assumed that there are always some imperfections in the sheet metal from manufacturing processes or geometrical imperfections like thickness variation etc. During the forming process progressive evolution of these imperfections makes the sheet metal to begin the localized in them, which causes the necking phenomenon of the sheets.

Bleck et al. [17] compared three kind of forming limit in the forming of (IF) steels. He concluded that forming limit diagram is affected by the thickness, the yield and tensile strength, and the strain hardening and strain-rate sensitivity. None of the models can

predict the forming-limit diagram reliably. The empirical NADDRG model can predict the value of FLD at the plane strain tension better than Hill-Swift's [14] one.

Avila and Vieira [18] proposed an algorithm for the prediction of the right-hand side of forming limit diagram (FLD) using the methodology proposed by Marciniak and Kuczynski. Five different yield criteria were used. It was observed that the predicted FLD was strongly influenced by the type of yield criterion used in the analysis.

Aghaie-Khafri and Mahmudi [19] proposed an analytical approach for calculation of forming limits in sheets having planner anisotropy. This method can estimate the FLC of the steel materials but it is not suitable for aluminum alloys. Despite previous models this model is capable of using different constitutive equations related to different deformation phases. They calculated the homogenous deformation phase based on both rate-sensitive and rate-insensitive hardening laws.

Slota and Spisak [20] had a comparative investigation of three mathematical models (M-K model, Hill Swift model, Sing-Rao) and an experimental model NADDRG in their work. They showed that the classical Hill-Swift and M-K models deliver too small  $FLD_0$  values. The method proposed by Sing-Rao was in good agreement with experimental methods for some steel sheets. They also found that FLD is affected by the thickness, the yield and tensile strength, and the strain hardening of the blank.

Wang and Lee [21] were the other researchers who investigated on the effect of yield criterion on the shape of forming limit curves. They considered three yield criteria Hill48, Hill90 and Hill93 with two materials SPCC (JIS G3141) and Al6061-T4. A small wrinkle appeared in the simulated result when Hill90 was found, which was the main difference compared with the result using Hill48. However, for Al6061-T4, it is shown that the simulation result with Hill90 could define the drawing process more accurately than Hill48 but there is not huge differences in between and Hill48 model still can be used effectively.

Despite all capabilities of the forming limit curves (FLCs) which are the main reason still most of the industries are using them, these curves have some limitations and shortcomings that question their reliability and trustfulness which also limits their extensive use in the scientific works. Strain path dependency and complicated experimental test requirements are some of those problems.

Yoshida et al. [22] studied the effect of changing strain paths on the forming limit stresses of sheet metals using a phenomenological plasticity model. They successfully measured the forming limit stresses of an aluminum alloy tube for many linear and combined stress paths, using a servo-controlled, internal pressure–axial load type testing. They found that the forming limit stress curves (FLSCs) were almost path-independent, at least within their experimental range of parameters. They also found that forming limit stresses for the combined loading, which consists of two linear strain paths without unloading between the first and second loadings, clearly depended on the strain path; thus, to have an independent FLSC's there should be unloading between the first and second loadings clearly.

Chakrabarty and Chen [23] showed a complete solution for the plastic instability of a plane sheet. Sheet is biaxially stretched in such a way that the ratio of the loads applied in two orthogonal directions in the plane is held constant during the uniform straining that precedes instability. Analytical expressions are derived for the effective strain and the principal surface strains at instability as functions of parameters representing the initial and final stress ratios, permitting a numerical evaluation of the physical quantities in a straightforward manner.

Arreieux [24] proposed a method for calculation of forming limit stress curves (FLSC) to decrease the effect of strain path on the FLC's. He used Hill48 yield criterion to model anisotropic material and calculated FLSC for anisotropic titanium sheets. To show the effectiveness of the method, forming limit curves for various strain path shapes were determined experimentally and their related FLSC were calculated and plotted. He concluded that FLSC is not dependent to strain path where the FLC's are.

Boudeau and Gelin [25] investigated some macroscopic and microscopic effects of material parameters on the forming limit curves. They understood that the anisotropy has less effects on the FLCs while  $\rho < 0$  but it has significant effects on the right hand side of the diagrams ( $\rho > 0$ ). Also they observed that the crystalline structure has strong effect on the FLCs due to the differences in the number of the slip lines in the material crystals. They concluded that the cubic materials have better formability than the FCC materials.

Nurcheshmeh et al. [26] proposed a method based on the M-K model to calculate the forming limit stress curves (FLSC) for steel and titanium materials. They investigated

the dependency to the strain path of the conventional FLCs too and showed that their relation can overcome the path dependency issue very effectively for the pre-strain where  $\bar{\epsilon} < 0.35$ , but for the loading histories with larger pre-strains the curves shift upward. It means that for the higher values of the pre-strains, the FLSC curves also show slightly path dependency.

Yield criteria and their effects on the forming processes have been investigated by many and different kinds of isotropic yield formulations have been developed. Beside all isotropic yield criteria, there are so many anisotropic yield criteria which have been developed in recent years to get more accurate material models.

In 1948, Hill [27] proposed an anisotropic yield criterion as a generalization of the Von-Mises criterion. He assumed the materials with three orthogonal axes of anisotropy, x, y, and z about which the properties have symmetry. The yz, zx, and xy planes are the planes of mirror symmetry. In a rolled sheet it is conventional to take the x, y, and z axes as the rolling direction, the transverse direction, and the sheet normal. The theory also assumes the equal tensile and compressive yield strengths in every direction. He developed another criterion in 1993 [28]. The new yield criterion attempted to model some basic aspects of the yielding and plastic flow of textured sheet, especially a specific combination of properties which is relatively common but not covered by existing theories. A particular attention was paid to situations where the ratio  $r_0/r_{90}$  may be far from unity, while  $\sigma_0/\sigma_{90}$  may or may not be equal to one. This criterion utilizes five independent material parameters, which can be determined from uniaxial and biaxial experiments, to describe a wide range of material properties of sheet metals.

Siguang et al. [29] investigated on forming limits of thin sheets using a yield criterion recently proposed by Hill (1993). He found that limit strains are strongly dependent on the shape of the yield locus. A more rounded yield locus increases the forming limits, while its elongation along the balanced biaxial tension direction reduces the limit strains. In the positive minor strain regime of the FLD (typical for stretching operations), the parameter  $\alpha_b$  ( $\sigma_0/\sigma_b$ ) is found to exert significant influence on the limit strains. An increase in  $r_0$  or  $r_{90}$  will enhance the formability of the sheet.

Hosford [30] proposed a yield criterion independently of Hill which one may consider this criterion as a particular case of Hill's yield criterion. The essential difference

between the approaches by them consist in the different way of the determining the exponent of relation where Hosford related the exponent with crystallographic structure of the material and concluded that the best approximation for the exponent is 6 for FCC materials and 8 for BCC materials. Barlat et al. [31] proposed a general six-component yield criterion  $(\sigma_x, \sigma_y, \sigma_z, \tau_{xy}, \tau_{xz}, \tau_{yz})$  that could be adopted with no restriction to any stress state. They rewrote Hosford's isotropic criterion in a form containing the deviator principal stresses  $S_1, S_2$  and  $S_3$ . The yield function defined above was generalized to the anisotropic case using some weighting coefficients where they identified by three uniaxial tensile tests in the directions of orthotropic axes and three pure sheering tests. Barlat et al. [32] also proposed a more general expression of the yield function introduced by him in 1991. This is a criterion for the materials like Aluminum which have a plastic behavior that is very difficult to model with the other existing models. The yielding behavior was measured using biaxial compression tests on cubic specimens made from laminated sheet samples. The yield surfaces were also predicted from a polycrystal model using crystallographic texture data as input and from a phenomenological yield function proposed previously. He took into account the angles between the principal directions of the stresses tensor and the anisotropic axes to improve the performance of his previous criterion.

Kuroda and Tvergaard [33] investigated the effect of anisotropic yield criteria on the necking phenomenon by assuming that the necking is modeled with M-K hypothesis. They showed that the yield criteria have significant effects on the sheet forming processes by drawing the related forming limit curves. They also showed that the predicted localization strains are quite sensitive to the deviations from the usual assumptions in M-K-model analyses like the initial orthotropic axes of the anisotropy.

Banabic et al. [34] proposed a new anisotropic yield criterion using the phenomenological descriptions of the material. The anisotropy was introduced by means of a linear transformation of the Cauchy stress tensor applied to the material whereas Barlat's [31] approach is based on representation theorems of tensor functions. Biaxial tensile deformation tests were carried out on cruciform specimens using a computer controlled stretch drawing facility. The beginning of plastic yield was monitored by temperature measurements. Comparison with data shows that the tested criteria can successfully describe anisotropic behavior of AA3103-O aluminum sheets.

Wu et al. [35] proposed a new method for implementing some of the popular yield criteria (Hill, Barlat91, Barlat97, Barlat2005) for deep drawing of aluminum sheets. The constants of the yield functions were determined from experimental measurements of the plane-stress yield surfaces as well as yield stress and r-values. The uniaxial tensile tests along the rolling direction were employed to determine the work hardening properties of the material. They showed that all yield criteria are not suitable for sheet metals and there should be a cautious in the selecting of the proper criterion to avoid the inaccurate numerical results.

Banabic et al. [36] proposed a non-quadratic yield criterion for orthotropic sheet metals under plane-stress conditions. The criterion is derived from the one proposed by Barlat [31]. Three additional coefficients have been introduced in order to allow a better representation of the plastic behavior of the sheet metals. The new criterion has an increased flexibility due to the fact that it uses seven coefficients in order to describe the yield surface. The minimization of an error-function has been used for the numerical identification of the coefficients.

Banabic et al. [37] proposed another non-quadratic yield criterion for orthotropic sheet metals in which two additional coefficients have been introduced instead of three in previous work. The associated flow rule predicts very accurately the distribution of the Lanckford coefficient (r-value) and uniaxial yield stress, respectively.

Barlat et al. [38] proposed new linear transformation based anisotropic yield functions. Two specific convex formulations are proposed to describe the anisotropic behavior of metals and alloys for a full stress state (3D). The first yield function contains 18 parameters and can describe the anisotropic properties, flow stresses and r-values in uniaxial tension of sheet materials very accurately. As a result, this function is expected to predict at least six ears in the deep drawing simulations of circular blanks. The second function, Yld2004-13p, contains 13 parameters and does not require as much experimental data compared to Yld2004-18p for the determination of its coefficients. As a result, it can not reproduce all details of the tensile flow stress and r-value anisotropy in sheet samples, but it provides a very reasonable description of the main trends.

Aretz [39] proposed a new plane stress yield function for orthotropic sheet metals called 'Yld2003'. The yield function contains eight anisotropy parameters which can be fitted to selected experimental input data. The main feature of the new yield function



lies in its very simple mathematical form which makes it very effective and thus quite interesting for implementation in finite element codes. Special attention is paid to the flexibility of the new yield function to reproduce experimental input data. There should be an optimization method to find the required constants for the numerical analysis using the experimental tests data.

Vrh et al. [40] introduced a new yield function for highly anisotropic materials called BBC2008 which adopts the finite element numerical methods to predict the number of ears in the cup drawing process. Depending to the number of experimental data, eight-pointed and sixteen-panted models have been proposed. If the number of experimental data is lower, using an especial optimization method to find the missing constant numerically. This model is free from complicated linear transformation techniques given in the most of Barlat models and then it is very convenient to be implemented to finite element codes.

Beside all yield criteria which can affect the accuracy of the numerical simulations of the plastically deformed materials, hardening rules are the other effective issue that changes the constitutive response of the material.

Hollomon [41] maybe is the first one who showed a comprehensive equation to model the isotropic hardening behavior of the material theoretically. The constants which was proposed by Hollomon are used as material parameters extensively in all books and journals which are dealing with the plasticity. Strain hardening index ( $n$ ) and strength coefficient ( $K$ ) that were introduced by him can be calculated directly from the uniaxial tension tests to be implemented to the numerical finite element codes.

Prager [42] proposed a new method to model the work hardening behavior of the materials in the solids which was considering the effects of the cyclic loads in the forming processes. Fatigue problems for example are one of those processes where isotropic hardening models cannot give the desired accuracy. In this model the center of the yielding criterion will translate in the stress space to meet the new conditions implementing a new parameter called *back stress*, despite the isotropic hardening where the yielding locus expands and the center point will not move.

Hodge [43] proposed a method to model the constitutive equations of the materials by implementing a piecewise linear approximation techniques. In this method the flow

curve of the material is divided to the small linear parts and consequently the accuracy of any predicted yield point is directly depended on the slope of the approximated line.

Lemitre and Chaboche [44] decided to employ both isotropic and kinematic hardening models and simulate any work hardening behavior with a general model. Their formulation contains two parts where one of them models the isotropic work hardening and the other one the kinematic work hardening behavior. This is a nonlinear model in which the yield surface both expands and translates to include the Bauschinger effect of the material in the process dealing with the cyclic loadings.

Many researchers have tried to find a way to predict the initiation time and place of the fracture in the metal forming processes.

Huang et al. [45] adopted the fracture thickness of a specimen in the simple tension test as the fracture criterion of the forming limit, and is applied as fracture criterion in the FEM code. The model was based on the updated Lagrangian formulation using Hill's yield criterion. In the course of analysis, if blank thickness is equal to fractured thickness, it is considered that the forming limit of the blank has been reached.

Ozturk and Lee [46] investigated on the application of some ductile fracture criteria for the prediction of the forming limit diagram (FLD) of the sheets. Critical thinning in thickness is commonly used in press shop to determine the necking. It is assumed as necking when the thickness strain is around 18–20%. The limit strains of the forming limit diagram can be determined by substituting various stress and strain values obtained from the finite element analyses into the ductile fracture criteria. The main goal was to predict fracture or necking using the combination of finite element methods with the ductile fracture criteria.

Zadpoor et al. [47] had extensive studies on the theoretical formability prediction of high strength aluminum sheets. The studied approaches are phenomenological ductile fracture modeling, physical modeling of ductile fracture mechanism based on a porous metal plasticity model, the M–K model of sheet metal instability and a combined porous metal plasticity. They categorized the ductile fracture models to two groups. The first category of the applied models is the category of phenomenological ductile fracture criteria. These criteria do not directly model the physical mechanism of ductile fracture but predict the onset of damage, based on a macroscopically defined damage accumulation function. The second category of prediction methods are based on the

porous metal plasticity theory and deal with the nucleation and growth of voids in the metal.

Li et al. [48] investigated numerous ductile criteria and their applicability and reliability. Several criteria under the categories of ‘uncoupled damage criterion’ and the ‘coupled damage criterion’, including the continuum damage mechanics (CDM)-based Lemaitre model and the Gurson–Tvergaard–Needleman (GTN) model, are investigated to determine their reliability in ductile failure prediction. They found that a decrease of stress triaxiality ( $\eta$  -value) leads to a reduction in the accuracy of ductile fracture (DF) prediction by the DFCs in both categories (uncoupled and coupled), due to the interplay between the principal stress dominant fracture and the shear–stress dominant factor. Also for deformations with a higher  $\eta$  -value, both categories of DFCs predict the fracture location reasonably well. For those with a lower or even negative  $\eta$  -value, the GTN and CDM-based criteria and some of the uncoupled criteria, including the C&L, Ayada and Brozzo models. Besides, the applicability of the DFCs depends on the use of suitable damage evolution rules (void nucleation / growth / coalescence and shear band) and consideration of several influential factors, including pressure stress, stress triaxiality, the Lode parameter, and the equivalent plastic strain or shear stress.

Freudenthal [49] is the first one who implemented the generalized plastic work to estimate the onset of the fracture in the metals. In the proposed model,  $\bar{\sigma}$  (equivalent stress), and  $\bar{\epsilon}$  (equivalent strain), were used to calculate a constant which was utilized as the element energy capacity in the numerical models. Cockroft and Latham [50] observed that the largest tensile stress plays an important role in the ductile fractures and assumed that the fracture takes place where the maximum stress exists. Brozzo et al. [51] assumed that in addition to maximum tensile stress, the mean stress ( $\sigma_m$ ) has a significant effect in the ductile fractures and with some modifications in the Cockroft model, they proposed a new DFC model. Oh et al. [52], on the other hand, believed that the main factors affecting the ductile fractures are maximum tensile stress and equivalent stress; therefore their model included both stress terms. They showed that their model is reliable enough to estimate the fracture initiation especially in the bulk forming processes. Ayada [53] proposed a model that is based on this assumption that the ratio of mean stress to equivalent stress ( $\sigma_m/\bar{\sigma}$ ) is the most effective factor in the

ductile fracture criteria. This factor is called *triaxiality* and has been used widely in the coupled DFCs to estimate the evolution of the cracks after nucleation phenomenon.

Chen et al. [54] introduced a new model for limit prediction of sheet metal forming. They built a relationship model between maximum allowable integral value of the general plastic work criterion and the strain path. They showed that the prediction results based on plastic deformation energy are not accurate if a single material constant is used for the different strain paths; therefore, they introduced a new criterion in which there is a function of material parameters like hardening index, normal anisotropy and blank thickness instead of a single constant.

Shahani et al. [55] investigated the effect of thickness on ductile fracture toughness of thin specimens made of steel alloy. The results show the significant effect of thickness on fracture toughness. It is observed that in low thickness,  $J_c$  (critical  $J$ -integral near the onset of slow stable crack growth) increases with the thickness increase until it reaches a maximum; however, further increase in the thickness causes the  $J_c$ -value to decrease.

Micari et al [56] proposed a method for prediction of ductile fracture in square boxes. Their formulation is based on Tvergaard and Needleman yield condition. The flow rule associated with the yield criterion is introduced in a finite element explicit formulation. By this method the developed method allows to calculate the void volume fraction value during the deep drawing process to predict the insurgence of tearing by comparing the maximum achieved void volume fraction with the value corresponding to the coalescence of microvoids.

Han and Kim [57] investigated on the forming limit curves at fracture (FLCF) and forming limit curves at necking (FLCN) of steel sheets. To determine the constants of the various uncoupled ductile fracture criteria [49-53], a numerical procedure, which is based on plane stress condition and Barlat's non-quadratic anisotropic yield criterion [31], was used. To predict precisely the experimental FLCFs with both the linear and the non-linear strain paths, a combination of the Cockroft–Latham [50] ductile fracture criterion and the maximum shear stress criterion which is an empirical ductile fracture criterion in sheet metal forming process was suggested. The criterion could well predict the FLCFs with the rather complex shape as well as the linear one.

Komori [58] investigated the mechanics of ductile fracture in bulk metal forming processes using node separation method by a finite-element method. In this method, when the fracture criterion is satisfied for an element, the nodes belonging to both the element and neighboring elements are separated. Since a crack will grow along the sides of the element, the physical meaning of fracture is clear. The effect of six ductile fracture criteria on the behavior of crack propagation in shearing is investigated using suitable simulation program.

Tahuda et al. [59] studied the reliability, applicability and the accuracy of the different uncoupled ductile fracture criteria on the prediction of the fracture initiation using Hill48 anisotropic yield criteria. Four kind of materials have been used to show that these kind of criteria not only are effective on the highly ductile materials like steels but also they can be used to estimate the fracture on the low ductile materials too. For this purpose three aluminum alloys have been utilized in the experimental tests.

Shim et al. [60] used some of the ductile fracture criteria mentioned before [49-53] in determining the onset of tearing in the blanking of thin sheets. Due to the thin materials, it is essential to control the burr occurred during operation process. To predict the burr formation in blanking process, a commercial finite element program was used, and the ductile fracture criterion with combination of the element killing method was used to estimate when the fracture happens and to investigate the section of the sheared surface in this process.

Bai and Wierzbicki [61] considered that both the hydrostatic pressure effect and the effect of the third deviatoric stress invariant (or Lode angle parameter) on the constitutive description of the material in contrast to classical metal plasticity theory which assumes that the hydrostatic pressure has no effect on the material strain hardening, and the flow stress is not dependent to the Lode angle parameter. A new 3D asymmetric fracture locus, in the space of equivalent fracture strain, stress triaxiality and the Lode angle parameter, was suggested.

Uthaisangsuk et al. [62] applied the continuum damage mechanics model as a sheet metal failure criterion for typical car body steel. Continuum damage mechanics describe the damage evolution in the microstructure with physical equations, so that crack initiation due to mechanical loading can be predicted. The maximum points of the load-displacement curves, which characterize the macroscopic crack initiation in the experiment, were estimated by the simulations using GTN yield function. To apply

the different failure criterions, an attempt was made to predict crack initiation by two-step forming tests. The hole expansion test allows for simultaneous radial compressive and tangential tensile stresses around the hole area. It can be observed that the FLD does not provide a satisfactory prediction of crack initiation, because of the change in the forming history by the two-step forming tests and because of the complex loading by the hole expansion tests. However, the FLSD presented a better failure criterion and a more precisely prediction.

Khelifa and Oudjene [63] investigated the anisotropic constitutive equation coupled with ductile damage in prediction of the time and place of the fracture during the 3D stamping operations. A new approach based on the strong coupling between anisotropic elasto-plasticity with mixed non-linear work hardening (isotropic and kinematic) and a ductile damage is proposed. This model is implemented in ABAQUS/Explicit finite element code. The approach presented here describes the ductile damage based on the thermodynamics of irreversible processes with state variables.

Saanoumi [64] proposed an advanced fully coupled numerical methodology for virtual metal forming including the ductile damage occurrence from both theoretical and numerical point of views. He used a fully coupled constitutive equations associated with isotropic and kinematic hardening rule as well as the ductile damage implemented into the general purpose finite element code for metal forming simulation. Also the GTN damage theory model [48] which is based on the void volume fraction evolution and its effect on the plastic yielding was used.

Stoughton and Yoon [65] investigated the maximum shear stress (MSS) fracture criterion combined with the stress-based forming limit curve to develop a complete description of metal forming limits including both necking and fracture. Fracture polygon was predicted from the stress-based FLC and an analytical equation with the function of the local fracture strain. The locally measured fracture strain dominates the accuracy of the predicted fracture stress for the analytical approach. The new forming limit criterion determines fracture and necking indices on the top and bottom surfaces of the sheet which helps to define a through-thickness parameter for the fracture. The criterion is capable of differentiating forming processes where fracture may occur without necking, even for ductile metals.

Hongsheng et al. [66] adopted the combination of FE simulation with tension tests to predict accurately the forming limit in sheets. Material constants determined by means of the combination method can increase the prediction precision of forming limit. Usually, simple test method is applied to determine material constants. In the present study, uniaxial tensile test and plane strain tensile test with a notch located on the test samples are adopted. For sheet metal with obvious necking in tension process, the strain path change after necking, which is difficult to be measured, is unable to be considered in the determination of material constants, thus the determined material constants are not accurate enough.

Li and Wierzbicki [67] modified the Mohr–Coulomb and proposed a partially-coupled approach that is used to have the advantages of both coupled and uncoupled models. The equivalent strain at fracture is calibrated from the three-parameter Modified Mohr–Coulomb (MMC) criterion and the damage-induced softening is introduced in the post-initiation range where the increment of damage is proportional to the increment of plastic strain. When adopting this approach to the FEM simulation, the fracture begins in the element after the locus of equivalent plastic strain at fracture is reached and then the softening phenomenon is started in the post-initiation process. The element will not be deleted until the damage reaches to a critical value.

Li et al. [68] proposed an extensive experimental and numerical study in deep drawing leading to initiation and propagation of cracks within the realm of MMC fracture model. Shear-induced fractures which cannot be predicted by the existing FLD approach can be modeled easily here. Furthermore, the strain paths at critical locations were not proportional so that the history dependent fracture model to be outlined in what follows must be used. Shear-induced fracture are very sensitive to the failure criteria during sheet metal forming and the MMC fracture criterion is proved to be an accurate criterion in calibrating the fracture limit of sheet metal forming.

Xue [69] proposed that the bifurcation point for the localized deformation can be defined from the sense of energy dissipation. It is understood that the localization mode takes the least energy for the same prescribed boundary condition, which in the present case is understood as the onset of the diffused necking. He showed that the governing factor for the shape of forming limit curves is not the damage itself, but the rate of damage and the rate of weakening from the plasticity induced damage, which is a function of the stress states on the loading path.

Kim et al. [70] proposed a new model named as phenomenological stress-modified fracture model. The main advantage of this model is that, for the given material, the model parameters can be determined easily from notched bar tensile test results. When the stress-modified fracture strain model is settled, incremental damage will be calculated by the ratio of the plastic strain increment to the fracture strain and then total damage will be measured using linear summation. When the accumulated damage reaches to unity at a finite element integration point, all stress components will be reduced to a small value to simulate progressive failure.

The finite element method has been extensively used to analyze the forming processes. Vladimirov et al. [71] considered the plastic anisotropy and nonlinear kinematic and isotropic hardening rule and proposed a new method for numerical calculation of fracture model. The model is obtained from a thermodynamic framework and is established upon the classical decomposition of the deformation gradient into elastic and plastic parts. A new kind of the exponential algorithm that keeps both the plastic volume and the symmetry of the internal variables were implemented for obtaining the time integration of the evolution equations. The algorithm uses the spectral decomposition to calculate the exponential tensor functions in closed form.

Dunne and Petrinick [72] have given comprehensive information about the plasticity in the solid mechanics including the various yield and hardening models and their formulations. The different constitutive models have been explained in details and the methods for calibrating and validating of these models have been explained widely. They have applied the plasticity models numerically into the finite element analyses including many one-dimensional examples enhancing understanding and developing insight and also several examples of implicit and explicit plasticity implementations into commercial finite element software.

The work by Reddy [73] is one of the most well-known studies in the finite element method which contains strong conceptual approaches, clear examinations of the mathematical fundamentals of FEM, and also provides a general approach of engineering application areas. This approach is somewhere between the approaches that are completely mathematical and those that are structural mechanics oriented. It is known for its detailed and carefully selected example problems covering a wide range of engineering problems.



Joaquim and Spencer [74] have given the basic methods used in finite difference, finite element and finite volume solving the partial differential equations. They have started to consider the general governing equation of the computational mechanics which shows the mechanical behavior of the bodies and known as conservation laws. Then using the conservation of mass and energy together with the momentum theory, they derived the necessary relations to model the mechanical behaviors in the numerical methods. They have also solved some well-known problems to compare the applicability these three numerical methods.

Thomee [75] proposed a comprehensive work about the history of numerical analysis starting from partial differential equations in 1928. They have given the first attempts in the development of the finite difference and finite element methods step by step. In this work the mathematical basis of the important issues in the numerical analysis like stability and convergence have been explained extensively.

Reddy and Gartling [76] introduced the basic theory of FEM which gives an updated presentation of basic finite element methods in two and three-dimensional spaces. It is effectively implemented to analyze problems of heat transfer and fluid mechanics. It also contains good examples, problems, and references of the plasticity governing equations and integration schemes.

Rebello et al [77] proposed a good study on the numerical modeling of the forming processes. Although most of the numerical methods used in this work are based on the finite difference solution procedure, but it includes some finite element methods employed on the industrial forming processes too. This work clearly defines the numerical difficulties of each process and proposes a possible solutions to that.

Hibbitt and Karlsson [78] gathered a very comprehensive information about finite element modeling of continua and fluids using over 100 journals and books which have been published as a theory manual for the commercial finite element software ABAQUS. The key concepts of all approaches in the finite element analyses used in this software have been proposed in this work. The formulations related to the explicit and implicit methods, the contact algorithms, the element formulations and the constitutive models have been explained extensively by simple examples.

Analyses of nonlinear static problems in solid mechanics is the issue Kutt et al. [79] investigated precisely. They showed that the application of slow-dynamic, quasi-static

methods in the static problems may result in unwanted dynamic effects due to the inertia force effects on the governing equations. To minimize these undesirable dynamic effects in the simulations, some numerical techniques have been proposed and proved to be operative enough.

## CHAPTER 3

### SCOPE OF THE THESIS

Forming limit curves perhaps are the most applicable tools in the sheet metal forming processes. However, due to some limitations especially in the deformations with nonlinear strain paths or fracture phenomena, their reliability has been questioned. Due to dependency on the strain paths, their instability predictions are not accurate enough and also in the processes where the prediction of the fracture is desired, the conventional FLC curves are not that applicable. Furthermore, experimentally determination of the FLCs is very complicated, expensive and time consuming process. On the other hand, DFC is a method free from these limitations and is able to precisely predict the fracture initiation too.

There are so many approaches to model the fracture initiation in the forming processes but paying attention to some challenges will help to select the appropriate DFC regarding to the deformation realities:

- The model parameters should be easily validated and conveniently calibrated.
- Use of the numerical methods with its shortcomings and challenges are inevitable because the onset of the fracture and evolution process of the cracks have not been physically measured yet.
- The proposed approaches should be convenient enough to be implemented to the numerical analyses.

In the present work a new empirical uncoupled ductile fracture criterion has been successfully developed and proposed which considers the entire range of elastic-plastic deformation up to the fracture. For this purpose, the existing fracture initiation models (*energy based, damage parameter based, shear induced etc.*) have been studied extensively and a new ductile fracture has been proposed to overcome the basic shortcomings of the forming limit curves in the fracture predictions and fit the experimental data better than existing models.

The new model has been developed with some experimental tests and can be used for any sheet metal forming process by carrying out a simple uniaxial tension test. To verify the reliability of the criterion, many numerical analyses have been conducted and the results have been compared with some existing ductile fracture criteria too.

The new DFC is theoretically based on the general plastic work incorporated with the maximum shear stress criterion and to acquire the strain-path history independency, strain ratio parameter has been included in the new criterion.

Different experimental tests have been accomplished to calibrate and validate the new DFC. Forming limit curves at fracture (FLCF) of different materials (aluminum and steel alloys) have been used to calibrate the new model. Since the new DFC have four constants which should be calculated using the material parameters like hardening index, strength coefficient, blank thickness and anisotropy coefficients, the effect of each parameter should be considered cautiously. Therefore, in the calibration period, the effects of these material parameters on the shape of FLCFs were studied extensively using the data mentioned above to determine the effective parameters on each constant of the new DFC.

The new ductile fracture algorithm has been implemented to the commercial finite element code, ABAQUS, using user subroutines. The effects of different hardening models (isotropic, kinematic, and combined) and various isotropic and anisotropic yield criteria have been investigated on the new ductile fracture to determine the best formulation in which the new DFC can give the most reliable results.

In this work, to minimize the errors of the numerical calculations, two different numerical optimization methods have been implemented in the determination of the constants.

To better understand the benefits and efficiency of new ductile fracture criterion, the model have been applied to predict of the fracture in cylindrical and squared cup drawing processes as case studies and the results have been also compared with the other existing uncoupled ductile fracture models.

Experimental tests and numerical simulations have been carried out for three materials; SS304, DKP6112 (DIN EN 10130-1999) and AA5054 aluminum alloy and also four different materials extracted from the previous researches to establish and validate the reliability of the new DFC. For this purpose the criterion has been implemented to the

numerical models to predict the fracture in the Nakazima test specimens and the results have been compared with the experimental data to validate the criterion reliability.



## CHAPTER 4

### FINITE ELEMENT METHOD

#### 4.1 Introduction

Three numerical methods are commonly used to solve partial differential equations throughout a two- or three-dimensional domain: the finite difference method, the finite element method, and the boundary integral or boundary element method. A fourth, the finite volume method, is sometimes regarded as separate, and sometimes regarded as a type of finite difference method.

Finite Element Analysis (FEA) as a numerical method firstly is utilized to solve a vibration problem in 1943. The Ritz method was used in the numerical analysis and minimization of variational calculus to obtain approximate solutions for that vibration problem [75]. By the early 70's, due to the cost of newly developed computers which were owned by the aerospace, defense, and automotive industries, finite element analysis was limited. Since the computers were developed very fast through the next decade, their computing power was increased and their utilization cost was decreased simultaneously. These phenomena turned FEA into a noticeable method in the engineering and scientific system analysis due to its incredible precision.

#### 4.2 Finite Element Method

The fundamental concept of finite element method involves dividing the body under study (domain) into a finite number of pieces (subdomains) called elements. Each element has some special points called as “nodes” where solution of the problems can be obtained directly. Using so-called interpolation or approximation functions, particular assumptions on the unknown dependent variables across each element will be made and solution will be obtained due to these interpolation functions. Through this discretization process (mesh), the method sets up an algebraic system of equations for unknown nodal values which approximate the continuous solution. Since element

size, shape and approximating scheme can be varied to suit the problem, the method can accurately simulate solutions to problems of complex geometry and loadings

But to get the more accurate solutions (less error) the number of elements in the mesh should be increased. Increasing the element numbers will raise the volume of computations which will lead to some other errors and also will increase solution time. They are three sources of errors in FEM, domain approximations (discretization errors), numerical approximations (spatial and time integrations) and computation approximations (round off errors). Therefore there must be an optimal size for elements which leads to minimum errors in the final solution.

#### 4.2.1 Virtual Work Principle

Finite element schemes are generally based on an integral statement of the problem, and in continuum mechanics this statement often takes the form of a virtual work equation. In the absence of body forces, the virtual work equation for a volume  $V$  with surface  $S$  may be written as,

$$\int_V \bar{\boldsymbol{\sigma}} : \delta \dot{\boldsymbol{\epsilon}} dV = \int_S \mathbf{t} \cdot \delta \mathbf{v} dS \quad (4.1)$$

where  $\delta \mathbf{v}$  is an arbitrary vector function, termed a virtual velocity field, and  $\delta \dot{\boldsymbol{\epsilon}}$  is the corresponding virtual strain rate. The surface traction,  $\mathbf{t}$ , is related to the stress tensor by,

$$\mathbf{t} = \bar{\boldsymbol{\sigma}} \cdot \mathbf{n} \quad (4.2)$$

where  $\mathbf{n}$  is the unit outward normal to the surface. It may be shown that if equation (4.1) is satisfied for all possible functions  $\delta \mathbf{v}$ , then the stress field  $\bar{\boldsymbol{\sigma}}$ , satisfies the force equilibrium equations. If equation (4.1) is only satisfied for a finite set of functions  $\delta \mathbf{v}$ , force equilibrium is only satisfied in some conditions, and for this reason the virtual work equation is sometimes defined as a *weak form* of the equilibrium equations.

#### 4.2.2 Shape Functions

A finite element solution consists of a set of nodal values of a quantity, and an interpolation rule for calculating values at points between the nodes. The interpolation



rule is expressed through a set of shape functions which multiply the nodal values. Therefore, a velocity field  $v(x, y)$  may be written,

$$v(x, y) = \sum_{m=1}^M \Psi^m(x, y) v^m \quad (4.3)$$

where  $\{v^m\}$  is the set of nodal values ( $M$  is the total number of nodes) and  $\{\Psi^m\}$  is the corresponding set of shape functions. The shape functions are usually defined with reference to a master element, to which the actual elements are related by a coordinate transformation. Expressions for secondary variables may be derived from the interpolating function used for the primary variable. For example, the strain rate  $\dot{\boldsymbol{\epsilon}}$  is found by differentiating,

$$\dot{\epsilon}_{ij} = \sum_{m=1}^M \frac{1}{2} \left( \frac{\partial \Psi^m}{\partial x_j} v_i^m + \frac{\partial \Psi^m}{\partial x_i} v_j^m \right) \quad (4.4)$$

The strain rate components are therefore linear functions of the nodal velocities, with the coefficients being spatial derivatives of the shape functions [75].

### 4.2.3 Equations of Finite Elements

In order to solve problem for a set of  $2M$  nodal velocity components, it is necessary to generate a set of  $2M$  linear algebraic equations. This is done by selecting  $2M$  different virtual velocity fields and substituting them into the virtual work equation, generating an algebraic equation with each. In the Galerkin finite element method, the velocity fields chosen each have one zero component and one non-zero component which is equal to a shape function.

The unknown nodal values appear through the constitutive relationship on substitution of the interpolating functions for the primary variables. The nodal values can be brought outside the virtual work integrals (provided the integrands are linear functions of these values), because they are not themselves functions of position. The result is a matrix equation, with the matrix components expressed as integrals of the shape functions and their derivatives [76],

$$\begin{bmatrix} 2K_{11} + K_{22} & K_{21} & -Q_1 \\ K_{22} & K_{11} + 2K_{22} & -Q_2 \end{bmatrix} \begin{bmatrix} v_1 \\ v_2 \\ v_3 \end{bmatrix} = \begin{bmatrix} F_1 \\ F_2 \end{bmatrix} \quad (4.5)$$

where  $v_1$  and  $v_2$  are  $M$  element vectors of the  $x$ - and  $y$ -components of the nodal velocities respectively. The  $K_{ij}$  are  $M \times M$  matrices, with the component in the  $m^{\text{th}}$  row and  $n^{\text{th}}$  column being,

$$K_{ij}^{mn} = \int_V \mu \frac{\partial \Psi^m}{\partial x_i} \frac{\partial \Psi^m}{\partial x_j} dV \quad (4.6)$$

The  $Q_i$  are  $M \times L$  matrices, with the component in the  $m^{\text{th}}$  row and  $l^{\text{th}}$  column being,

$$Q_i^{ml} = \int_V \frac{\partial \Psi^m}{\partial x_i} \Phi^l dV \quad (4.7)$$

And the  $F_i$  are  $M$  component vectors, with the  $m^{\text{th}}$  component being,

$$F_i^m = \int_S t_i \Psi^m dS \quad (4.8)$$

This integral is evaluated from the information of the problem boundary conditions.

The integrals in (4.8), (4.9) and (4.10) are usually evaluated numerically using *Gaussian quadrature*, each integral being replaced by a summation and the integration is carried out element by element.

### 4.3 Finite Element Solvers

In the solid mechanics, and especially nonlinear quasi-static problems, finite element solution methods can generally be classified as either implicit or explicit and are typically solved incrementally. In the implicit approaches, a solution to the set of finite element equations needs iteration until a convergence criterion is satisfied for each increment. On the other hand, the explicit method can be used directly to determine the solution at the end of the increment, without iteration.

Rebelo et al. [77] showed that the implicit method to be desirable in smaller two dimensional (2D) problems where the explicit approach can be more preferable and efficient for sophisticated problems which are involving with contact conditions. The main reason is that the implicit solvers can experience numerical difficulties in converging to desirable solution in the analysis with large deformation history, contact

between surfaces or highly nonlinear plasticity. For solving smooth nonlinear problems, it is better to use implicit methods, but for the wave propagation analysis for example, explicit method is the first choice. There are, however, so many static or quasi-static problems that can be simulated effectively with both methods. In a typical manner, problems usually would be solved with implicit methods but some of them may have big difficulties in converging problems resulting in a large number of iterations. Such analyses are expensive in implicit method because each of the iterations requires the large set of linear equations to be solved simultaneously. The given problem may require a large number of time increments to be solved using the explicit method. However, the analysis can be more efficient implementing explicit method than the implicit one with so many iterations sometimes. [78].

If the strain and stress values at time  $t$  are known then to updated stresses ( $\sigma + \Delta\sigma$ ) and strains at time  $t + \Delta t$ , these information can be used implementing *Euler* equations; this is called an *explicit method* scheme. For example using first order *Euler* equation, stress and plastic strain can be updated as;

$$\sigma_{t+\Delta t} = \sigma_t + \Delta\sigma_t \quad \text{and} \quad \varepsilon_{t+\Delta t}^p = \varepsilon_t^p + \Delta\varepsilon_t^p \quad (4.9)$$

On the other hand, if the information in the current time is utilized to update the finite element solution, then the integration scheme is called *implicit method*.

#### 4.3.1 Implicit and Explicit Methods

Implicit integration methods are often preferred to the explicit one since they determine the residual force at each step and use iteration within the step to minimize the residual force to the specified tolerance. There are technically three methods for implicit scheme; *the tangential stiffness* method, *the initial tangential stiffness* method and *the Newton–Raphson* method. Considering the quasi-static problem, inertia effects can be negligible and then for simple static equilibrium equation for example the *tangential stiffness method* is:

$$\mathbf{K} \mathbf{u} - \mathbf{F} = \text{Res} \neq 0 \quad (4.10)$$

The solution starts with iteration from an initially guessed value for initial displacement,  $\mathbf{u}_0$ , and the corresponding tangential stiffness matrix  $K(\mathbf{u}_0)$ . In every

step the correction  $\Delta u$  will be added to previous solution to get the preferable tolerance.

$$u_{i+1} = u_i + \Delta u_i \quad (4.11)$$

where,

$$\Delta u_i = [K(u_i)]^{-1}(Res)^i \quad (4.12)$$

If the correction term to the displacement, given in equation (4.14), is calculated based upon the initial tangential stiffness matrix,  $K(u_0)$ , this is called the *initial tangential stiffness* method.

In the Newton–Raphson method the Taylor expansion of the residual forces calculated in equation (4.12) will be used and higher order terms will be neglected. The iteration will be continued until the desired tolerance is achieved [78].

In the explicit scheme, since the displacements and velocities are calculated in terms of quantities that are known at the beginning of an increment, it is not necessary to calculate the global mass and stiffness matrices and invert them. Hence, each increment in the explicit method is relatively inexpensive compared to the increments in an implicit integration scheme. The size of the time increment in an explicit analysis is limited, however, because the central-difference or forward-difference Euler operator is only conditionally stable; whereas the implicit operators are unconditionally stable and increment size has no limits.

The analysis cost in the explicit method rises only linearly with problem size, whereas the cost of solving the nonlinear problems associated with implicit integration rises more rapidly. Therefore, explicit scheme is attractive for very large problems. The explicit integration method is often more efficient than the implicit integration method for solving extremely discontinuous short-term events or processes. Also problems involving stress wave propagation can be far more efficient computationally in the explicit method than the implicit one [78].

In the *high-speed dynamic events* where it can be extremely costly to analyze them using implicit solvers where dynamic explicit methods can do the same analysis very fast and reliable. As an example of such a simulation, the effect of a short-duration blast load on a steel plate where the load is applied rapidly and is very severe, and the

response of the structure changes rapidly. Accurate tracking of stress waves through the plate is important for capturing the dynamic response.

In the *complex contact* problems, the contact conditions are formulated more easily using an explicit method than an implicit one. The explicit method is particularly well-suited for analyzing the transient dynamic response of structures that are subject to impact loads and subsequently undergo complex contact interaction within the structure. An example is the drop test where the problem involves a rapidly changing contact conditions between the specimen and floor.

The *complex post buckling* events which are unstable problems, are solved readily in the explicit solvers. In such problems the stiffness of the structure changes considerably as the loads are applied. Post buckling response often includes the effects of contact interactions.

In the *highly nonlinear quasi-static* problems where for a variety of reasons explicit method is often very efficient [78]. Quasi-static simulation problems involving complex contact such as forging, rolling, and sheet-forming generally fall within these classes. Sheet forming problems usually include very large membrane deformations, wrinkling, and complex frictional contact conditions.

The problems where the *materials with degradation and failure* exist, often lead to severe convergence difficulties in implicit analysis programs, but explicit method can model such materials very well. An example of material degradation is the concrete cracking model, in which tensile cracking causes the material stiffness to become negative. The ductile failure model for metals in which material stiffness can degrade until it reduces to zero is an example of material failure where the failed elements are removed from the model entirely [78].

### **4.3.2 Dynamic Explicit Method**

The direct-integration dynamic procedure offers a choice of implicit methods for integration of the equations of motion, while explicit method generally uses the central-difference formulations of Euler. In choosing an approach to a nonlinear dynamic problem, the length of time in implicit method compared to the stability limit of the explicit method; the size of the problem; pure displacement method or modified

second-order elements etc. can be helpful. In some cases the choice is obvious, but in many problems of practical interest the choice depends on details of the specific case.

The stability limit for the central-difference method (the largest time increment that can be taken without the method generating large, rapidly growing errors) is closely related to the time required for a *stress wave* to cross the smallest element dimension in the model; thus, the time increment in an explicit dynamic analysis can be very short if the mesh contains small elements or if the stress wave speed in the material is very high. A stability limit determines the size of the time increment as [78]:

$$\Delta t \leq \frac{2}{\omega_{max}} \quad (4.13)$$

where  $\omega_{max}$  is the highest frequency in the system. A conservative and practical method of implementing the above inequality is:

$$\Delta t = \min\left(\frac{L^e}{c_d}\right) \quad (4.14)$$

where  $L^e$  is the characteristic element length which is belonged to the smallest element of the mesh and  $c_d$  is the dilatational wave speed:

$$c_d = \sqrt{\frac{\lambda + 2\mu}{d}} \quad (4.15)$$

$\lambda$  and  $\mu$  are the *Lame'* elastic constants and  $d$  is the material density. Although the incremental solution is easy to be obtained using the explicit method, it is not unusual for this method to have so many increments (more than 100000) to solve the problem; therefore, if the number of the increments is very large, using double precession method is suggested. In order to maintain efficiency of the analyses it is important to ensure that the sizes of the elements are as regular as possible. This is so that one small element does not reduce the time increment for the whole model.

### 4.3.3 Explicit time integration

Abaqus/Explicit uses a central difference rule to integrate the equations of motion explicitly through the time, using the kinematic conditions at the current increment to calculate the conditions at the next increment. At the beginning of the increment the program solves for dynamic equilibrium, which states that the nodal mass matrix,  $\mathbf{M}$ ,

times the nodal accelerations,  $\ddot{\mathbf{u}}$ , equals the net nodal forces (the difference between the external applied forces,  $\mathbf{F}$ , and internal element forces,  $\mathbf{I}$ ):

$$\mathbf{M}\ddot{\mathbf{u}} = \mathbf{F} - \mathbf{I} \quad (4.16)$$

The accelerations at the beginning of the current time ( $t$ ) are calculated as,

$$\ddot{\mathbf{u}}^t = \mathbf{M}^{-1} \cdot (\mathbf{F} - \mathbf{I})^t \quad (4.17)$$

The acceleration of any node is determined completely by its mass and the net force acting on it, making the nodal calculations very inexpensive. The accelerations are integrated through the time using the central difference rule, which calculates the change in velocity assuming that the acceleration is constant;

$$\dot{\mathbf{u}}^{t+\frac{\Delta t}{2}} = \dot{\mathbf{u}}^{t-\frac{\Delta t}{2}} + \frac{\Delta t^{t+\Delta t} + \Delta t^t}{2} \ddot{\mathbf{u}}^t \quad (4.18)$$

The velocities are integrated through the time and added to the displacements at the beginning of the increment to determine the displacements at the end of the increment:

$$\mathbf{u}^{t+\Delta t} = \mathbf{u}^t + \Delta t^{t+\Delta t} \dot{\mathbf{u}}^{t+\frac{\Delta t}{2}} \quad (4.19)$$

Thus, satisfying dynamic equilibrium at the beginning of the increment provides the accelerations. Knowing the accelerations, the velocities and displacements can be obtained explicitly through the time. The term *explicit* refers to the fact that the state at the end of the increment is based merely on the displacements, velocities, and accelerations at the beginning of the increment. To be sure that the method is giving true results, the time increments must be quite small so that the accelerations are nearly constant during an increment. But each increment is inexpensive enough because it is not necessary to solve simultaneous equations like what is done in the implicit methods. Most of the computational expense lies in the element calculations to determine the internal forces of the elements acting on the nodes. The element calculations include determination of the element strains and applying material constitutive relationships (the element stiffness) to determine element stresses and, consequently, internal forces.

In the quasi-static analyses also the speed of the analysis often can be increased substantially without severely degrading the quality of the quasi-static solution; the end result of the slow case and a somewhat accelerated case are nearly the same.

However, if the analysis speed is increased to a point at which inertial effects dominate, the solution tends to localize, and the results are quite different from the quasi-static solution.

#### 4.3.4 Speeding up methods in the explicit solvers

It is often impractical to run a quasi-static analysis using its true time scale as the runtime would be very large. A number of methods can be used to artificially reduce the runtime of the simulation. The first involves simply speeding up the applied deformation or *loading rate* and the second involves scaling the density of the material in the model. According to the equations (4.16) and (4.17), when the density is scaled by a factor  $f^2$ , the runtime is reduced by a factor  $f$ . The latter method is called *mass scaling* and is preferable most of the times as it does not affect the strain rate in the rate-dependent materials.

It is important when performing a quasi-static simulation that the inertial forces do not affect the mechanical response and provide unrealistic dynamic results. To reduce the dynamic effects, Kutt et al. [79] recommend that the ratio of the duration of the load and the fundamental natural period of the model should be greater than five. It has been shown that by keeping the ratio of kinetic energy to the total internal strain energy in the range lower than 10 percent, dynamic effects in the model are negligible [78]. This is the criterion for quasi-static behavior that is employed in all simulations accomplished explicitly.

Mass scaling enables an analysis to be performed economically without artificially increasing the loading rate. Mass scaling is the only option for reducing the solution time in simulations involving a rate-dependent material or rate-dependent damping, such as dashpots. In such simulations increasing the loading rate is not an option because material strain rates increase by the same factor as the loading rate. When the properties of the model change with the strain rate, artificially increasing the loading rate artificially changes the process.

According to the Equations 4.15-4.17, when the global stability limit is increased, fewer increments are required to perform the same analysis, which is the goal of mass scaling. Scaling the mass, however, has exactly the same influence on inertial effects as artificially increasing the loading rate. Therefore, excessive mass scaling, just like excessive loading rates, can lead to inaccurate solutions. The suggested approach to



determining an acceptable mass scaling factor, then, is similar to the approach to determining an acceptable loading rate scaling factor. The only difference to the approach is that the speedup associated with mass scaling is the square root of the mass scaling factor, whereas the speedup associated with loading rate scaling is proportional to the loading rate scaling factor. For example, a mass scaling factor of 100 corresponds exactly to a loading rate scaling factor of 10.

In all simulations which the explicit method has been used, both loading rate and mass scaling factor have been used to effectively decrease the simulation time and the kinetic energy to internal energy ratio has been used to control the stability of the solutions and consequently obtain the reliable results for every simulation.

#### 4.4 Subroutines in the commercial ABAQUS software

There are many built-in models in the commercial ABAQUS containing various element types, contact algorithms, material constitutive models, fracture models, loading and unloading diversity, frictional behavior etc. which have made this software favorable in the scientific works. If there needed to be a modification in the present built-in models or the new models are necessary to be implemented into the numerical analysis, the current models will not cover the requirements completely and therefore it is necessary to implement the theory in the form of a user-defined algorithm.

ABAQUS has prearranged 48 different subroutines for each solver which can be used to implement user codes. These subroutines are different for implicit and explicit solvers. FRIC, UEL, UHARD (hardening parameters for isotropic plasticity or combined hardening models) and UMAT (defines a material's mechanical behavior) are some of the most utilized subroutines in implicit solutions of the solid mechanics.

UMAT subroutines must provide *material stiffness matrix* for use in the forming of the *Jacobian* matrix for the nonlinear equilibrium equations as,

$$J = \frac{\Delta\sigma}{\Delta\varepsilon} = \left( \frac{\partial\sigma}{\partial\varepsilon} \right)^{t+\Delta t} \quad (4.20)$$

In contrary to the UMAT subroutines, in the VUMAT subroutines there is no need to compose a Jacobian matrix and the calculations in the current increment are done using the results obtained in the previous time increment.

The same subroutines starting with the letter “V” can be used for the explicit solutions; however, the coding algorithm and the utilized functions are totally different from each other. For example the subroutines VUHARD and VUMAT are employed to define the hardening parameters and the desired material’s constitutive equations respectively. VUHARD subroutine which is used to implement the hardening model in the constitutive equations can be used either independently from or simultaneously with the VUMAT subroutines in the explicit solvers. Since the VUMAT and VUHARD subroutines have been used extensively in this study, it is necessary to have a brief background about these subroutines.

The operating algorithm of the VUMAT subroutine has been shown schematically in the figure 4.1 where just the important parts of the subroutine have been drawn roughly and there are so many other complicated steps in the writing process which have not been shown.

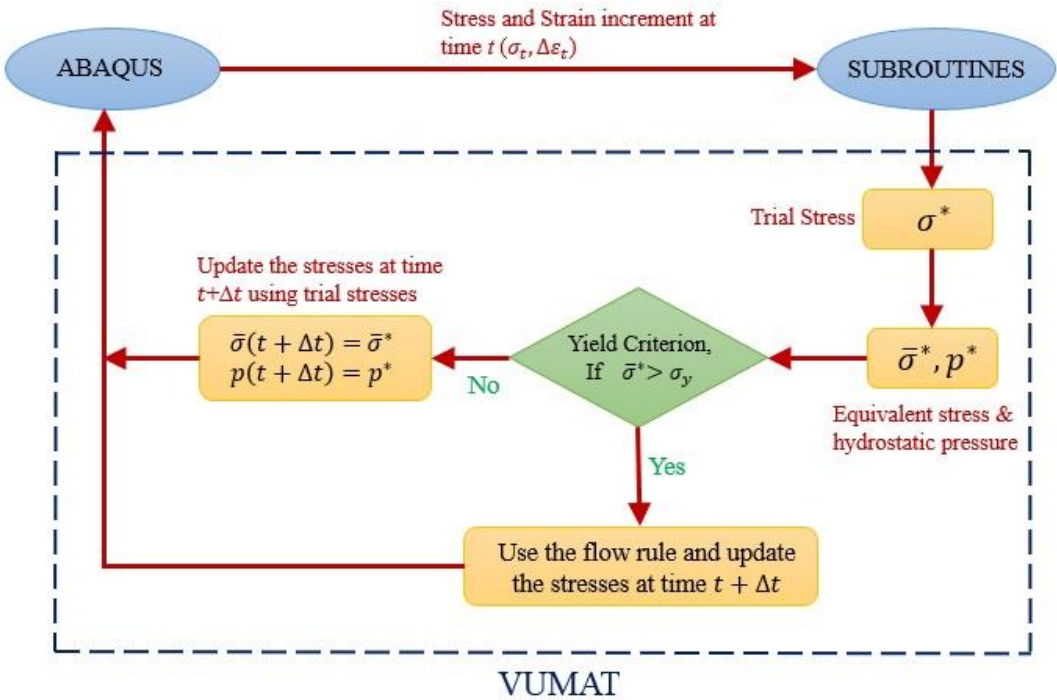


Figure 4.1. VUMAT operational flowchart

Most of the user subroutine interfaces use the FORTRAN language, although these user subroutines can be written using the C and C++ languages too but it requires considerable expertise to make ABAQUS get compatible with the written code which has been explained in the documentations widely [78]. These subroutines, written in

FORTRAN, implement the theory in the form of a stress update algorithm that is called at each integration point for every iteration during a finite element simulation.

There are some other functions named as *utility routines* which can be invoked within the subroutines to help simplify the code and get benefitted from ABAQUS predefined functions. For example, VSPRINC utility routine has been called in the codes written in this study to get access to the principal stresses and strains directly within the subroutine and simply use them in the relations they are needed.

To use a subroutine in the compatible form with ABAQUS, first of all it is needed to write the code with FORTRAN (\*.for file) and debug it. Secondly, the FEM model which includes the nodes, elements, boundary condition etc. should be prepared using ABAQUS and the input file (\*.inp file) should be created. Then using an especial interface software named as *FORTRAN build environment* the prepared model and subroutine files will be called and the analysis will start to run. The obtained results can be directly passed to ABAQUS for post processing analysis. In the figure 4.2 an example of the generated files and also the FORTRAN build environment interface have been shown. The complete view of each software environment has been shown in the appendix A.

Solution dependent state variables (SDVs) are the user defined variables in the subroutine which can be updated in every increment and can be used to monitor the desired output with identifiers SDV1, SDV2, etc. these variables can be reported as a contour, path, or X–Y plots of any output needed and can be seen in ABAQUS/Viewer directly. These variables have been extensively used in the codes written to model constitutive equations in this work.

#### **4.5 Finite element model specifications**

Since most of the sheet metal processes show geometrical and material nonlinearity characteristics and also there are complicated contact interactions between the surfaces, the explicit solver has been used in this study. The Updated Lagrangian (UL) formulation has been chosen to calculate strains and displacements where it is the default method for solid mechanic simulations in the ABAQUS software; however the Total Lagrangian (TL) method can be used if desired. Also the elasto-plastic constitutive model have been adopted to model the material behavior throughout the

deformation. To prevent the *shear locking* phenomenon reduced integration method is used.

There are two types to define the rigid parts in the ABAQUS; discrete and analytical. Discrete rigid parts can be meshed and any field variables like temperature, magnetic effects etc. can be assigned to them. On the other hand, analytical rigid parts are not that convenient in the modeling process but are computationally less expensive and if possible they should be desired first; however, the profile shape of an analytical rigid part should be smooth enough and is not arbitrary. In this study, all rigid parts have been chosen as an analytical rigid [78].

To obtain the simulation results at a reasonable cost, the element's type and size plays an important role. Mesh distortions should be minimized as much as possible where inaccurate results are inevitable by using the coarse meshes with distorted linear elements. For the analysis involving large strains, a fine mesh of linear, reduced-integration elements should be preferred. Also hexahedral (brick-shaped) elements are the utmost choice for three dimensional analysis. However, wedge and tetrahedral elements are better for the complex shapes which cannot be mesh perfectly with hexahedral elements. Based on what have been told above, to model the three dimensional blank in the sheet metal simulations, the general purpose C3D8R (8-node linear brick, reduced integration with hourglass control) element is used because it better models the thickness strain and also the diffuse and localized necking phenomena can easily be observed. In this work a fine mesh ( $0.25 \times 0.5 \times 1 \text{ mm}$ ) have been implemented to get more accurate results for most of the analyses.

However, the S4R shell element (4-node, quadrilateral, stress/displacement shell with reduced integration and a large-strain formulation) also has been utilized to investigate the effect of different constitutive models on the DFCs reliability because, most of the newly developed yield criteria have been proposed for the plane stress conditions which modeled with the shell elements, then using the shell element was inevitable. The element size in these simulations is ( $0.5 \times 0.5 \times 1 \text{ mm}$ ) where it provides reasonable results and the finer mesh is not necessary.

As a general contact algorithm, *penalty contact* method was selected which applies node into face and edge into edge penetrations in the current configuration. Coulomb friction model has been used and the friction coefficients have been taken as 0.05 for

lubricated surfaces and 0.15 for dry surfaces. For the faces where Teflon strips together with grease have been used, the friction coefficient is much lower. Based on the calculations, the friction coefficients in those interfaces is taken as 0.02.



## CHAPTER 5

### CONSTITUTIVE EQUATIONS AND DUCTILE FRACTURE CRITERIA

#### 5.1 Yield Criterion

A yield criterion is a key concept in the plasticity which defines the limit of elastic deformations in a material under any possible combination of stresses and also can be described as the onset of plastic deformation indicator. It is utilized together with a stress-strain curve obtained experimentally as the material input for numerical analyses of forming processes. The yield surface and hardening law coupling together can determine the constitutive equations which directly are implemented to the numerical frameworks to define the material behavior.

To better model the material deformation behavior, it is a must to consider every parameter that can help the better modeling experience. Isotropic, anisotropic or orthotropic material, ductile or brittle material, crystallography, type of material (steel, aluminum, etc.) and the geometry (sheet, bulk, etc.) are some parameters which have been considered to have a precise yielding criterion by the many researches [27-39]. Von-Mises is the most common isotropic criterion which is used in any analysis as a first choice to model the process. Hill48 is the most desired anisotropic criterion due to user friendly formulation, which can consider the anisotropy behavior of the materials significantly well. There are many newly developed criteria which should be used in the specific conditions mentioned briefly above. Some of them have considered the crystallography [30] and the geometry [31, 33, and 38] depending on the process. Beside the isotropic Von-Mises criterion, three anisotropic yield criteria (Hill48, YLD2003 and BBC2008) have been chosen here to be implemented to finite element model and investigate the effect of constitutive equations on the ductile fracture models.

### 5.1.1 Von-Mises yield criterion

When an external load is applied to a solid material, it starts to deform. Then, the work done by the external forces during the elastic deformation is stored in the solid material as the potential energy, which is called the strain energy. The strain energy density,  $U_0$ , is introduced as the energy per unit volume. Therefore, the strain energy of the whole body can be easily attained by integrating on the domain as:

$$U = \iiint_V U_0(x, y, z) dV \quad (5.1)$$

The strain energy density normally is thought to be composed of two parts, one because of the change in the volume and the other part because of the distortion or change in the shape which are referred as dilatational strain energy and distortional energy, respectively.

According to the Von-Mises theory, the ductile solids will yield when the distortional energy density reaches a critical value for that material. The yielding function for this criterion is defined as below:

$$\left(\frac{3}{2} S_{ij} S_{ij}\right)^{\frac{1}{2}} - \sigma_y(\bar{\varepsilon}^p) = 0 \quad (5.2)$$

where  $S_{ij}$  is called the deviatoric stress,

$$S_{ij} = \sigma_{ij} - \frac{1}{3} \delta_{ij} \sigma_{kk} \quad (5.3)$$

and  $\bar{\varepsilon}^p$  is the equivalent plastic strain as:

$$\bar{\varepsilon}^p = \int_0^t \dot{\bar{\varepsilon}}^p dt, \quad \dot{\bar{\varepsilon}}^p = \left(\frac{2}{3} \dot{\varepsilon}_{ij}^p \dot{\varepsilon}_{ij}^p\right)^{\frac{1}{2}} \quad (5.4)$$

### 5.1.2 Hill'48 Yield Criterion

Hill [27] proposed a quadratic anisotropic yield criterion which is one of the most commonly used anisotropic yield criteria in the researches. In this criterion, the hypothesis is that the material has an anisotropy with three orthogonal symmetry planes. The criterion is given by the following equation:



$$F(\sigma_{22} - \sigma_{33})^2 + G(\sigma_{33} - \sigma_{11})^2 + H(\sigma_{11} - \sigma_{22})^2 + 2L(\sigma_{23})^2 + 2M(\sigma_{31})^2 + 2N(\sigma_{12})^2 = 1 \quad (5.5)$$

where F, G, H, L, M and N are the material anisotropy constants which should be calculated using the experimental tests. The first axis of the material orientations is believed to be on the rolling direction (RD), and the second axis is parallel to the transverse direction (TD) and then the third axis is on the normal direction of the sheet metal. If X, Y and Z be the tensile yield stresses in the stated principal anisotropy directions of the material,

$$\frac{1}{X^2} = G + H \quad (5.6)$$

$$\frac{1}{Y^2} = H + F \quad (5.7)$$

$$\frac{1}{Z^2} = F + G \quad (5.8)$$

and F, G and H can be expressed by uniaxial yield stresses as:

$$2F = \frac{1}{Y^2} + \frac{1}{Z^2} - \frac{1}{X^2} \quad (5.9)$$

$$2G = \frac{1}{Z^2} + \frac{1}{X^2} - \frac{1}{Y^2} \quad (5.10)$$

$$2H = \frac{1}{X^2} + \frac{1}{Y^2} - \frac{1}{Z^2} \quad (5.11)$$

if R, S and T be the shear stresses related to the same anisotropy direction, then the other three constant can be calculated as:

$$2L = \frac{1}{R^2} \quad , \quad 2M = \frac{1}{S^2} \quad , \quad 2N = \frac{1}{T^2} \quad (5.12)$$

Now taking into account the associated flow rule, the equivalent stress and equivalent strain terms can be calculated as:

$$d\varepsilon_{ij}^p = d\lambda \frac{\partial f}{\partial \sigma_{ij}} \quad (5.13)$$

and then,

$$\frac{d\varepsilon_{11}^p}{d\lambda} = H(\sigma_{11} - \sigma_{22}) + G(\sigma_{11} - \sigma_{33}) \quad (5.14)$$

$$\frac{d\varepsilon_{22}^p}{d\lambda} = F(\sigma_{22} - \sigma_{33}) + H(\sigma_{22} - \sigma_{11}) \quad (5.15)$$

$$\frac{d\varepsilon_{33}^p}{d\lambda} = G(\sigma_{33} - \sigma_{11}) + F(\sigma_{33} - \sigma_{22}) \quad (5.16)$$

since the equivalent stress for Hill48 criterion is defined as,

$$\bar{\sigma} = \left[ \frac{3}{2} \frac{F(\sigma_{22} - \sigma_{33})^2 + G(\sigma_{33} - \sigma_{11})^2 + H(\sigma_{11} - \sigma_{22})^2}{F + G + H} + \frac{2L(\sigma_{23})^2 + 2M(\sigma_{31})^2 + 2N(\sigma_{12})^2}{F + G + H} \right]^{\frac{1}{2}} \quad (5.17)$$

the generalized equivalent strain increment ( $d\bar{\varepsilon}$ ) can be obtained using the work relation ( $dw = \bar{\sigma}d\bar{\varepsilon}$ ) and implementing the equations 5.4 and 5.14 as below,

$$d\bar{\varepsilon} = \frac{d\lambda}{\bar{\sigma}} = \left( \frac{2}{3} (F + G + H) \left( F \left( \frac{Gd\varepsilon_{22} - Hd\varepsilon_{33}}{(FG + GH + HF)} \right)^2 + \dots \frac{2d\varepsilon_{23}^2}{L} \right) \right)^{\frac{1}{2}} \quad (5.18)$$

For plane stress condition ( $\sigma_{33} = 0$ ,  $\sigma_{31} = \sigma_{23} = 0$ ) which has been also used in this work the yield criterion relation turns into:

$$\sigma_{11}^2(G + H) - 2H\sigma_{11}\sigma_{22} + \sigma_{22}^2(H + F) + 2N(\sigma_{12})^2 = 1 \quad (5.19)$$

Using  $X = \sigma_0$ ,  $Y = \sigma_{90}$ ,  $Z = \sigma_{45}$  where  $\sigma_0, \sigma_{45}, \sigma_{90}$  are the yield stresses and  $r_0, r_{45}, r_{90}$  which are the Lankford anisotropy coefficients obtained from the uniaxial tension tests and the following equation can be obtained:

$$r_0 = \frac{H}{G}, \quad r_{45} = \frac{N}{F + G} - \frac{1}{2}, \quad r_{90} = \frac{H}{F} \quad (5.20)$$

Then using Lankford anisotropy functions, the yield criterion for plane stress conditions takes the following form,

$$\sigma_{11}^2 - \frac{2r_0}{1+r_0}\sigma_{11}\sigma_{22} + \frac{r_0(1+r_{90})}{r_{90}(1+r_0)}\sigma_{22}^2 + \frac{r_0+r_{90}}{r_{90}(1+r_0)}(2r_{45}+1)\sigma_{12}^2 = \sigma_0^2 \quad (5.21)$$

For a sheet metal process which is subjected to the plane stress with rotational symmetry about Z axis, the normal anisotropy parameter can be calculated as:

$$r = \frac{H}{F} = \frac{H}{G} \quad (5.22)$$

Then both equations 5.18 and 5.19 turn into the simpler form as:

$$\bar{\sigma} = \left( \frac{3}{2} \left( \frac{\sigma_{11}^2 + \sigma_{22}^2 + r(\sigma_{11} - \sigma_{22})^2}{2+r} \right) \right)^{\frac{1}{2}} \quad (5.23)$$

$$d\bar{\varepsilon} = \left( \frac{2}{3} \left( \frac{2+r}{(1+2r)^2} [(d\varepsilon_{22} - rd\varepsilon_{33})^2 + (d\varepsilon_{11} - rd\varepsilon_{33})^2 + r(d\varepsilon_{11} - d\varepsilon_{22})^2] \right) \right)^{\frac{1}{2}} \quad (5.24)$$

### 5.1.3 Aretz's Yld2003 Criterion

Aretz [39] proposed a new plane stress yield function for orthotropic sheet metals called 'Yld2003'. The yield function contains eight anisotropy parameters which can be fitted to selected experimental input data. The simplicity of the model in mathematical form makes it very effective and thus quite interesting for implementation in finite element codes. Hosford's [30] non-quadratic yield function is:

$$|\sigma_{11} - \sigma_{22}|^m + |\sigma_{22} - \sigma_{33}|^m + |\sigma_{33} - \sigma_{11}|^m = 2Y_{ref}^m \quad (5.25)$$

where  $m$  is an exponent depending on the crystallographic structure of the material. For plane stress,  $\sigma_{33} = 0$ , using the principal stress notation the following equation can be extracted:

$$|\sigma_1 - \sigma_2|^m + |\sigma_1|^m + |\sigma_2|^m = 2Y_{ref}^m \quad (5.26)$$

where

$$\sigma_{1,2} = \frac{\sigma_{11} + \sigma_{22}}{2} \pm \sqrt{\left(\frac{\sigma_{11} - \sigma_{22}}{2}\right)^2 + \sigma_{12}\sigma_{21}} \quad (5.27)$$

Aretz generalized the equation 5.26 and proposed the following yield criterion,

$$|\sigma_1'|^m + |\sigma_2'|^m + |\sigma_1'' - \sigma_2''|^m = 2Y_{ref}^m \quad (5.28)$$

where

$$\sigma_{1,2}' = \frac{a_8\sigma_{11} + a_1\sigma_{22}}{2} \pm \sqrt{\left(\frac{a_2\sigma_{11} - a_3\sigma_{22}}{2}\right)^2 + a_4^2\sigma_{12}\sigma_{21}} \quad (5.29)$$

and

$$\sigma_{1,2}'' = \frac{\sigma_{11} + \sigma_{22}}{2} \pm \sqrt{\left(\frac{a_5\sigma_{11} - a_6\sigma_{22}}{2}\right)^2 + a_7^2\sigma_{12}\sigma_{21}} \quad (5.30)$$

Then the yield function,  $F$ , can be given as,

$$F(a_i, \boldsymbol{\sigma}) = \bar{\sigma}(a_i, \boldsymbol{\sigma}) - Y_{ref} = 0 \quad (5.31)$$

and the equivalent stress,  $\bar{\sigma}$ , is,

$$\bar{\sigma} = \left\{ \frac{1}{2} (|\sigma_1'|^m + |\sigma_2'|^m + |\sigma_1'' - \sigma_2''|^m) \right\}^{\frac{1}{m}} \quad (5.32)$$

With eight anisotropy parameters ( $a_1, \dots, a_8$ ), eight different experimental tests have to be carried out to determine that constants. The uniaxial tensile test and bulge tests have been used to determine the constants of the YLD2003. The exponent  $m$  is equal to 6 for the steel materials and 8 for aluminum materials.

To find of the eight anisotropy constants  $\sigma_0, \sigma_{45}, \sigma_{90}, r_0, r_{45}, r_{90}, \sigma_b$  and  $r_b$  must be determined experimentally. In the sheet forming  $Y_{ref}$  is assumed to be equal with  $\sigma_0$  while it is an arbitrary and can be selected from the other tests too. Aretz [39] has given a seven parameter model too where he proposed to take  $a_1 = 1$  and neglect the test which is used to find  $r_b$  constant. Here the seven parameters have been calculated using the derivatives and the equations 5.27 – 5.32.

According to the tensor transformation rules, the stress components in a uniaxial tension test specimen with the angle  $\theta$  from the rolling direction can be calculated as follows

$$\sigma_{11} = \sigma_{\theta} \cos^2 \theta \quad (5.33)$$

$$\sigma_{22} = \sigma_{\theta} \sin^2 \theta \quad (5.34)$$

$$\sigma_{12} = \sigma_{12} = \sigma_{\theta} \sin \theta \cos \theta \quad (5.35)$$

If  $\theta = 0^\circ$  (specimen cut on the RD), the equations 5.28-5.35 will lead to the following relations in the rolling direction,

$$\sigma_{11} = \sigma_0, \sigma_{22} = 0, \sigma_{12} = \sigma_{21} = 0 \quad (5.36)$$

$$\sigma'_1 = \frac{\sigma_0}{2} + \left[ \left( \frac{a_2 \sigma_0}{2} \right)^2 \right]^{\frac{1}{2}} = \frac{\sigma_0}{2} (1 + a_2) \quad (5.37)$$

$$\sigma'_2 = \frac{\sigma_0}{2} - \left( \frac{a_2 \sigma_0}{2} \right) = \frac{\sigma_0}{2} (1 - a_2) \quad (5.38)$$

$$\sigma''_1 = \frac{\sigma_0}{2} + \left( \frac{a_5 \sigma_0}{2} \right) = \frac{\sigma_0}{2} (1 + a_5) \quad (5.39)$$

$$\sigma''_2 = \frac{\sigma_0}{2} - \left( \frac{a_5 \sigma_0}{2} \right) = \frac{\sigma_0}{2} (1 - a_5) \quad (5.40)$$

then from equations 5.31 and 5.32,

$$\left[ \frac{1}{2} \left[ \left| \frac{\sigma_0}{2} (1 + a_2) \right|^6 + \left| \frac{\sigma_0}{2} (1 - a_2) \right|^6 \right. \right. \quad (5.41)$$

$$\left. \left. + \left| \frac{\sigma_0}{2} + \frac{\sigma_0 a_5}{2} - \frac{\sigma_0}{2} + \frac{\sigma_0 a_5}{2} \right|^6 \right] \right]^{\frac{1}{6}} - \sigma_0 = 0$$

In the same way, if  $\theta = 45^\circ$ ,

$$\sigma_{11} = \sigma_{45} \cos^2(45)^\circ = \frac{1}{2} \sigma_{45}, \sigma_{22} = \frac{1}{2} \sigma_{45}, \sigma_{12} = \sigma_{21} = \frac{1}{2} \sigma_{45} \quad (5.42)$$

$$\sigma'_1 = \frac{1}{4} \sigma_{45} (1 + a_1) + \left[ \left( \frac{1}{4} \sigma_{45} (a_2 - a_3) \right)^2 + \frac{1}{4} \sigma_{45}^2 a_4^2 \right]^{\frac{1}{2}} \quad (5.43)$$

$$\sigma'_2 = \frac{\sigma_{45}}{4} (1 + a_1) - \left[ \left( \frac{\sigma_{45}}{4} (a_2 - a_3) \right)^2 + \frac{1}{4} \sigma_{45}^2 a_4^2 \right]^{\frac{1}{2}} \quad (5.44)$$

$$\sigma_1'' = \frac{\sigma_{45}}{4} + \left[ \left( \frac{\sigma_{45}}{4} (a_5 - a_6) \right)^2 + \frac{\sigma_{45}}{4} a_7^2 \right]^{\frac{1}{2}} \quad (5.45)$$

$$\sigma_2'' = \frac{\sigma_{45}}{4} - \left[ \left( \frac{\sigma_{45}}{4} (a_5 - a_6) \right)^2 + \frac{\sigma_{45}}{4} a_7^2 \right]^{\frac{1}{2}} \quad (5.46)$$

then,

$$\begin{aligned} & \left[ \frac{1}{2} \left[ \left( \frac{\sigma_{45}}{4} (1 + a_1) + \left[ \left( \frac{\sigma_{45}}{4} (a_2 - a_3) \right)^2 + \frac{\sigma_{45}}{4} a_4^2 \right]^{\frac{1}{2}} \right)^6 \right. \right. \\ & \quad \left. \left. + \left( \frac{\sigma_{45}}{4} (1 + a_1) - \left[ \left( \frac{\sigma_{45}}{4} (a_2 - a_3) \right)^2 + \frac{\sigma_{45}}{4} a_4^2 \right]^{\frac{1}{2}} \right)^6 \right. \right. \\ & \quad \left. \left. + \left[ \frac{\sigma_{45}}{4} + \left[ \left( \frac{\sigma_{45}}{4} (a_5 - a_6) \right)^2 + \frac{\sigma_{45}}{4} a_7^2 \right]^{\frac{1}{2}} - \frac{\sigma_{45}}{4} \right. \right. \right. \\ & \quad \left. \left. \left. + \left[ \left( \frac{\sigma_{45}}{4} (a_5 - a_6) \right)^2 + \frac{\sigma_{45}}{4} a_7^2 \right]^{\frac{1}{2}} \right]^6 \right]^{\frac{1}{6}} \right] - \sigma_0 = 0 \end{aligned} \quad (5.47)$$

If  $\theta = 90^\circ$  (transverse direction),

$$\sigma_{11} = 0, \quad \sigma_{22} = \sigma_{90} \sin^2 90 = \sigma_{90}, \quad \sigma_{12} = \sigma_{21} = 0 \quad (5.48)$$

$$\sigma_1' = \frac{a_1 \sigma_{90}}{2} + \left[ \left( \frac{-a_3 \sigma_{90}}{2} \right)^2 \right]^{\frac{1}{2}} = \frac{\sigma_{90}}{2} (a_1 + a_3) \quad (5.49)$$

$$\sigma_2' = \frac{a_1 \sigma_{90}}{2} - \left[ \left( \frac{-a_3 \sigma_{90}}{2} \right)^2 \right]^{\frac{1}{2}} = \frac{\sigma_{90}}{2} (a_1 - a_3) \quad (5.50)$$

$$\sigma_1'' = \frac{\sigma_{90}}{2} + \left[ \left( \frac{-a_6 \sigma_{90}}{2} \right)^2 \right]^{\frac{1}{2}} = \frac{\sigma_{90}}{2} (1 + a_6) \quad (5.51)$$

$$\sigma_2'' = \frac{\sigma_{90}}{2} - \left[ \left( \frac{-a_6 \sigma_{90}}{2} \right)^2 \right]^{\frac{1}{2}} = \frac{\sigma_{90}}{2} (1 - a_6) \quad (5.52)$$

then,

$$\left[ \frac{1}{2} \left[ \left| \frac{\sigma_{90}}{2} (a_1 + a_3) \right|^6 + \left| \frac{\sigma_{90}}{2} (a_1 - a_3) \right|^6 + \left| \frac{\sigma_{90}}{2} + \frac{\sigma_{90} a_6}{2} - \frac{\sigma_{90}}{2} + \frac{\sigma_{90} a_6}{2} \right|^6 \right] \right]^{\frac{1}{6}} - \sigma_0 = 0 \quad (5.53)$$

Choosing DKP6112 steel material where the material parameters have given in the table 5.1, three equations of the seven which are needed for YLD2003 model, can be obtained using the following material parameters considering that  $Y_{ref} = \sigma_0$ .

Table 5.1 The material parameters of DKP6112 used to calculate the YLD2003 yield criterion constants

Material	$\sigma_0$ (MPa)	$\sigma_{45}$ (MPa)	$\sigma_{90}$ (MPa)	$\sigma_b$ (MPa)	$r_0$	$r_{45}$	$r_{90}$
DKP6112	250	256	242	281	1.34	0.99	1.67

For  $\theta = 0^\circ$ , by using the material data in equation 5.41, the following equation is obtained,

$$\left[ \frac{1}{2} \left[ (125(1 + a_2))^6 + (125(1 - a_2))^6 + (250a_5)^6 \right] \right]^{\frac{1}{6}} - 250 = 0 \quad (5.54)$$

and for  $\theta = 45^\circ$  using the material data in equation 5.47,

$$\left[ \frac{1}{2} \left[ \left( 64 (1 + a_1) + \left[ (64 (a_2 - a_3))^2 + 64 a_4^2 \right]^{\frac{1}{2}} \right)^6 + \left( 64 (1 + a_1) - \left[ (64 (a_2 - a_3))^2 + 64 a_4^2 \right]^{\frac{1}{2}} \right)^6 + 2 \left[ (64 (a_5 - a_6))^2 + 64 a_7^2 \right]^{\frac{1}{2}} \right] \right]^{\frac{1}{6}} - 250 = 0 \quad (5.55)$$

and for  $\theta = 90^\circ$  using the material data in equation 5.53,

$$\left[ \frac{1}{2} \left[ (121(a_1 + a_3))^6 + (121(a_1 - a_3))^6 + (242a_6)^6 \right] \right]^{\frac{1}{6}} - 250 = 0 \quad (5.56)$$

To obtain the additional equations, the anisotropy relations should be implemented.

From the definitions, the related formulas are as follows

$$r_0 = - \left[ \frac{\frac{\partial F}{\partial \sigma_{22}}}{\frac{\partial F}{\partial \sigma_{11}} + \frac{\partial F}{\partial \sigma_{22}}} \right]_{\sigma_0} \quad (5.57)$$

$$r_{90} = - \left[ \frac{\frac{\partial F}{\partial \sigma_{11}}}{\frac{\partial F}{\partial \sigma_{11}} + \frac{\partial F}{\partial \sigma_{22}}} \right]_{\sigma_{90}} \quad (5.58)$$

$$r_{45} = - \left[ \frac{\frac{1}{2} \frac{\partial F}{\partial \sigma_{11}} - \frac{\partial F}{\partial \sigma_{12}} + \frac{1}{2} \frac{\partial F}{\partial \sigma_{22}}}{\frac{\partial F}{\partial \sigma_{11}} + \frac{\partial F}{\partial \sigma_{22}}} \right]_{\sigma_{45}} \quad (5.59)$$

since

$$\bar{\sigma}^{2k} = \hat{\sigma}, \quad F = \frac{\bar{\sigma}^{2k}}{Y_{ref}^{2k}} - 1 = 0 \quad \Rightarrow \quad \frac{\partial F}{\partial \hat{\sigma}} = \frac{1}{Y_{ref}^{2k}} \quad (5.60)$$

where  $m = 2k$ , the general form of the derivatives are obtained as follows

$$\frac{\partial F}{\partial \sigma_{11}} = \frac{\partial F}{\partial \hat{\sigma}} \left[ \frac{\partial \hat{\sigma}}{\partial \sigma'_1} \frac{\partial \sigma'_1}{\partial \sigma_{11}} + \frac{\partial \hat{\sigma}}{\partial \sigma'_2} \frac{\partial \sigma'_2}{\partial \sigma_{11}} + \frac{\partial \hat{\sigma}}{\partial \sigma''_1} \frac{\partial \sigma''_1}{\partial \sigma_{11}} + \frac{\partial \hat{\sigma}}{\partial \sigma''_2} \frac{\partial \sigma''_2}{\partial \sigma_{11}} \right] \quad (5.61)$$

$$\frac{\partial F}{\partial \sigma_{22}} = \frac{\partial F}{\partial \hat{\sigma}} \left[ \frac{\partial \hat{\sigma}}{\partial \sigma'_1} \frac{\partial \sigma'_1}{\partial \sigma_{22}} + \frac{\partial \hat{\sigma}}{\partial \sigma'_2} \frac{\partial \sigma'_2}{\partial \sigma_{22}} + \frac{\partial \hat{\sigma}}{\partial \sigma''_1} \frac{\partial \sigma''_1}{\partial \sigma_{22}} + \frac{\partial \hat{\sigma}}{\partial \sigma''_2} \frac{\partial \sigma''_2}{\partial \sigma_{22}} \right] \quad (5.62)$$

$$\frac{\partial F}{\partial \sigma_{12}} = \frac{\partial F}{\partial \hat{\sigma}} \left[ \frac{\partial \hat{\sigma}}{\partial \sigma'_1} \frac{\partial \sigma'_1}{\partial \sigma_{12}} + \frac{\partial \hat{\sigma}}{\partial \sigma'_2} \frac{\partial \sigma'_2}{\partial \sigma_{12}} + \frac{\partial \hat{\sigma}}{\partial \sigma''_1} \frac{\partial \sigma''_1}{\partial \sigma_{12}} + \frac{\partial \hat{\sigma}}{\partial \sigma''_2} \frac{\partial \sigma''_2}{\partial \sigma_{12}} \right] \quad (5.63)$$

where

$$\frac{\partial \bar{\sigma}}{\partial \sigma'_1} = \frac{1}{2} m |\sigma'_1|^{m-1} = 3 |\sigma'_1|^5 \quad (5.64)$$



$$\frac{\partial \bar{\sigma}}{\partial \sigma_2'} = \frac{1}{2} m |\sigma_2'|^{m-1} = 3 |\sigma_2'|^5 \quad (5.65)$$

$$\frac{\partial \bar{\sigma}}{\partial \sigma_1''} = \frac{1}{2} m |\sigma_1'' - \sigma_2''|^{m-1} = 3 |\sigma_1'' - \sigma_2''|^5 \quad (5.66)$$

$$\frac{\partial \bar{\sigma}}{\partial \sigma_2''} = \frac{-1}{2} m |\sigma_1'' - \sigma_2''|^{m-1} = -3 |\sigma_1'' - \sigma_2''|^5 \quad (5.67)$$

$$\frac{\partial \sigma_1'}{\partial \sigma_{11}} = \frac{1}{2} + \frac{1}{2} \left[ \left( \frac{a_2 \sigma_{11} - a_3 \sigma_{22}}{2} \right)^2 + a_4^2 \sigma_{12}^2 \right]^{-\frac{1}{2}} \left( \frac{a_2^2 \sigma_{11} - a_2 a_3 \sigma_{22}}{2} \right) \quad (5.68)$$

$$\frac{\partial \sigma_2'}{\partial \sigma_{11}} = \frac{1}{2} - \frac{1}{2} \left[ \left( \frac{a_2 \sigma_{11} - a_3 \sigma_{22}}{2} \right)^2 + a_4^2 \sigma_{12}^2 \right]^{-\frac{1}{2}} \left( \frac{a_2^2 \sigma_{11} - a_2 a_3 \sigma_{22}}{2} \right) \quad (5.69)$$

$$\frac{\partial \sigma_1'}{\partial \sigma_{22}} = \frac{1}{2} a_1 + \frac{1}{2} \left[ \left( \frac{a_2 \sigma_{11} - a_3 \sigma_{22}}{2} \right)^2 + a_4^2 \sigma_{12}^2 \right]^{-\frac{1}{2}} \left( \frac{-a_2 a_3 \sigma_{11} + a_3^2 \sigma_{22}}{2} \right) \quad (5.70)$$

$$\frac{\partial \sigma_1'}{\partial \sigma_{12}} = \frac{1}{2} \left[ \left( \frac{a_2 \sigma_{11} - a_3 \sigma_{22}}{2} \right)^2 + a_4^2 \sigma_{12}^2 \right]^{-\frac{1}{2}} 2 \sigma_{12} a_4^2 \quad (5.71)$$

$$\frac{\partial \sigma_2'}{\partial \sigma_{22}} = \frac{1}{2} a_1 - \frac{1}{2} \left[ \left( \frac{a_2 \sigma_{11} - a_3 \sigma_{22}}{2} \right)^2 + a_4^2 \sigma_{12}^2 \right]^{-\frac{1}{2}} \left( \frac{a_3^2 \sigma_{22} - a_2 a_3 \sigma_{11}}{2} \right) \quad (5.72)$$

$$\frac{\partial \sigma_2'}{\partial \sigma_{12}} = \frac{-1}{2} \left[ \left( \frac{a_2 \sigma_{11} - a_3 \sigma_{22}}{2} \right)^2 + a_4^2 \sigma_{12}^2 \right]^{-\frac{1}{2}} 2 \sigma_{12} a_4^2 \quad (5.73)$$

$$\frac{\partial \sigma_1''}{\partial \sigma_{11}} = \frac{1}{2} + \frac{1}{2} \left[ \left( \frac{a_5 \sigma_{11} - a_6 \sigma_{22}}{2} \right)^2 + a_7^2 \sigma_{12}^2 \right]^{-\frac{1}{2}} \left( \frac{a_5^2 \sigma_{11} - a_5 a_6 \sigma_{22}}{2} \right) \quad (5.74)$$

$$\frac{\partial \sigma_1''}{\partial \sigma_{22}} = \frac{1}{2} + \frac{1}{2} \left[ \left( \frac{a_5 \sigma_{11} - a_6 \sigma_{22}}{2} \right)^2 + a_7^2 \sigma_{12}^2 \right]^{-\frac{1}{2}} \left( \frac{a_6^2 \sigma_{22} - a_5 a_6 \sigma_{11}}{2} \right) \quad (5.75)$$

$$\frac{\partial \sigma_1''}{\partial \sigma_{12}} = \frac{1}{2} \left[ \left( \frac{a_5 \sigma_{11} - a_6 \sigma_{22}}{2} \right)^2 + a_7^2 \sigma_{12}^2 \right]^{-\frac{1}{2}} (2 \sigma_{12} a_7^2) \quad (5.76)$$

$$\frac{\partial \sigma_2''}{\partial \sigma_{12}} = -\frac{1}{2} \left[ \left( \frac{a_5 \sigma_{11} - a_6 \sigma_{22}}{2} \right)^2 + a_7^2 \sigma_{12}^2 \right]^{-\frac{1}{2}} (2\sigma_{12} a_7^2) \quad (5.77)$$

$$\frac{\partial \sigma_2''}{\partial \sigma_{11}} = \frac{1}{2} - \frac{1}{2} \left[ \left( \frac{a_5 \sigma_{11} - a_6 \sigma_{22}}{2} \right)^2 + a_7^2 \sigma_{12}^2 \right]^{-\frac{1}{2}} \left( \frac{a_5^2 \sigma_{11} - a_5 a_6 \sigma_{22}}{2} \right) \quad (5.78)$$

$$\frac{\partial \sigma_2''}{\partial \sigma_{22}} = \frac{1}{2} - \frac{1}{2} \left[ \left( \frac{a_5 \sigma_{11} - a_6 \sigma_{22}}{2} \right)^2 + a_7^2 \sigma_{12}^2 \right]^{-\frac{1}{2}} \left( \frac{a_6^2 \sigma_{22} - a_5 a_6 \sigma_{11}}{2} \right) \quad (5.79)$$

Now if the material data (DKP6112) obtained from uniaxial tension tests is used in the above formulations the additional equations can be extracted.

Then if orientation angle  $\theta = 0^\circ$ ,

$$\frac{\partial \sigma_1'}{\partial \sigma_{11}} = \frac{1}{2} + \frac{1}{2} \left[ \left( \frac{a_2 \sigma_0}{2} \right)^2 \right]^{-\frac{1}{2}} \left( \frac{a_2^2 \sigma_0}{2} \right) = \frac{1}{2} + \frac{1}{2} a_2 \quad (5.80)$$

$$\frac{\partial \sigma_2'}{\partial \sigma_{11}} = \frac{1}{2} - \frac{1}{2} a_2 \quad (5.81)$$

$$\frac{\partial \sigma_1'}{\partial \sigma_{22}} = \frac{1}{2} a_1 + \frac{1}{2} \left[ \left( \frac{a_2 \sigma_0}{2} \right)^2 \right]^{-\frac{1}{2}} \left( \frac{a_2^2 \sigma_0}{2} \right) = \frac{1}{2} a_1 + \frac{1}{2} a_2 \quad (5.82)$$

$$\frac{\partial \sigma_1'}{\partial \sigma_{12}} = \frac{1}{2} \left[ \left( \frac{a_2 \sigma_0}{2} \right)^2 \right]^{-\frac{1}{2}} \times 0 = 0 \quad (5.83)$$

$$\frac{\partial \sigma_2'}{\partial \sigma_{22}} = \frac{1}{2} a_1 - \frac{1}{2} \left[ \left( \frac{-a_2 \sigma_0}{2} \right)^2 \right]^{-\frac{1}{2}} \left( \frac{-a_2 a_3 \sigma_0}{2} \right) = \frac{1}{2} a_1 + \frac{1}{2} a_3 \quad (5.84)$$

$$\frac{\partial \sigma_2'}{\partial \sigma_{12}} = 0 \quad (5.85)$$

$$\frac{\partial \sigma_1''}{\partial \sigma_{11}} = \frac{1}{2} + \frac{1}{2} \left[ \left( \frac{a_5 \sigma_0}{2} \right)^2 \right]^{-\frac{1}{2}} \left( \frac{a_5^2 \sigma_0}{2} \right) = \frac{1}{2} + \frac{1}{2} a_5 \quad (5.86)$$

$$\frac{\partial \sigma_1''}{\partial \sigma_{22}} = \frac{1}{2} + \frac{1}{2} \left[ \left( \frac{a_5 \sigma_0}{2} \right)^2 \right]^{-\frac{1}{2}} \left( \frac{-a_5 a_6 \sigma_0}{2} \right) = \frac{1}{2} - \frac{1}{2} a_6 \quad (5.87)$$

$$\frac{\partial \sigma_1''}{\partial \sigma_{12}} = \frac{1}{2} \left[ \left( \frac{a_5 \sigma_0}{2} \right)^2 \right]^{-\frac{1}{2}} \times 0 = 0 \quad (5.88)$$

$$\frac{\partial \sigma_2''}{\sigma_{12}} = 0 \quad (5.89)$$

$$\frac{\partial \sigma_2''}{\partial \sigma_{11}} = \frac{1}{2} - \frac{1}{2} \left[ \left( \frac{a_5 \sigma_0}{2} \right)^2 \right]^{-\frac{1}{2}} \left( \frac{a_5^2 \sigma_0}{2} \right) = \frac{1}{2} - \frac{1}{2} a_5 \quad (5.90)$$

$$\frac{\partial \sigma_2''}{\partial \sigma_{11}} = \frac{1}{2} - \frac{1}{2} \left[ \left( \frac{a_5 \sigma_0}{2} \right)^2 \right]^{-\frac{1}{2}} \left( \frac{a_5^2 \sigma_0}{2} \right) = \frac{1}{2} - \frac{1}{2} a_5 \quad (5.91)$$

$$\frac{\partial \sigma_2''}{\partial \sigma_{22}} = \frac{1}{2} - \frac{1}{2} \left[ \left( \frac{a_5 \sigma_0}{2} \right)^2 \right]^{-\frac{1}{2}} \left( \frac{-a_5 a_6 \sigma_0}{2} \right) = \frac{1}{2} + \frac{1}{2} a_6 \quad (5.92)$$

then using  $r_0$  relation given by Equation 5.57,

$$\begin{aligned} \frac{\partial F}{\partial \sigma_{11}} |_{\theta=0} &= \frac{1}{\sigma_{ref}} \left[ 3|\sigma_1'|^5 \left( \frac{1}{2} + \frac{1}{2} a_2 \right) + 3|\sigma_2'|^5 \left( \frac{1}{2} - \frac{1}{2} a_2 \right) \right. \\ &\quad + 3|\sigma_1'' - \sigma_2''|^5 \cdot \left( \frac{1}{2} + \frac{1}{2} a_5 \right) \\ &\quad \left. + (-3|\sigma_1'' - \sigma_2''|^5) \left( \frac{1}{2} - \frac{1}{2} a_5 \right) \right] \end{aligned} \quad (5.93)$$

$$\begin{aligned} \frac{\partial F}{\partial \sigma_{22}} |_{\theta=0} &= \frac{1}{\sigma_{ref}^{2k}} \left[ 3|\sigma_1'|^5 \left( \frac{1}{2} a_1 + \frac{1}{2} a_2 \right) + 3|\sigma_2'|^5 \left( \frac{1}{2} a_1 - \frac{1}{2} a_2 \right) \right. \\ &\quad \left. + 3|\sigma_1'' - \sigma_2''|^5 \cdot \left( \frac{1}{2} - \frac{1}{2} a_6 \right) - 3|\sigma_1'' - \sigma_2''|^5 \left( \frac{1}{2} + \frac{1}{2} a_6 \right) \right] \end{aligned} \quad (5.94)$$

and for the orientation angle of  $\theta = 90^\circ$ ,

$$\frac{\partial \sigma_1'}{\partial \sigma_{22}} = \frac{1}{2} a_1 + \frac{1}{2} \left[ \left( \frac{-a_3 \sigma_{90}}{2} \right)^2 \right]^{-\frac{1}{2}} \left( \frac{a_3^2 \sigma_{90}}{2} \right) = \frac{1}{2} a_1 + \frac{1}{2} a_3 \quad (5.95)$$

$$\frac{\partial \sigma_2'}{\partial \sigma_{22}} = \frac{1}{2} a_1 - \frac{1}{2} \left[ \left( \frac{-a_3 \sigma_{90}}{2} \right)^2 \right]^{-\frac{1}{2}} \left( \frac{a_3^2 \sigma_{90}}{2} \right) = \frac{1}{2} a_1 - \frac{1}{2} a_3 \quad (5.96)$$

$$\frac{\partial \sigma_1''}{\partial \sigma_{22}} = \frac{1}{2} + \frac{1}{2} \left[ \left( \frac{-a_6 \sigma_{90}}{2} \right)^2 \right]^{-\frac{1}{2}} \left( \frac{a_6^2 \sigma_{90}}{2} \right) = \frac{1}{2} + \frac{1}{2} a_6 \quad (5.97)$$

$$\frac{\partial \sigma_2''}{\partial \sigma_{22}} = \frac{1}{2} - \frac{1}{2} a_6 \quad (5.98)$$

$$\frac{\partial \sigma_1'}{\partial \sigma_{11}} = \frac{1}{2} + \frac{1}{2} \left[ \left( \frac{-a_3 \sigma_{90}}{2} \right)^2 \right]^{-\frac{1}{2}} \left( \frac{-a_2 a_3 \sigma_{90}}{2} \right) = \frac{1}{2} - \frac{1}{2} a_2 \quad (5.99)$$

$$\frac{\partial \sigma_2'}{\partial \sigma_{11}} = \frac{1}{2} - \frac{1}{2} \left[ \left( \frac{-a_3 \sigma_{90}}{2} \right)^2 \right]^{-\frac{1}{2}} \left( \frac{-a_2 a_3 \sigma_{90}}{2} \right) = \frac{1}{2} + \frac{1}{2} a_2 \quad (5.100)$$

$$\frac{\partial \sigma_1''}{\partial \sigma_{11}} = \frac{1}{2} + \frac{1}{2} \left[ \left( \frac{-a_6 \sigma_{90}}{2} \right)^2 \right]^{-\frac{1}{2}} \left( \frac{-a_5 a_6 \sigma_{90}}{2} \right) = \frac{1}{2} - \frac{1}{2} a_5 \quad (5.101)$$

$$\frac{\partial \sigma_2''}{\partial \sigma_{11}} = \frac{1}{2} + \frac{1}{2} a_5 \quad (5.102)$$

$$\frac{\partial \sigma_1'}{\partial \sigma_{12}} = \frac{\partial \sigma_2'}{\partial \sigma_{12}} = \frac{\partial \sigma_1''}{\partial \sigma_{12}} = \frac{\partial \sigma_2''}{\partial \sigma_{12}} = 0 \quad (5.103)$$

$$\frac{\partial \sigma_2''}{\partial \sigma_{11}} = \frac{1}{2} + \frac{1}{2} a_5 \quad (5.104)$$

then,

$$\begin{aligned} \frac{\partial F}{\partial \sigma_{11}} \Big|_{\theta=90} &= \frac{1}{\sigma_{ref}^{2k}} \left[ 3|\sigma_1'|^5 \left( \frac{1}{2} - \frac{1}{2} a_2 \right) + 3|\sigma_2'|^5 \left( \frac{1}{2} + \frac{1}{2} a_2 \right) \right. \\ &\quad + 3|\sigma_1'' - \sigma_2''|^5 \cdot \left( \frac{1}{2} - \frac{1}{2} a_5 \right) \\ &\quad \left. + (-3|\sigma_1'' - \sigma_2''|^5) \left( \frac{1}{2} + \frac{1}{2} a_5 \right) \right] r_{90} \end{aligned} \quad (5.105)$$

$$\begin{aligned} \frac{\partial F}{\partial \sigma_{22}} \Big|_{\theta=90} &= \frac{1}{\sigma_{ref}^{2k}} \left[ 3|\sigma_1'|^5 \left( \frac{1}{2} a_1 + \frac{1}{2} a_3 \right) + 3|\sigma_2'|^5 \left( \frac{1}{2} a_1 - \frac{1}{2} a_3 \right) \right. \\ &\quad \left. + 3|\sigma_1'' - \sigma_2''|^5 \cdot \left( \frac{1}{2} + \frac{1}{2} a_6 \right) - 3|\sigma_1'' - \sigma_2''|^5 \left( \frac{1}{2} - \frac{1}{2} a_6 \right) \right] \end{aligned} \quad (5.106)$$

and for orientation angle  $\theta = 45^\circ$

$$\frac{\partial \sigma_1'}{\partial \sigma_{11}} = \frac{1}{2} + \frac{1}{2} \left[ \left( \frac{\sigma_{45} a_2 - a_3 \sigma_{45}}{4} \right)^2 + \frac{\sigma_{45}}{4} a_4^2 \right]^{-\frac{1}{2}} \left( \frac{\sigma_{45} a_2^2 - \sigma_{45} a_2 a_3}{4} \right) \quad (5.107)$$

$$\frac{\partial \sigma'_2}{\partial \sigma_{11}} = \frac{1}{2} - \frac{1}{2} \left[ \left( \frac{\sigma_{45} a_2 - a_3 \sigma_{45}}{4} \right)^2 + \frac{\sigma_{45}^2}{4} a_4^2 \right]^{-\frac{1}{2}} \left( \frac{\sigma_{45} a_2^2 - \sigma_{45} a_2 a_3}{4} \right) \quad (5.108)$$

$$\frac{\partial \sigma'_1}{\partial \sigma_{22}} = \frac{1}{2} a_1 + \frac{1}{2} \left[ \left( \frac{a_2 \sigma_{45} - a_3 \sigma_{45}}{4} \right)^2 + \frac{\sigma_{45}^2}{4} a_4^2 \right]^{-\frac{1}{2}} \left( \frac{a_3^2 \sigma_{45} - a_2 a_3 \sigma_{45}}{4} \right) \quad (5.109)$$

$$\frac{\partial \sigma'_1}{\partial \sigma_{12}} = \frac{1}{2} \left[ \left( \frac{a_2 \sigma_{45} - a_3 \sigma_{45}}{4} \right)^2 + a_4^2 \frac{\sigma_{45}^2}{4} \right]^{-\frac{1}{2}} (a_4^2 \sigma_{45}) \quad (5.110)$$

$$\frac{\partial \sigma'_2}{\partial \sigma_{22}} = \frac{1}{2} a_1 - \frac{1}{2} \left[ \left( \frac{a_2 \sigma_{45} - a_3 \sigma_{45}}{4} \right)^2 + a_4 \frac{\sigma_{45}^2}{4} \right]^{-\frac{1}{2}} \left( \frac{a_3^2 \sigma_{45} - a_2 a_3 \sigma_{45}}{4} \right) \quad (5.111)$$

$$\frac{\partial \sigma'_2}{\partial \sigma_{12}} = \frac{-1}{2} \left[ \left( \frac{a_2 \sigma_{45} - a_3 \sigma_{45}}{4} \right)^2 + \frac{\sigma_{45}^2}{4} a_4^2 \right]^{-\frac{1}{2}} (\sigma_{45} a_4^2) \quad (5.112)$$

$$\frac{\partial \sigma''_1}{\partial \sigma_{11}} = \frac{1}{2} + \frac{1}{2} \left[ \left( \frac{a_5 \sigma_{45} - a_6 \sigma_{45}}{4} \right)^2 + \frac{\sigma_{45}^2}{4} a_7^2 \right]^{-\frac{1}{2}} \left( \frac{a_5^2 \sigma_{45} - a_5 a_6 \sigma_{45}}{4} \right) \quad (5.113)$$

$$\frac{\partial \sigma''_1}{\partial \sigma_{22}} = \frac{1}{2} + \frac{1}{2} \left[ \left( \frac{a_5 \sigma_{45} - a_6 \sigma_{45}}{4} \right)^2 + \frac{\sigma_{45}^2}{4} a_7^2 \right]^{-\frac{1}{2}} \left( \frac{a_6^2 \sigma_{45} - a_5 a_6 \sigma_{45}}{4} \right) \quad (5.114)$$

$$\frac{\partial \sigma''_1}{\partial \sigma_{12}} = \frac{1}{2} \left[ \left( \frac{a_5 \sigma_{45} - a_6 \sigma_{45}}{4} \right)^2 + a_7^2 \frac{\sigma_{45}^2}{4} \right]^{-\frac{1}{2}} (\sigma_{45} a_7^2) \quad (5.115)$$

$$\frac{\partial \sigma''_2}{\partial \sigma_{12}} = \frac{-1}{2} \left[ \left( \frac{a_5 \sigma_{45} - a_6 \sigma_{45}}{4} \right)^2 + a_7^2 \frac{\sigma_{45}^2}{4} \right]^{-\frac{1}{2}} (\sigma_{45} a_7^2) \quad (5.116)$$

$$\frac{\partial \sigma''_2}{\partial \sigma_{11}} = \frac{1}{2} - \frac{1}{2} \left[ \left( \frac{a_5 \sigma_{45} - a_6 \sigma_{45}}{4} \right)^2 + a_7^2 \frac{\sigma_{45}^2}{4} \right]^{-\frac{1}{2}} \left( \frac{a_5^2 \sigma_{45} - a_5 a_6 \sigma_{45}}{4} \right) \quad (5.117)$$

$$\frac{\partial \sigma''_2}{\partial \sigma_{22}} = \frac{1}{2} - \frac{1}{2} \left[ \left( \frac{a_5 \sigma_{45} - a_6 \sigma_{45}}{4} \right)^2 + a_7^2 \frac{\sigma_{45}^2}{4} \right]^{-\frac{1}{2}} \left( \frac{a_6^2 \sigma_{45} - a_5 a_6 \sigma_{45}}{4} \right) \quad (5.118)$$

then,

$$\begin{aligned} \frac{\partial F}{\partial \sigma_{11}}|_{\theta=45} &= \frac{1}{\sigma_{ref}^{2k}} \left[ 3|\sigma'_1|^5 \left( \frac{\partial \sigma'_1}{\partial \sigma_{11}} \right) + 3|\sigma'_2|^5 \left( \frac{\partial \sigma'_2}{\partial \sigma_{11}} \right) \right. \\ &\quad \left. + 3|\sigma''_1 - \sigma''_2|^5 \cdot \frac{\partial \sigma''_1}{\partial \sigma_{11}} - 3|\sigma''_1 - \sigma''_2|^5 \frac{\partial \sigma''_1}{\partial \sigma_{12}} \right] \end{aligned} \quad (5.119)$$

$$\begin{aligned} \frac{\partial F}{\partial \sigma_{22}}|_{\theta=45} &= \frac{1}{\sigma_{ref}^{2k}} \left[ 3|\sigma'_1|^5 \left( \frac{\partial \sigma'_1}{\partial \sigma_{22}} \right) + 3|\sigma'_2|^5 \left( \frac{\partial \sigma'_2}{\partial \sigma_{22}} \right) \right. \\ &\quad \left. + 3|\sigma''_1 - \sigma''_2|^5 \cdot \frac{\partial \sigma''_1}{\partial \sigma_{22}} - 3|\sigma''_1 - \sigma''_2|^5 \frac{\partial \sigma''_2}{\partial \sigma_{22}} \right] \end{aligned} \quad (5.120)$$

$$\begin{aligned} \frac{\partial F}{\partial \sigma_{12}}|_{\theta=45} &= \frac{1}{\sigma_{ref}^{2k}} \left[ 3|\sigma'_1|^5 \left( \frac{\partial \sigma'_1}{\partial \sigma_{12}} \right) + 3|\sigma'_2|^5 \left( \frac{\partial \sigma'_2}{\partial \sigma_{12}} \right) \right. \\ &\quad \left. + 3|\sigma''_1 - \sigma''_2|^5 \cdot \frac{\partial \sigma''_1}{\partial \sigma_{12}} - 3|\sigma''_1 - \sigma''_2|^5 \frac{\partial \sigma''_2}{\partial \sigma_{12}} \right] \end{aligned} \quad (5.121)$$

And finally to obtain another equation the equibiaxial conditions should be considered and  $\sigma_b$  should be used. The stress conditions considering the plane stress state for DKP6112 material are:

$$\sigma_{11} = \sigma_{22} = \sigma_b, \quad \sigma_{12} = \sigma_{21} = 0 \quad \sigma_b = 281 \text{ MPa} \quad (5.122)$$

$$\sigma'_1 = \frac{\sigma_b + a_1 \sigma_b}{2} + \left[ \left( \frac{a_2 \sigma_b - a_3 \sigma_b}{2} \right)^2 \right]^{\frac{1}{2}} = \frac{\sigma_b}{2} [1 + a_1 + |a_2 - a_3|] \quad (5.123)$$

$$\sigma'_2 = \frac{\sigma_b}{2} [1 + a_1 - |a_2 - a_3|^2] \quad (5.124)$$

$$\sigma''_1 = \sigma_b + \left[ \left( \frac{a_5 \sigma_b - a_6 \sigma_b}{2} \right)^2 \right]^{\frac{1}{2}} = \frac{\sigma_b}{2} [2 + |a_5 - a_6|] \quad (5.125)$$

$$\sigma''_2 = \frac{\sigma_b}{2} [2 - |a_5 - a_6|] \quad (5.126)$$

$$\begin{aligned} \left[ \frac{1}{2} \left[ \left| \frac{\sigma_b}{2} (1 + a_1 + |a_2 - a_3|) \right|^6 + \left| \frac{\sigma_b}{2} (1 + a_1 - |a_2 - a_3|) \right|^6 \right. \right. \\ \left. \left. + |\sigma_b |a_5 - a_6|^6 \right] \right]^{\frac{-1}{6}} - Y_{ref} = 0 \end{aligned} \quad (5.127)$$

Now there are seven equations (Equations 5.54-5.59 and 5.127) with seven unknowns ( $a_1, a_2, a_3, a_4, a_5, a_6, a_7$ ) which have to be solved to get the material anisotropy constants of YLD2003 yield criterion.

Aretz [39] have given a least square based error function to be minimized to obtain the seven unknown constants as below,

$$\epsilon(a_1, \dots, a_7) = \sum_{i=1}^3 \left( \frac{\bar{\sigma}_{\theta_i} - Y_{ref}}{Y_{ref}} \right)^2 + \sum_{i=1}^3 \left( \frac{r_{\theta_i} - r_{\theta}^{exp}}{r_{\theta}^{exp}} \right)^2 + \left( \frac{\bar{\sigma}_b - Y_{ref}}{Y_{ref}} \right)^2 = \text{minimum} \quad (5.128)$$

To minimize this error function, commercial MATHEMATICA software was used. Two methods of minimization namely *Nelder-Mead* and the *Random Search* algorithms were implemented. The Nelder–Mead method works with the direct searching algorithm where in the minimization process of a function with some variables, a set of  $(n + 1)$  points which composes the vertices of a polytope will be maintained in the  $n$  –dimensional space. Then iteratively by shrinking the polytope, the better points will be found. The random search method on the other hand utilizes the local optimization technique by producing a set of random starting guess points and making each of the starting points to converge to a local minimum. The best local minimum obtained in this way will be selected as solution [80]. The results obtained from this two algorithms for DKP6112 steel material using YLD2003 yielding criterion, have been shown in the table 5.2.

Table 5.2. YLD2003 anisotropy constants obtained using the optimization methods for DKP6112 steel material

Constants	$a_1$	$a_2$	$a_3$	$a_4$	$a_5$	$a_6$	$a_7$
Nelder-Mead	1.162	0.727	0.727	0.050	1.080	1.089	0.080
Random Search	1.158	0.729	0.729	0.050	1.080	1.090	0.050

Since both methods have given very close results to each other, the random search method's results have been chosen and implemented to the finite element code using the material subroutines.

#### 5.1.4 BBC2008 yield criterion

The BBC2008 yield criterion is a plane-stress criterion developed to model the exact earrings formation in the highly orthotropic materials. It has two different types with 8 and 16 unknowns where the former one is used to determine the four ears and the later one can be used to estimate the eight ears in the simulations. The criterion function can be written as:

$$F(\sigma_{11}, \sigma_{22}, \sigma_{12}, Y) = \bar{\sigma}(\sigma_{11}, \sigma_{22}, \sigma_{12}) - Y(\varepsilon^p) = 0 \quad (5.129)$$

where  $\bar{\sigma}(\sigma_{11}, \sigma_{22}, \sigma_{12} = \sigma_{21})$  is the equivalent stress and  $Y > 0$  is the yield stress. Here  $\sigma_{11}, \sigma_{22}$  and  $\sigma_{12} = \sigma_{21}$  are the components of the stress tensor overlaid to the local axes of plastic orthotropy [38].

In the BBC2008 yield criterion, the equivalent stress is described as below:

$$\frac{\bar{\sigma}^{2k}}{w-1} = \sum_{i=1}^s \left[ w^{i-1} \left( [L^{(i)} + M^{(i)}]^{2k} + [L^{(i)} - M^{(i)}]^{2k} \right) + w^{s-i} \left( [M^{(i)} + N^{(i)}]^{2k} + [M^{(i)} - N^{(i)}]^{2k} \right) \right] \quad (5.130)$$

where

$$L^{(i)} = l_1^{(i)} \sigma_{11} + l_2^{(i)} \sigma_{22} \quad (5.131)$$

$$M^{(i)} = \left( [m_1^{(i)} \sigma_{11} - m_2^{(i)} \sigma_{22}]^2 + [m_3^{(i)} (\sigma_{12} + \sigma_{21})]^2 \right)^{\frac{1}{2}} \quad (5.132)$$

$$N^{(i)} = \left( [n_1^{(i)} \sigma_{11} - n_2^{(i)} \sigma_{22}]^2 + [n_3^{(i)} (\sigma_{12} + \sigma_{21})]^2 \right)^{\frac{1}{2}} \quad (5.133)$$

$$W = \left( \frac{3}{2} \right)^{1/s} > 1 \quad (5.134)$$

$k, l_1^{(i)}, l_2^{(i)}, m_1^{(i)}, m_2^{(i)}, m_3^{(i)}, n_1^{(i)}, n_2^{(i)}$  and  $n_3^{(i)}$  ( $i = 1, \dots, s$ ) are the material parameters.

According to the crystallographic structure of the sheet metal, for BCC alloys  $k = 3$  and for FCC alloys  $k = 4$ .



To identify the other parameters in the above equations, either the 8-point or the 16-point formulations should be used. For 8-point formulation, eight different experimental tests are needed. Similar to the YLD2003 criterion,  $\sigma_0, \sigma_{45}, \sigma_{90}, \sigma_b, r_0, r_{45}, r_{90}, r_b$ , must be determined using experimental tests. For 8-point model, the parameter  $s$  is equal to one ( $s = 1$ ) and for the 16-point model the parameter  $s$  is equal to two ( $s = 2$ ).

If  $\sigma_\theta$  is the yield stress with the angle of  $\theta$  with respect to the rolling direction, then the equivalent stress can be calculated as below:

$$\bar{\sigma}|_\theta = \sigma_\theta F_\theta \quad (5.135)$$

where  $F_\theta$  is defined by the relation as follow,

$$\frac{F_\theta^{2k}}{w-1} = \sum_{i=1}^s \left[ w^{i-1} \left( [L^{(i)} + M^{(i)}]^{2k} + [L^{(i)} - M^{(i)}]^{2k} \right) + w^{s-i} \left( [M^{(i)} + N^{(i)}]^{2k} + [M^{(i)} - N^{(i)}]^{2k} \right) \right] \quad (5.136)$$

and

$$L_\theta^{(i)} = l_1^{(i)} \cos^2 \theta + l_2^{(i)} \sin^2 \theta \quad (5.137)$$

$$M_\theta^{(i)} = \left( [m_1^{(i)} \cos^2 \theta - m_2^{(i)} \sin^2 \theta]^2 + [m_3^{(i)} \sin 2\theta]^2 \right)^{\frac{1}{2}} \quad (5.138)$$

$$N_\theta^{(i)} = \left( [n_1^{(i)} \cos^2 \theta - n_2^{(i)} \sin^2 \theta]^2 + [n_3^{(i)} \sin 2\theta]^2 \right)^{\frac{1}{2}} \quad (5.139)$$

If simplify the equations 5.135 – 5.139 and normalize them with a reference yield stress, then three of the eight theoretical equations related to each experimental test can be obtained using below relation,

$$y_\theta = \frac{\sigma_\theta}{Y_{ref}} = \frac{1}{F_\theta} \quad (5.140)$$

and if use the Lankford anisotropy coefficients, the other three equations can be obtained as follows:

$$r_\theta = \frac{F_\theta}{G_\theta} - 1 \quad (5.141)$$

where  $G_\theta$  is determined as,

$$\begin{aligned} \frac{F_\theta^{2k-1} G_\theta}{w-1} = & \sum_{i=1}^s \left( w^{i-1} [\hat{L}_\theta^{(i)} + \hat{M}_\theta^{(i)}] [L_\theta^{(i)} + M_\theta^{(i)}]^{2k-1} \right. \\ & + w^{i-1} [\hat{L}_\theta^{(i)} - \hat{M}_\theta^{(i)}] [L_\theta^{(i)} - M_\theta^{(i)}]^{2k-1} \\ & + w^{s-i} [\hat{M}_\theta^{(i)} + \hat{N}_\theta^{(i)}] [M_\theta^{(i)} + N_\theta^{(i)}]^{2k-1} \\ & \left. + w^{s-i} [\hat{M}_\theta^{(i)} - \hat{N}_\theta^{(i)}] [M_\theta^{(i)} - N_\theta^{(i)}]^{2k-1} \right) \end{aligned} \quad (5.142)$$

where,

$$\hat{L}_\theta^{(i)} = l_1^{(i)} + l_2^{(i)} \quad (5.143)$$

$$\hat{M}_\theta^{(i)} = [m_1^{(i)} - m_2^{(i)}] [m_1^{(i)} \cos^2 \theta - m_2^{(i)} \sin^2 \theta] / M_\theta^{(i)} \hat{L}_\theta^{(i)} = l_1^{(i)} + l_2^{(i)} \quad (5.144)$$

$$\hat{N}_\theta^{(i)} = [n_1^{(i)} - n_2^{(i)}] [n_1^{(i)} \cos^2 \theta - n_2^{(i)} \sin^2 \theta] / N_\theta^{(i)} \quad (5.145)$$

To find the other two equations, equibiaxial tension test and step by step Erichson test data have been used. The plane stress components of the stress tensor can be obtained as,

$$\sigma_{11}|_b = \sigma_b, \quad \sigma_{22}|_b = \sigma_b, \quad \sigma_{12}|_b = \sigma_{21}|_b = 0 \quad (5.146)$$

Then the equivalent stress for equibiaxial conditions can be obtained as below,

$$\bar{\sigma}|_b = \sigma_b F_b \quad (5.147)$$

where  $F_b$  is defined by the relationships

$$\begin{aligned} \frac{F_b^{2k}}{w-1} = & \sum_{i=1}^s \left[ w^{i-1} \left( [L_b^{(i)} + M_b^{(i)}]^{2k} \right. \right. \\ & + [L_b^{(i)} - M_b^{(i)}]^{2k} \left. \right) \\ & \left. + w^{s-i} \left( [M_b^{(i)} + N_b^{(i)}]^{2k} + [M_b^{(i)} - N_b^{(i)}]^{2k} \right) \right] \end{aligned} \quad (5.148)$$

and ,

$$L_b^{(i)} = l_1^{(i)} + l_2^{(i)} \quad (5.149)$$

$$M_b^{(i)} = m_1^{(i)} + m_2^{(i)} \quad (5.150)$$

$$N_b^{(i)} = n_1^{(i)} + n_2^{(i)} \quad (5.151)$$

then the normalized equibiaxial yield stress is,

$$y_b = \frac{\sigma_b}{Y_{ref}} = \frac{1}{F_b} \quad (5.152)$$

Which gives the 7<sup>th</sup> equation needed to determine the criterion constants. Then after some simple mathematical manipulations the 8<sup>th</sup> equation can be obtained using the below relation.

$$r_b = \frac{F_b}{G_b} - 1 \quad (5.153)$$

where is defined by the relationships,

$$\begin{aligned} \frac{F_b^{2k-1} G_b}{w-1} = & \sum_{i=1}^s \left( w^{i-1} [\hat{L}_b^{(i)} + \hat{M}_b^{(i)}] [L_b^{(i)} + M_b^{(i)}]^{2k-1} \right. \\ & + w^{i-1} [\hat{L}_b^{(i)} - \hat{M}_b^{(i)}] [L_b^{(i)} - M_b^{(i)}]^{2k-1} \\ & + w^{s-i} [\hat{M}_b^{(i)} + \hat{N}_b^{(i)}] [M_b^{(i)} + N_b^{(i)}]^{2k-1} \\ & \left. + w^{s-i} [\hat{M}_b^{(i)} - \hat{N}_b^{(i)}] [M_b^{(i)} - N_b^{(i)}]^{2k-1} \right) \end{aligned} \quad (5.154)$$

$$\hat{L}_b^{(i)} = l_1^{(i)} \quad (5.155)$$

$$\hat{M}_b^{(i)} = m_1^{(i)} \quad (5.156)$$

$$\hat{N}_b^{(i)} = n_1^{(i)} \quad (5.157)$$

then if simplify all equations proposed above considering these parameters,

$$F_\theta^6 = \frac{1}{2} ([L_\theta + M_\theta]^6 + [L_\theta - M_\theta]^6 + [M_\theta + N_\theta]^6 + [M_\theta - N_\theta]^6) \quad (5.158)$$

The parameters  $L_\theta$ ,  $M_\theta$  and  $N_\theta$  can be calculated using the equations 5.137 - 5.139.

and

$$G_\varphi = \frac{1}{2F_\varphi^5} \left( [\hat{L}_\theta + \hat{M}_\theta][\hat{L}_\theta + \hat{M}_\theta]^5 + [\hat{L}_\theta - \hat{M}_\theta][\hat{L}_\theta - \hat{M}_\theta]^5 \right. \\ \left. + [\hat{M}_\theta + \hat{N}_\theta][\hat{M}_\theta + \hat{N}_\theta]^5 + [\hat{M}_\theta - \hat{N}_\theta][\hat{M}_\theta - \hat{N}_\theta]^5 \right) \quad (5.159)$$

where the parameters  $\hat{L}_\theta$ ,  $\hat{M}_\theta$  and  $\hat{N}_\theta$  can be calculated using the equations 5.143 - 5.145.

The relations 5.140 and 5.158 give three equations for  $0^\circ$ ,  $45^\circ$  and  $90^\circ$  using tensile tests and another three equations can be extracted using equations 5.141, 5.158 and 5.159. The other two equations can be obtained using equibiaxial and Erichsen test. Then if apply the stress states in the mentioned relations the required equations can be extracted as follows:

If  $\theta = 0^\circ$ , the 1<sup>st</sup> equation can be obtained using the below relations and equation 5.140.

$$F_0^6 = \frac{1}{2} ([L_0 + M_0]^6 + [L_0 - M_0]^6 + [M_0 + N_0]^6 + [M_0 - N_0]^6) \quad (5.160)$$

where,

$$L_0 = l_1 \quad (5.161)$$

$$M_0 = |m_1| \quad (5.162)$$

$$N_0 = |n_1| \quad (5.163)$$

and using anisotropy data in the RD, the 4<sup>th</sup> equation can be obtained as,

$$r_0 = \frac{F_0}{G_0} - 1 \quad (5.164)$$

where,

$$G_0 = \frac{1}{2F_0^5} \left( [\hat{L}_0 + \hat{M}_0][L_0 + M_0]^5 + [\hat{L}_0 - \hat{M}_0][L_0 - M_0]^5 \right. \\ \left. + [\hat{M}_0 + \hat{N}_0][M_0 + N_0]^5 + [\hat{M}_0 - \hat{N}_0][M_0 - N_0]^5 \right) \quad (5.165)$$

and

$$\hat{L}_0 = l_1 + l_2 \quad (5.166)$$

$$\hat{M}_0 = \frac{(m_1 - m_2)m_1}{|m_1|} \quad (5.167)$$

$$\hat{N}_0 = \frac{(n_1 - n_2)n_1}{|n_1|} \quad (5.168)$$

and if  $\theta = 45^\circ$ , using the stress data, the 2<sup>nd</sup> equation is obtained.

$$F_{45}^6 = \frac{1}{2} ([L_{45} + M_{45}]^6 + [L_{45} - M_{45}]^6 + [M_{45} + N_{45}]^6 + [M_{45} - N_{45}]^6) \quad (5.169)$$

where,

$$L_{45} = \frac{1}{2}l_1 + \frac{1}{2}l_2 \quad (5.170)$$

$$M_{45} = \left[ \left( \frac{1}{2}m_1 - \frac{1}{2}m_2 \right)^2 + m_3^2 \right]^{\frac{1}{2}} \quad (5.171)$$

$$N_{45} = \left[ \left( \frac{1}{2}n_1 - \frac{1}{2}n_2 \right)^2 + n_3^2 \right]^{\frac{1}{2}} \quad (5.172)$$

then using the anisotropy data in this direction the 5<sup>th</sup> equation is obtained.

$$r_{45} = \frac{F_{45}}{G_{45}} - 1 \quad (5.173)$$

where,

$$G_{45} = \frac{1}{2F_{45}^5} ([\hat{L}_{45} + \hat{M}_{45}][L_{45} + M_{45}]^5 + [\hat{L}_{45} - \hat{M}_{45}][L_{45} - M_{45}]^5 + [\hat{M}_{45} + \hat{N}_{45}][M_{45} + N_{45}]^5 + [\hat{M}_{45} - \hat{N}_{45}][M_{45} - N_{45}]^5) \quad (5.174)$$

and,

$$\hat{L}_{45} = l_1 + l_2 \quad (5.175)$$

$$\hat{M}_{45} = \frac{(m_1 - m_2) \left( \frac{1}{2}m_1 - \frac{1}{2}m_2 \right)}{\sqrt{\left( \frac{1}{2}m_1 - \frac{1}{2}m_2 \right)^2 + m_3^2}} \quad (5.176)$$

$$\hat{N}_{45} = \frac{(n_1 - n_2) \left( \frac{1}{2}n_1 - \frac{1}{2}n_2 \right)}{\sqrt{\left( \frac{1}{2}n_1 - \frac{1}{2}n_2 \right)^2 + n_3^2}} \quad (5.177)$$

If  $\theta = 90^\circ$ , the 3<sup>rd</sup> equation can be obtained using  $\sigma_{90}$  value and the below relations.

$$F_{90}^6 = \frac{1}{2} ([L_{90} + M_{90}]^6 + [L_{90} - M_{90}]^6 + [M_{90} + N_{90}]^6 + [M_{90} - N_{90}]^6) \quad (5.178)$$

where,

$$L_{90} = l_2 \quad (5.179)$$

$$M_{90} = |m_2| \quad (5.180)$$

$$N_0 = |n_2| \quad (5.181)$$

and with the anisotropy data in TD, the 6<sup>th</sup> equation will be obtained.

$$r_{90} = \frac{F_{90}}{G_{90}} - 1 \quad (5.182)$$

where,

$$G_{90} = \frac{1}{2F_{90}^5} ([\hat{L}_{90} + \hat{M}_{90}][L_{90} + M_{90}]^5 + [\hat{L}_{90} - \hat{M}_{90}][L_{90} - M_{90}]^5 + [\hat{M}_{90} + \hat{N}_{90}][M_{90} + N_{90}]^5 + [\hat{M}_{90} - \hat{N}_{90}][M_{90} - N_{90}]^5) \quad (5.183)$$

and,

$$\hat{L}_{90} = l_1 + l_2 \quad (5.184)$$

$$\hat{M}_{90} = \frac{(m_1 - m_2)(-m_2)}{|m_2|} \quad (5.185)$$

$$\hat{N}_{90} = \frac{(n_1 - n_2)(-n_2)}{|n_2|} \hat{L}_{90} \quad (5.186)$$

The considering the equibiaxial test,

$$\sigma_{11}|_b = \sigma_b, \sigma_{22}|_b = \sigma_b, \sigma_{12}|_b = \sigma_{21}|_b = 0 \Rightarrow \bar{\sigma}|_b = \sigma_b F_b \quad (5.187)$$

and ,

$$\bar{\sigma}|_b = \sigma_b F_b \quad (5.188)$$

where,

$$F_b^6 = \frac{1}{2} ([L_b + M_b]^6 + [L_b - M_b]^6 + [M_b + N_b]^6 + [M_b - N_b]^6) \quad (5.189)$$

and,

$$L_b = l_1 + l_2 \quad (5.190)$$

$$M_b = m_1 - m_2 \quad (5.191)$$

$$N_b = n_1 - n_2 \quad (5.192)$$

then the 7<sup>th</sup> equation is:

$$y_b = \frac{\sigma_b}{Y_{ref}} = \frac{1}{F_b} \quad (5.193)$$

then using anisotropy data the 8<sup>th</sup> equation can be obtained as,

$$r_b = \frac{F_b}{G_b} - 1 \quad (5.194)$$

where,

$$G_b = \frac{1}{2F_b^5} \left( [\hat{L}_b + \hat{M}_b][L_b + M_b]^5 + [\hat{L}_b - \hat{M}_b][L_b - M_b]^5 \right. \\ \left. + [\hat{M}_b + \hat{N}_b][M_b + N_b]^5 + [\hat{M}_b - \hat{N}_b][M_b - N_b]^5 \right) \quad (5.195)$$

where,

$$\hat{L}_b = l_1 \quad (5.196)$$

$$\hat{M}_b = m_1 \quad (5.197)$$

$$\hat{N}_b = n_1 \quad (5.198)$$

To determine the material constants ( $l_1, l_2, m_1, m_2, m_3, n_1, n_2$  and  $n_3$ ) the below error function needs to be minimized using some optimization methods.

$$\epsilon(l_1, l_2, m_1, m_2, m_3, n_1, n_2, n_3) \\ = \sum_{i=1}^3 \left( \frac{y_{\theta_i}^{exp}}{y_{\theta_i}} - 1 \right)^2 + \sum_{i=1}^3 (r_{\theta_i}^{exp} - r_{\theta_i})^2 \\ + \left( \frac{y_b^{exp}}{y_b} - 1 \right)^2 + (r_b^{exp} - r_b)^2 = \text{minimum} \quad (5.199)$$

To minimize this error function, as explained beforehand, two methods of minimization (*Nelder-Mead* and the *Random Search*) algorithms were used. The results obtained from these methods for DKP6112 steel material have been shown in the table 5.3.

Then to implement the above model to the FEM simulations, the associated flow rule has to be employed.

$$\Delta \varepsilon_{ij}^p = \Delta \lambda \frac{\partial F}{\partial \sigma_{ij}} \quad (5.200)$$

Table 5.3. BBC2008 constants obtained using the optimization methods for DKP6112 steel material

Constants	$l_1$	$l_2$	$n_1$	$n_2$	$n_3$	$m_1$	$m_2$	$m_3$
Nelder-Mead	0.470	0.453	0.536	0.526	0.436	0.442	0.422	0.526
Random Search	0.470	0.453	0.537	0.527	0.437	0.442	0.423	0.527

Therefore the yield function can be rewritten as follows:

$$f = \frac{\bar{\sigma}^{2k}(\sigma_{ij})}{Y^{2k}} - 1 = \frac{\hat{\sigma}(\sigma_{ij})}{Y^{2k}} - 1 = 0 \quad (5.201)$$

Then the related derivatives are as below,

$$\frac{\partial f}{\partial \sigma_{ij}} = \frac{\partial f}{\partial \hat{\sigma}} \left[ \frac{\partial \hat{\sigma}}{\partial L} \frac{\partial L}{\partial \sigma_{ij}} + \frac{\partial \hat{\sigma}}{\partial M} \frac{\partial M}{\partial \sigma_{ij}} + \frac{\partial \hat{\sigma}}{\partial N} \frac{\partial N}{\partial \sigma_{ij}} \right] \quad (5.202)$$

$$\frac{\partial f}{\partial \hat{\sigma}} = \frac{1}{Y^{2k}} \quad (5.203)$$

$$\frac{\partial \hat{\sigma}}{\partial L} = k[(L + M)^{2k-1} + (L - M)^{2k-1}] \quad (5.204)$$

$$\frac{\partial \hat{\sigma}}{\partial N} = k[(M + N)^{2k-1} - (M - N)^{2k-1}] \quad (5.205)$$

$$\frac{\partial \hat{\sigma}}{\partial M} = k \left[ [(L + M)^{2k-1} - (L - M)^{2k-1}] + [(M + N)^{2k-1} - (M - N)^{2k-1}] \right] \quad (5.206)$$

$$\frac{\partial L}{\partial \sigma} = \{l_1, l_2, -(l_1 + l_2), 0\} \quad (5.207)$$

$$\frac{\partial M}{\partial \sigma} = \frac{1}{M} \{ \hat{M}m_1, -\hat{M}m_2, M(m_2 - m_1), m_3 2\sigma_{12} \} \quad (5.208)$$



$$\frac{\partial N}{\partial \sigma} = \frac{1}{N} \{ \hat{N}n_1, -\hat{N}n_2, \hat{N}(n_2 - n_1), n_3 2\sigma_{12} \} \quad (5.209)$$

$$\hat{M} = m_1\sigma_{11} - m_2\sigma_{22} \quad (5.210)$$

$$\hat{N} = n_1\sigma_{11} - n_2\sigma_{22} \quad (5.211)$$

the plastic multiplier increment can be then calculated from consistency condition.

$$\Delta\lambda = \frac{\frac{df}{d\sigma_{ij}} C_{ijkl} \Delta\varepsilon_{kl}}{\frac{df}{d\sigma_{ij}} C_{ijkl} \frac{df}{d\sigma_{kl}} - \frac{df}{dY} \frac{dY}{d\bar{\varepsilon}^p} \frac{\sigma_{kl}}{Y} \frac{df}{d\sigma_{kl}}} \quad (5.212)$$

Finally the VUMAT subroutines were used to implement these equations directly to the FEM simulations to investigate the effect of the constitutive equations.

## 5.2 Hardening rules

In the plastic region, metals are typically *work-hardened* or *strain-hardened* where the flow stress monotonically increases with accumulated plastic strain. The change and evolution of the yield surface due to strain is also thought as important as initial shape of the yield surface. In the increasing case of flow stress, yield surface changes its shape (isotropic hardening) or position (kinematic hardening) or both shape and position (mixed hardening) to accommodate this new stress state due to the definition of all stress states are laid on or within the yield surface (Figure 5.1).

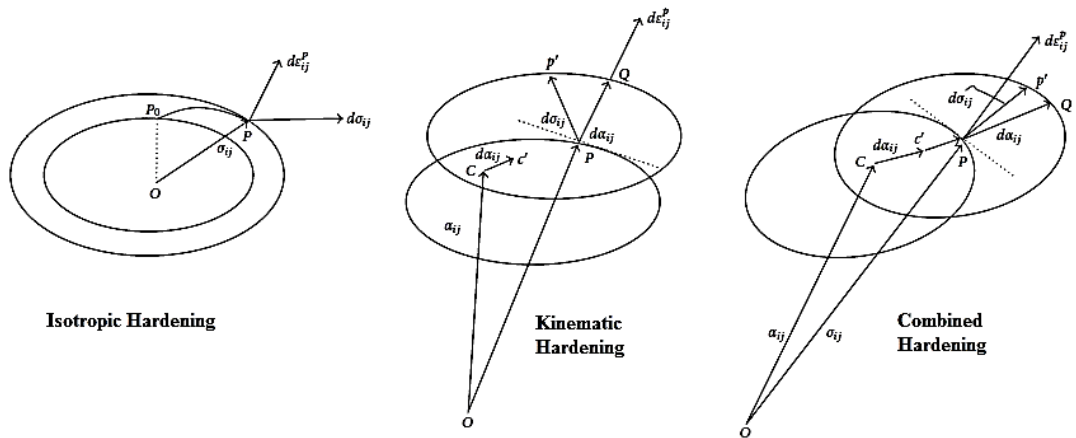


Figure 5.1. Schematic view of hardening rules

The hardening models used in this study and their implementation scheme are summarized as below,

### 5.2.1 Implementation of the isotropic hardening rule

To implement the isotropic hardening rule in the FEM models using Von-Mises yield criterion and radial return convention, the elastic- plastic governing equations have to be employed.

The elastic part of the governing equation is,

$$\sigma_{ij} = \lambda \delta_{ij} \varepsilon_{kk}^e + 2\mu \varepsilon_{ij}^e \quad (5.213)$$

where  $\lambda$  and  $\mu$  are Lamé constants.

For the plastic part of the equation, the previously mentioned equivalent stress and equivalent plastic strain equations (5.2, 5.4) have been employed. Then using the associated flow rule will help to calculate the plastic strain rate as:

$$\dot{\varepsilon}_{ij}^p = \frac{3 S_{ij}}{2 Y} \dot{\bar{\varepsilon}}^p \quad (5.214)$$

where  $S_{ij}$  is called the deviatoric stress. Then firstly the Von-Mises stress should be calculated based on the purely elastic behavior of the material to find the elastic predictor as:

$$\bar{\sigma}^{pr} = \left( \frac{3}{2} S_{ij}^{pr} S_{ij}^{pr} \right)^{\frac{1}{2}}, \quad S_{ij}^{pr} = S_{ij}^0 + 2\mu \Delta \varepsilon_{ij}^e \quad (5.215)$$

If the elastic predictor is larger than the current yield stress, plastic flow has been started. After some manipulation the elastic predictor can be calculated as:

$$\bar{\sigma}^{pr} - 3\mu \Delta \bar{\varepsilon}^p = Y(\bar{\varepsilon}^p) \quad (5.216)$$

To update the stress and the plastic strain the following equations are used:

$$\sigma_{ij} = \eta_{ij} \sigma_y + \frac{1}{3} \delta_{ij} \sigma_{kk}^{pr} \quad (5.217)$$

$$\Delta \varepsilon_{ij}^p = \frac{3}{2} \eta_{ij} \Delta \bar{\varepsilon}^p \quad (5.218)$$

where

$$\eta_{ij} = S_{ij}^{pr} / \bar{\sigma}^{pr} \quad (5.219)$$

These formulations have been implemented to the explicit finite element codes associated with yield criterion as a constitutive model of the material.

### 5.2.1.1 Hollomon (power law) model

This model which was proposed by Hollomon [41] is an isotropic hardening model where the equivalent yield stress,  $\bar{\sigma}$ , is a power law function of equivalent plastic strain as:

$$\bar{\sigma} = K \bar{\epsilon}^n \quad (5.220)$$

where  $K$  is known as the hardening coefficient or strength coefficient and  $n$  is the hardening index. There is a standard test method which defines how to determine these two coefficients using tensile tests. These parameters are a good norm about the formability of the materials where for example low ductile materials have very low hardening index.

### 5.2.1.2 Piecewise linear model

In this model experimentally determined stress-strain points are used and a linear relation is formulated considering the successive points,

$$\Delta \bar{\sigma} = H \Delta \bar{\epsilon} \quad (5.221)$$

where  $H$  is the slope of the stress-strain curve at mentioned state.

## 5.2.2 Implementation of the kinematic hardening

The general expression for Zeigler-Prager model was proposed by Prager [42] and Ziegler did a modification and assumed that the translation is not toward the outward normal and the direction is a vector which joins the current stress point to the surface center of the yield loci. The governing equation for elastic part is,

$$\sigma_{ij} = \lambda \delta_{ij} \epsilon_{kk}^e + 2\mu \epsilon_{ij}^e \quad (5.222)$$

and for the plastic part of the equations, the Von-Mises yield function has been changed to include the back stress,  $\alpha$ , as follows:

$$\left(\frac{3}{2}(S_{ij} - \alpha_{ij})(S_{ij} - \alpha_{ij})\right)^{\frac{1}{2}} - Y = 0 \quad (5.223)$$

Then the equivalent plastic strain rate can be calculated as,

$$\dot{\bar{\epsilon}}^p = \left(\frac{2}{3} \dot{\epsilon}_{ij}^p \dot{\epsilon}_{ij}^p\right)^{\frac{1}{2}} \quad (5.224)$$

where,

$$\dot{\epsilon}_{ij}^p = \frac{3}{2}(S_{ij} - \alpha_{ij}) \dot{\bar{\epsilon}}^p / Y \quad (5.225)$$

and the back stresses can be calculated as below,

$$\dot{\alpha}_{ij} = \frac{2}{3} H \dot{\epsilon}_{ij}^p \quad (5.226)$$

If the backward Euler method is used to integrate the equation 5.233 and 5.234 then the plastic strain increment can be obtained as:

$$\Delta \epsilon_{ij}^p = \frac{3}{2}(S_{ij}^{pr} - \alpha_{ij}^0) \Delta \bar{\epsilon}^p / \bar{\sigma}^{pr} \quad (5.227)$$

and after some mathematical manipulation, the equivalent plastic strain increment will be attained as follows:

$$\Delta \bar{\epsilon}^p = (\bar{\sigma}^{pr} - Y) / (H + 3\mu) \quad (5.228)$$

This leads to the following update equations for the stresses, the plastic strains and the back stresses

$$\Delta \alpha_{ij} = \eta_{ij} h \Delta \bar{\epsilon}^p \quad (5.229)$$

$$\Delta \epsilon_{ij}^p = \frac{3}{2} \eta_{ij} \Delta \bar{\epsilon}^p \Delta \alpha_{ij} \quad (5.230)$$

$$\sigma_{ij} = \alpha_{ij}^0 + \Delta\alpha_{ij} + \eta_{ij}Y + \frac{1}{3}\delta_{ij}\sigma_{kk}^{pr} \quad (5.231)$$

$$\eta_{ij} = (S_{ij}^{pr} - \alpha_{ij}^0)/\bar{\sigma}^{pr} \quad (5.232)$$

The above formulations were used to model kinematic hardening using VUMAT subroutines.

### 5.2.3 Implementation of the combined hardening model

This formulation is also called “combined” or “mixed” since it employs the characteristics of both isotropic and kinematic hardening.

The Chaboche-Zeigler combined model formulation which was employed in this study, contains five different parameters [44]. The related equations are;

$$\bar{\sigma} = \sigma_0 + Q(1 - e^{-b\bar{\varepsilon}^p}) \quad (5.233)$$

and for the evolution of the kinematic part,

$$d\alpha_{ij} = C \frac{d\bar{\varepsilon}^p}{\bar{\sigma}} (S - \alpha_{ij}) - \gamma \alpha_{ij} d\bar{\varepsilon}^p \quad (5.234)$$

where  $\sigma_0$  is the yield stress,  $Q$  and  $b$  are the isotropic part constants and  $\gamma$  and  $C$  are the constants of the kinematic part.

If  $C_{ijkl}$  is the matrix of elastic constants then the incremental stress components for updating the stresses can be obtained as below,

$$d\sigma_{ij} = C_{ijkl} (d\varepsilon_{kl} - d\varepsilon_{kl}^p) \quad (5.235)$$

The equivalent plastic strain then is calculated using the below relation,

$$d\bar{\varepsilon}^p = \frac{\frac{dF}{d\sigma_{ij}} C_{ijkl} d\varepsilon_{kl}}{Qbe^{-b\bar{\varepsilon}^p} + C - \gamma \frac{dF}{d\sigma_{ij}} C_{ijkl} d\alpha_{kl} + \frac{dF}{d\sigma_{ij}} C_{ijkl} \frac{dF}{d\sigma_{kl}}} \quad (5.236)$$

where  $F$  is the Von-Mises yield function.

### 5.3 Forming Limit Diagrams

The forming limit diagram (FLD) is an important concept utilized for the evaluation of the formability of sheet metals. A plot of in-plane minor and major strains compose a forming limit diagram (FLD) or *Keeler* diagram [13]. By the use of these diagrams, the onset of failure due to necking, or potential trouble areas on the deformed part under various loading types can be estimated and investigated.

FLDs can be measured by various methods such as the uniaxial tensile test using specimens having various dimensions with and without notches. Common to all these tests is that numerous specimens or die geometries have to be used to simulate various principal strain ratios corresponding to various points on the diagram.

Extensive theoretical and empirical studies have been conducted on the instability analysis and FLD prediction of the metallic sheets. Maximum Load, Strain Propagation [12], Swift model [14], Storen and Rice model [15], M-K model [16] etc. are some of these studies.

Swift [14] determined the condition for forming as diffuse neck is satisfied when the load reaches a maximum along both principal directions; Therefore,

$$dF = 0 \quad (5.237)$$

The other theoretical approach is the M-K model [16] which assumes a pre-existing defect in the material that leads to the local necking phenomenon. This defect can in principle be due to any combination of geometric and material non-uniformity, but the most common approach is to characterize the defect by a variation in the material thickness. Although this procedure is the most widely used method for the generation of forming limit curves (FLCs) in the absence of experimental data, but it suffers from the path dependency problem either. The initial imperfection, is defined geometrically by the below ratio:

$$f_{t_0} = \frac{t_0^b}{t_0^a} < 0 \quad (5.238)$$

where  $f_{t_0}$  is the imperfection coefficient and  $t_0^b$  and  $t_0^a$  are the initial thicknesses of zone  $b$  and zone  $a$ , respectively (Figure 5.2).

FLC diagrams require a good knowledge of the numerical simulations because they contain some constants which should be identified using numerical methods.

The parallel concept for these FLC diagrams are the diagrams designed to show the onset of the fracture in the deformed parts instead of the necking. Due to these definition, the forming limit curves which show the necking instability are called FLCN (forming limit curve at necking) and the forming limit curves which show the fracture initiation are called FLCF (forming limit curve at fracture).

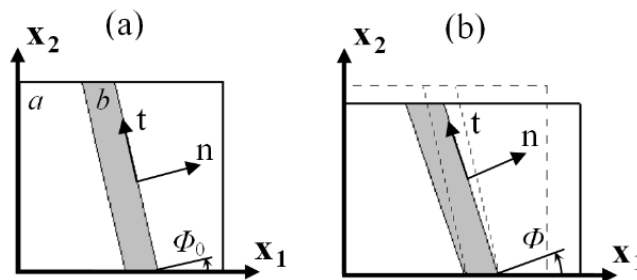


Figure 5.2. Scheme of the M-K model, a) unreformed, b) deformed

## 5.4 Fracture in sheet metal

Fracture is one of the most important and key concepts in the entire field of materials science and engineering. For engineering materials there are only two possible modes of fracture, ductile or brittle. In general, the main difference between brittle and ductile fracture can be attributed to the amount of plastic deformation that the material undergoes before fracture occurs.

*Ductile fracture criteria* (DFCs) should be able to consider nonlinear stress and strain loading histories in plastic deformation. However systematic knowledge of the reliability and applicability of DFCs and their correlation with ductile failure phenomena remains lacking which limits their industrial applications.

Several criteria can be classified under the categories of ‘*uncoupled damage criterion*’ and the ‘*coupled damage criterion*’.

### 5.4.1 Uncoupled ductile fracture criteria

The main goal of the ductile fracture criterion is to predict when and where the cracks can appear in the workpiece during the forming process. In the uncoupled ductile

fracture criteria category, the damage is formulated empirically or semi-empirically with the general function as [48]:

$$\int_0^{\bar{\varepsilon}_f} f(\sigma, \bar{\varepsilon}) d\bar{\varepsilon} \geq C \quad (5.239)$$

where  $\bar{\varepsilon}$  is the equivalent plastic strain,  $\bar{\varepsilon}_f$  is the equivalent plastic strain at fracture and  $\sigma$  is the Cauchy stress tensor. The coefficient  $C$  is determined by the experimental tests such as uniaxial tension, biaxial tension etc. Freudenthal [49] is the first one who used generalized plastic work to predict the fracture in the metals as given below,

$$\int_0^{\bar{\varepsilon}_f} \bar{\sigma} d\bar{\varepsilon} = C_F \quad (5.240)$$

where  $\bar{\sigma}$  is the equivalent stress. In this model the strain energy is related only to the equivalent stress and strain and the model could be inadequate where the distributions of stress and strain are non-uniform. Cockroft and Latham [50] observed that ductile fracture in the processes tend to occur where the largest tensile stress exists and proposed the following equation

$$\int_0^{\bar{\varepsilon}_f} \sigma_{max} d\bar{\varepsilon} = C_C \quad (5.241)$$

where  $\sigma_{max}$  is the largest stress.

Brozzo et al. [51] suggested the following relation which includes both maximum and mean stresses.

$$\int_0^{\bar{\varepsilon}_f} \frac{2\sigma_{max}}{3(\sigma_{max} - \sigma_m)} d\bar{\varepsilon} = C_B \quad (5.242)$$

where  $\sigma_m$  is the mean stress. Oh et al. [52] modified the Cockroft and Latham model to include both maximum tensile stress and equivalent stress

$$\int_0^{\bar{\varepsilon}_f} \frac{\sigma_{max}}{\bar{\sigma}} d\bar{\varepsilon} = C_O \quad (5.243)$$

here are also many researches in which hydrostatic stress has been considered. Ayada et al. [53] proposed the following criterion



$$\int_0^{\bar{\epsilon}_f} \frac{\sigma_m}{\bar{\sigma}} d\bar{\epsilon} = C_A \quad (5.244)$$

To calculate the constants in these relations, uniaxial tensile tests have been conducted and the essential parameters have been extracted using theory of plasticity.

Most of the mentioned ductile fracture criteria are giving close results to the experimental tests while linear strain paths are considered. However non-linear strain paths will cause a big discrepancy in the results, making the problem to be discussed under the strain path dependency [22-26]. Since the material parameters have not been included directly in these DFCs, most of them are suitable only for a specific material (steel, aluminum...). Therefore, for the materials other than the one utilized to identify the criterion constant, the obtained results will not be satisfying.

These problems made some researchers to modify the uncoupled DFC's and changed the general plastic work function to be able to consider strain path dependency and some material parameters like anisotropy and strain hardening coefficient. For this purpose the constants in the above relations was assumed as a function of some material parameters and strain path to make the estimation more accurate and also be usable for different strain paths, such as

$$\int_0^{\bar{\epsilon}_f} \bar{\sigma} d\bar{\epsilon} = g \quad (5.245)$$

where  $g$  is a function of material parameters to determine the limit plastic deformation energy which the material can endure. Chen et al. [54] for example assumed that  $g$  is in the form of an absolute function as below,

$$g = W [(1 + |\rho|)^a - b] \quad (5.246)$$

where  $W$  is the criterion constant that needs to be determined by the experimental test,  $a$  and  $b$  are relevant material properties depended on the sheet thickness,  $r$ -value and hardening index.  $\rho$  is the ratio of strain increments for each increment step.

Han et al. [57] introduced other modification for Cockroft and Latham's model and considered thickness strain and shear stresses. This modification makes the criterion to be able to be used for both linear and complex strain paths in sheet forming. Actually the proposed is a combination of Cockroft and Latham's criterion with the maximum

shear stress criterion where thickness strain has been added to better model the necking process and its effect on the fracture. Also the maximum shear stress term has been added to the model to make the criterion to be used for shear induced fractures normally seen in the low ductile materials like aluminum.

$$\int_0^{\epsilon_f} \sigma_{max} d\epsilon + A_1 \tau_{max} + A_2 \epsilon_t = A_3 \quad (5.247)$$

where  $A_1$ ,  $A_2$  and  $A_3$  are the material parameters which should be determined by experimental tests;  $\tau_{max}$  and  $\epsilon_t$  are maximum shear stress and thickness strain, respectively. Three different tests are essential to find the constants of the material which makes the criterion to be hard and expensive to use.

#### 5.4.2 Coupled ductile fracture criteria

On the other hand coupled DFCs incorporate damage accumulation in the constitutive equation. These models allow the yield surface of the materials to be modified by the damage-induced density change (D). This kind of DFC is difficult to incorporate into the finite element codes [48]. Some of the well-known coupled DFCs are the GTN model, Johnson-Cook, Lemaitre and Xue et al.

The GTN model is in the form of,

$$\varphi(\sigma, \bar{\epsilon}, f) = \left[ \frac{\bar{\sigma}}{\sigma_0 \bar{\epsilon}} \right]^2 + 2q_1 f^*(f) \cosh \left[ -\frac{3q_2 \sigma_m}{2\sigma_0 \bar{\epsilon}} \right] - (1 + q_3 [f^*(f)]^2) = 0 \quad (5.248)$$

where

$$f^*(f) = \begin{cases} f & \text{if } f \leq f_c \\ f_c + \frac{1/q_1 - f_c}{f_f - f_c} (f - f_c) & \text{if } f > f_c \end{cases} \quad (5.249)$$

and  $f$  is the void volume fraction,  $f_c$  the critical void volume fraction, and  $f_f$  is the void volume fraction at rupture. One of the most studied cases corresponds to the situation when the nucleation is produced by plastic strain.

In this model a damage parameter (D) describes the porosity,  $f$ , of the material. The damage parameter can vary from a value ( $f = 0$ ) for undamaged material to ( $f = 1$ ) for a completely damaged material. Because of the inability of predicting instability

caused by coalescence of micro voids in the original Gurson model, it was modified by Tvergaard and Needleman and named as the GTN model.

The Johnson-Cook failure model is a purely phenomenological model and is based on the plastic strain. The model uses a damage parameter,  $D$ , and when this parameter reaches the value of “1”, ultimate fracture is expected.

$$\left\{ \begin{array}{l} D = \int \frac{1}{\varepsilon_{fr}} d\bar{\varepsilon} \\ \varepsilon_f = \left( d_1 + d_2 e^{-d_3 \frac{\sigma_m}{\sigma_{VM}}} \right) \left[ 1 + d_4 \ln \left( \frac{\dot{\varepsilon}^p}{\dot{\varepsilon}_0} \right) \right] (1 + d_5 T) \end{array} \right. \quad (5.250)$$

$T$  in this model is the non-dimensional temperature defined as,

$$T = \begin{cases} 0 & \text{for } T_c < T_{tr} \\ (T_c - T_{tr}) / (T_m - T_{tr}) & \text{for } T_{tr} < T_c < T_m \\ 1 & \text{for } T_c > T_m \end{cases} \quad (5.251)$$

where  $T_c$  is the current temperature,  $T_m$  is the melting temperature, and  $T_{tr}$  is the transition temperature.

The CDM model is originally proposed for the brittle materials but with some modifications, it could be employed for the ductile materials too. One of these modifications, has combined the CDM and Lemaitre models to be able to model the crack initiation and propagation in the ductile materials. The criterion is,

$$\dot{D} = \frac{\partial F_D(Y, \bar{\varepsilon}, D \dots)}{\partial Y} \dot{\varepsilon} (1 - D) \quad (5.252)$$

where  $D$  is the damage parameter.

Xue showed that the governing factor of the localization condition for damage plastic solids is not the damage itself, but the resulting effect of the rate of the weakening from the plasticity damage, which is a function of the stress states on the loading path. Effects of the pressure sensitivity, the Lode angle dependence, the damage accumulation and weakening here also explored through parametric studies [69].

$$\dot{D} = m \left( \frac{\varepsilon_p}{\varepsilon_f} \right)^{m-1} \left( \frac{\dot{\varepsilon}_p}{\dot{\varepsilon}_f} \right) \quad (5.253)$$



## CHAPTER 6

### THE NEW DUCTILE FRACTURE CRITERION

The existing uncoupled ductile fracture criteria have been developed semi or fully empirically based on the general plastic energy equation. The new uncoupled ductile fracture criterion, which is developed in this study, is also based on the plastic energy equation which determines the onset of the fracture in the sheet metals.

#### 6.1 The objectives of the new criterion

This ductile fracture criterion is empirical in nature where the macroscopic process parameters have been considered and the general plastic energy has been used to define the energy dissipation in the elements. The uncoupled criteria usually expressed in terms of the stress, strain or strain path parameters. Maximum tensile stress, equivalent stress, mean stress, equivalent strain, thickness strain etc. are some parameters which have been directly implemented to develop a ductile fracture criterion by many researchers [49-55].

Chen et al. [54] showed that the results of the uncoupled ductile fracture criteria with single material constant cannot be reliable enough and are sensitive to the linearity of the strain history. He proposed using more than one constant which are dependent to the material parameters and strain ratio to decrease the strain path sensitivity of the DFCs.

Han et al. [57] proposed combining the general plastic work relation with the maximum shear stress criterion to be able to model the fracture initiation phenomenon in the low ductile materials like aluminum. Although the equation was quite successful in the predicting of the fracture initiation, at least three experimental tests are required to determine the criterion constants.

In Figure 6.1 the accuracy of the different ductile fracture criteria on the prediction of the forming limit curve at fracture (FLCF) of the DKP6112 steel material are shown. As it is clear, some DFCs like Freudenthal and Cockroft and Latham are far from the

prediction of the fracture initiation when  $\varepsilon_2 < 0$  and  $\varepsilon_2 > 0$  where some others are accurate for  $\varepsilon_2 < 0$  or  $\varepsilon_2 > 0$  like Ayada et al. which has close estimation of the fracture initiation when  $\varepsilon_2 < 0$ . These inaccuracies are believed to be dependent to the fact that the single constant of the criteria is calculated using one experimental test; hence it is unable to adopt the strain path effects completely. If the uniaxial tension test is used the left hand side will be well predicted than the right hand side of the FLCF and if the bulge test is carried out the right hand side will be more accurate. However, none of the criteria are able to precisely determine the whole FLCF using just one constant. Considering this issue, some researchers like Chen et al. [54] and Han et al. [57] proposed using more than one constant. Han et al. determined the constants experimentally using three different experimental tests (uniaxial tension, plane strain tension and bulge test) while Chen et al. preferred to include material parameters like Lankford anisotropy coefficient and hardening index to the formulation and employ only one experimental test.

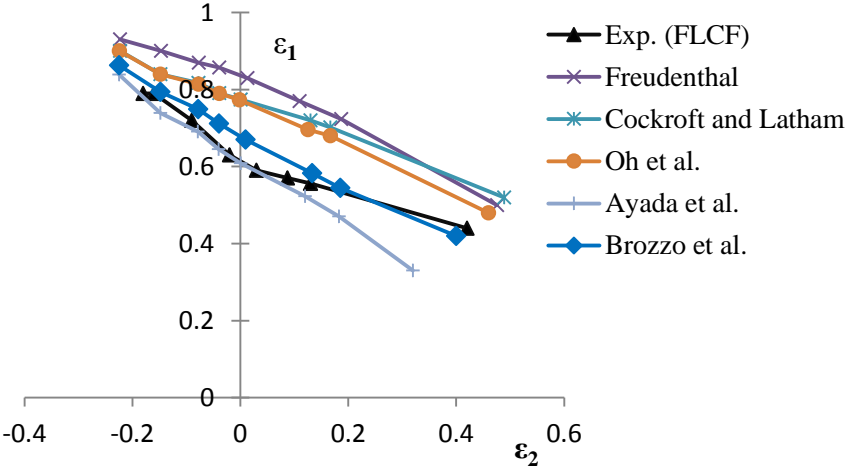


Figure 6.1. Comparison of various uncoupled criteria in determination of FLCF for DKP6112 steel

The new uncoupled ductile fracture criterion needed to be applicable for low ductile materials too, then in addition to the strain path parameters, the maximum shear stress effect has been considered as well. Therefore main objectives of the new criterion are defined as:

- To consider general plastic energy
- To consider shear stress effects especially in low ductile materials like aluminum alloys.

- To consider strain-path effects.
- To be able to determine the criterion constants using minimum experimental tests available.
- To better consider the effect of material parameters on the forming limits curves of the sheets.
- To estimate the FLCFs better than any previously developed uncoupled criteria.

Considering above characteristics, the new ductile fracture criterion proposed in a way that only one experimental test will be sufficient to determine the criterion constants which are related to the material parameters to predict the fracture better for all strain ratio values.

## 6.2 Parameters affecting the criterion

The changes on the strain-path affect the predictions of the DFCs indirectly. Any change in the strain values is related to the changes in the stresses and consequently affect the maximum stress, equivalent stress, mean stress or any other parameter that has been used to define the ductile fracture criterion. It is known that using just one constant to determine the criterion unknown could not implement the strain history changes perfectly; thus, the diversions from the experimental results emerge. To avert this problem, instead of using a single constant in the general plasticity function, a function of material parameters and strain-path is developed as:

$$\int_0^{\bar{\varepsilon}_f} f(\sigma, \bar{\varepsilon}) d\bar{\varepsilon} \geq g(\rho) \quad (6.1)$$

where  $\rho$  is the strain ratio given as,

$$\rho = d\varepsilon_2/d\varepsilon_1 \quad (6.2)$$

To make the criterion more accurate and predictive for both for  $\varepsilon_2 < 0$  and  $\varepsilon_2 > 0$  in the FLCF, the function  $g(\rho)$  has been proposed with more than one constant. This approach helps the criterion to be able to adopt the strain path history effects more precisely. One of the constants is calculated using uniaxial tension test and the others are calculated with the empirical formulas depending on the material parameters. The important material parameters which are believed to have determinative effects on the

fracture initiation point and consequently on the shape of the FLCFs can be listed as: sheet thickness ( $t$ ), strain hardening index ( $n$ ), strength coefficient ( $K$ ), anisotropy factor ( $r$ ) and modulus of the elasticity ( $E$ ).

To determine the effect of each parameter on the FLCF shape, several FLCF curves extracted from the researches were studied in details. The materials which have been reported in those works are shown in the table 6.1 with their related material characteristics.

Table 6.1 Different materials utilized to determine the material parameters effects on the forming limit curves at fracture

Material	$t(mm)$	$n$	$r$	$K(MPa)$	$E(GPa)$	$\bar{\epsilon}_f$	Reference
AKDQ steel	1	0.215	1.75	480	200	0.71	Ozturk et al. [46]
IF Steel	1	0.23	1.81	526	206	0.65	Chen et al. [54]
St14	0.8	0.249	1.8	589	173	0.74	Chen et al. [54]
St14	0.85	0.251	1.59	534	200	0.81	Chen et al. [54]
HS steel	0.92	0.156	1.04	734	206	0.47	Chen et al. [54]
S1 Steel	0.3	0.16	1.097	608	206	0.3	Han et al. [57]
S2 Steel	1.6	0.19	0.93	645	207	0.76	Han et al. [57]
S3 Steel	2.3	0.17	0.95	610	210	0.65	Han et al. [57]
S4 Steel	2.5	0.21	0.97	482	211	0.57	Han et al. [57]
AA6111-T4	0.9	0.268	0.76	504	70	0.67	Han et al. [57]
AA1100-T4	1	0.26	0.8	171	71	0.62	Takuda et al. [59]

The effect of thickness variation on the FLCFs are shown in Figure 6.2 where the St14 steel material with two different thicknesses have been compared with each other. It can obviously be observed that increasing in the sheet thickness, makes the whole FLCF curve to move upward. It indicates that the higher thickness of the sheet will lead to better formability and delays the fracture initiation time in the specimen. This conclusion also has been reported by Davis [7] and Han et al. [57] and furthermore Han et al. showed that for the higher thicknesses, the FLCFs tend to become a linear line.

Strain hardening index ( $n$ ) is one the important parameters in sheet metal forming. The greater the strain-hardening of the sheet, the better it performs in processes where there is considerable stretching; the straining will be more uniformly distributed, and the



blank will resist tearing when strain-hardening is high. In addition, since necking failures are associated with the strain hardening exponent ( $n$ ), materials having higher  $n$  will exhibit better formability.

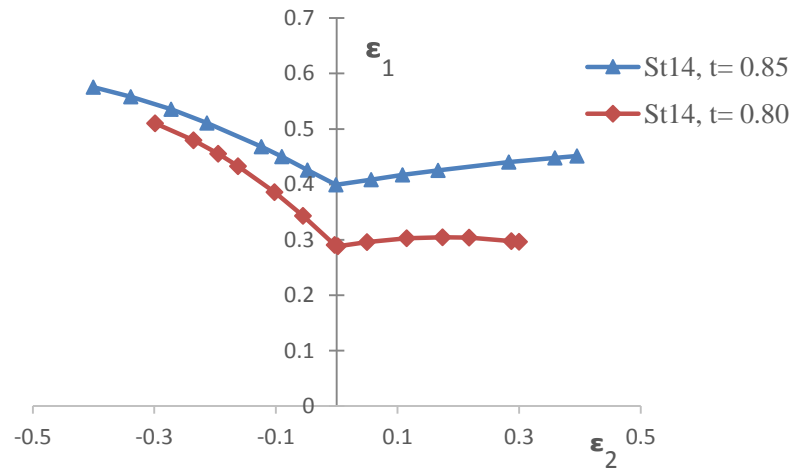


Figure 6.2. Effect of initial sheet thickness on the shape of FLCFs in St14 steel sheets [54]

Anisotropy is the other determinative parameter in deep drawing. It is defined as the directionality of properties and it is associated with the variance of atomic or ionic spacing within crystallographic directions. The development of texture in sheet is a consequence of the fact that plastic deformation is limited to specific crystallographic slip systems. Therefore, it can be said that crystallographic texture affects material properties via crystal anisotropy. A high  $r$ -value suggests that there is a high resistance to thinning and therefore a high strength in biaxial tension in the plane of the sheet. Earing phenomenon is one of the defects which caused by anisotropic properties of the sheet.

In Figure 6.3, three different steel materials with the same thicknesses have been shown to discover the effect of hardening index ( $n$ ) and normal anisotropy ( $r$ ). It is clear that increasing the amount of hardening index enhances the formability of the sheets and causes the curve to move upward. At the right hand side of the forming limit curves ( $\epsilon_2 > 0$ ) especially near the equibiaxial conditions, the materials getting failed almost in the same strain conditions where it is believed that the normal anisotropy has a decisive role in this region and lower  $r$ -value (Table 6.1) of AA1100 causes the sheet to get fractured very earlier than expected.

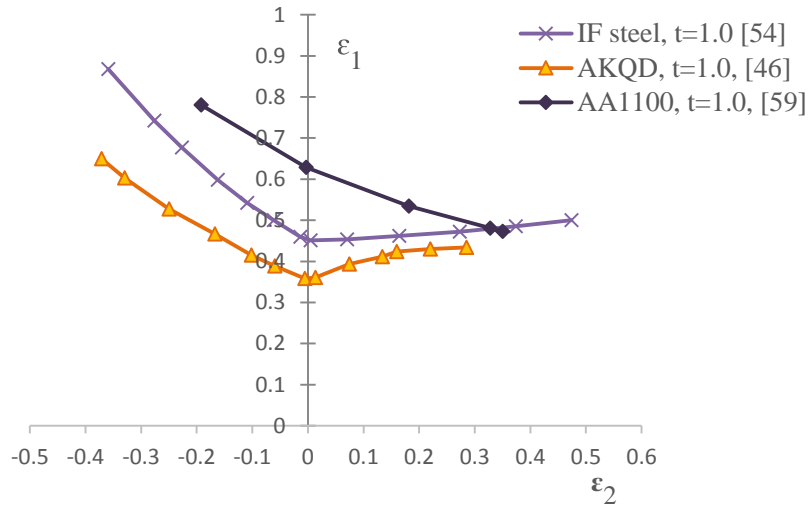


Figure 6.3. Effect of hardening index ( $n$ ) and normal anisotropy ( $r$ ) considering three materials with the same thicknesses

The previous researches show that the low ductile materials mostly have higher  $K$ -values and lower  $n$ -values and it can be concluded that the  $K$ -value has effects on the value of  $FLD_0$  (the FLD value on the plane strain line). Therefore for the low ductile materials where the shear stress value gets important, the  $K$ -value should be reflected in the constants. The  $K$ -value effects can be observed in Figure 6.4 where the FLCF of the AA1100 has been located higher than the FLCF of AA6111 due to the very low  $K$ -value; even though there is a little difference between the thickness values too which cannot be neglected.

According to the discussions above the thickness variation, hardening index and strength coefficient have significant effects in the location of the FLCFs. The amount of influence of each parameter was carefully studied to be able to propose the better empirical formulas. The thickness and strain hardening index might better have presented in Figure 6.5 where the  $K$ -values and  $r$ -values of all materials are almost the same (Table 6.1) and the differences in the position of the curves are due to the thickness and hardening index variations.

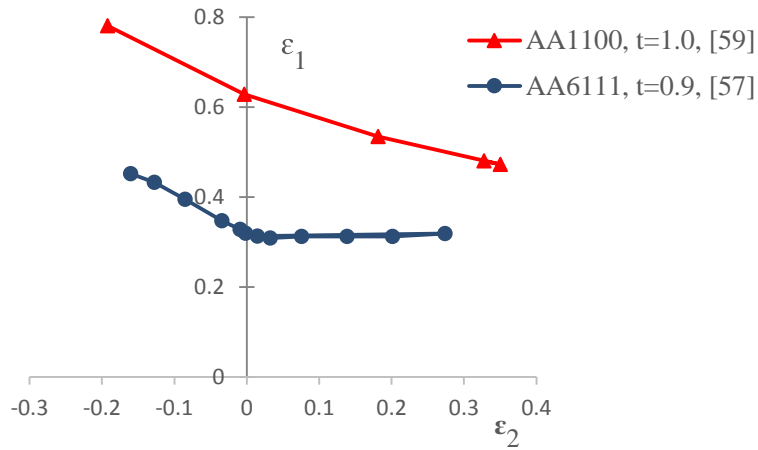


Figure 6.4. Effect of strength coefficient ( $K$ ) on the height of the FLCFs

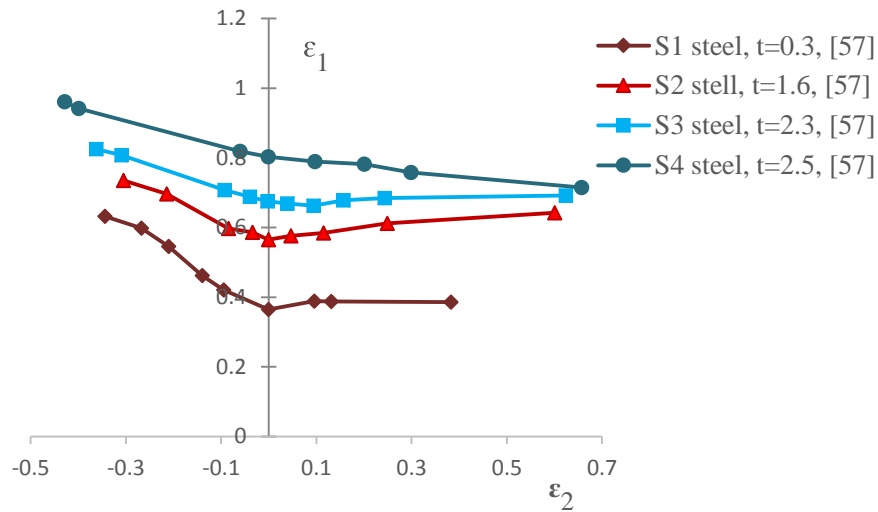


Figure 6.5. Effect of thickness and strain hardening parameters on the FLCFs of the materials with almost identical  $K$  and  $r$ -values

Davis [7] also showed that the low flow stress to elastic modulus ( $\sigma_F/E$ ) will decrease wall wrinkling and will enhance the formability of the sheets which means it will make the FLCF to move up. Considering the ratio of flow stress to elastic modulus ( $\sigma_F/E$ ) together with the  $K$ -value effects, it can be deduced that the constant which defines the effect of the maximum shear stress in the new DFC could be related to the ratio of strength coefficient to elastic modulus ( $K/E$ ). The lower the ratio of the  $K/E$  moves the FLCF curve upward which denotes that in the same circumstances the material with lower  $K/E$  ratio will get fractured later which can obviously be observed in Figure 6.4 as well.

### 6.3 The new ductile fracture criterion

After some tryouts about the type of the  $g(\rho)$  function, the absolute value of  $\rho$  was chosen regarding the shape of the FLCFs. To better adopt the shape of the FLCF, some constants have been employed in the absolute function which have to be calculated using material parameters. The new criterion, being an uncoupled criterion includes the general plasticity function too. Furthermore, the maximum shear stress criterion has been combined with the energy function to make the criterion applicable for low ductile materials as well. Therefore, the new proposed criterion is in the form of,

$$\int_0^{\bar{\varepsilon}_f} \bar{\sigma} d\bar{\varepsilon} + C_4 \tau_{max} = B(C_1 + C_2 |2\rho|^{C_3}) \quad (6.3)$$

where first term is the energy term,  $\tau_{max}$  is the maximum shear stress term,  $C_1$ ,  $C_2$ ,  $C_3$  and  $C_4$  are the material constants that is calculated using material parameters,  $\rho$  is the strain ratio,  $\bar{\varepsilon}_f$  is the equivalent plastic strain at fracture and  $B$  is the criterion unknown needed to be calculated by numerical simulation of the uniaxial tensile test.

#### 6.3.1 Calculating the criterion constants

To determine the constants  $C_1$ ,  $C_2$ ,  $C_3$  and  $C_4$ , the material parameters given in Table 6.1 have been used.

The proposed relation for the constant  $C_1$  which plays the most effective role on the height of the FLCF has been given as,

$$C_1 = 1200 \frac{n^{0.5} t^{0.5}}{r K} \quad (6.4)$$

where  $t$  (mm) is the sheet thickness,  $n$  is the strain hardening index,  $K$  (MPa) is the strength coefficient and  $r$  is the anisotropy factor.

For constant  $C_2$  two different relations are defined for  $\varepsilon_2 < 0$  and  $\varepsilon_2 > 0$  as,

$$C_2 = \frac{1}{15} \frac{1}{n r t} \quad \varepsilon_2 \geq 0 \text{ (RHS of the FLCF)} \quad (6.5)$$

$$C_2 = \frac{1}{20} \frac{t^2 n}{r} \quad \varepsilon_2 < 0 \text{ (LHS of the FLCF)} \quad (6.6)$$

The constant  $C_3$  also has two different formulations for  $\varepsilon_2 < 0$  and  $\varepsilon_2 > 0$  as follows:

$$C_3 = \frac{1}{2} n r \quad \varepsilon_2 \geq 0 \text{ (RHS of the FLCF)} \quad (6.7)$$

$$C_3 = \frac{1}{2} \frac{n}{r} \quad \varepsilon_2 < 0 \text{ (LHS of the FLCF)} \quad (6.8)$$

The  $K/E$  ratio and the hardening index ( $n$ ), were concluded to have the most determinative role on the effect of maximum shear stress in the DFC and the following relation is proposed,

$$C_4 = 8 \frac{K}{E n} \quad (6.9)$$

where  $E$  (MPa) is the modulus of elasticity.

### 6.3.2 Implementation of the new criterion

To implement the new criterion;

- A uniaxial tension test is needed to determine the anisotropy coefficients, hardening index, strength coefficient, poisson's ratio and modulus of the elasticity of the material.
- Precise measurement of the fractured region's thickness and width is required which are used to calculate the equivalent strain at fracture.
- Constants  $C_1$ ,  $C_2$ ,  $C_3$  and  $C_4$  are calculated using proposed empirical formulas.
- A numerical simulation of the uniaxial tensile test is required to determine the value of criterion unknown B. The energy term ( $\int_0^{\bar{\varepsilon}_f} \bar{\sigma} d\bar{\varepsilon}$ ) which also is known as the plastic energy dissipation per unit volume, is obtained for any integration point through the numerical analysis explicitly. The equivalent plastic stress ( $\bar{\sigma}$ ) and equivalent plastic strain ( $\bar{\varepsilon}$ ) at every integration point of the elements can easily be obtained throughout the numerical simulation process by plasticity relations. Maximum shear stress,  $\tau_{max}$ , also is calculated directly throughout the simulation for any element.
- The deformation process of the UTT will be continued until the equivalent strain in an element gets equal to  $\bar{\varepsilon}_f$ . The value of constant B then is reported to be used for determination of the fracture initiation in the desired forming process.

This process has been briefly explained with a simple flowchart in Figure B.1 of Appendix B, to obviously clarify the steps required to define the criterion unknown using numerical simulation of the UTT.

In Figure 6.6, the simulated uniaxial tension test have been shown where by implementing the element deletion technique the fracture initiation phenomenon have been modeled successfully for the DKP6112 steel material. As it can be observed, the fracture has been followed the diffuse and localized necking phenomenon. ABAQUS uses the stress wave propagation technique to determine the necking phenomena in the explicit solvers [78].

In Figure 6.7, the necking phenomenon modeled with the ABAQUS/explicit solver, has been presented. The strain and stress values shown in this figure substantiate that the amount of the strains after the necking are greater than the fracture strain reported in the flow stress curve obtained by uniaxial tensile test and consequently this fact that the strain at fracture is very higher than expected for the materials with obvious necking, should be considered carefully.

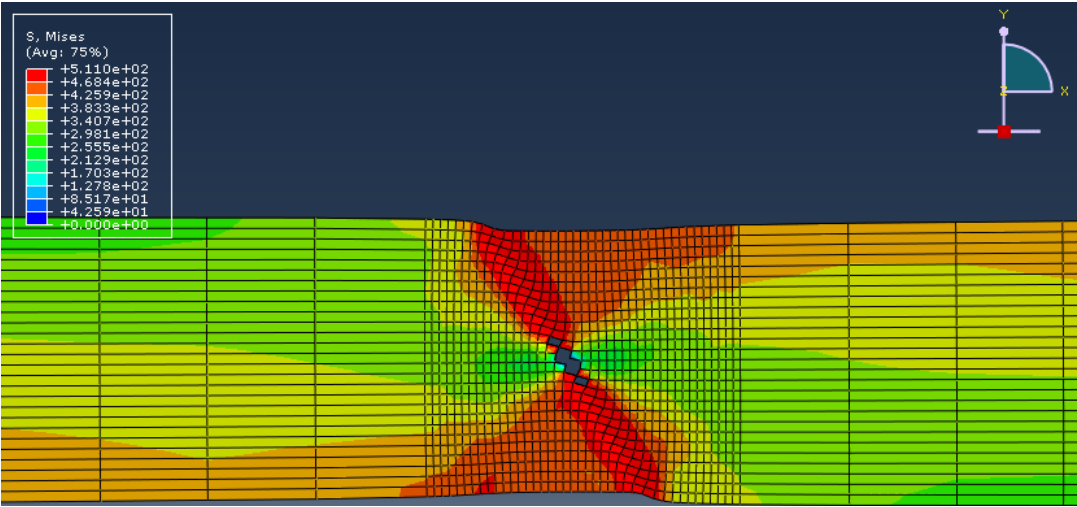


Figure 6.6. Simulation snapshot of the uniaxial tensile test showing the fracture initiation phenomenon

Since for a specific material all constants ( $C_1$ ,  $C_2$ ,  $C_3$ ,  $C_4$  and B) are calculated, the criterion can now be employed simply to determine the fracture initiation point in any other forming process.

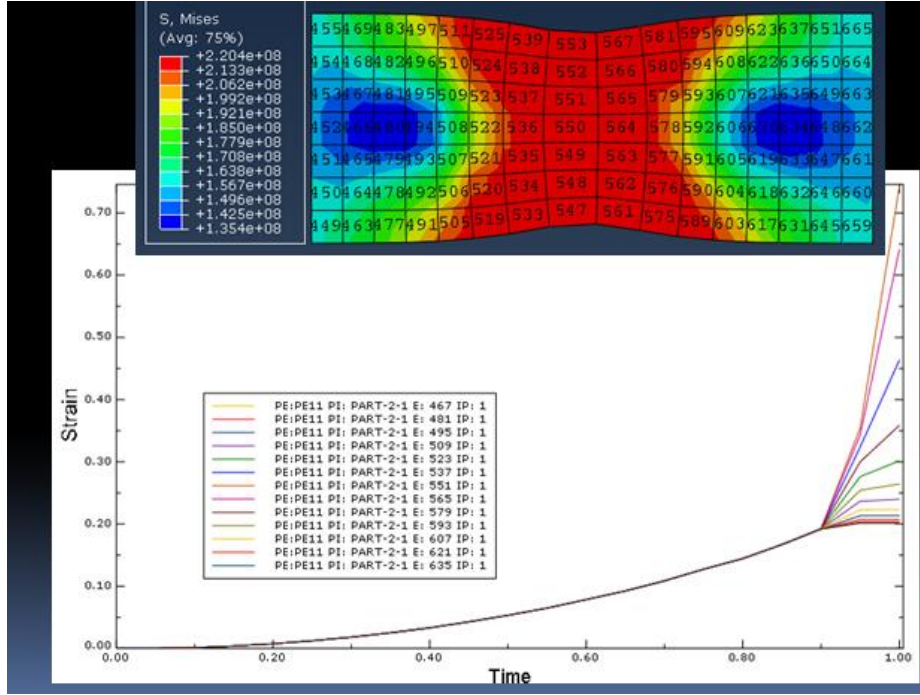


Figure 6.7. Simulation of the necking phenomenon in the uniaxial tension test using ABAQUS/Explicit

To find the fracture initiation point of the specific test with unknown deformation history, the energy term is calculated for each integration point and the strain ratio ( $\rho$ ) together with  $\tau_{max}$  is substituted to the criterion (Equation 6.3), then the fracture conditions is met if the below inequality is true.

$$\frac{\int_0^{\bar{\epsilon}_f} \bar{\sigma} d\bar{\epsilon} + C_4 \tau_{max}}{B(C_1 + C_2 |2\rho|^{C_3})} \geq 1 \quad (6.10)$$

then the amount of the stresses which element can carry will be equated to zero and the element number will be reported as a failed element. Also the in-plane values of the strains will be reported to get located in the FLCF curve and be compared with the experimental results of Nakazima test. This process briefly has been shown in Figure 6.8 as a flowchart.

### 6.3.3 Verification of the new criterion

To calibrate the new DFC, four materials (AKDQ steel [46], St14 [54], AA6111 [57] and AA110 [59]) from Table 6.1 were chosen and their FLCFs were used to adjust the empirical formulas proposed for calculating the criterion constants. The empirical formulas were modified so many times to finally the numerically obtained FLCF of

each material gets fitted to the experimental data. After so many tryouts, the numerical and experimental FLCFs for all four materials got fitted and the final equations proposed above (Equations 6.4-6.9) were extracted.

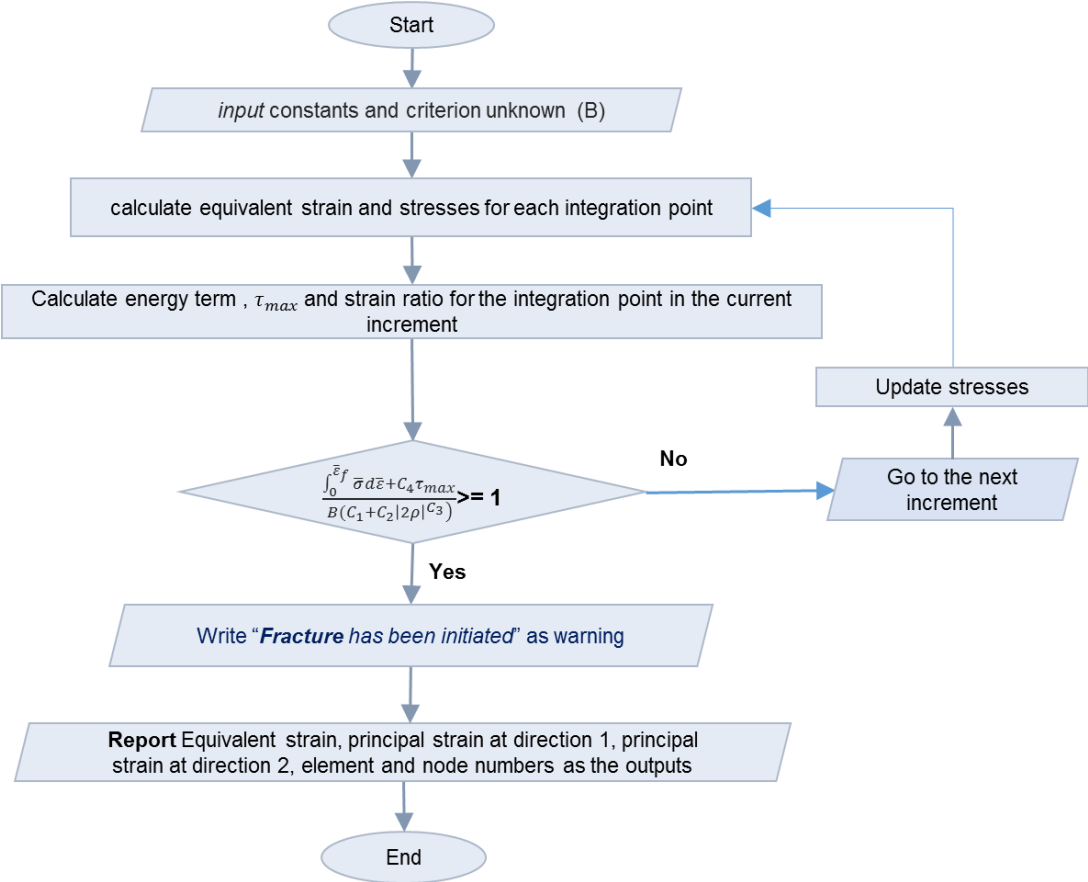


Figure 6.8. A flowchart to determine the fracture point in any desired test

Furthermore, to validate the criterion, three other materials (SS304 stainless steel, DKP6112 (DIN EN 10130-1999) steel and AA5054 aluminum alloy) were used. Then the Nakazima test specimens were modeled and using the new DFC the numerical FLCFs were drawn according to the implementation flowchart presented in Figure 6.8. The obtained FLCFs were compared to the experimental ones. Good agreements were obtained for steel materials. For Aluminum AA5450, the results are not as accurate as the steel materials but still are satisfactory enough. This is believed to be due to the highly localized necking of this material in the fractured region of the uniaxial tension test specimen. Because the thickness strain will directly affect the equivalent plastic strain at fracture and that finally affects the calculated unknown (B). The fracture strains for all materials have been measured rigorously using optical microscopes but



due to non-uniform fractured area in the region, the average values have been implemented for thickness measurements which are thought to be the source of small discrepancy for the FLCF of AA5450.

The FLCF curves of above seven materials have been shown and discussed in chapter eight. It can obviously be observed that the new criterion is very effective in the prediction of the FLCF for all materials.



## CHAPTER 7

### EXPERIMENTAL TESTS

The standard mechanical tests such as; uniaxial tension test, bulge test, torsion test etc., are the most important tools in the solid mechanics to verify and validate the theoretical and numerical methods. In metal forming processes, according to the deformation characteristics and the required parameters, various experimental tests can be utilized to obtain the necessary data.

Uniaxial tension test (UTT) is the easiest and extensively used experimental test which can give many material parameters needed to model a forming process. In sheet metal forming analyses, there are some tests which can give more accurate data about the material behavior than UTT. Nakazima test is one of those which is used widely in the sheet metal verification and validation processes. However it is one the most complicated and expensive tests in this category. Erichsen is another test which gives some information about the formability of the sheet metal. The other test is the deep drawing test which is used to investigate the possible problems that can be encountered in the complicated sheet metal forming processes. This test also gives a good idea about the drawability and formability of the sheets. There are also other tests that can be applied for special purposes but in this work stated four tests have been used to determine, verify or validate the necessary material parameters or empirical formulas.

Three materials; SS304, DKP6112 (DIN EN 10130-1999) and AA5054 aluminum alloy with sheet thicknesses of  $1\text{ mm}$ ,  $1\text{ mm}$  and  $1.45\text{ mm}$  respectively have been utilized in these tests.

#### 7.1 Uniaxial tension test of the sheet metals

The uniaxial tension tests (UTT) were performed on, Zwick/Roel Z020 (19.62 KN) tensile testing machine (Figure 7.1) was utilized. All specimens were prepared according to ASTM E008, E517 and E646 standards and were cut using laser cutting machines. To increase the reliability of the results, all tests were repeated three times.

Parameters like hardening index ( $n$ ), strength coefficient ( $K$ ), yield stress in the rolling direction ( $\sigma_0$ ), yield stress in the 45° direction ( $\sigma_{45}$ ), yield stress in the transverse direction ( $\sigma_{90}$ ), anisotropy coefficient in the rolling direction ( $r_0$ ), anisotropy coefficient in the 45° direction ( $r_{45}$ ), anisotropy coefficient in the transverse direction ( $r_{90}$ ), Poisson's ratio ( $\nu$ ) and elastic modulus ( $E$ ) have been obtained using these tests for three different materials. Also by precise measuring of the specimens before and after deformation, strain at fracture has been calculated using plasticity equations for all three material to be utilized in the ductile fracture criterion.



Figure 7.1. Uniaxial tension test equipment

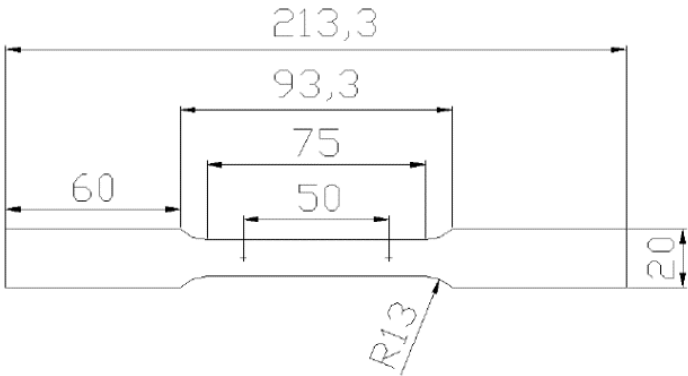


Figure 7.2. Schematic of the UTT specimen and its dimensions

In Figure 7.2, the dimensions of the UTT specimens according to the ASTM E008 are shown. All tested specimens presented in Figure 7.3 belong to DKP6112 (DIN EN 10130-1999) material and it can be clearly observed that the elongation of the specimens cut in the three directions are different from each other due to the anisotropy.



Figure 7.3. The DKP6112 specimens after UTT test

To obtain the strain at fracture ( $\bar{\epsilon}_f$ ), the width and the thickness of the specimens at the fracture area have been measured accurately. Then using the constant volume assumption, the strain at fracture can be determined accordingly.

To measure the thickness and width, in addition to the precise micrometers, the measurements were performed also by KEYENCE VHX-1000 optic microscope with high accuracy. In Figure 7.4, an example of the measured specimens for SS304 (stainless steel material) have been presented.

The material parameters obtained for three different materials using UTT tests are given in the tables 7.1, 7.2 and 7.3.

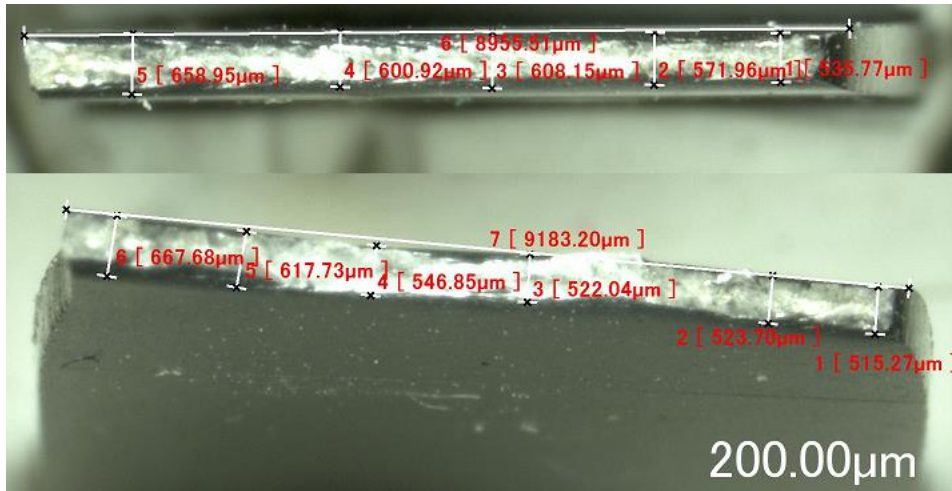


Figure 7.4. Measuring the thickness and width of the specimen (SS304) using high accuracy optical microscope

The results in the table 7.1, 7.2 and 7.3 have been extracted from the uniaxial tension tests performed using a machine equipped with displacement and force transducers.

Table 7.1 Material parameters of DKP 6112 (DIN EN 10130-1999) steel obtained by uniaxial tension tests (UTT)

UTT direction	0°	45°	90°
$E$ (GPa)	141	139.9	150.5
$\nu$	0.32	0.315	0.31
$\sigma_y$ (MPa)	250	256	242
$K$ (MPa)	643	668	632
$n$	0.247	0.252	0.241
$r$	1.34	0.99	1.67

Table 7.2 Material parameters of SS304 steel obtained by UTT

UTT direction	0°	45°	90°
$E$ (GPa)	194	192	200
$\nu$	0.269	0.27	0.277
$\sigma_y$ (MPa)	339	325	342
$K$ (MPa)	1196	1112	1210
$n$	0.32	0.31	0.32
$r$	0.81	1.19	0.86

Table 7.3 Material parameters of AA5450, aluminum alloy, obtained by UTT

UTT direction	0°	45°	90°
$E$ (GPa)	69	70	70
$\nu$	0.33	0.32	0.325
$\sigma_y$ (MPa)	155	147	151
$K$ (MPa)	249	242	255
$n$	0.1	0.096	0.103
$r$	0.705	0.97	1.115

## 7.2 Erichsen test

The Erichsen test is a ductility test, which evaluates the formability of the sheet metal under stretch forming condition. In the test a spherical ended punch is pressed against the blank with specific dimensions clamped by the blank holder and the die. The punch will deform the blank until a crack appears on the sheet surface. The punch travel is measured and reported to determine the formability of the material. This test is conducted to obtain equibiaxial yield stress ( $\sigma_b$ ) and  $r$ -value ( $r_b$ ) of the sheet materials in this work by providing good lubrication (Teflon and grease) between the punch and the blank. For this purpose, the major and minor strains on the top of the deformed blank were measured using the grid pattern analyzer (GPA-100) equipment. The tests were repeated at different punch travels to be able to find the anisotropy factor in the biaxial conditions.

$$r_b = \frac{\dot{\varepsilon}_{TD}^p}{\dot{\varepsilon}_{RD}^p} \quad (7.2)$$

where  $\dot{\varepsilon}_{TD}^p$  and  $\dot{\varepsilon}_{RD}^p$  are the plastic strain rate components in the rolling and transverse directions. Figure 7.5 shows the undeformed specimens cut and marked in patterns with laser to be used in three different test. In the Figure 7.6, one of those specimens (Figure 7.4c) was used to study the Erichsen test and the parts presented belongs to the SS304 material which have been deformed in different heights. This test has been performed using a punch with 32.5 mm in diameter and a die with 40 mm in diameter and 2 mm in shoulder radius.

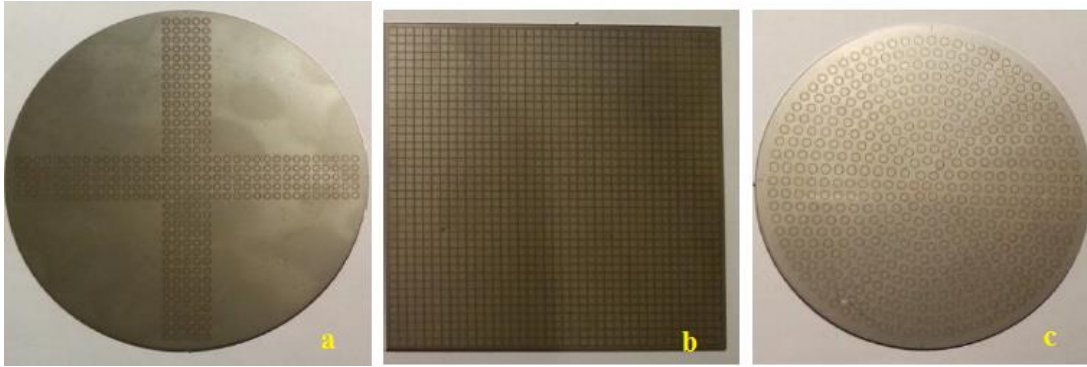


Figure 7.5. Marked specimens a) specimen for cylindrical cup drawing test b) specimen for squared-cup drawing c) specimen for Erichsen test



Figure 7.6. Various specimens with different heights deformed in the Erichsen test for SS304 material

Table 7.4 shows the equibiaxial yield stress and  $r$ -value of the stated materials obtained from this test. To obtain  $\sigma_b$ , FEM simulation of Erichsen test was used. Punch force-punch travel curve and apex point thickness distribution, were used to calibrate the numerical simulation of the process. The flow stress curve of the biaxial tension then was extracted implementing Hollomon hardening model and hill criterion constitutive equation using subroutines.

Table 7.4. The material parameters obtained Erichsen test

<b>material</b>	<b>DKP6112</b>	<b>SS304</b>	<b>AA5450</b>
$\sigma_b$ (MPa)	261	345	162
$r_b$	0.81	0.89	0.93



### 7.3 Nakazima test

Forming limit curves are usually drawn by experiments that involve nearly linear strain paths (i.e., the ratio of principal stresses to principal strains is nearly constant). However, in many real stampings, the strain path may vary non-linearly which has a very large effect on the forming limit curves. This is a challenging problem which can affect the determined FLCs. FLDs can be determined by various methods such as the uniaxial tensile test (UTT) using specimens having various dimensions with and without notches, the hydraulic bulge test (HBT) using elliptical dies and the punch stretching test (Nakazima) using specimens with different widths. Common to all these tests is that several specimens or die geometries have to be utilized to simulate different principal strain ratios corresponding to various points on the FLCs.

Nakazima test is believed to be one of the most accurate experimental methods to draw a forming limit curve of the sheet metals. Although it has some limitations and complex measuring procedure, its results are widely used in the studies related to the sheet metal. The several specimens are utilized to determine the forming limit curves at necking (FLCN) and fracture (FLCF) for all three materials. The specimens presented in Figure 7.7 belong to the DKP6112 steel material. Hereby, the specimens were marked in circles first. Then, the grid obtained after the forming processes were measured carefully with the *Grid Pattern Analyzer* (GPA) and the major and the minor strains were determined by special software. Finally, forming limit curve at necking (FLCN) and forming limit curve at fracture (FLCF) were obtained.

The tooling (Figure 7.8) contains a spherical punch, a die with the draw bead and a blank holder. The draw bead has been designed in a way to be useful for the blanks with thickness range of 1 mm – 2 mm.

The obtained forming limit curves at necking (FLCN) and at fracture (FLCF) have been shown in Figure 7.9. As it is clear, all materials undergo the necking phenomenon before the fracture takes place especially when the minor strain is negative ( $\varepsilon_2 < 0$ ). For the right hand side of the curves ( $\varepsilon_2 > 0$ ), SS304 and DKP6112 show almost no necking in the biaxial stretching test where AA5450 has little bit localized necking.

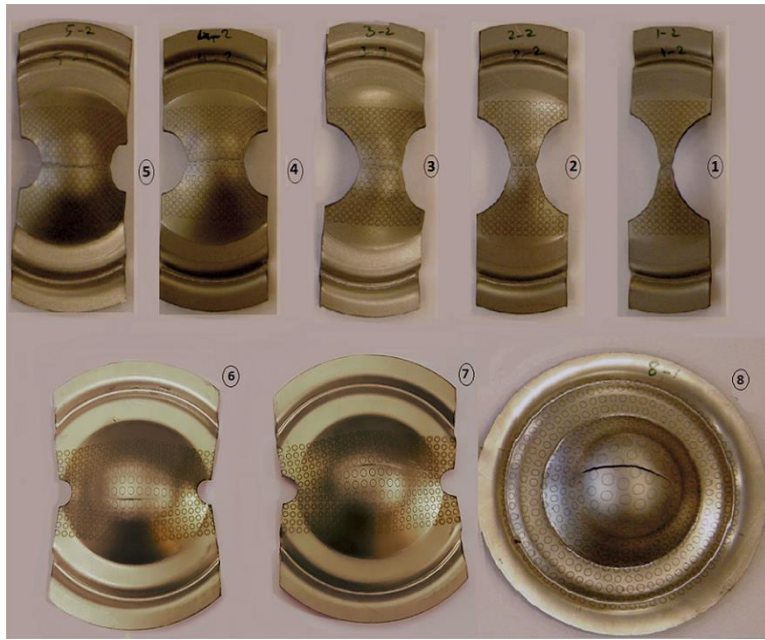


Figure 7.7. Deformed specimens by the Nakazima test for DKP 6112 steel

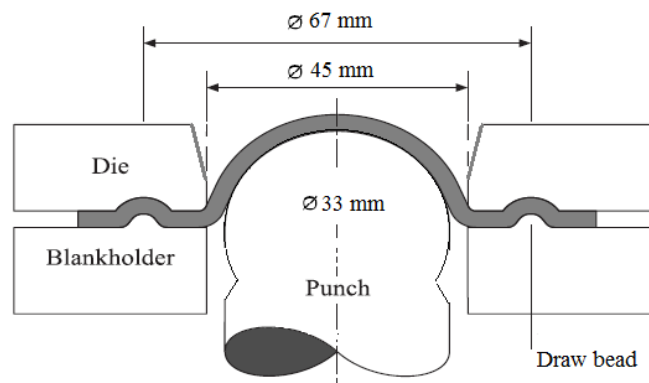


Figure 7.8. The schematic of the Nakazima test tooling

#### 7.4 Deep drawing test

Deep drawing tests were accomplished by Tinius-Olsen testing machine (Figure 7.10) which is able to show the blank holding force, the punch force and the cup height during the test. Cylindrical cup and squared cup drawing processes were conducted as a case studies to investigate the effect of various hardening rules and yield criteria on the reliability of mentioned DFCs. Grease together with Teflon were employed on the blank-die and blank-blankholder interfaces and also the blank-punch interface was kept dry intentionally to improve the drawability of the sheets. The Teflon on the other hand was observed to be very helpful in protecting the marked circles from getting erased by the frictional forces in the interfaces.

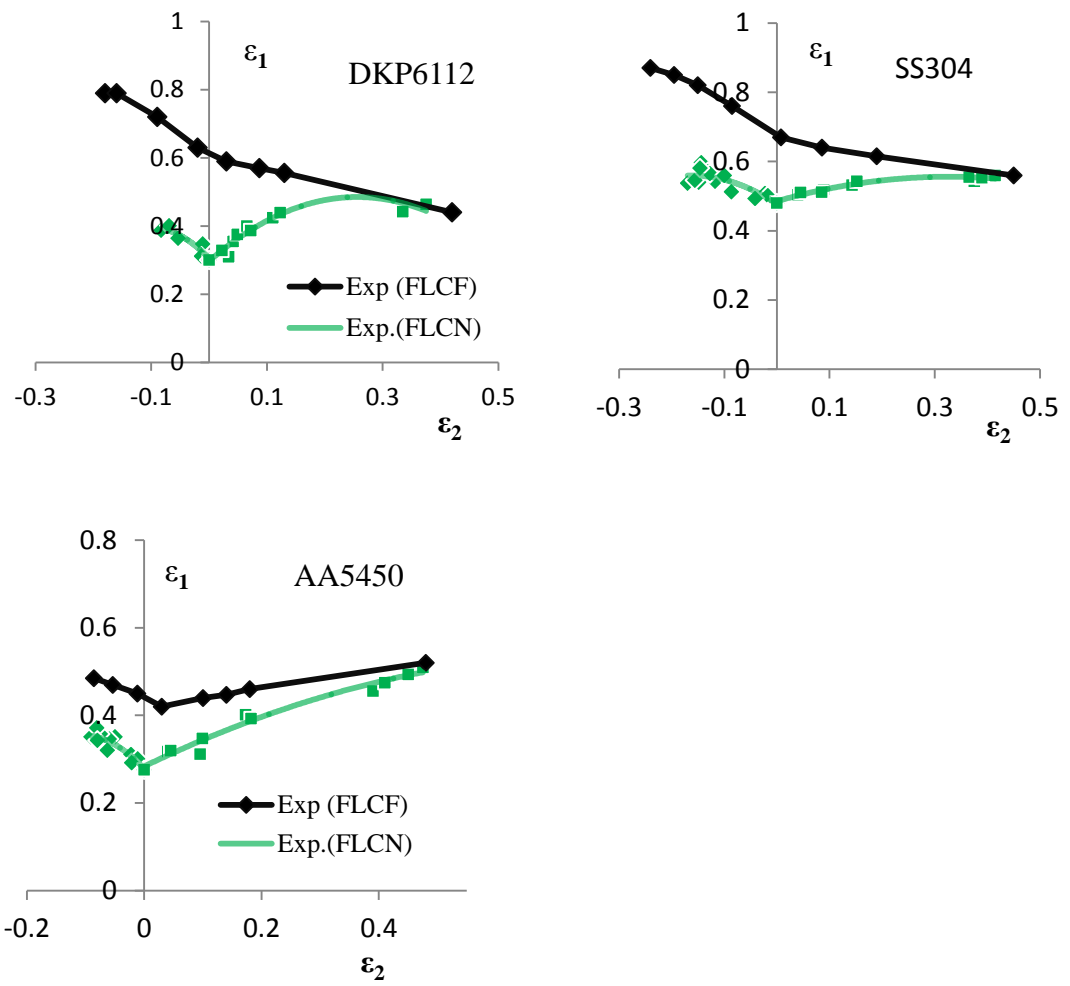


Figure 7.9. Experimentally obtained FLCN and FLCF curves for three materials



Figure 7.10. The deep drawing machine

In the cylindrical cup drawing the previously marked specimens were formed using the tools which dimensions have been given in Table 7.5. The blank were cut and marked with circles precisely. The cutting process were done using laser cut machine and the circle marking process were accomplished using low frequency laser marking device.

Table 7.5 Tooling dimensions in the cylindrical cup drawing

Tool specification	Dimension (mm)
Punch diameter	50
Punch shoulder radius	5
Die opening	53
Die shoulder radius	13.5

The deformed specimens in the different heights (15, 25, 35, 45 mm) for DKP6112 were shown in Figure 7.11 where the behavior of the material in the 0° and 90° from the rolling direction can be studied by measuring the strains on the formed ellipses. The obtained data are used to validate the anisotropic constitutive models and also the friction coefficient parameter of the penalty contact in the finite element model.

Some specimens were forced to get fractured in the various heights of the forming process by increasing the blank holding force and the ability of the DFCs in the predicting of the fracture place and time were studied. In Figure 7.12, the fractured specimens have been shown. It was observed that for the DKP6112 material, the fracture starts in the punch nose radius region in the 0° from the rolling direction where for SS304 it starts in the 45° direction.

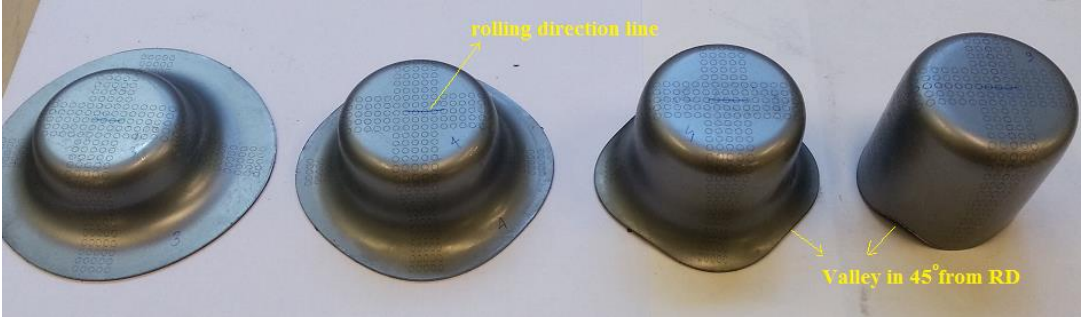


Figure 7.11. Cylindrical cup drawing of DKP6112



Figure 7.12. The fractured specimens in the 18 and 12 mm punch travels for DKP6112 material

In Figure 7.13 the fractured specimen of AA5450 in 14.5 mm of punch travel is shown. The fracture begins from the punch profile region in the 0° from the rolling direction similar to DKP6112 material.



Figure 7.13. The fractured cup in 14.5 mm of punch travel for AA5450 material

In the square cup drawing, the  $1\text{mm} \times 1\text{mm}$  squares were marked using laser marking device on the  $80\text{mm} \times 80\text{mm}$  blanks before deformation. The dimension of the tooling have been presented in Figure 7.14. The specimens which have been deformed to the specific heights (10, 15, 20, 25, 30 mm) have been shown in Figure 7.15. Also by increasing the blank holding force, some specimens were forced to fracture and the same process were modeled with the FEM to investigate the reliability of the ductile fracture criteria in the predicting of the fracture initiation time and place.

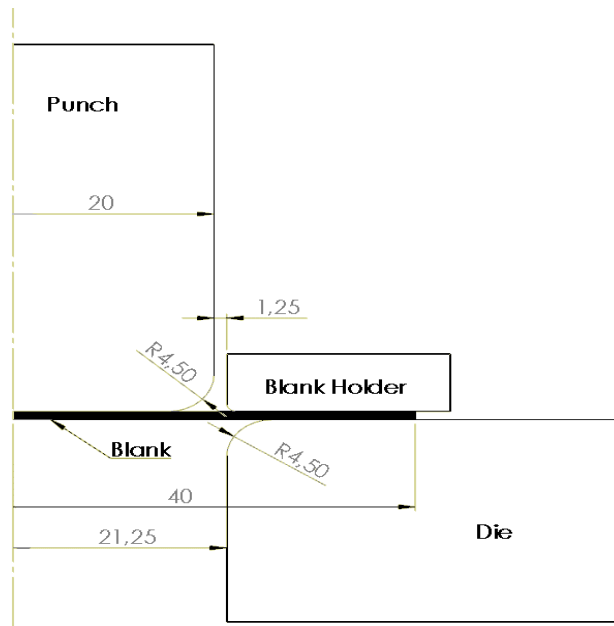


Figure 7.14. Squared cup drawing, tools dimensions

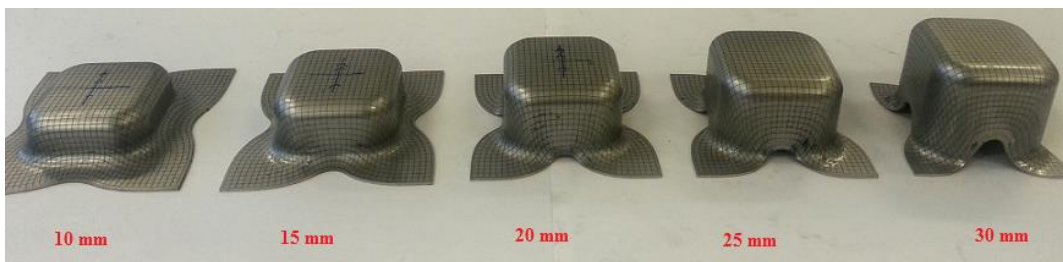


Figure 7.15. Squared cup drawing of SS304 steel

Figure 7.16 shows the deformed square specimen which was fractured in the 24.6 mm of the punch travel. The fracture starts from the punch corner region which lies in the  $45^\circ$  from the rolling direction.



Figure 7.16. The fractured part in the square cup drawing of DKP6112 material

## CHAPTER 8

### VERIFICATION, RESULTS AND DISCUSSION

#### 8.1 Verification of the numerical approach

Each experimental test in this work has been simulated using commercial finite element software ABAQUS. To verify the simulation results, the FEM settings and boundary conditions were adopted in a way that they reflect the experimental test conditions. Subsequently, some of the data were utilized to check the reliability of the simulations such as thickness distributions and dissipated energies, and some of them like punch force-punch travel diagrams were used to adjust the model parameters.

As discussed in Chapter 4, one of the important issues about the explicit solvers and their stability conditions, is the internal energy (IE) to kinetic energy (KE) ratio. To be able to assume a dynamic explicit simulation as a quasi-static solution, Kutt et al. [79] proved that the value of IE to KE ratio must be more than 5 where Hibbitt and Karlsson [78] have proposed a circumspectly value over 10 to have undeniably a quasi-static solution. Figure 8.1 shows the internal and kinetic energies of the DKP6112 material plotted for the deep drawing simulation. In the early steps of the simulation, due to the contact conditions, the kinetic energy has higher values but the solution gets stable gradually and it can be taken as quasi-static for most of the time steps of the solution.

Punch force- punch travel diagram is another parameter which is used to determine the friction coefficient in the simulations. The dry and not polished surfaces friction coefficient according to the Coulomb's law is taken in the range of 0.13 - 0.16 in most of the researches, but for the lubricated surfaces the punch force-punch travel diagrams were used. In Figure 8.2, the experimental and numerical results of the punch force-punch travel diagram for deep drawing process of DKP6112 material has been shown for experimental and numerical results. As it can be seen, for the friction coefficient of 0.05, the experimental and numerical results are very close to each other where the mixture of grease and industrial oil lubricant is used.

However in the Nakazima and Erichsen tests where the better lubrication was provided using Teflon and grease combination, the friction coefficient is determined as 0.02.

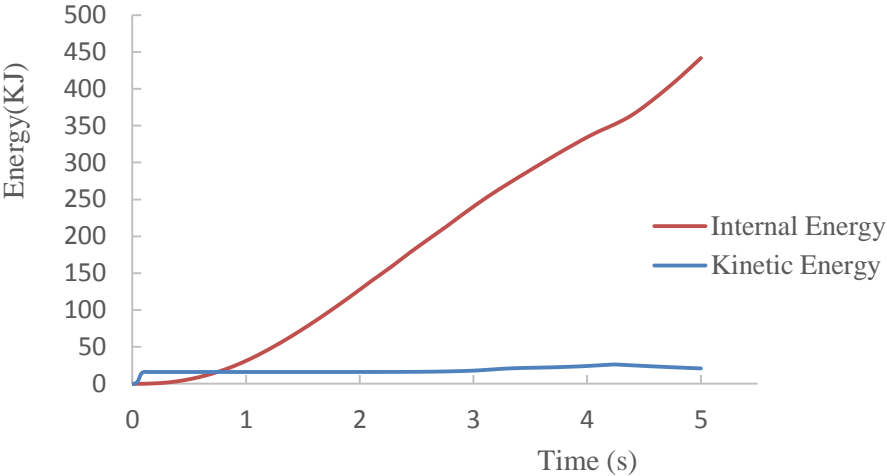


Figure 8.1. Internal and kinetic energy diagrams in the deep drawing process of the DKP6112 material

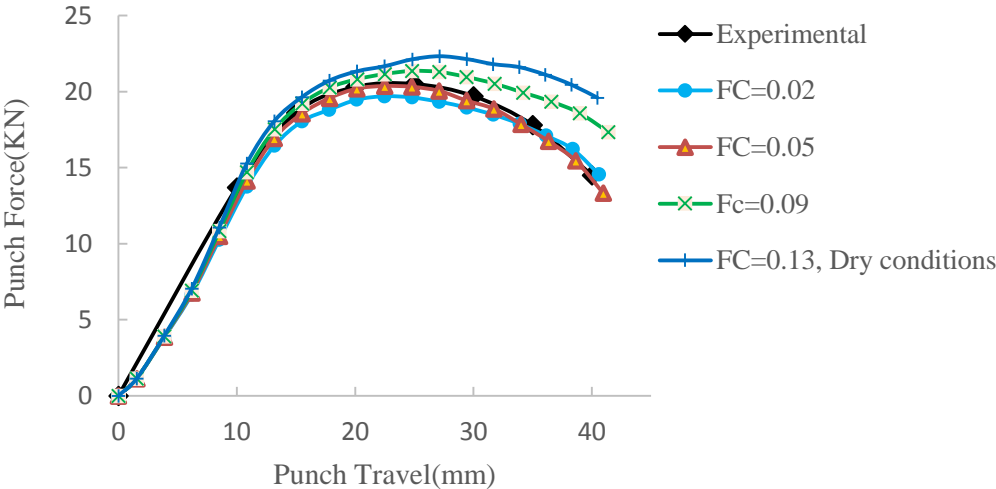


Figure 8.2. Punch force-punch displacement diagram of DKP6112 material in the cylindrical cup drawing process

Thickness distribution of the deformed parts in 0° and 90° directions are the other data which were utilized to verify the reliability of the numerical simulations using the anisotropic constitutive equations. The specimens which were marked in circles and squares when formed and the thickness strain and thickness variation was easily calculated using incompressibility conditions. Based on the distance of the each circle from the center of the specimen in the undeformed part, the thickness distribution-distance diagrams were extracted. These diagrams help to verify the anisotropic



behavior of the material that has been implemented to the FEM model. Also the material behavior through the forming process can be studied in the various directions using these type of curves because they indicate the thinning capability of the material in each direction.

In Figures 8.3-8.6, the thickness distribution diagrams using Von-Mises yield criterion and isotropic hardening model have been presented for punch travels of 15, 25, 35 and 45 mm respectively. As it can be seen the results are not accurate enough in the predicting of the thickness distributions of the DKP6112 material. Since it is an isotropic criterion, the numerical results for both rolling direction (RD) and transverse direction (TD) are the same.

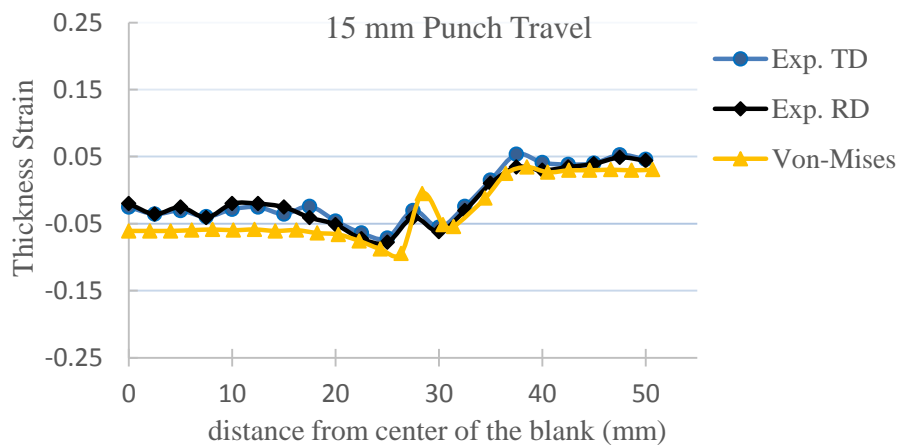


Figure 8.3. Thickness distribution-distance diagram of DKP6112 in the cylindrical cup drawing at 15 mm punch travel implementing Von-Mises yield criterion

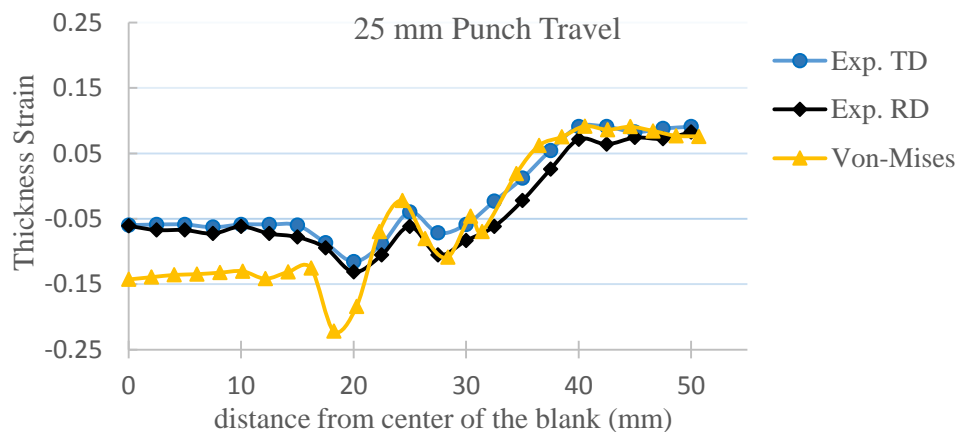


Figure 8.4. Thickness distribution-distance diagram of DKP6112 in the cylindrical cup drawing at 25 mm punch travel implementing Von-Mises yield criterion

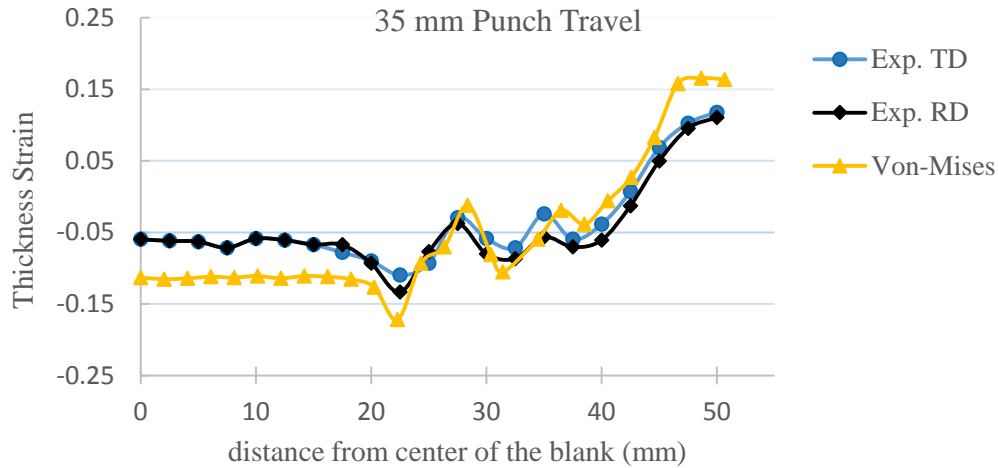


Figure 8.5. Thickness distribution-distance diagram of DKP6112 in the cylindrical cup drawing at 35 mm punch travel implementing Von-Mises yield criterion

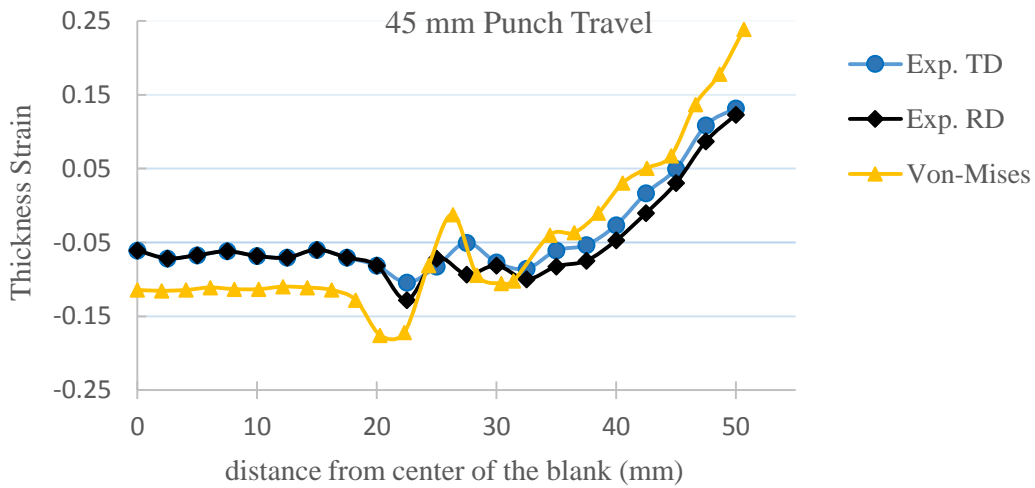


Figure 8.6. Thickness distribution-distance diagram of DKP6112 in the cylindrical cup drawing at 45 mm punch travel implementing Von-Mises yield criterion

Hill48 Yield criterion is one of the anisotropic criteria which implemented in this work, has been extensively used to model the anisotropic behavior of the sheets. In Figures 8.7-8.10, the thickness distribution diagrams of this constitutive model have been presented for 15, 25, 35 and 45 mm of punch travels. The results of anisotropic constitutive equation is far better than the isotropic Von-Mises model. In these figures the distribution in both rolling and transverse directions can be observed. In the last steps of the forming where the flange is drawn to the die, the results obtained for Hill48 criterion deviates from the experimental data especially in the rolling direction. The specimens for these tests have been shown in the figure 7.11 beforehand.

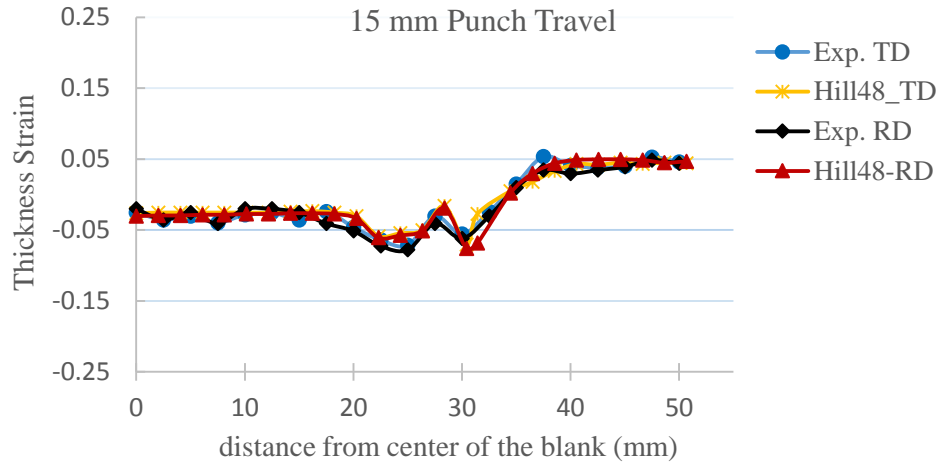


Figure 8.7. Thickness distribution-distance diagram of DKP612 in the cylindrical cup drawing at 15 mm punch travel implementing Hill48 yield criterion

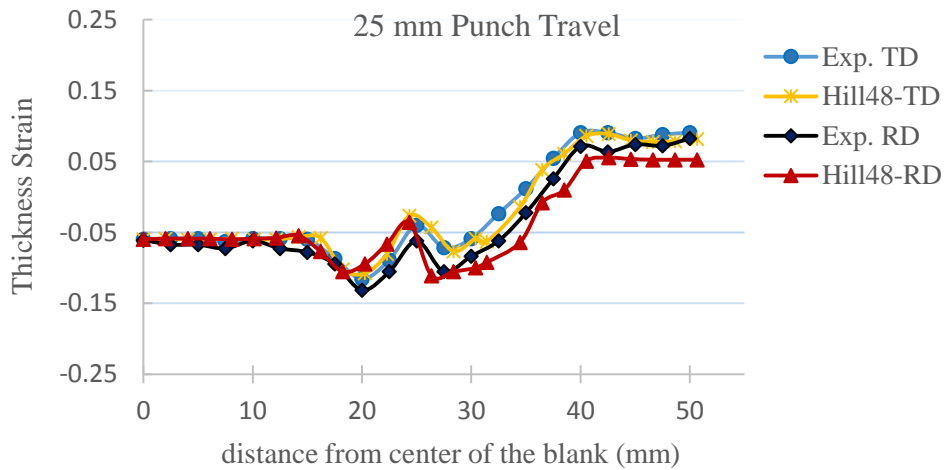


Figure 8.8. Thickness distribution-distance diagram of DKP612 in the cylindrical cup drawing at 25 mm punch travel implementing Hill48 yield criterion

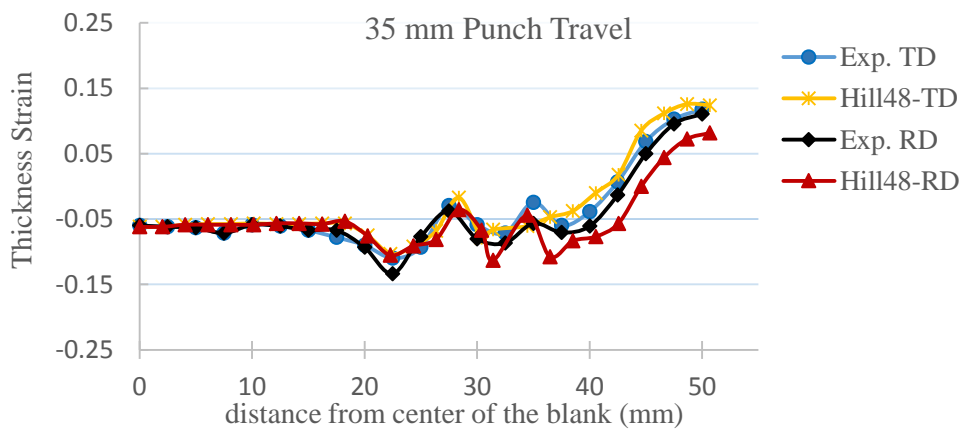


Figure 8.9. Thickness distribution-distance diagram of DKP612 in the cylindrical cup drawing at 35 mm punch travel implementing Hill48 yield criterion

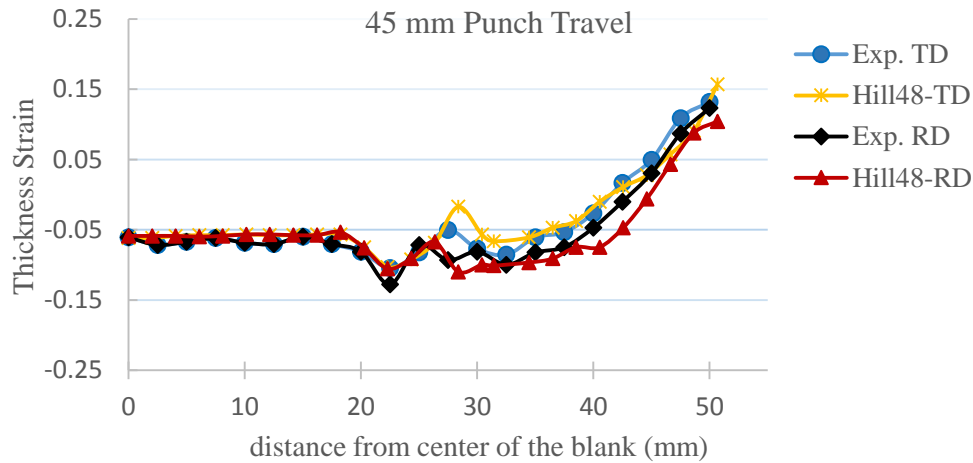


Figure 8.10. Thickness distribution-distance diagram of DKP6112 in the cylindrical cup drawing at 45 mm punch travel implementing Hill48 yield criterion

YLD2003 yield criterion is the other anisotropic criterion which was used in this study to simulate the anisotropic behavior of the sheet material. In Figures 8.11-8.14, the comparisons for thickness distributions have been shown for 15, 25, 35 and 45 mm of punch travels. The material behavior in all steps is better predicted comparing to the Von-Mises and Hill criteria. Although YLD2003 constitutive model constants are hard to be determined and the model itself is difficult to be implemented to the numerical simulations, it gives better estimations in the forming processes. Therefore, in the processes where very accurate results are needed, the YLD2003 model can be one of the choices compared to the other anisotropic yield criteria; however, the Hill48 model can effectively reflect the anisotropic behavior of the materials and besides it is very simple to be implemented to the numerical simulations.

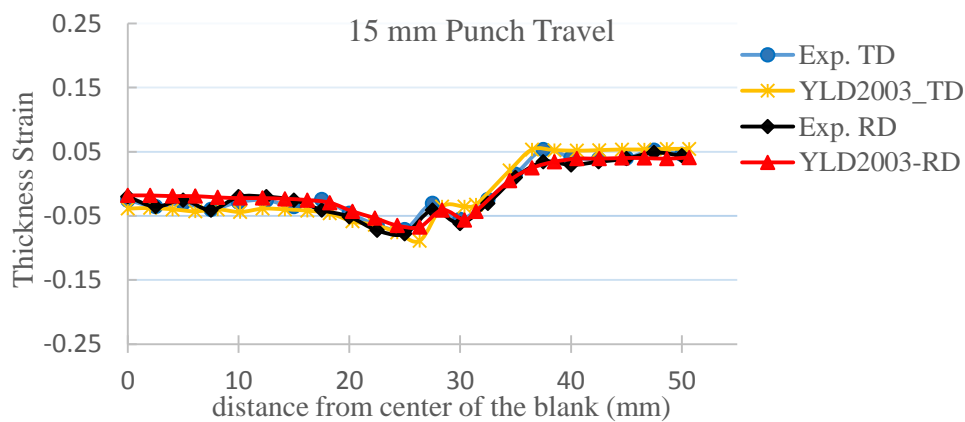


Figure 8.11. Thickness distribution-distance diagram of DKP6112 in the cylindrical cup drawing at 15 mm punch travel implementing YLD2003 yield criterion

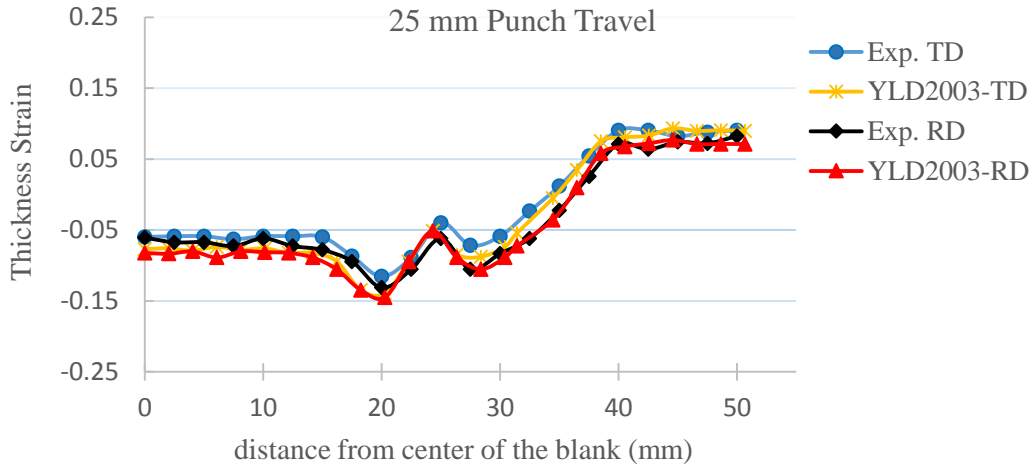


Figure 8.12. Thickness distribution-distance diagram of DKP6112 in the cylindrical cup drawing at 25 mm punch travel implementing YLD2003 yield criterion

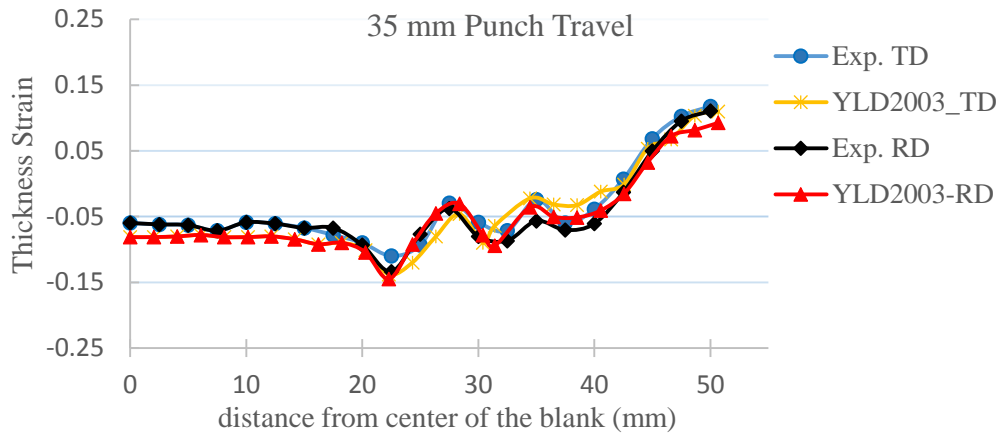


Figure 8.13. Thickness distribution-distance diagram of DKP6112 in the cylindrical cup drawing at 35 mm punch travel implementing YLD2003 yield criterion

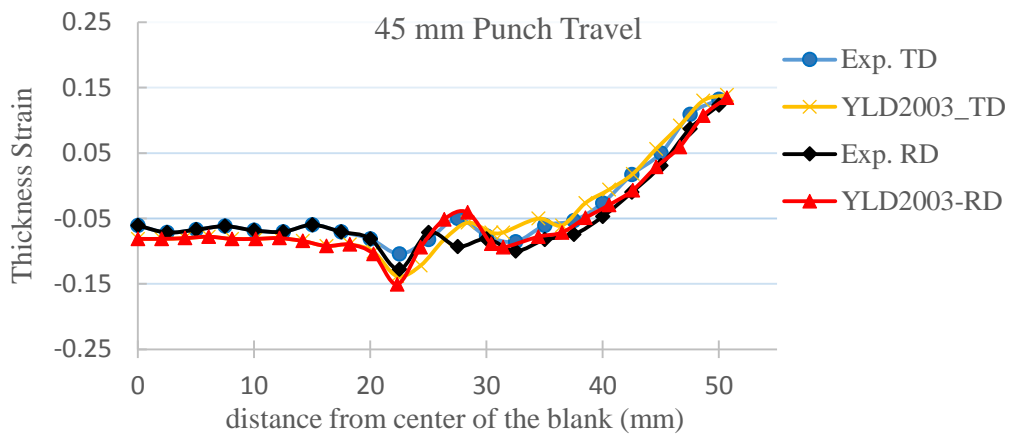


Figure 8.14. Thickness distribution-distance diagram of DKP6112 in the cylindrical cup drawing at 45 mm punch travel implementing YLD2003 yield criterion

BBC2008 constitutive model is similar to the YLD2003 model in principle however in the stress and strain calculations and the constant determination processes is different. As it can be observed in Figures 8.15-8.18 for 15, 25, 35 and 45 mm of punch travels, the thickness distribution predictions for this model is as accurate as YLD2003 model and in some cases it gives the better results.

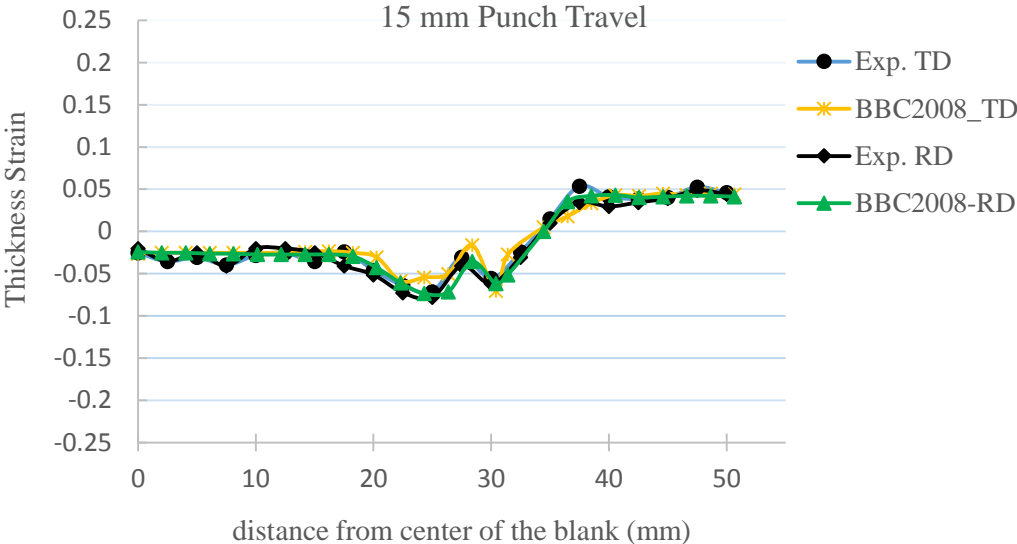


Figure 8.15. Thickness distribution-distance diagram of DKP6112 in the cylindrical cup drawing at 15 mm punch travel implementing BBC2008 yield criterion

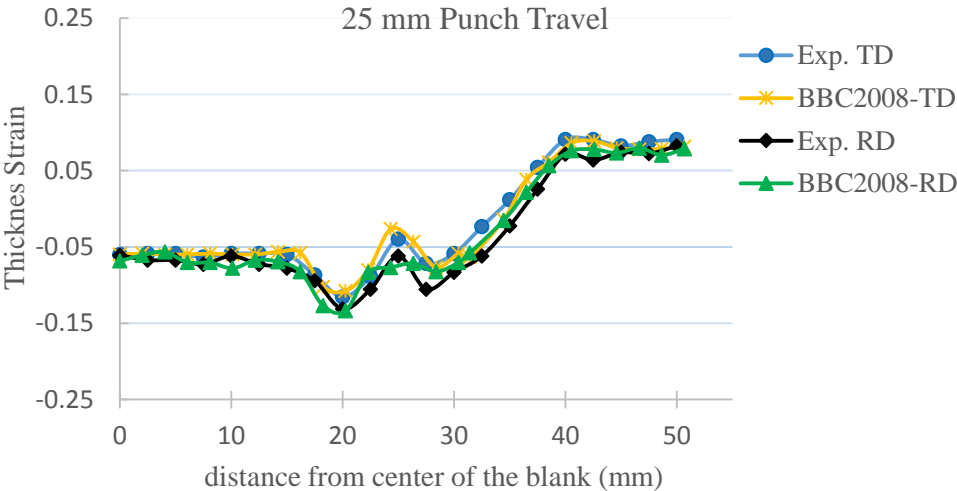


Figure 8.16. Thickness distribution-distance diagram of DKP6112 in the cylindrical cup drawing at 25 mm punch travel implementing BBC2008 yield criterion

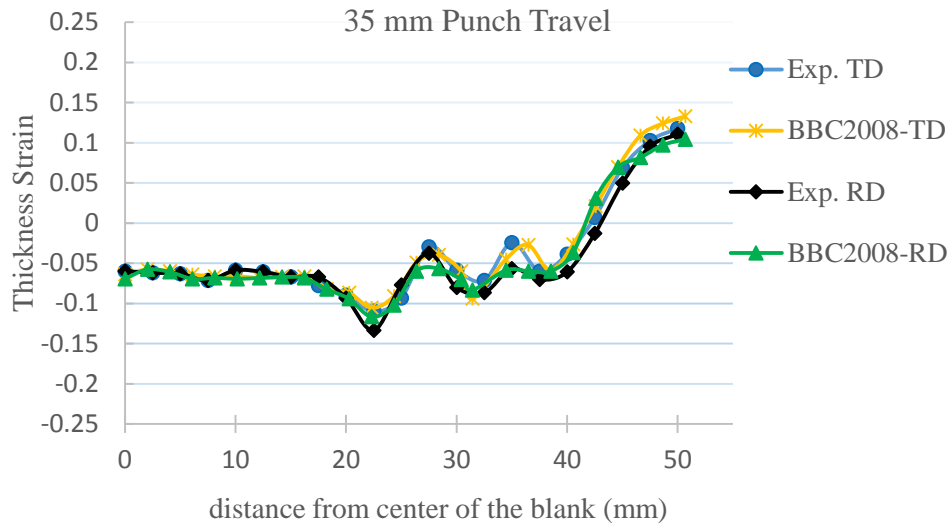


Figure 8.17. Thickness distribution-distance diagram of DKP6112 in the cylindrical cup drawing at 35 mm punch travel implementing BBC2008 yield criterion

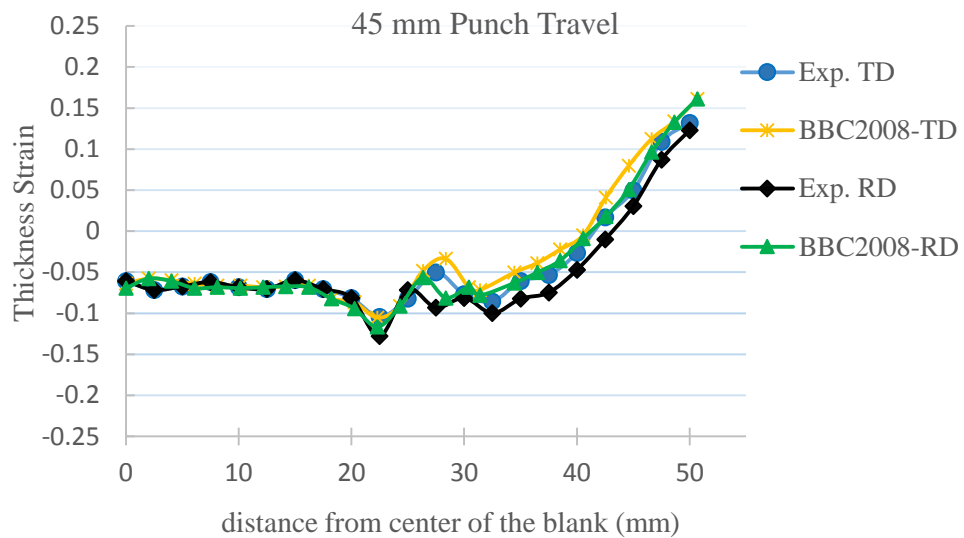


Figure 8.18. Thickness distribution-distance diagram of DKP6112 in the cylindrical cup drawing at 45 mm punch travel implementing BBC2008 yield criterion

In Figure 8.19, the deformed cup shapes are shown at 15, 25, 35 and 45 mm punch heights that have been obtained by finite element simulations based on Hill48 yield criterion. The earing phenomenon has been successfully determined by the anisotropic constitutive model and the valleys are on the 45° from the rolling direction for DKP6112 material.

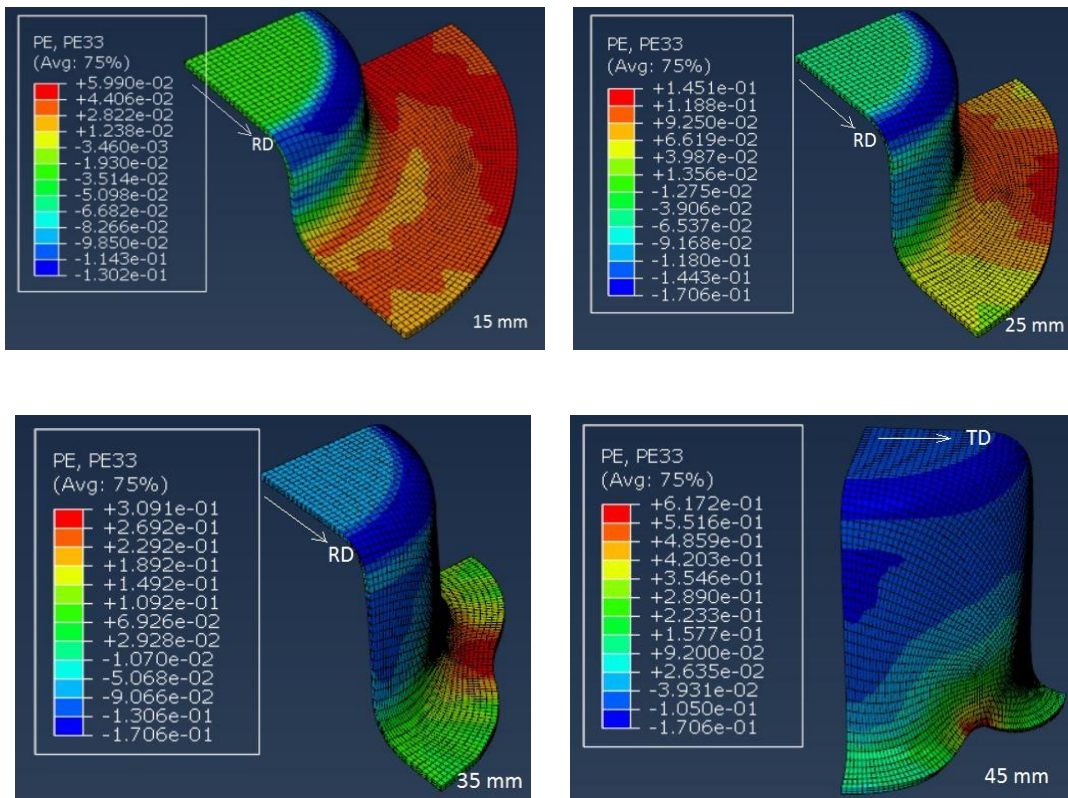


Figure 8.19. Thickness strain variations of DKP6112 in the different punch heights (15, 25, 35, 45 mm) implementing Hill48 yield criterion

On the other hand in Figure 8.20 the valleys are estimated along the  $0^\circ$  and  $90^\circ$  directions for SS304 materials.

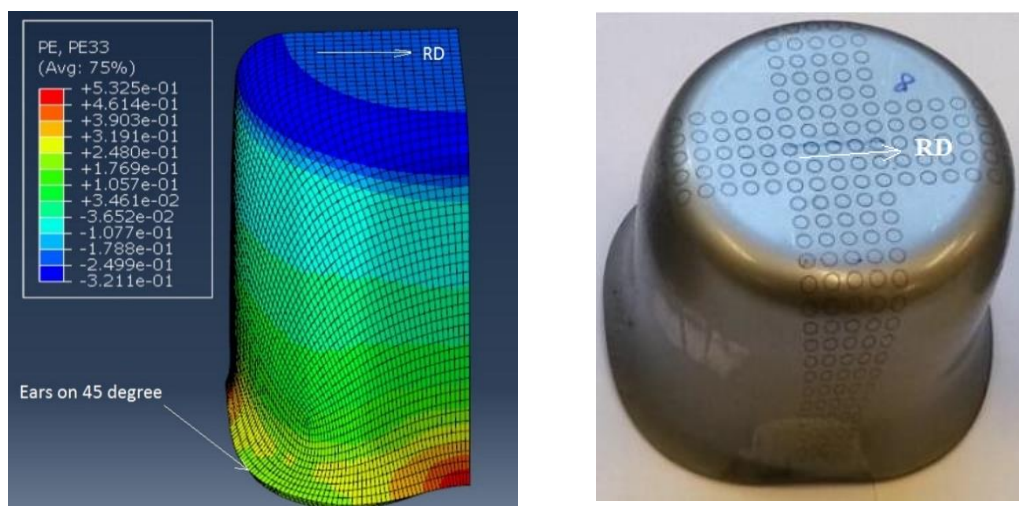


Figure 8.20. Successfully predicted ears in the drawn cup for SS304 material at 49 mm punch travel implementing Hill48 yield criterion



The thickness distribution diagram for SS304 has been shown in Figure 8.21 at the 49 mm punch travel for different constitutive models and the experimental data is given too. The predicted thickness for SS304 are accurate enough for almost all of the criteria but anisotropic criteria seem better than Von-Mises estimations.

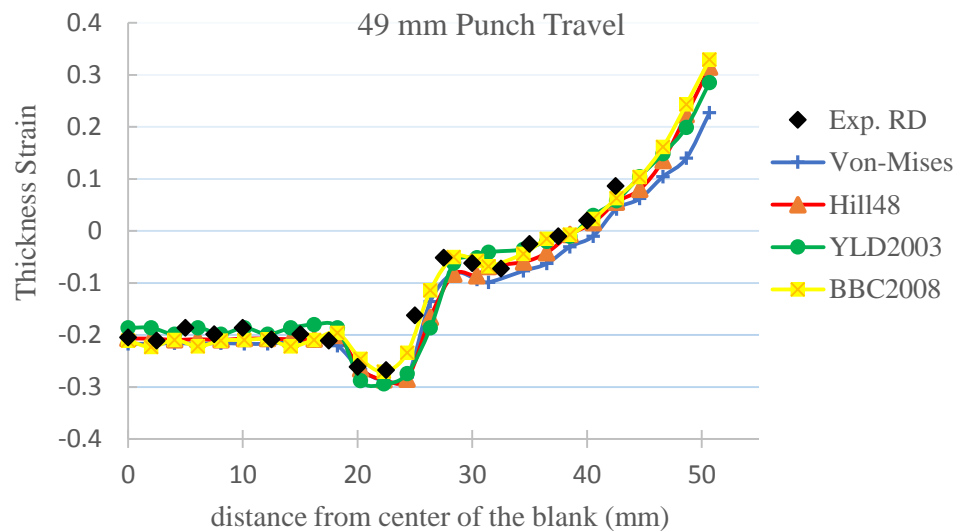


Figure 8.21. Thickness distribution of SS304 at the 49 mm punch travel in the rolling direction implementing various yield criteria

The ears direction and magnitude are related to the  $\Delta r$  value and since its magnitude is very small for AA5450, the ears are not distinctive as DKP6112 and SS304 materials. The drawn cup and its model for AA5450 are shown in Figure 8.22 where the four ears are hardly recognized. To better explore the thickness changes and anisotropic effects in the simulations, three dimensional solid element were used. Then the thickness variations and shear stress effects can easily be handled which are the main problems when the conventional shell elements are used. The thickness and shear stiffness values of the shell elements should be calculated and input manually to the numerical models before any simulation.

In Figure 8.23 the thickness distribution diagram for AA5450 at 29 mm of the punch travel in the rolling direction for different constitutive models is shown. The diagram indicates that the BBC2008 Yield criterion gives the better prediction between all constitutive equations and Von-Mises equation is the least accurate model.

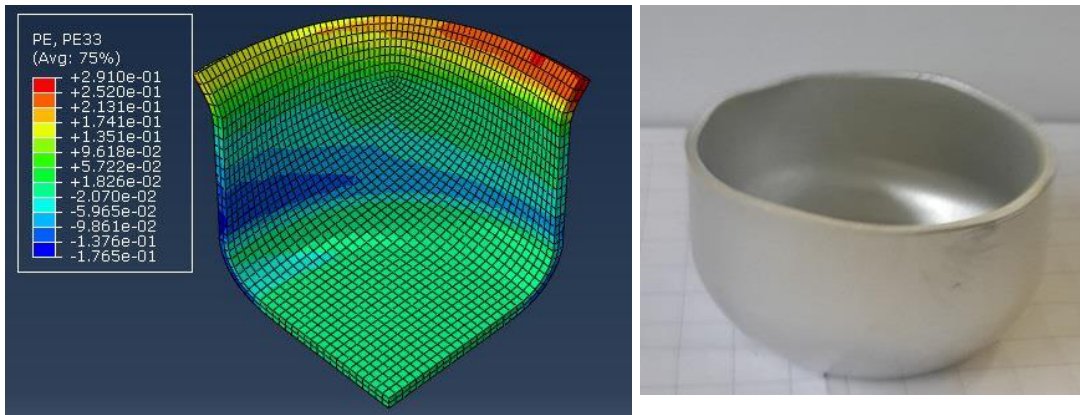


Figure 8.22. Successfully drawn cup for AA5450 material at 29 mm punch travel implementing Hill48 yield criterion

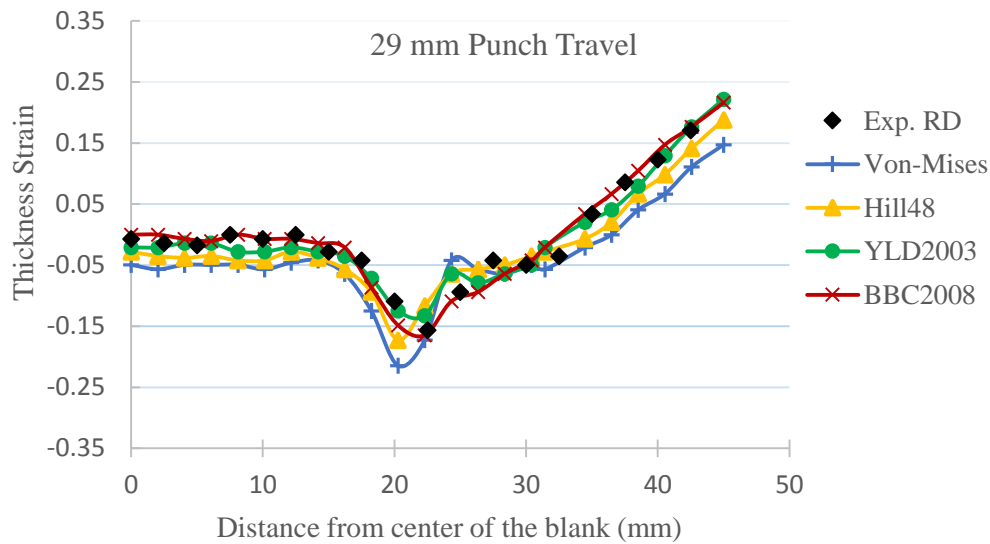


Figure 8.23. Thickness distribution of AA5450 at the 29 mm punch travel in the rolling direction implementing various yield criteria

## 8.2 Verification and validation of the new criterion

To determine the empirical formulas given in Chapter 6, four different materials were chosen and after many tryouts, the numerical FLCFs obtained using the new criterion successfully fit into the experimental data in whole range of the FLCFs. For this purpose, the empirical formulas were modified several times to achieve the better fit for all materials simultaneously. The final results have been presented in Figure 8.24 where they show that the new criterion is capable of predicting the fracture initiation for any material in any forming process.

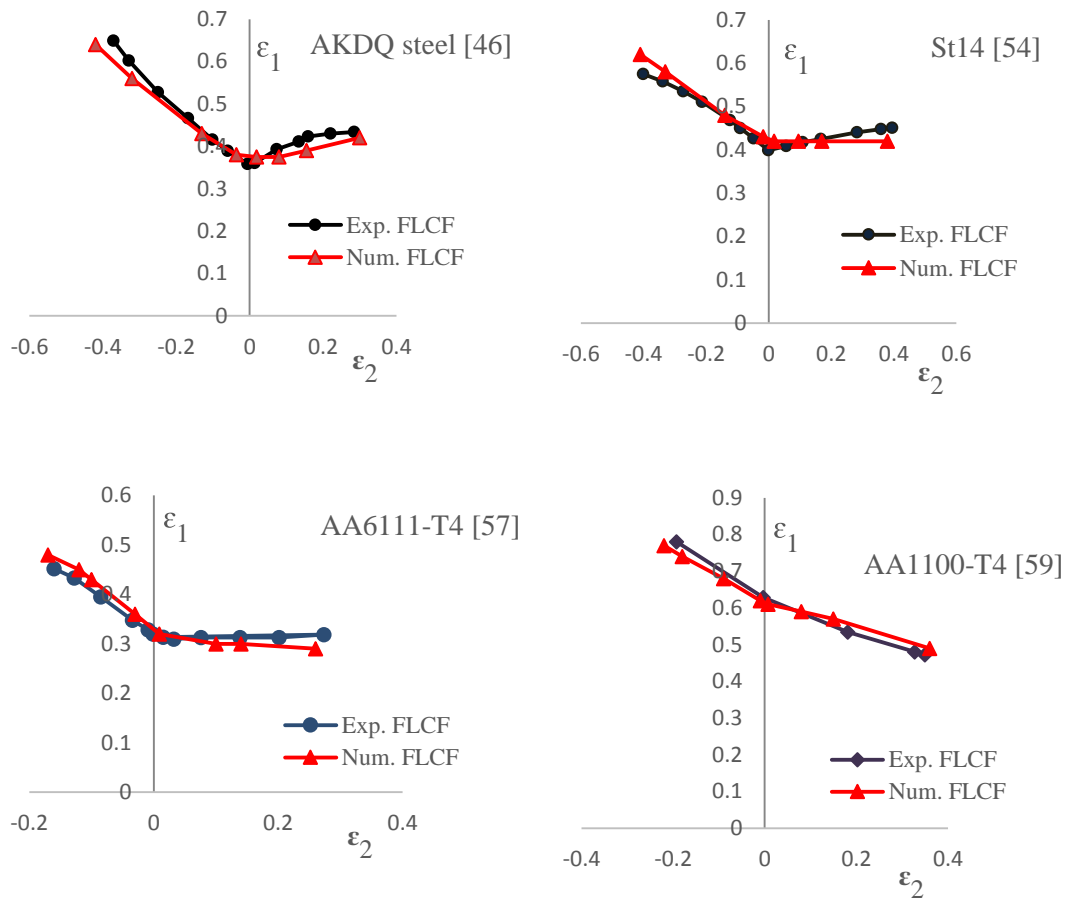


Figure 8.24. Comparison of the numerical and experimental FLCFs for four cases after fitting process

To demonstrate the ability of the new criterion in prediction of the fracture initiation, three other materials whose properties were reported extensively in the Chapter 7, are used. The numerical FLCFs of these materials were obtained using the implementation of the new criterion and empirical formulas to the numerical codes for the Nakazima test simulation. As it can be seen in Figure 8.25, the criterion is very robust tool in the estimation of the forming limit curves at fracture for all three materials; therefore, it can be expressed that the new criterion undoubtedly is able to predict fracture initiation in any forming process.

### 8.3 Predictions with new DFC

To better investigate the new DFC applicability and capability in the estimation of the fracture initiation, its functionality were confirmed implementing different hardening models (isotropic, kinematic, and combined) and isotropic (Von-Mises) and

anisotropic (Hill48, YLD2003 and BBC2008) constitutive models. Also the obtained results in any condition were compared to some widely used uncoupled DFCs (Freudenthal, Cockroft and Latham, Ayada et al., Brozzo et al. and Oh et al.) as well. Furthermore, to test the criterion in the complicated processes, deep drawing of cylindrical and square cups were accomplished as case studies.

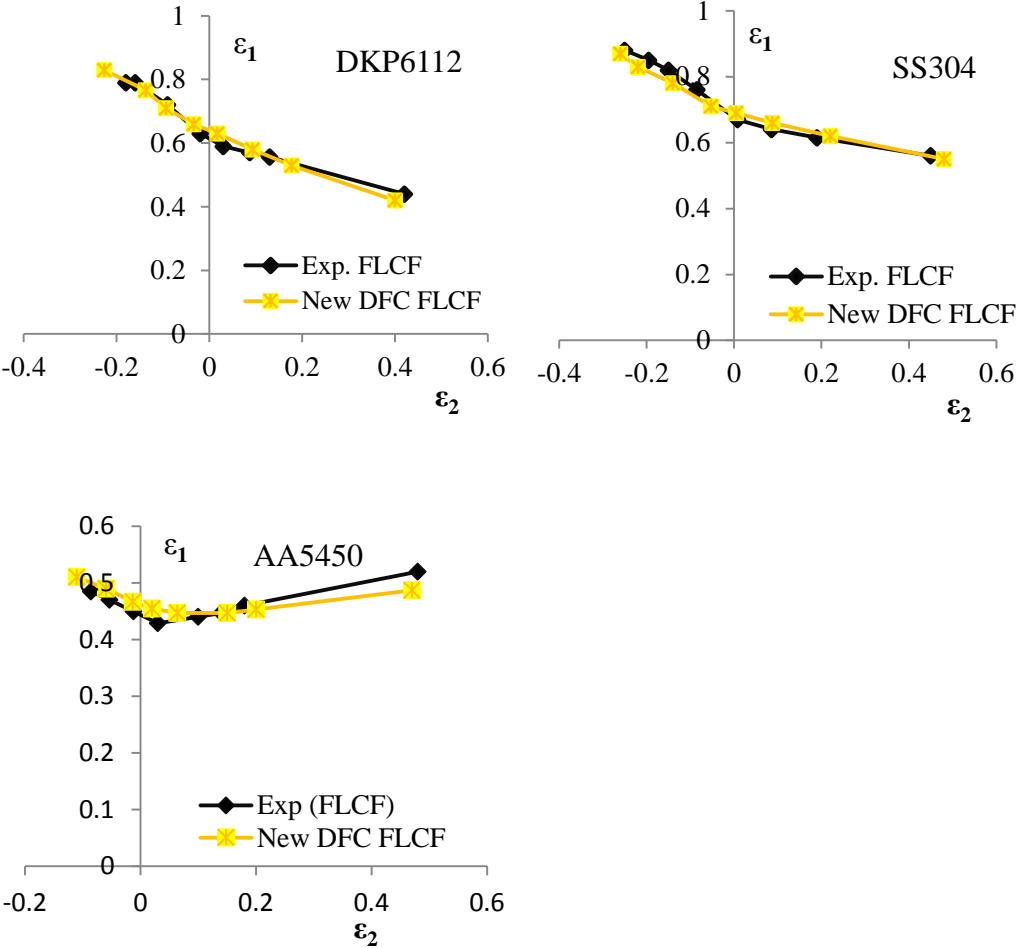


Figure 8.25. Comparison of the new DFC and experimental FLCFs for three different materials

**8.3.1 Effect of yielding functions on the DFCs**

To study the effect of various constitutive models, the Von-Mises isotropic yielding equation, and three anisotropic yielding equations, Hill48, YLD2003 and BBC2008, with piecewise isotropic hardening rule were chosen and implemented. Since the specified formulations are obtained for the plane stress conditions, shell elements were chosen for the simulations in this section. To compare the accuracy of the each

constitutive equation, the Nakazima test specimens were modeled numerically for each of them and the results were compared to the experimentally extracted FLCFs.

In Figures 8.26-8.29, the FLCFs of the various DFCs for DKP6112 material which have been obtained implementing various yield criteria are shown. Among all the DFCs studied, the new DFC estimated better with all of the constitutive equations compare to all other constitutive models. This is attributed to the consideration of shear stress, material parameters and strain path effects simultaneously. Other DFCs are accurate enough in the prediction of the fracture initiation for all specimens of the Nakazima tests.

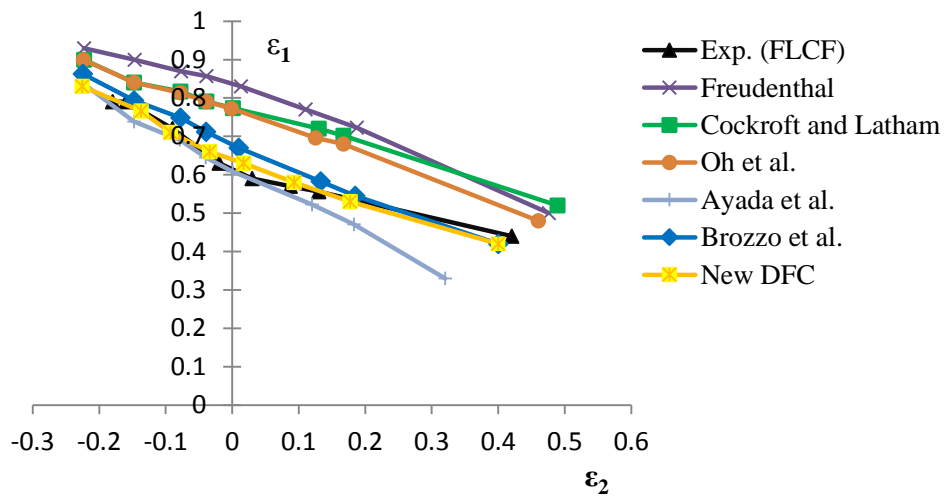


Figure. 8.26 FLCFs of various DFCs implementing Von-Mises constitutive equation for DKP6112 material

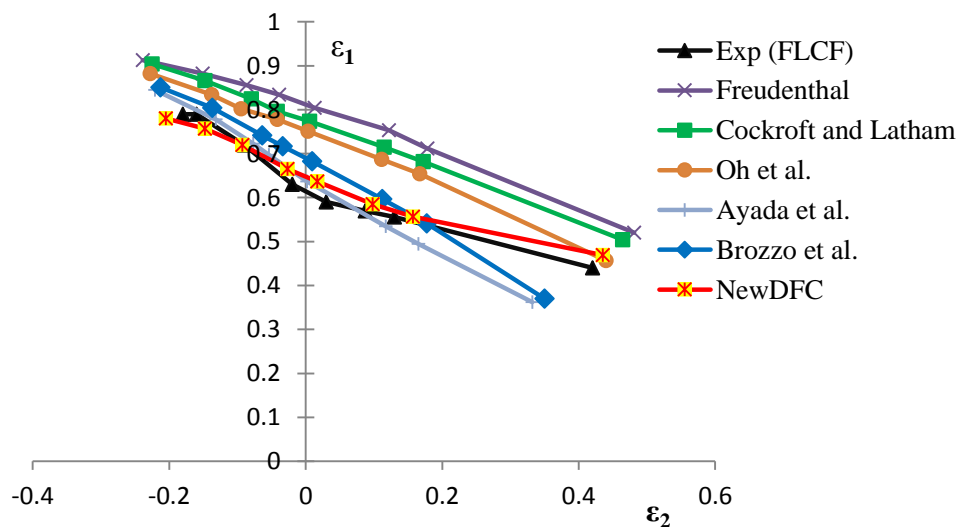


Figure. 8.27 FLCFs of various DFCs implementing Hill48 constitutive equation for DKP6112 material

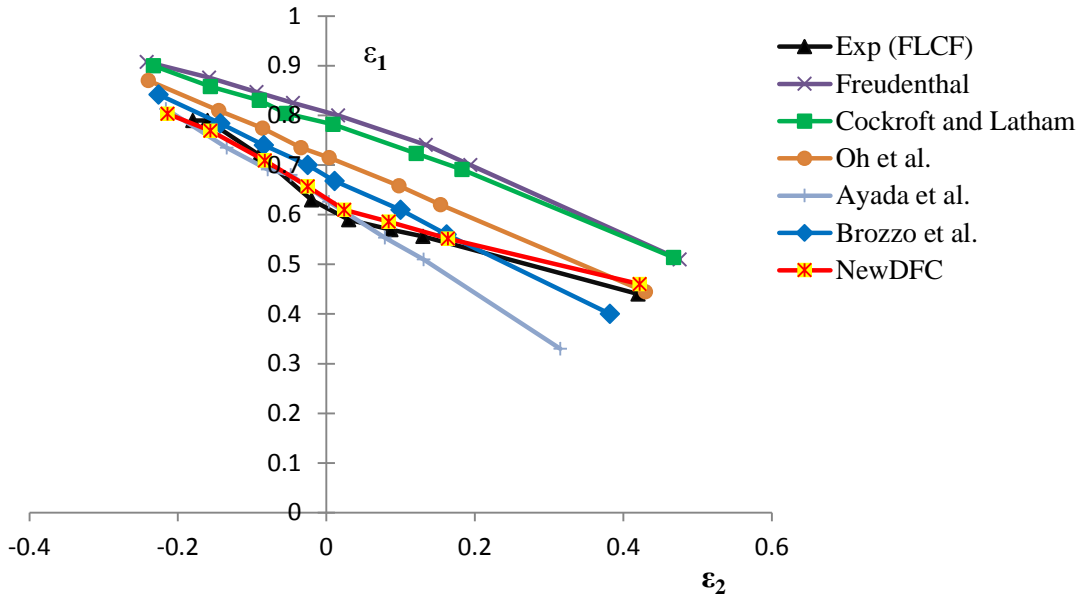


Figure 8.28. FLCFs of various DFCs implementing BBC2008 constitutive equation for DKP6112 material

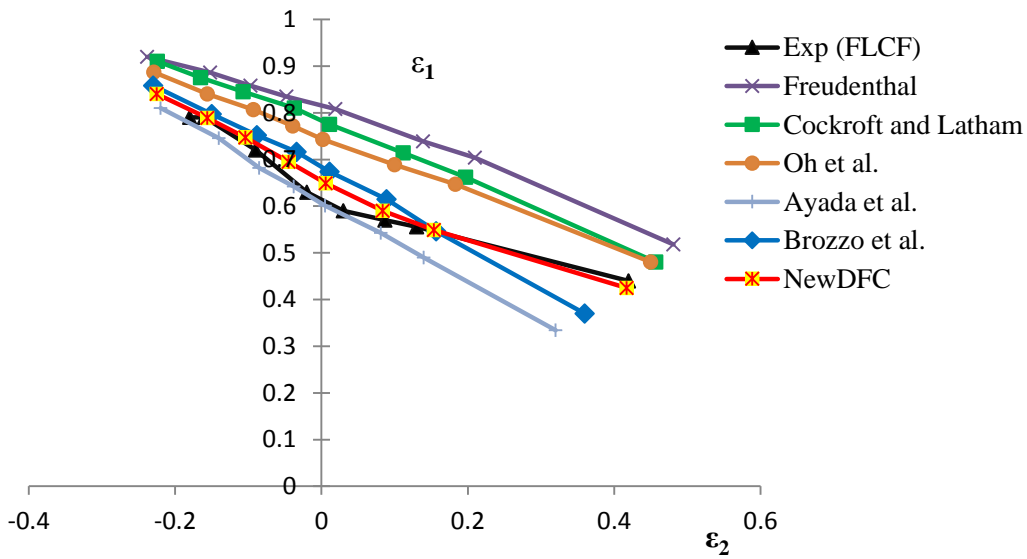


Figure 8.29. FLCFs of various DFCs implementing YLD2003 constitutive equation for DKP6112 material

As it can be observed, equation of Ayada et al. gives better results when  $\epsilon_2 < 0$  for all constitutive models but for  $\epsilon_2 > 0$ , the results are not that accurate. Therefore if the sheet metal is not going to encounter severe stretch forming processes, this DFC can be suggested. Models of Freudenthal and Cockroft et al. are still predicting the fracture initiation with noteworthy delay for plane strain conditions ( $\epsilon_2 = 0$ ). Oh et al. gives the better results comparing to the former two models but still the results for plane strain conditions are not suitable. In the case of BBC2008 yield criterion, equation of

Oh et al. results gives better predictions comparing to other constitutive equations which implies that if the Oh et al. model is selected, BBC2008 equation will be the best choice with lower deviations from the experimental results. DFC of Brozzo et al. is accurate enough for  $\varepsilon_2 < 0$  employing all constitutive models. Similar to the DFC of Ayada et al., in the processes where stretching conditions are dominant, Brozzo et al. criterion should not be chosen although for the whole range of the FLCF, the criterion gives the closest results to the experimental data after the new DFC.

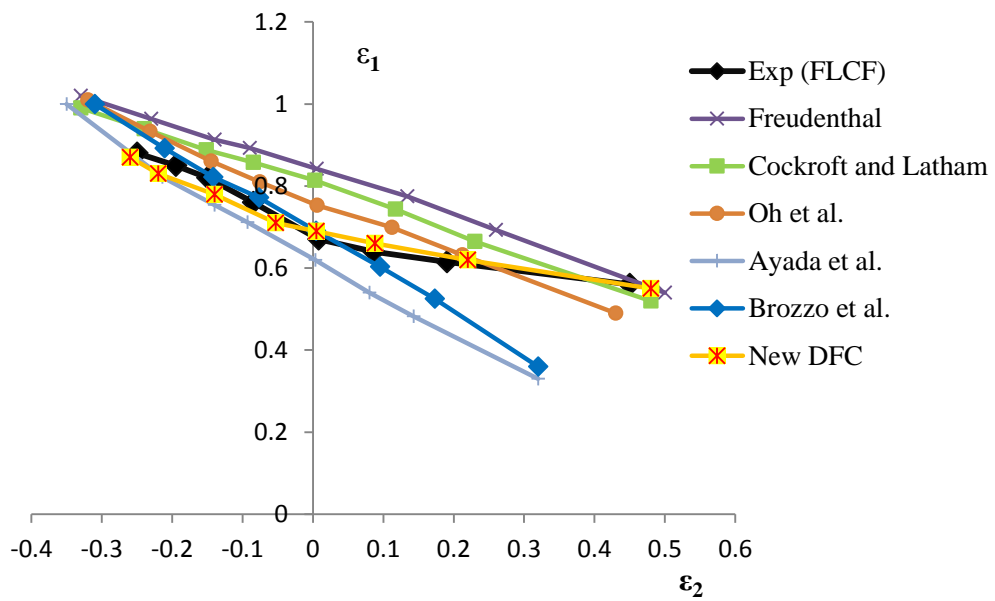


Figure 8.30. FLCFs of various DFCs implementing Von-Mises equation for SS304

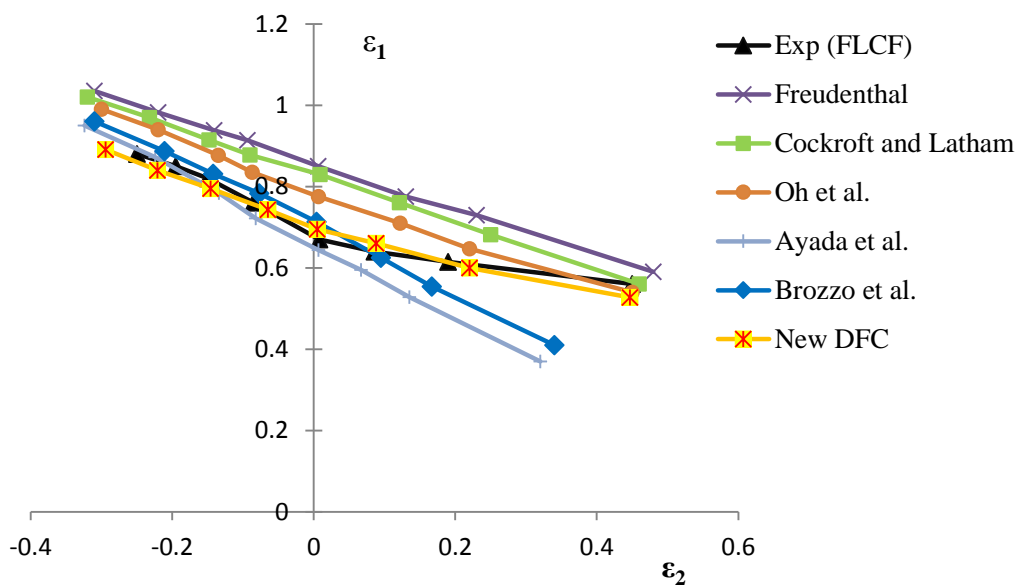


Figure 8.31. FLCFs of various DFCs implementing Hill48 equation for SS304

The same behavior have been observed for the SS304 material where new DFC is better than the other DFCs. The results of Brozzo et al. and Ayada et al. similarly are accurate when  $\varepsilon_2 < 0$  but not reliable for  $\varepsilon_2 > 0$ .

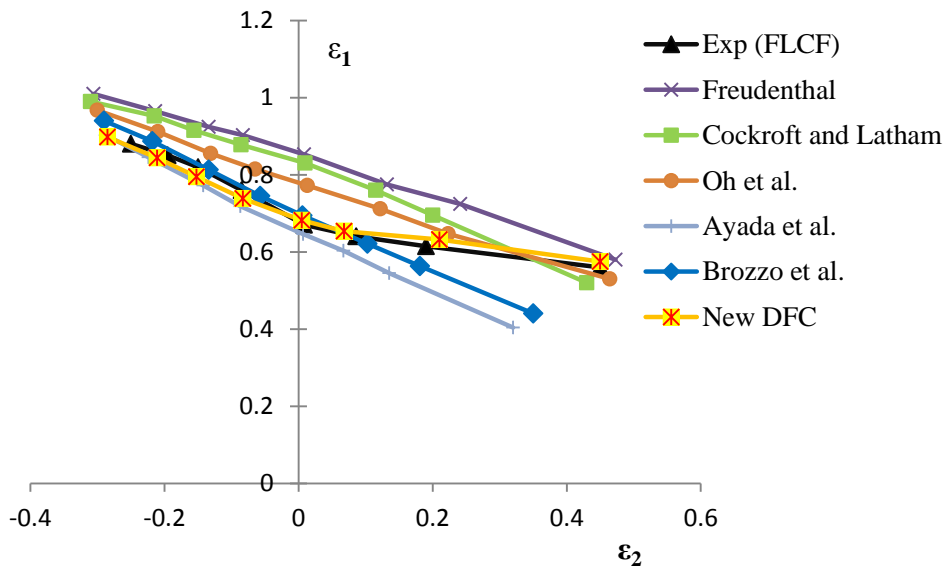


Figure 8.32 FLCFs of various DFCs implementing BBC2008 equation for SS304

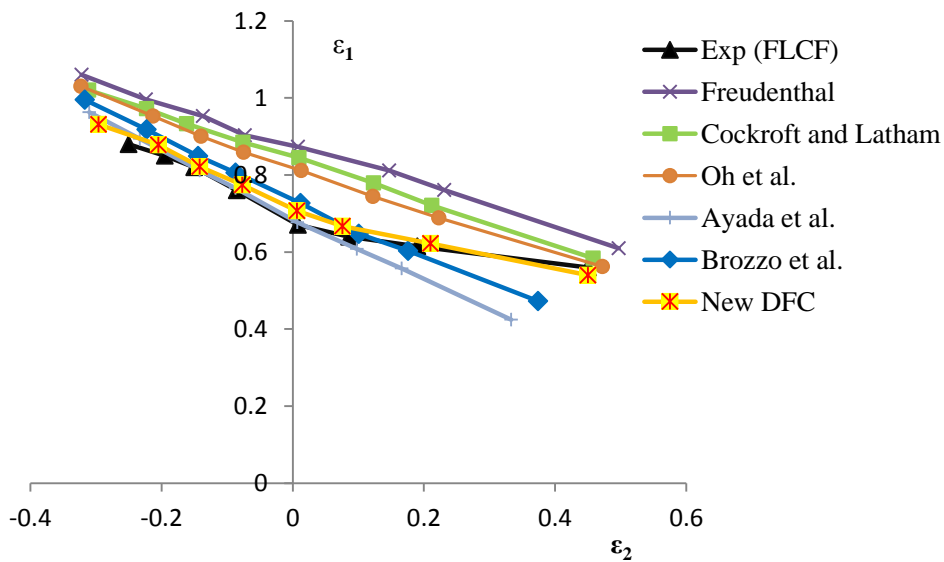


Figure 8.33. FLCFs of various DFCs implementing YLD2003 equation for SS304

For AA5450, the conditions are little bit different from the other two materials. In Figures 8.34-8.37 the FLCFs obtained for various DFCs using four different constitutive models and piecewise hardening are shown.



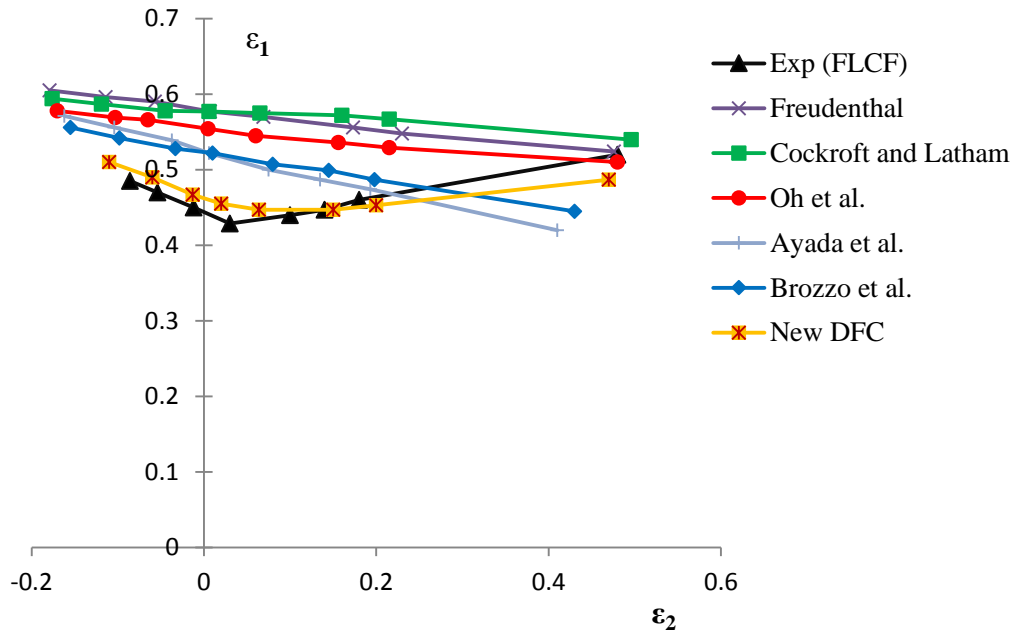


Figure 8.34. FLCFs of various DFCs implementing Von-Mises constitutive equation for AA5450 material

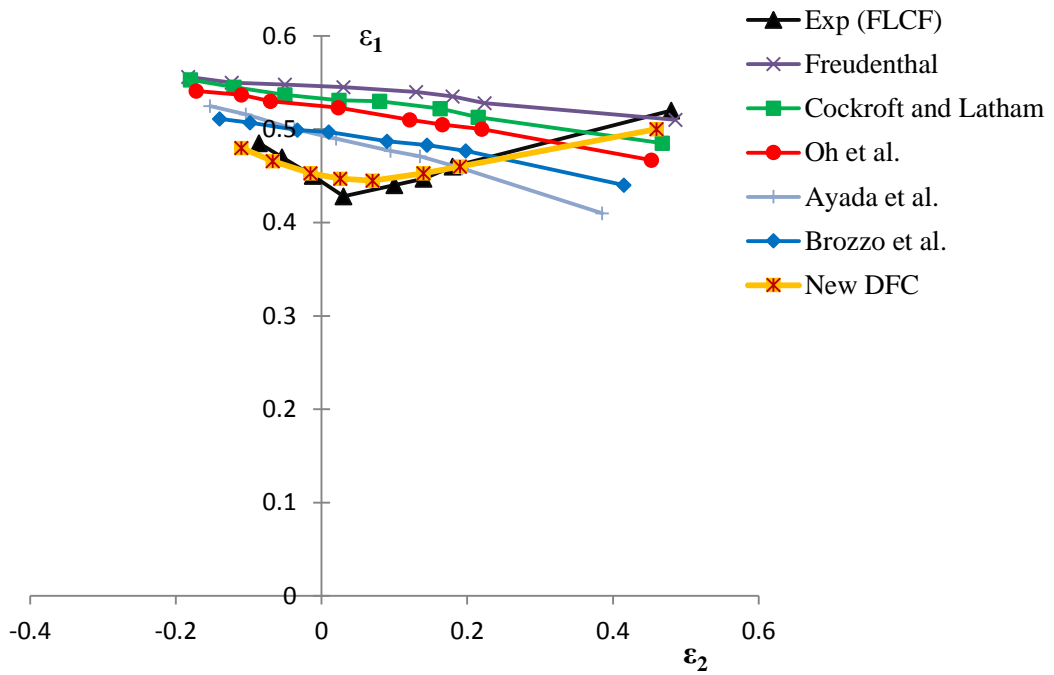


Figure. 8.35. FLCFs of various DFCs implementing Hill48 constitutive equation for AA5450 material

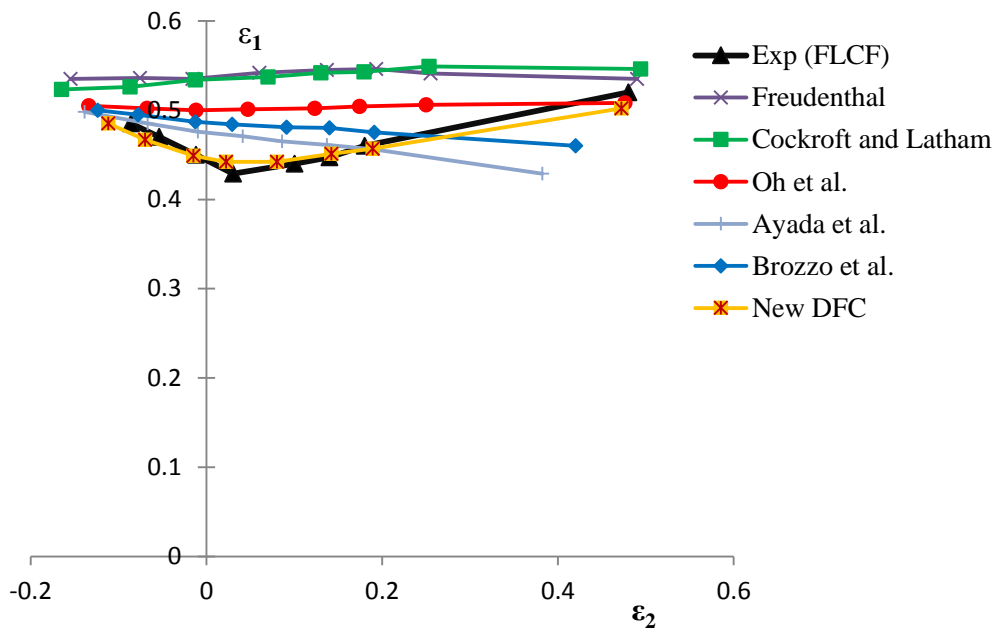


Figure 8.36. FLCFs of various DFCs implementing BBC2008 constitutive equation for AA5450 material

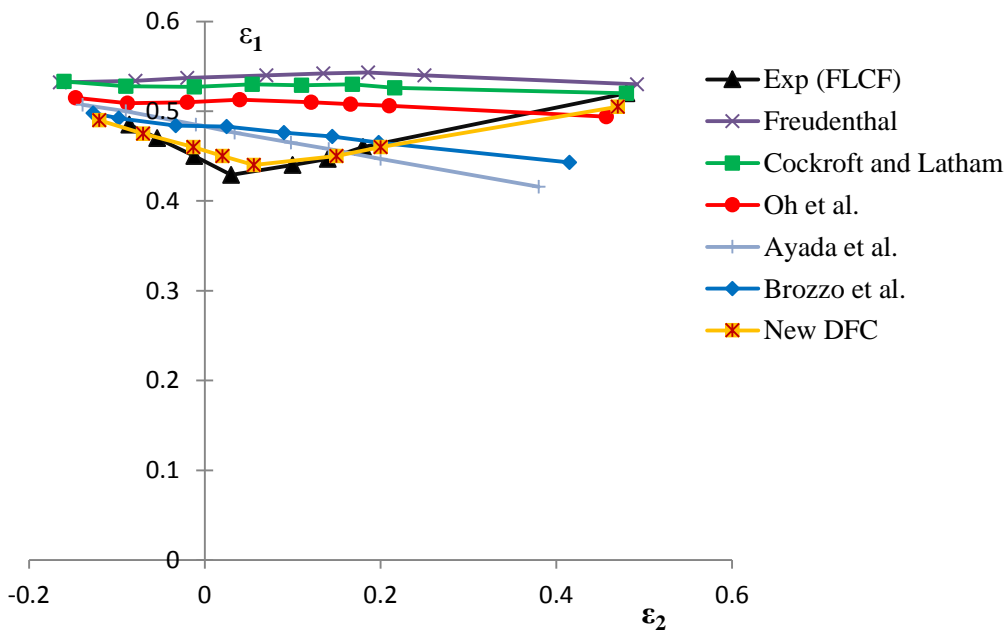


Figure 8.37. FLCFs of various DFCs implementing YLD2003 constitutive equation for AA5450 material

As it can be observed in the figures above, none of the DFCs are accurate enough when  $\epsilon_2 > 0$  except the new DFC, although the results of Ayada et al. and Brozzo et al. are closer than the others. In contrast to the other materials, DFCs of Brozzo et al. and Ayada et al. cannot estimate the fracture initiation as accurate as they can in the steel

materials. This shows that for the aluminum material, the DFCs should be chosen carefully and the nature of the deformation should be considered as well. For example, according to Figure 8.34, for the biaxial testing, Freudenthal DFC will be one of the best choices among all DFCs.

In Figures 8.38-8.40, the functionality of the new ductile fracture criterion with the different constitutive models has been studied. As it can be observed, the new DFC is very capable in the determination of the fracture initiation with all constitutive equations. The results of the BBC2008 equation is closer to the experimental data for both  $\varepsilon_2 < 0$  and  $\varepsilon_2 > 0$  considering the DKP6112 material. Although the criterion performs better when  $\varepsilon_2 < 0$  with all constitutive models, for  $\varepsilon_2 > 0$ , the results of the Von-Mises and Hill48 models are deviating slightly in the biaxial stretch forming region.

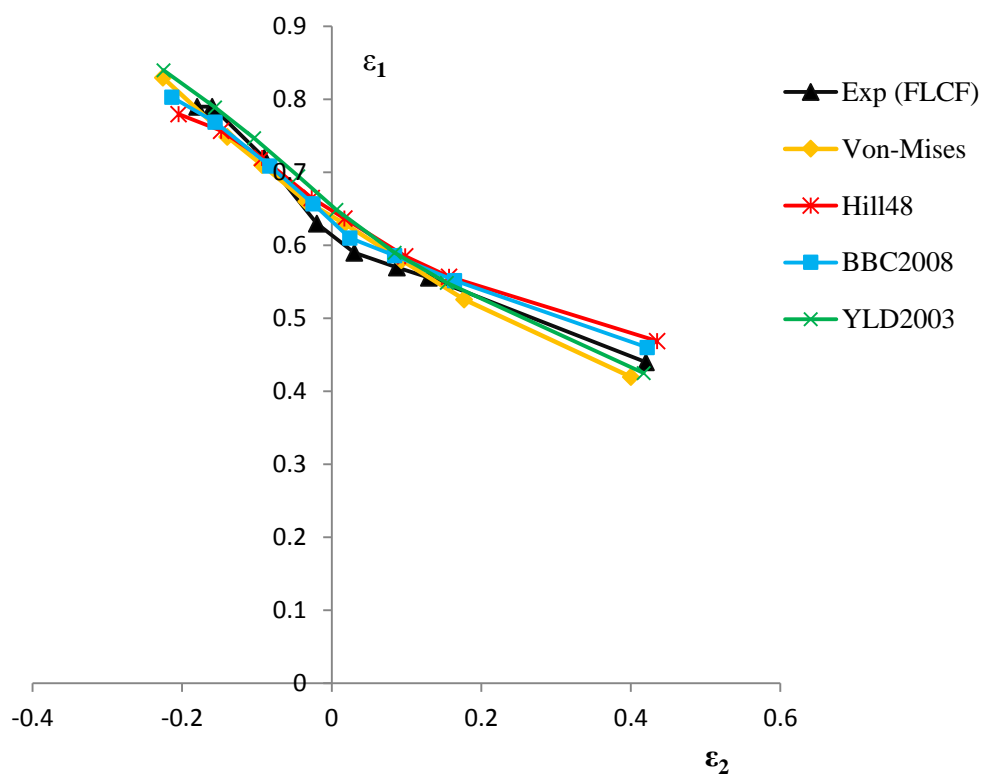


Figure. 8.38. FLCFs of the new DFC implementing various constitutive models for DKP6112 material

For SS304 material the fracture initiation is predicted earlier comparing to the experimental results for Von-Mises model. For YLD2003 on the other hand, the

fracture has been estimated slightly later for  $\varepsilon_2 < 0$  but it is reliable enough when  $\varepsilon_2 > 0$ .

For both DKP6112 and SS304 materials, the new criterion gives the better results when BBC2008 constitutive equation is employed; hence, the time and place of the fracture has been predicted precisely using this constitutive model.

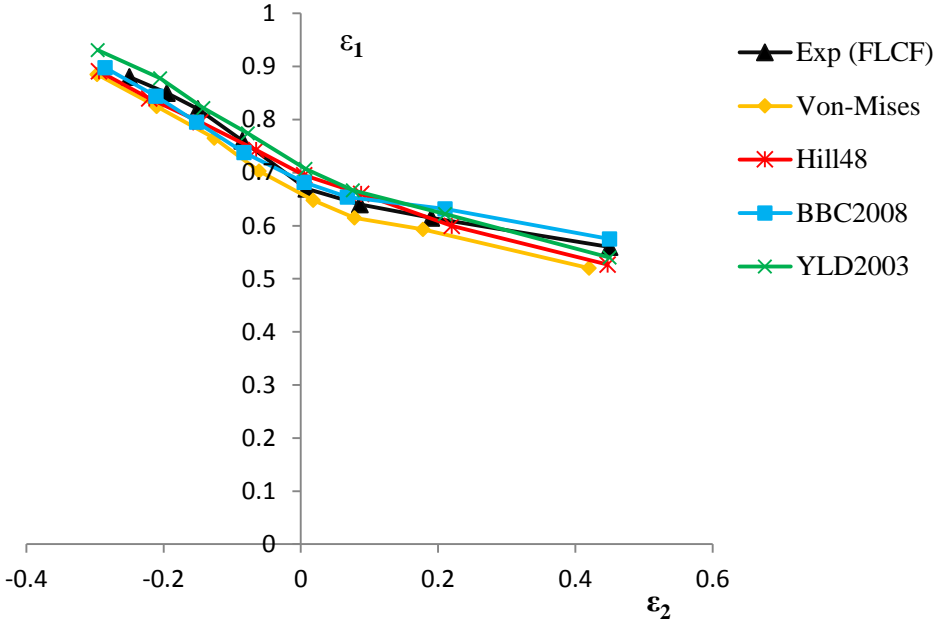


Figure. 8.39. FLCFs of the new DFC implementing various constitutive models for SS304 material

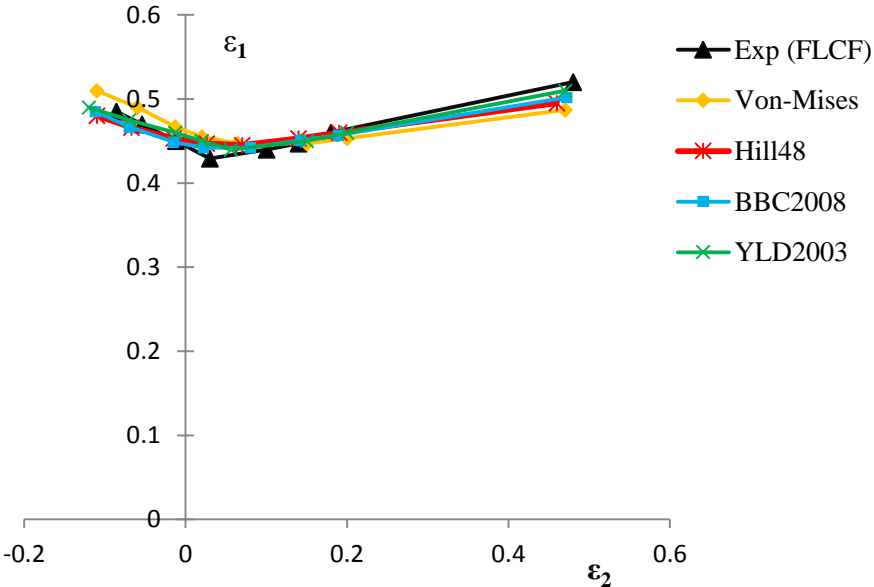


Figure. 8.40. FLCFs of the new DFC implementing various constitutive models for AA5450 material

For AA5450, the Von-Mises criterion has predicted the fracture initiation with some delay for  $\varepsilon_2 < 0$  and slightly earlier for  $\varepsilon_2 > 0$  in the FLCF where the other models give almost the same results for both  $\varepsilon_2 < 0$  and  $\varepsilon_2 > 0$ . The results show that for this material one of the anisotropic constitutive models should be preferred using the new DFC.

### 8.3.2 Effect of hardening models on the DFCs

Five different uncoupled ductile fracture models (Freudenthal, Cockroft and Latham, Brozzo et al., Oh et al. and Ayada et al.) were chosen to determine the effect of hardening models on the DFCs. The criteria constants were extracted numerically by simulating the uniaxial tensile tests for each DFC. For this purpose, the experimentally determined material parameters ( $n, r, K, E, \nu$ ) and measured strain at fractures were directly implemented to the FE code. The constants of the criteria that were calculated using Equations 5.240-5.244 are given in Table 8.1 for DKP6112 and SS304 materials.

Table 8.1. DFC constants for DKP 6112 and SS304 materials

		CONSTANTS				
Material	Hardening model	$C_F$	$C_C$	$C_B$	$C_O$	$C_A$
<b>DKP6112</b>	Isotropic Hardening	463.18	498.93	1.049	1.039	0.398
	Kinematic Hardening	404.30	416.70	0.976	0.973	0.342
	Combined Hardening	452.60	499.50	1.064	1.041	0.420
<b>SS304</b>	Isotropic Hardening	922.5	989.5	0.996	0.985	0.371
	Kinematic Hardening	843	872	0.901	0.855	0.313
	Combined Hardening	903.4	995.6	1.02	1.007	0.392

The comparison of different ductile fracture criteria for isotropic hardening rule using piecewise hardening model and Von-Mises constitutive model with the experiments is given in Figure 8.26 beforehand.

Figure 8.41 shows the comparison of the experimental results with the numerical results for different ductile fracture criteria that were found by employing the isotropic hardening rule with the Holloman equation. In Figure 8.42, the results of various ductile fracture criteria obtained by implementing kinematic hardening rule with Zeigler-Prager hardening model, have been compared with the experimental data. Also

in Figure 8.43, all ductile fracture criteria results obtained by using combined hardening rule and Chaboche-Zeigler hardening model have been compared with the experiments.

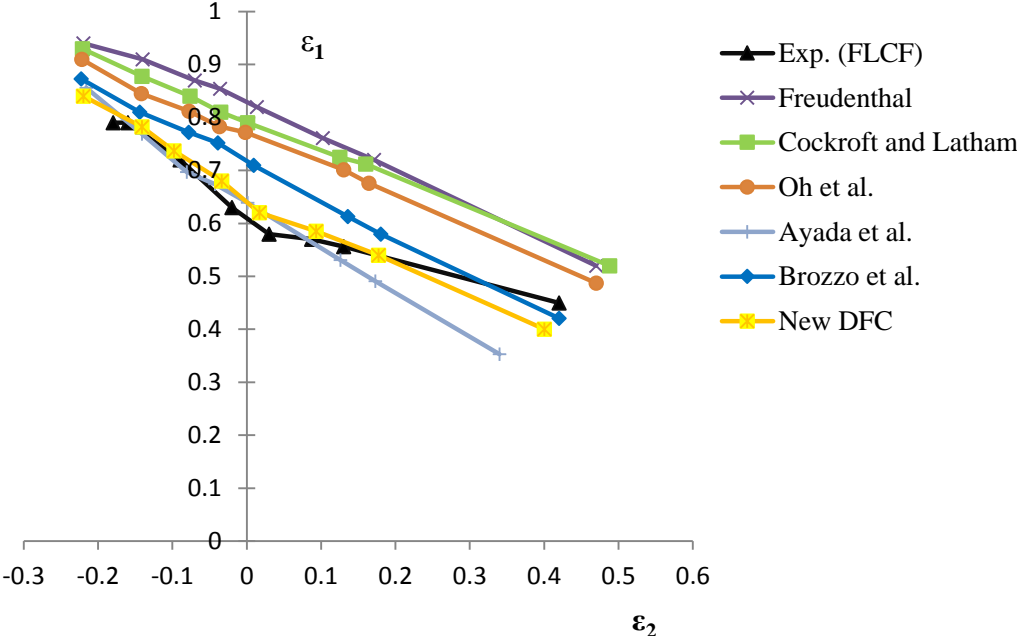


Figure 8.41. Nakazima test results for isotropic hardening rule that uses Hollomon hardening equation for DKP6112

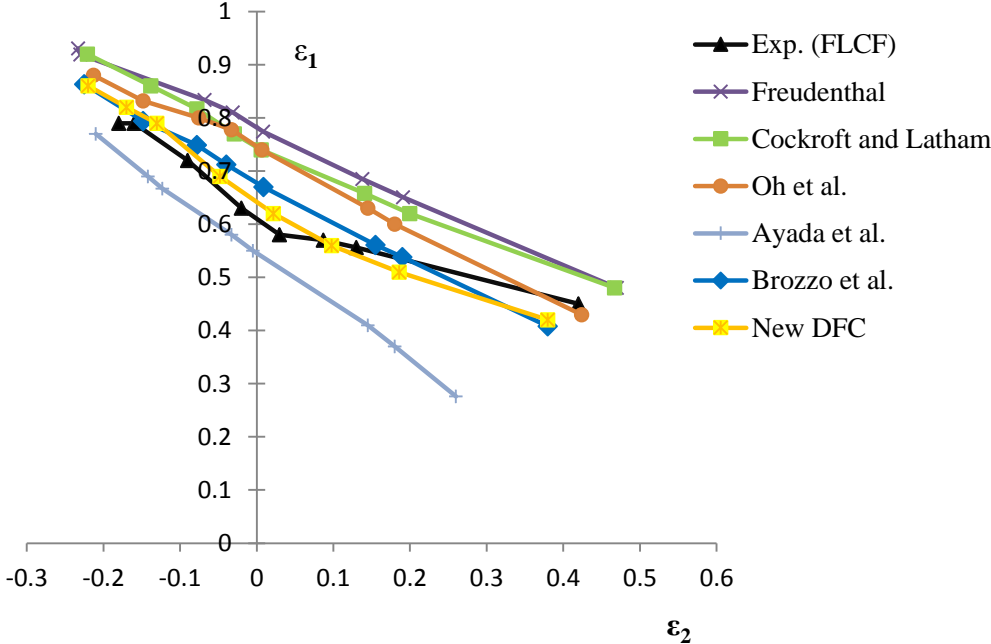


Figure. 8.42. Nakazima test results for kinematic hardening that uses Zeigler-Prager equation for DKP6112

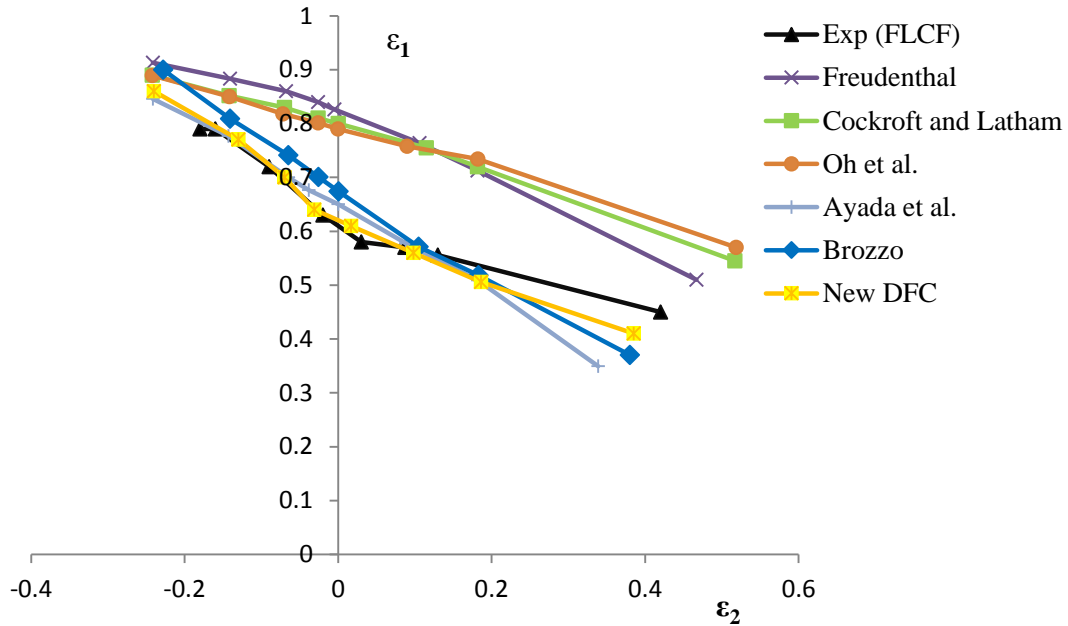


Figure. 8.43. Nakazima test results for combined hardening that uses Chaboche-Zeigler equation for DKP6112

Considering the DKP6112 material, it is observed from the diagrams given that the ductile fracture criteria of Freudenthal, Cockroft and Latham, and Oh et al. result in forming limit curves at fracture which are close to each other whereas the curves determined by the criteria of Ayada et al. and Brozzo et al., being closer to each other deviate from the former ones for all hardening parameters.

The ductile fracture criterion proposed by Ayada et al. gives the closest values to the experimental results for  $\varepsilon_2 < 0$ , however for  $\varepsilon_2 > 0$  it deviates significantly from the experimentally determined FLCF for all of the hardening models. For  $\varepsilon_2 > 0$  the best results are obtained by the DFC proposed by Brozzo et al. and the results of this criterion is still acceptable for  $\varepsilon_2 < 0$ .

The forming limit curves at fracture that were obtained by the ductile fracture criteria of Freudenthal, Cockroft and Latham, and Oh et al. are almost linear lines with a negative slope. All of the curves are far away from the experimental values especially for the region where  $-0.15 < \varepsilon_2 < 0.3$ .

The better results obtained by the ductile fracture criteria of Ayada et al. and Brozzo et al. can be attributed to the consideration of both mean stress and equivalent plastic strain simultaneously in their relation which have been proved to have a significant effect on the fracture mechanisms by many authors [66, 69, 70].

The difference between the forming limit curves obtained by isotropic hardening rules which use piecewise and Holloman hardening equations is found insignificant.

The best result is obtained by the isotropic hardening for the DFC of Ayada et al. whereas the maximum deviation is observed in results of the simulations executed by kinematic hardening for  $\epsilon_2 > 0$ . It would be appropriate to use the isotropic hardening or combined hardening for the DFC of Brozzo et al. The forming limit curves formed by the ductile fracture criteria of Freudenthal, Cockroft and Latham, and Oh et al. are closest to the experimental results when the kinematic hardening rule is used.

Figure 8.44 shows that the forming limit curves at fracture predicted by the new DFC are very close to each other for different hardening rules while all other DFCs have some shortcomings. It is important to mention that the new DFC accurately predicts the material behavior for both  $\epsilon_2 < 0$  and  $\epsilon_2 > 0$  which can be attributed to the consideration of the material properties and strain path effects. Between the three hardening rules, the new DFC gives the better results using combined and piecewise isotropic hardening rules respectively although the results of the combined hardening deviates slightly in the biaxial region.

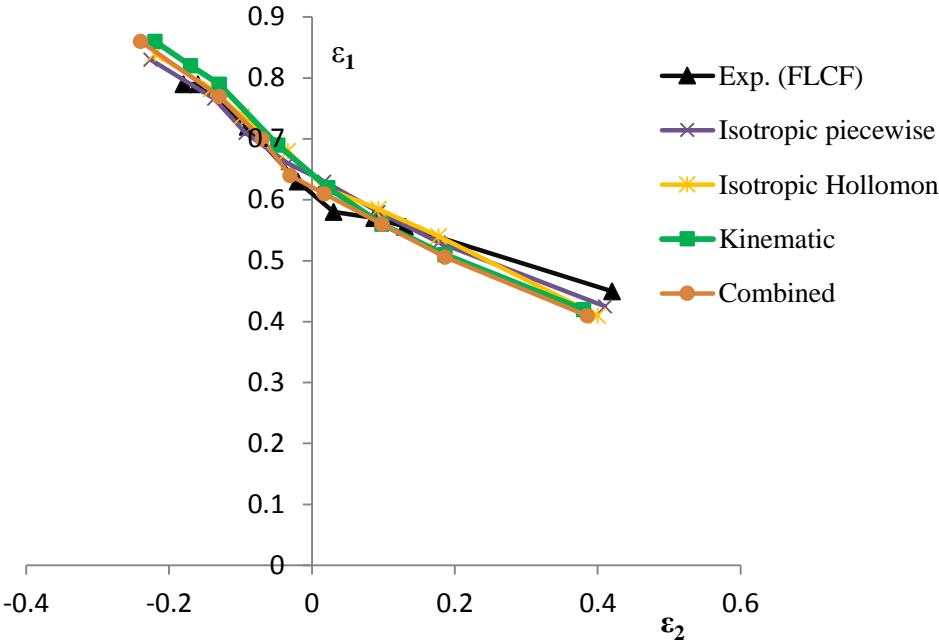


Figure. 8.44. FLCFs of the New DFC that uses four different hardening equations for DKP6112 material

The same comparisons were made for SS304 material too. Since the results for Hollomon and piecewise isotropic hardenings are very close to each other for



DKP6112, therefore only one of them has been chosen to be studied with SS304 material. The results for piecewise isotropic, Zeigler-Prager kinematic and Chaboche-Zeigler combined hardening rules have been shown in Figures 8.30, 8.45 and 8.46 respectively.

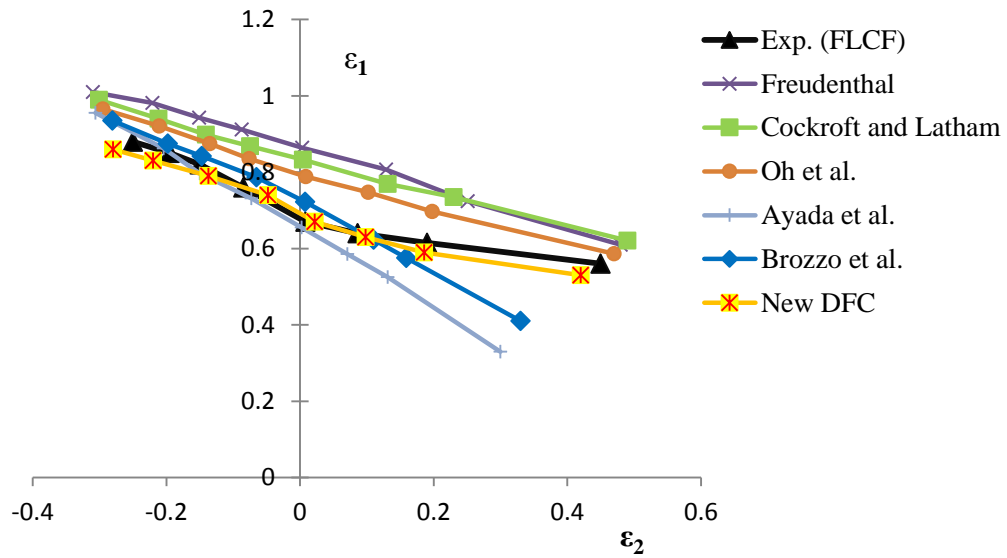


Figure. 8.45. Nakazima test results for kinematic hardening that uses Zeigler-Prager equation for SS304 material

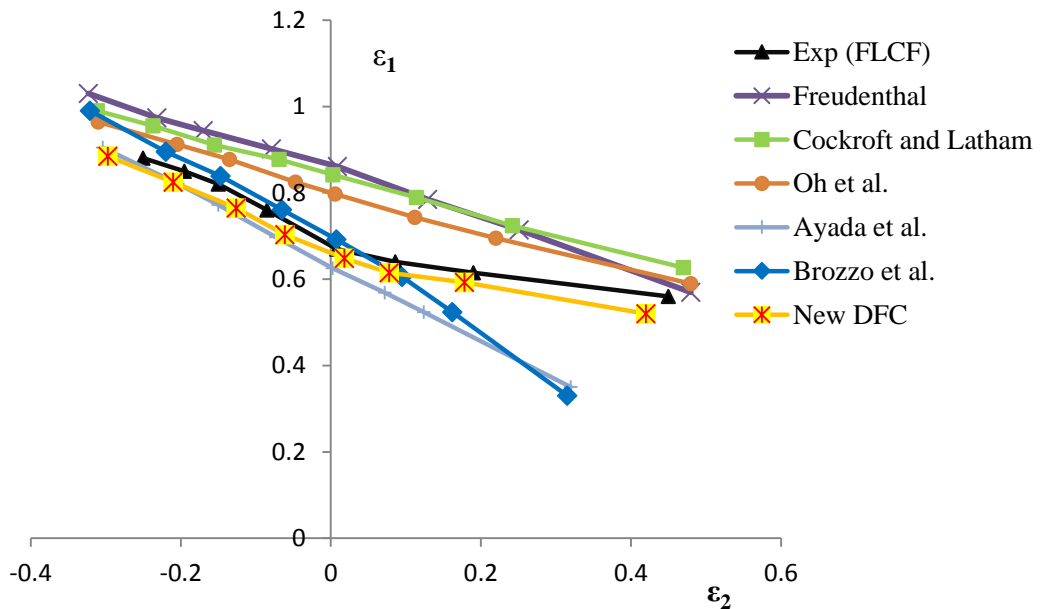


Figure. 8.46. Nakazima test results for combined hardening that uses Chaboche-Zeigler equation for SS304 material

Most of the comments given for the DKP6112 material are approximately valid for SS304 material too. The ductile fracture criteria of Freudenthal, Cockroft and Latham,

and Oh et al. are better in predicting the fracture initiation comparing to the DKP6112 material. Also the Brozzo et al. criterion which was good in the DKP6112 material, is not that accurate especially when the Chaboche-Ziegler combined hardening is used and the stretching conditions are dominant ( $\epsilon_2 > 0$ ). For the kinematic hardening, still Brozzo et al. is better than the other models. Again the new DFC is far better than the other criteria both for  $\epsilon_2 < 0$  and  $\epsilon_2 > 0$ .

The FLCF is well predicted by the new DFC using both isotropic and combined hardening models for DKP6112 and both isotropic and kinematic hardening rules for SS304 material; even though the results of the combined hardening do not deviate significantly. Figure 8.47 indicates that with the combined hardening rule, the new DFC has predicted the fracture initiation earlier than the other hardening models for whole range of the FLCF in SS304 material. However Figure 8.46 showed that the obtained results using the new DFC still are better than the predictions of the other employed DFCs.

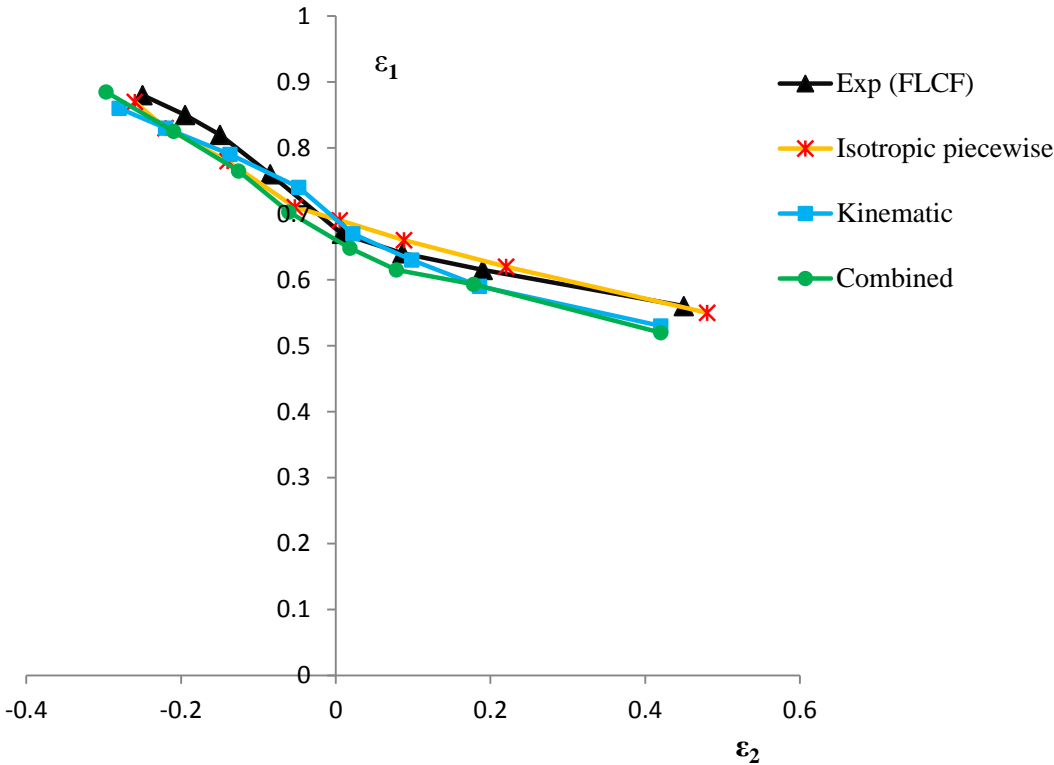


Figure. 8.47. FLCFs of the new DFC using three different hardening models for SS304 material

### 8.3.3 Case studies

In addition to the comparisons given for different conditions using Nakazima tests to check the reliability of a DFCs, two different forming processes were accomplished to evaluate the DFCs functionality in the complicated strain paths. For this purpose cylindrical and square cup drawings were performed and the blank holding forces intentionally were increased to enforce the specimens fail in the early and middle stages of the forming processes.

To study the effect of the hardening models, the squared cup drawing process was simulated using Von-Mises yield criterion. The isotropic hardening rule with piecewise hardening, kinematic hardening rule with Zeigler-Prager equation and the combined hardening rule based on Chaboche-Zeigler equation have been used to compare the results of various ductile failure criteria.

As an example, the distribution of the values of  $\int_0^{\bar{\epsilon}^f} \sigma_{max} d\bar{\epsilon}$  function that is indicating the possibility of fracture initiation in the elements at 24 mm of the punch travel for DKP6112 material is shown in Figure 8.48 for the case in which Cockroft and Latham criterion with isotropic hardening rule has been used.

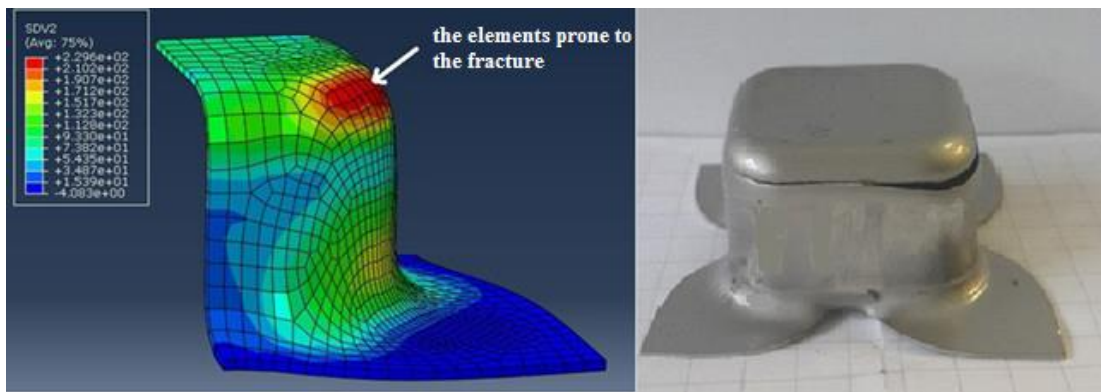


Figure. 8.48. Distribution of the DFC constant (SDV2) at 24 mm of the punch travel for DKP6112 material

In Figure 8.49 the results of the new DFC for three hardening rules are compared with the other DFCs and where the points show the strain values at fracture for square cup drawing. It is observed that the new DFC predicts the fracture better than the other studied DFCs with all hardening rules and the estimation with the combined hardening seems to be better than other hardening models, even though the predictions are little bit earlier for all models comparing to the experimentally measured point.

As it can be seen the DFC of Brozzo et al. with combined hardening and the DFC of Cockroft and Latham with kinematic hardening have shown the best estimation between all DFCs except the new DFC. The same result is observed in Figure 8.43 for the DFC of Brozzo et al. as well. DFC of Ayada et al. predicted the closest result when the isotropic hardening is used. The DFC of Oh et al. predicts the location and the time of the fracture better than any other DFCs with kinematic hardening rule among the all DFCs were studied here except the new DFC.

On the other hand, Figure 8.49 indicates that, DFC of Ayada et al. is far away from predicting the fracture when kinematic hardening model is used. This outcome is also seen in figure 8.42 as the result obtained by using the DFC of Ayada et al. deviates from the experimental data significantly for biaxial tension region ( $\epsilon_2 > 0$ ). The fracture predicted by the DFC of Freudenthal for all of the hardening rules deviate significantly from the experimental data. The same deduction can be acquired for the DFC of Ayada et al. when kinematic hardening rule is used.

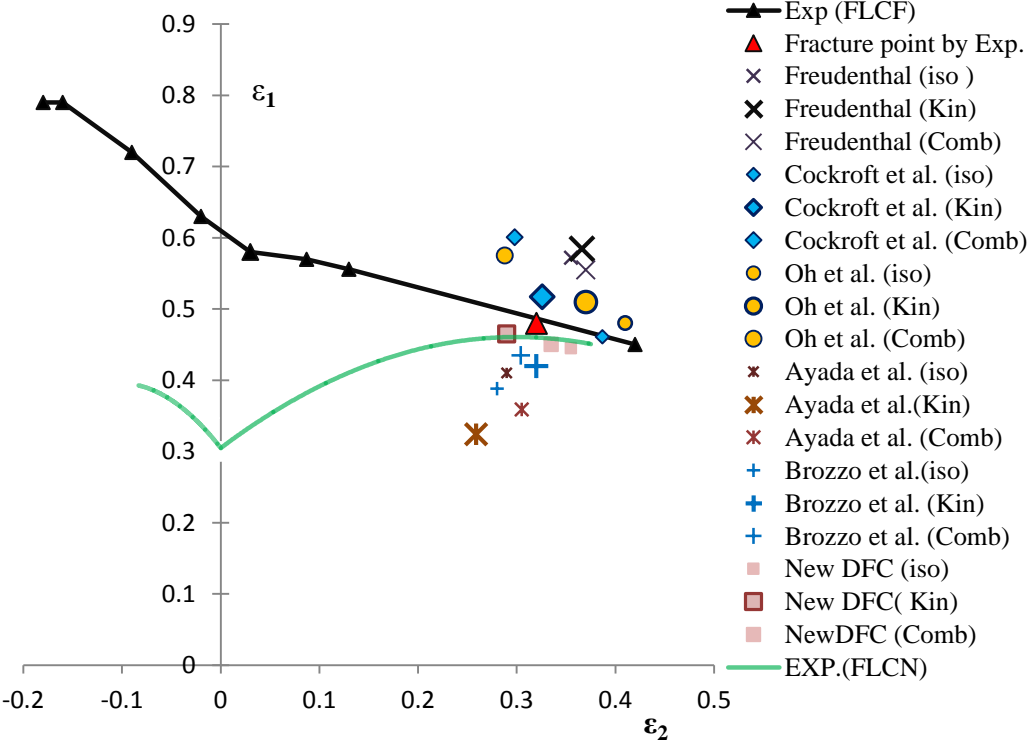


Figure. 8.49. Comparison of different DFCs for square cup drawing of DKP6112 at 24.6 mm of punch travel using Von-Mises constitutive model

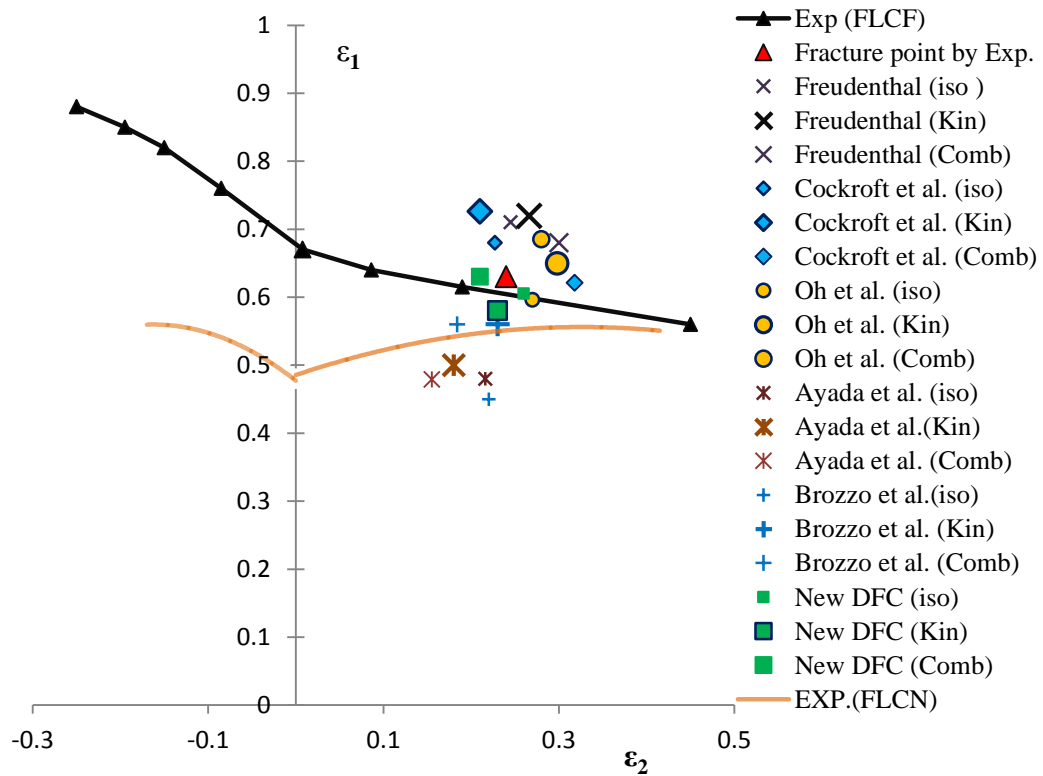


Figure. 8.50. Comparison of different DFC results for square cup drawing of SS304 at 23.2 mm of punch travel using Von-Mises constitutive model

Another issue which should be mentioned is that it is difficult to implement the combined hardening rule to the finite element model and determine the related constants whereas the kinematic hardening rule is the simplest equation to be implemented using the subroutines. Therefore for the conditions where kinematic and combined hardening rules are giving the closer results, the kinematic hardening model is suggested.

The same diagram which has been extracted for SS304 material is shown in Figure 8.50. This figure indicates that after new DFC which is accurate enough in predicting the fracture point with all hardening models and especially with the piecewise hardening, the Oh et al. and Cockroft models have given the better predictions with piecewise isotropic hardening rule. In the case of the kinematic hardening model, Oh et al and Brozzo et al. have better estimations than the others.

Almost none of the studied DFCs are accurate enough with combined hardening rule except the new DFC. Although the results of Brozzo et al. is closer to the experimental data than the other four criteria.

the effects of different constitutive models in the square cup drawing, implementing the new DFC and piecewise isotropic hardening model have been studied for DKP6112 and SS304 materials and the results are shown in Figures 8.51 and 8.52 respectively. Hill48 and BBC2008 criteria are more accurate for DKP6112 material but in the case of SS304, almost all of the yield functions have the same accuracy.

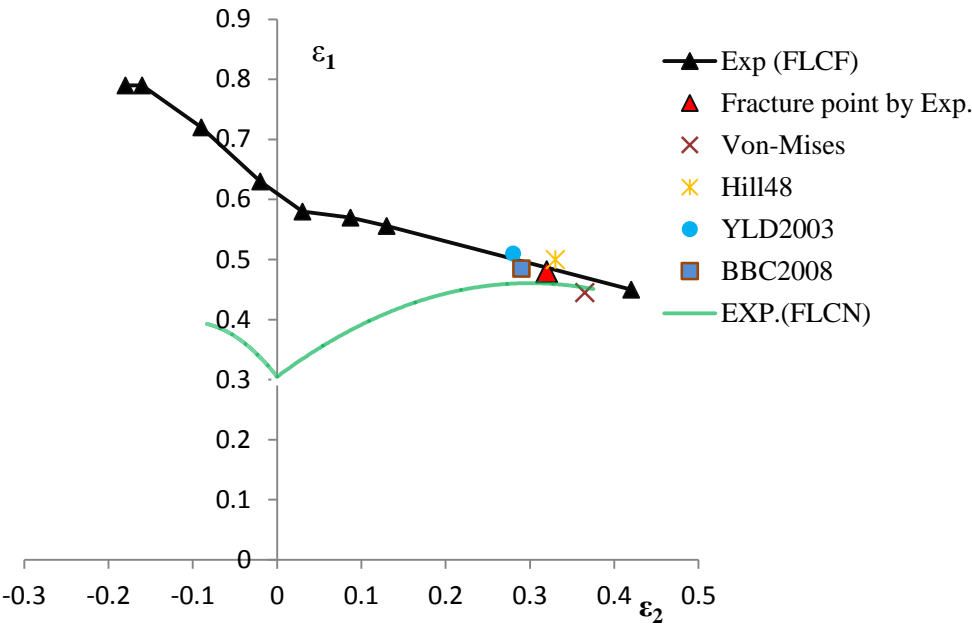


Figure. 8.51. Comparison of the different yield criteria in the prediction of the fracture at 24.6 mm of punch travel for squared cup of DKP6112

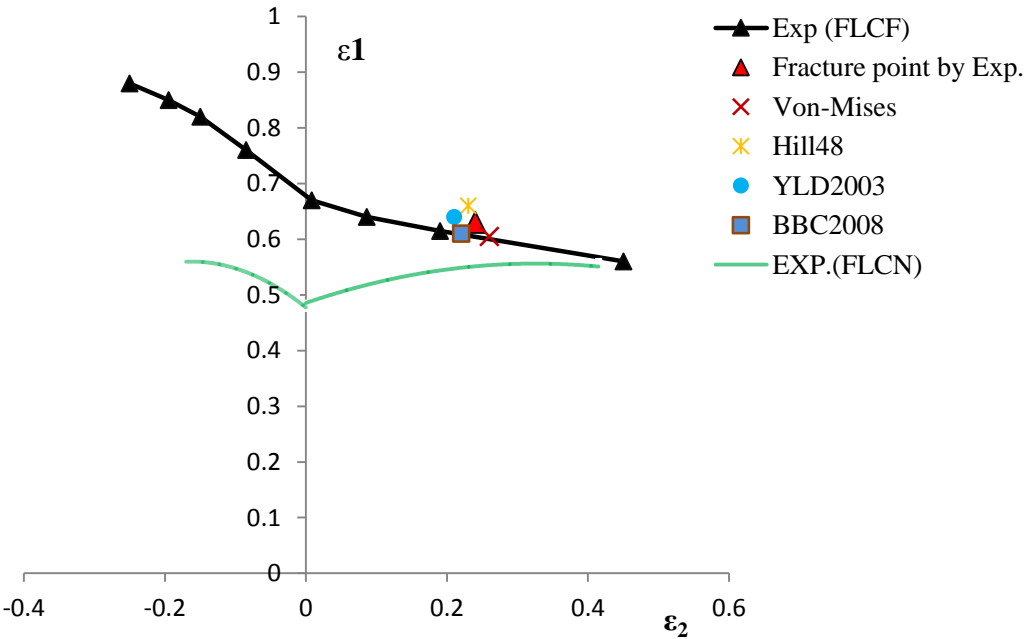


Figure. 8.52. Comparison of the different yield criteria in the prediction of the fracture at 23.2 mm of punch travel for squared cup of SS304

As a second case the effect of different constitutive models on the DFCs have been studied for cylindrical cup drawing where piecewise isotropic hardening has been used for all simulations. In Figures 8.53 and 8.54, the deformed specimens are shown for DKP6112 material (Figure 7.12) which have been estimated by simulations. The fracture initiation place and time have been designated by a *fracture indicator parameter (FIP)*. It is defined in a way that if the value of *FIP* gets equal to the one, the fracture will start. Then the element in which the fracture initiates can be easily recognized in the post processing step. From Equations 6.3 and 6.10, *FIP* for new DFC is defined as,

$$FIP = \frac{\int_0^{\bar{\epsilon}_f} \bar{\sigma} d\bar{\epsilon} + C_4 \tau_{max}}{B(C_1 + C_2 |2\rho|^{C_3})} \quad (8.1)$$

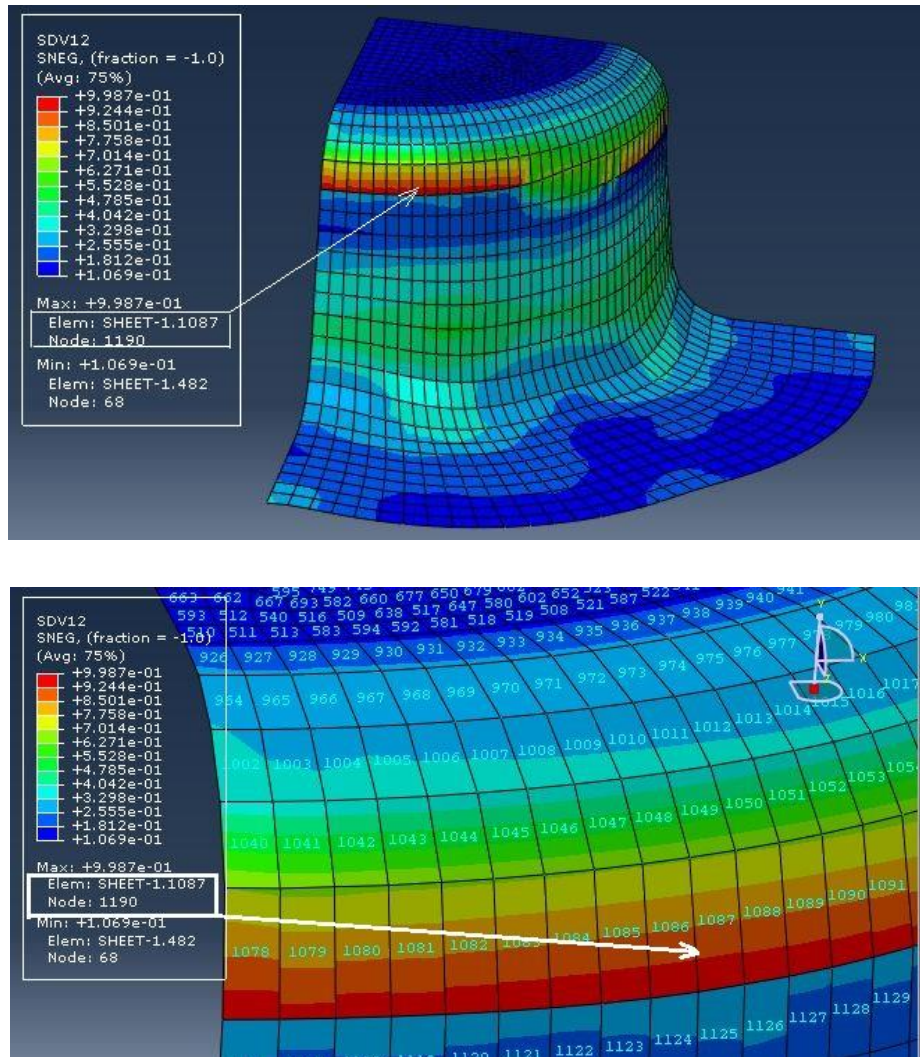


Figure. 8.53. Distribution of the *FIP* at 17.9 mm of the punch travel for DKP6112 using BBC2008 yield criterion

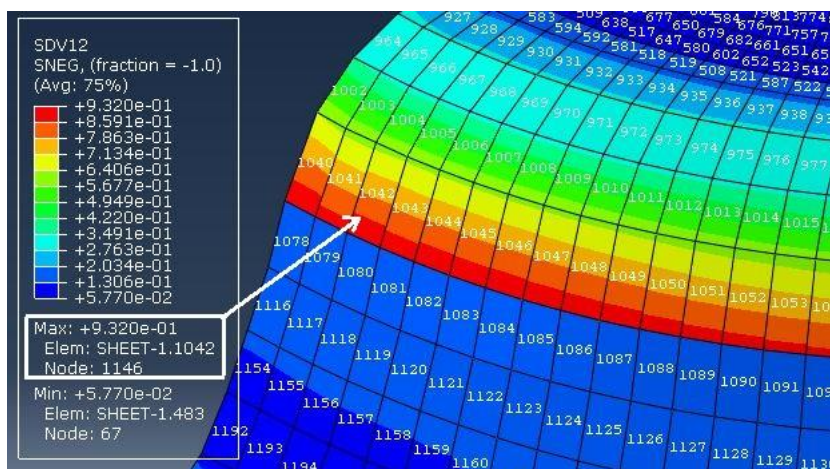
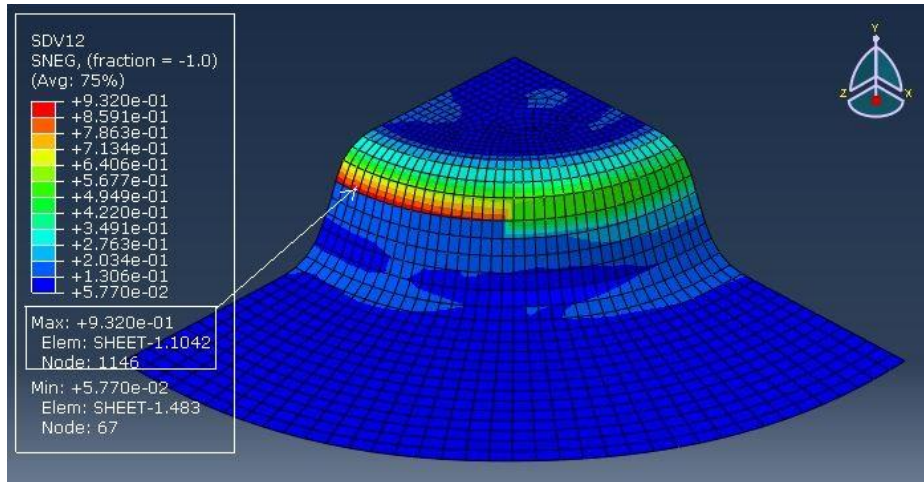


Figure. 8.54. Distribution of the *FIP* at 11.7 mm of the punch travel for DKP6112 using BBC2008 yield criterion

The SDV12 values in Figures 8.53 and 8.54 shows the value of *FIP* in the simulation steps which will help to identify the elements prone to the fracture in any step of the simulation.

In Figure 8.55 the comparison of the different DFCs in the prediction of the fracture place and time using BBC2008 constitutive equation have been presented. As it is clear, the fracture has taken place in the nearly plane strain conditions and all DFCs have predicted this critical situation correctly where the new DFC is the most accurate one between all. The DFCs of Ayada et al. and Brozzo et al. have closer estimations too. The DFCs of Cockroft and Latham and Freudenthal are delayed in the time of the fracture although they have successfully predicted the place of it. DFC of Oh et al. seen to be work better with the BBC2008 constitutive model previously (Figure 8.28) and gives the better estimations for the above case as well.



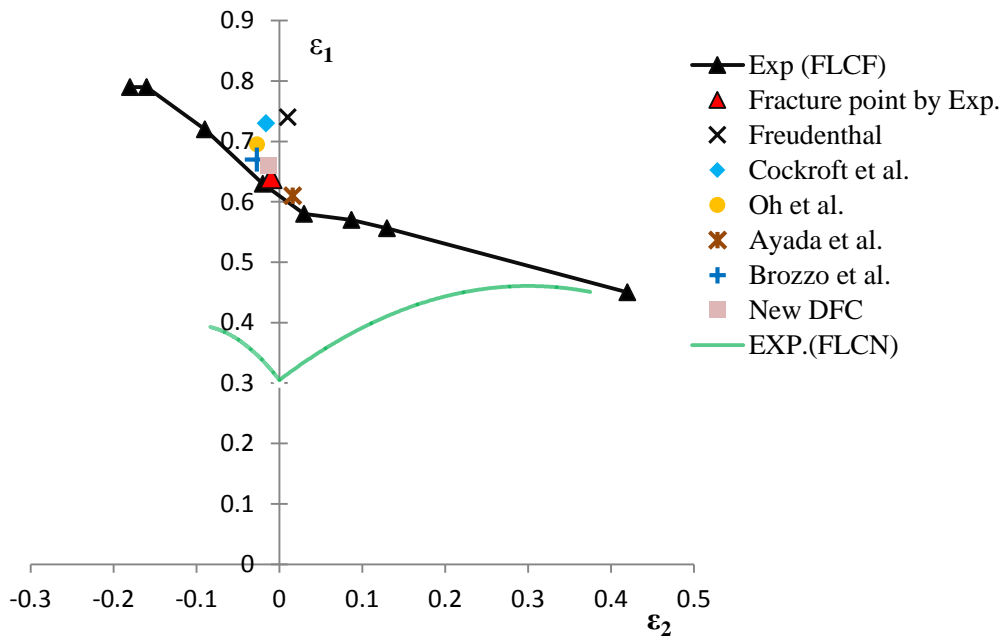


Figure. 8.55. Comparison of the different DFCs using BBC2008 yield criterion in the prediction of the fracture at 18 *mm* for cylindrical cup of DKP6112

In Figure 8.56 the same comparison has been made for the case in which the fracture occurred in 12 mm of the punch travel in the experimental test because of deliberately increasing in the blank holding force to 6 KN. Again the new DFC, Brozzo et al. and Ayada et al. have better estimations respectively where the fracture has happened closer to the plane strain condition.

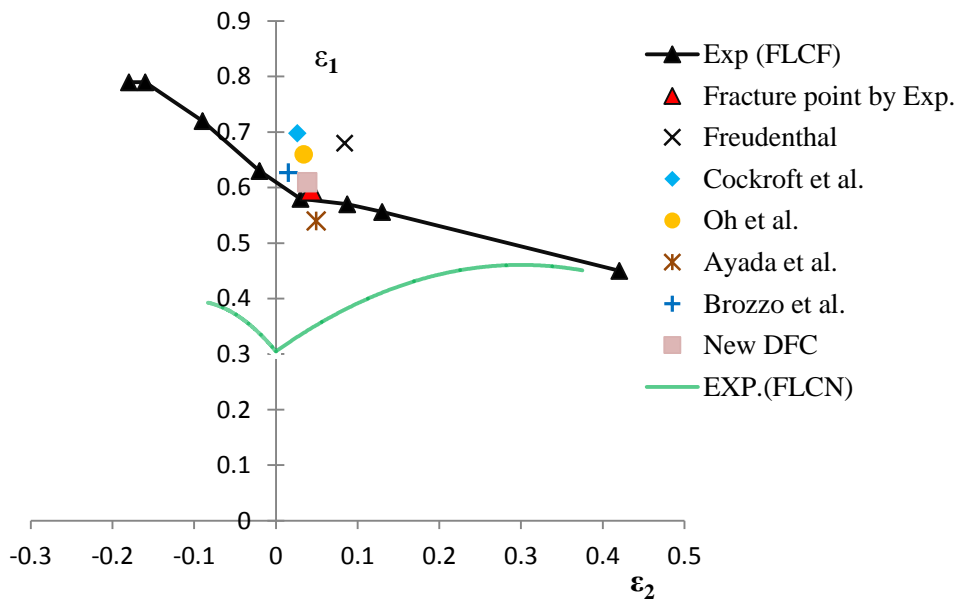


Figure. 8.56. Comparison of the different DFCs using BBC2008 yield criterion in the prediction of the fracture at 12 *mm* for cylindrical cup of DKP6112

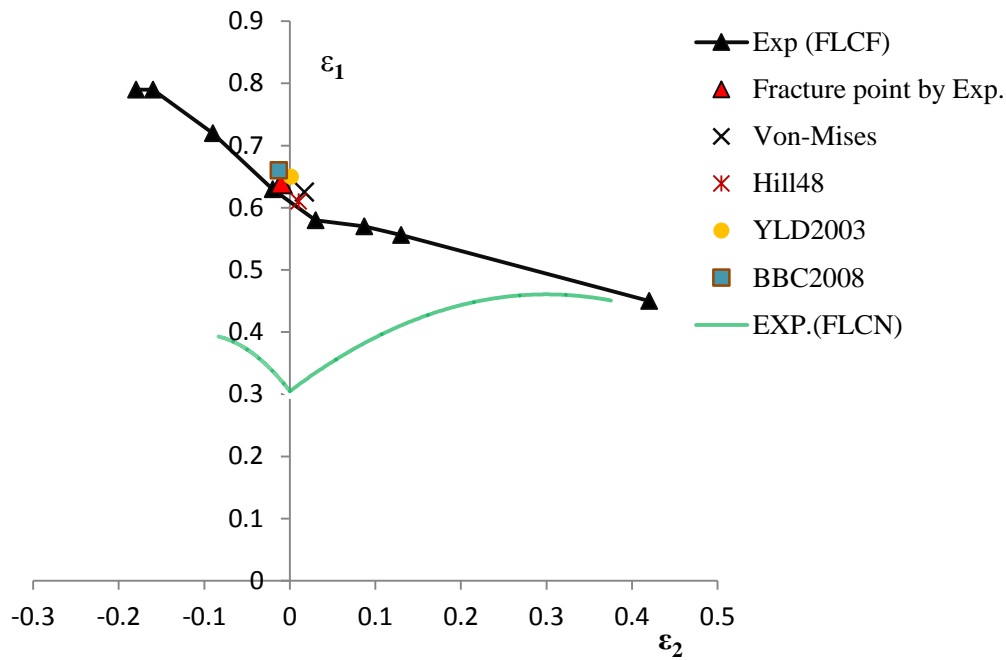


Figure. 8.57. Comparison of the different constitutive models in the prediction of the fracture using the new DFC at 18 *mm* of punch travel for DKP6112

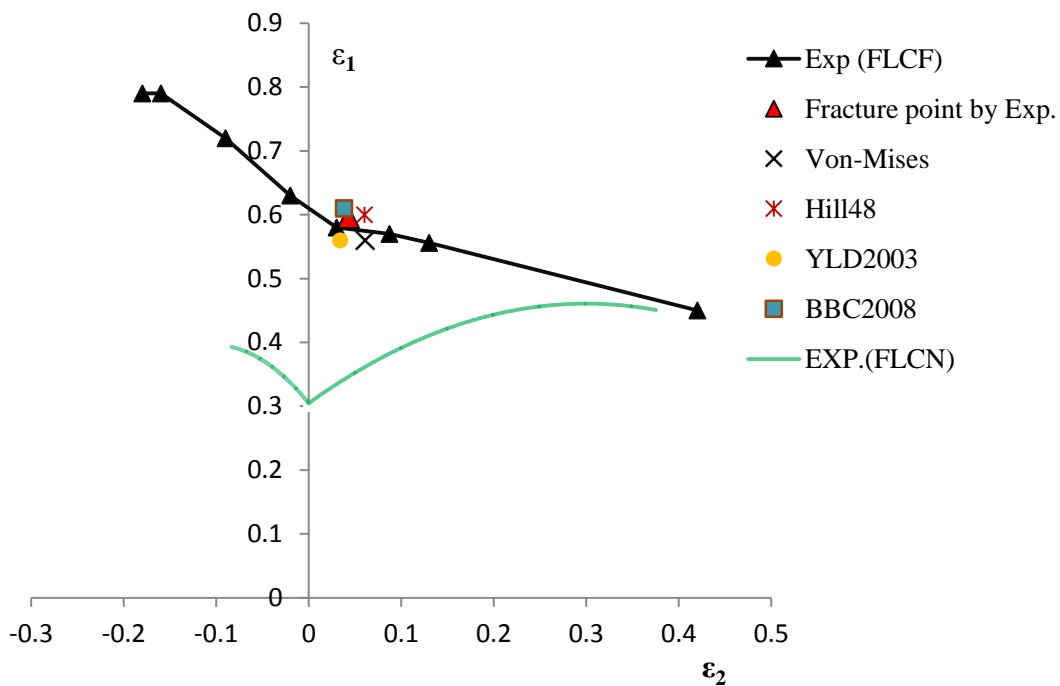


Figure. 8.58. Comparison of the different constitutive models in the prediction of the fracture using the new DFC at 12 *mm* of punch travel for DKP6112

In Figures 8.57 and 8.58 the comparison of the different yield criteria for the prediction of the fracture which was observed experimentally at 18 *mm* and 12 *mm* of the cylindrical cup using the new DFC and piecewise hardening model are presented. As it is clear from the figures, the new DFC has predicted very well with all constitutive

equations; however, the results for BBC2008 and YLD 2003 are better than the others. In Figure 8.59 the fracture points for a SS304 cup at 19 mm of punch travel implementing various constitutive models are shown. The new DFC is able to predict the fracture accurately employing all yield criteria; however the result of BBC2008 is closer than the other models to the experimental fracture point.

For AA5450 the cylindrical cup fractured at 14.5 mm of the punch travel where the blank holding force was 3 KN. As it is observed in Figure 8.60, the new DFC has predicted the fracture initiation with small delay implementing all of the constitutive models. Although the anisotropic yield criteria were suggested to be implemented if AA5450 material is formed, the isotropic Von-Mises criterion estimates the fracture with small deviation from the experimental results comparing to the other criteria. This is because of the strain conditions in the fractured region where all of the studied yield criteria were capable enough to predict the fracture initiation point accurately in the plain strain conditions (Figure 8.40).

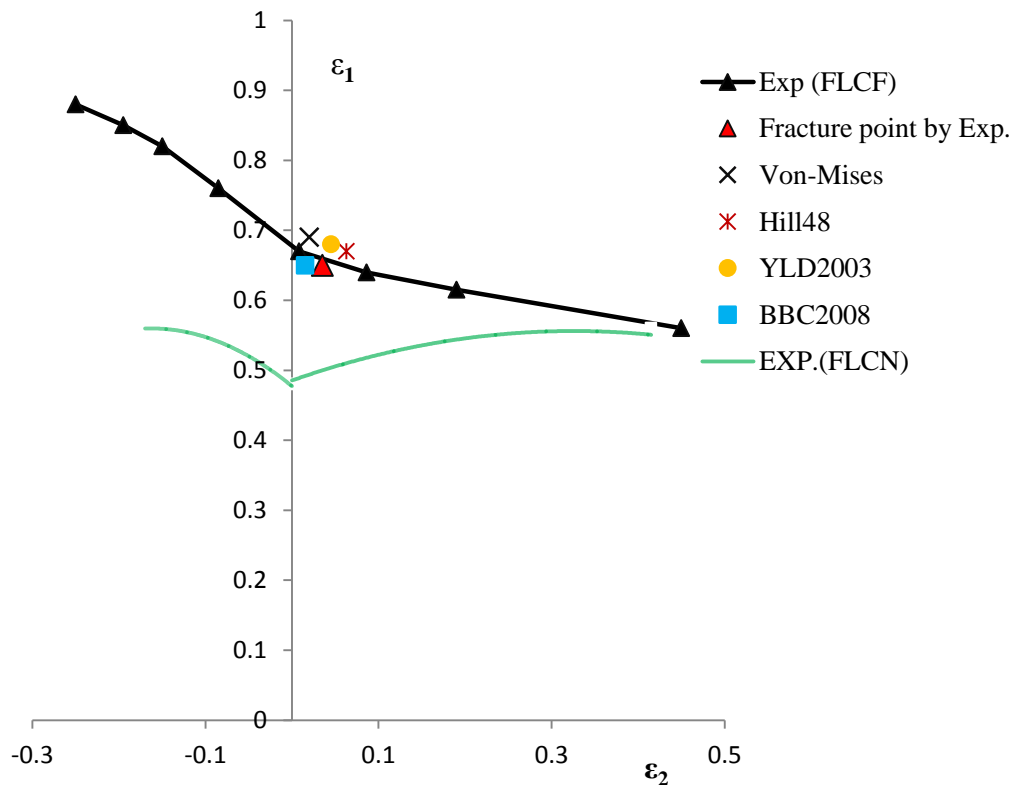


Figure. 8.59. Comparison of the different constitutive models in the prediction of the fracture using the new DFC at 19 mm of punch travel for SS304

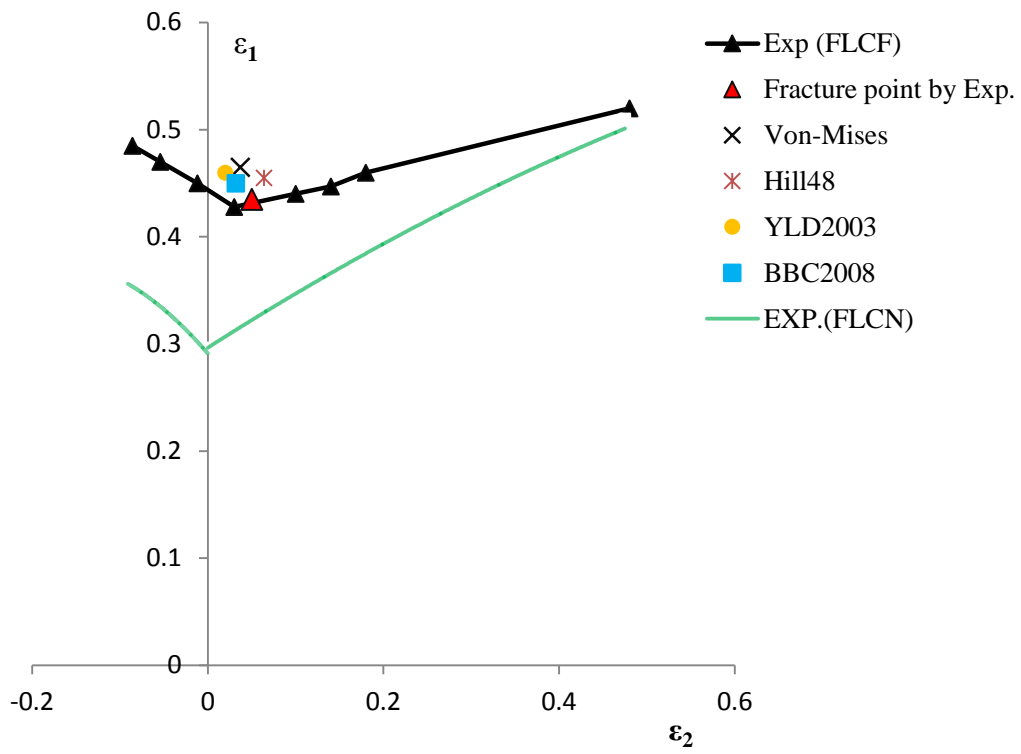


Figure. 8.60. Comparison of the different constitutive models in the prediction of the fracture using the new DFC at 14.5 mm of punch travel for AA5450

## CHAPTER 9

### CONCLUSIONS AND FUTURE WORKS

Fracture phenomenon, as an important issue in the sheet material forming processes, was studied macroscopically with paying attention to the energy dissipations. The conventional forming limit curves (FLC) which are strain path dependent in nature, are unable to clarify the fracture initiation time and place in the forming processes, therefore ductile fracture criteria (DFC) showed up to encounter this problem. The new forming limit curves that are drawn implementing DFCs are called forming limit curves at fracture (FLCF). DFCs determine the fracture initiation and propagation in the metal forming applications and can be categorized in two types, coupled and uncoupled, accordingly. In this study a new uncoupled ductile fracture criterion which is based on the general plastic energy is proposed successfully.

The former uncoupled DFCs are unable to adopt the strain path effects completely and this shortcoming is resolved in the new DFC by considering the strain ratio ( $\rho$ ) effects as a parameter in the criterion. Also to make the criterion be usable for low ductile materials like aluminum, the maximum shear stress effects are regarded as another determinative parameter.

To establish and verify the new DFC, seven different materials were used and four different experimental tests were accomplished. Uniaxial tension and Erichsen tests were used to define the material parameters and Nakazima tests were used for calibration and verification processes. Furthermore, deep drawing of cylindrical and square cup were utilized to test the reliability of the new DFC in the complicated forming processes.

To implement these DFCs to the numerical codes, user subroutines written with FORTRAN coding language, were linked to the commercial ABAQUS software and finally the explicit solvers were used to run the simulations.

The new DFC only needs a single experimental test to determine all constants and the criterion unknown. This is one of the most important characteristics that differs it from most of the coupled DFCs which need more than two experimental tests to be used.

Five different uncoupled DFCs namely, Freudenthal, Cockroft and Latham, Ayada et al., Oh et al. and Brozzo et al. were chosen and compared with the new DFC results in the fracture initiation prediction process. Also three hardening rules (isotropic, kinematic and combined) and four different constitutive equations (Von-Mises, Hill48, YLD2003 and BBC2008) were chosen to investigate the effect of hardening models and constitutive equations on the functionality of the DFCs.

## 9.1 Conclusions

According to the results obtained for different hardening models and constitutive equations the following conclusions are achieved:

1. Choosing the appropriate hardening model which can reflect the deformation nature effectively is an important issue in the fracture prediction processes with DFCs.
2. All studied DFCs show better performance for  $\varepsilon_2 < 0$  in the FLCFs for all materials comparing to their performance for the situations when  $\varepsilon_2 > 0$ . Therefore if the strain history is contained the stretching processes, the appropriate DFC should be selected very carefully.
3. The anisotropic constitutive models have better estimations with all DFCs than the von-Mises model.
4. DFCs of Ayada et al. and Brozzo et al. lead to the better estimations especially with piecewise isotropic and combined hardening models. However the results for  $\varepsilon_2 > 0$  are not satisfactory enough. The existing DFCs are found to estimate the fracture initiation with remarkable delay for all materials.
5. The results of BBC2008 and YLD2003 are very close to each other and give the better predictions with most of the DFCs comparing to the other yield criteria.
6. Between the other DFCs, Oh et al., Brozzo et al. and Ayada et al. DFCs give the better estimations for steel materials in aggregate, although the results of Brozzo et al. and Ayada et al. for  $\varepsilon_2 > 0$  are not that accurate.
7. In the case of the AA5450, the YLD2003 and BBC2008 give the better results especially with the DFC of Oh et al. when uniaxial and biaxial conditions are

present, but all of the existing DFCs are incapable of the accurate estimation for plane strain situation except the new DFC.

8. Unlike the most of the previously developed DFCs, the new DFC is applicable for variety of the materials.
9. The predictions obtained with the new DFC show that that the results are more accurate if BBC2008 constitutive equation is adopted especially for the steel materials.
10. The new DFC is better in the predicting the fracture initiation for all range of the FLCFs and also it is reliable enough with all studied yield functions comparing to the existing uncoupled DFC.
11. In the case of the AA5450 material, the new DFC is slightly conservative when  $\varepsilon_2 > 0$  , while it estimates with some delays for  $\varepsilon_2 < 0$ .
12. The case studies show that the new DFC is a robust tool in the prediction of the fracture initiation in the complicated forming processes and it undoubtedly can be used in any deformation in which the fracture estimation are necessary.

To conclude, the proposed criterion can be applied and utilized easily by using a single experimental test, and is capable of predicting the fracture initiation in almost all deformation conditions accurately. The new DFC gives reliable results with most of the isotropic and anisotropic constitutive models and hardening rules which differs it from the other uncoupled and coupled DFCs.

## **9.2 Future works**

Although the uncoupled DFCs have been effectively used to determine the fracture initiation point, there is no post fracture and crack propagation model for these criteria. Therefore, as a future work, the phenomena after the fracture initiation can be macroscopically studied.





## REFERENCES

1. Grote K.H., Antonsson K. (Eds.), Springer handbook of mechanical engineering, Springer, 2009.
2. Beddoes J., Bibby M.J., Principles of metal manufacturing processes, Elsevier Butterworth-Heinemann, 2003.
3. Semiatin S.L., Introduction to Bulk-Forming Processes, ASM Handbook, 14(A), Metalworking: Bulk Forming, 2005.
4. Hosford W.F., Coddell R.M., Metal Forming Mechanics and Metallurgy, Prentice Hall, 1983.
5. Johnson W., Mellor P.B., Engineering Plasticity, Ellis Horwood Ltd. Cambridge University Press, 3<sup>rd</sup> Edition, 2007.
6. Siegert K., Wagner S., Deep Drawing, EAA, training in aluminum application technologies (TALAT), lecture 3704, 1994.
7. Davis J.R., Tensile Testing, ASM International, Second edition, 2004
8. El-Sebaie M.G., Mellor P. B., Plastic instability conditions in the deep-drawing of a circular blank of sheet metal, Int. Journal of Mech. Sci., 14, 535-540, 1972.
9. Colgan M., John M., Deep drawing process: analysis and experiment, Journal of Mat. Proc. And Tech., 132, 35–41, 2003.
10. Gavas M., Izciler M., Effect of blank holder gap on deep drawing of square cups, Materials and Design, 28, 1641–1646, 2007.
11. Lang L., Danckert J., K. Nielsen B., Investigation into hydrodynamic deep drawing assisted by radial pressure Part I. Experimental observations of the forming process of aluminum alloy, Journal of Mat. Proc. Tech., 148, 119–131, 2004.
12. Sanay B., Kaftanoglu B., Comparison of Different Instability Criteria in Sheet Metal Forming, 6<sup>th</sup> Int. Con. and Exh. On Design and Prod. Of machines and Dies/Molds, 23-26 June, Ankara, Turkey, 2011.

13. Keeler S.P., Plastic Instability and Fracture in Sheet Stretched over Rigid Punches, ASM TRANS Q. 56, 25-48, 1963.
14. Swift, H., W., Plastic Instability under plane stress, J. Mech. Phys. Solids, 1-18, 1952.
15. Storen, S., Rice, J., R., Localized Necking in Thin Sheets, J. Mech. Phys. Solids, 23, 421-41, 1975.
16. Marciniak, Z., Kuczynski, K., "Limit strains in the processes of stretch forming sheet steel". J. Mech. Phys. Solids, 1, 609–620, 1967.
17. Bleck W., Deng Z, Papamantellos K., Gusek K.O., A comparative study of the forming-limit diagram models for sheet steels, J. of Mat. Proc. Tech., 83, 223–230, 1998.
18. Avila A. F., Vieira E.L.S., "Proposing a better forming limit diagram prediction: a comparative study", J. of Mat. Proc. Tech., 141, 101–108, 2003.
19. Aghaie-Khafri M., Mahmudi R., Predicting of plastic instability and forming limit diagrams, Int. J. of Mech. Sci., 46, 1289–1306, 2004.
20. Slota J., Spisak E., Comparison of the forming limit diagram (FLD) models for drawing quality (DQ) steel sheets, Metalurgija, 44, 249-253, 2005.
21. Wang L., Le T.C., The effect of yield criteria on the forming limit curve prediction and the deep drawing process simulation, Int. J. of Machine Tools & Manu., 46, 988–995, 2006.
22. Yoshida K., Kuwabara T., Kuroda M., Path-dependence of the forming limit stresses in a sheet metal, Int. J. of Plasticity, 23, 361-384, 2007.
23. Chakrabarty J., Chen F.K., Influence of loading path on the plastic instability strain in anisotropic plane sheets, J. of Mat. Proc. Tech., 166, 218–223, 2005.
24. Arrieux R., Determination of forming limit stress curve for anisotropic sheets, Annals of the CIRP, Vol. 36, 195-198, 1987.
25. Boudeau N., Gelin J., Necking in sheet metal forming. Influence of macroscopic and microscopic properties of materials, Int. J. of Mech. Sci., 42, 2209-2232, 2000.
26. Nurcheshmeh M., Green D.E., Investigation on the strain-path dependency of stress-based forming limit curves, Int. J. Mater., 4, 25–37, 2011.

27. Hill R. A theory of the yielding and plastic flow of anisotropic metals, Proc. Roy. Soc. London, 193, 281–297., 1948.
28. Hill R., User-friendly theory of orthotropic plasticity in sheet metals, Int. J. of Mech. Sci., 35, 19-25, 1993.
29. Siguang X., Weinmann K.J., Chandra A., Analysis of forming limits using the hill 1993 yield criterion, Trans. Of the ASME, 120, 236-241, 1998.
30. Hosford W F., ON the crystallographic basis of yield criteria, Textures and Microstructures, 26, 479-493, 1996.
31. Barlat F., Lege D., Brem J.C., A six-component yield function for anisotropic materials, Int. J. of Plasticity, 7, 693-712, 1991.
32. Barlat F., Becker R.C., Hayashid Y., Maed Y., Yanagaw M., Yielding description for solution strengthened aluminum alloys, Int. J. of Plasticity, 13, 385-401, 1997.
33. Kuroda M, Tvergaard V., Forming limit diagrams for anisotropic metal sheets with different yield criteria, Int. J. of Solids and Structures, 37, 5037-5059, 2000.
34. Banabic D., Cazacu O., Barlat F., Comsa D., Wagner S., Siegert K., Recent anisotropic yield criteria for sheet metals, Proc. Of the Romanian academy, 3, 2002.
35. Wu P.D., Jain M., Savoie J., MacEwen S.R., Tug P., Neale K.W., Evaluation of anisotropic yield functions for aluminum sheets, Int. J. of Plasticity, 19, 121-138, 2003.
36. Banabic D., Kuwabara T., Balan T., Comsa D.S., Julean D., Non-quadratic yield criterion for orthotropic sheet metals under plane-stress conditions, Int. J. of Mech. Sci., 45, 797-811, 2003.
37. Banabic D., Kuwabara T., Balan T., Comsa D.S., An anisotropic yield criterion for sheet metals, J. of Mat. Proc. Tech., 127, 462-465, 2004.
38. Barlat F., Aretz H., Yoon J.W., Karabin M.E., Brem J.C., Dick R.E., Linear transformation-based anisotropic yield functions, Int. J. of Plasticity, 21, 1009-1039, 2005.
39. Aretz H., A non-quadratic plane stress yield function for orthotropic sheet metals, J. of Mat. Proc. Tech., 168, 1-9, 2005.

40. Vrh M., Halilović M., Starman B., Štok B., Comsa D.S., Banabic D., Earing prediction in cup drawing using the BBC2008 yield criterion, Numisheet 2011, Seoul, 142-149, August 2011.
41. Hollomon J.H. Tensile Deformation”, *Trans. AIME*, 162, 268–90, 1945.
42. Prager W., A new method of analyzing stress and strains work-hardening plastic solids. *Journal of Applied Mechanics*, 23, 493-496, 1956.
43. Hodge P.J., Automatic Piecewise Linearization in Ideal Plasticity”, *Computer Methods in Applied Mechanics and Engineering*, 10, 249–272, 1977.
44. Lemaitre J, Chaboche L., *Mechanics of solid materials*, Cambridge university press, U.K., 1990.
45. Huang Y.M., Tsai Y.W., Li C.L., Analysis of forming limits in metal forming processes, *J. of Mat. Proc. Tech.*, 201, 385–389, 2008.
46. Ozturk F., Lee D., Analysis of forming limits using ductile fracture criteria, *Int. J. of Mat. Proc. Tech.*, 147, 397–404, 2004.
47. Zadpoor A.A., Sinke J., Benedictus R., Formability prediction of high strength aluminum sheets, *Int. Journal of Plasticity*, 25, 2269–2297, 2009.
48. Li H., Fu M.W., Lua J., Yang H., Ductile fracture: Experiments and computations, *Int. Journal of Plasticity*, 27, PP 147-180, 2011.
49. Freudenthal, F.A., *The inelastic behavior of engineering materials and structures*, Wiley, New York, 1950.
50. Cockroft M.G., Latham D.J., Ductility and workability of metals, *J. Inst. Metall.* 96, 33–39, 1968.
51. Brozzo P., Deluca B., Rendina R. A new method for the prediction of formability limits of metal sheets, *Sheet Metal Forming and Formability*, Proceedings of the Seventh Biennial Congress of International Deep Drawing Research Group, Amsterdam, Netherlands. 1972.
52. Oh S.I., Chen C.C., Kobayashi S.” Ductile fracture in axisymmetric extrusion and drawing”. *J. Eng. Ind. Trans. ASME*, 101, 36–44, 1979.

53. Ayada M., Higashino T., Mori K. Central bursting in extrusion of inhomogeneous materials, In Proceedings of the First ICTP. Adv. Tech. of Pals. Tokyo, Japan, 1, 553–558, 1984.
54. Chen J., Zhou X., Chen Jun., Sheet metal forming limit prediction based on plastic deformation energy, Journal of Mat. Proc. Tech., 210, 315–322, 2010.
55. Shahani A.R., Rastegar M., Botshekanan M., Moayeri H., Experimental and numerical investigation of thickness effect on ductile fracture toughness of steel alloy sheets, Eng. Frac. Mech., 77, 646–659, 2010.
56. Micari F., Fratini L., Locasto S., Alberti N., Prediction of ductile fracture occurrence in deep drawing of square boxes, Annals of the CIRP, 45, 259-262, 1996.
57. Han H.N., Kim K.H., A ductile fracture criterion in sheet metal forming process, J. of Mat. Proc. Tech., 142, 231-238, 2003.
58. Komori K., Ductile fracture criteria for simulating shear by node separation method, Theoretical and Applied Fracture Mechanics, 43, 101–114, 2005.
59. Takuda H., Mori K., Hatta N., the application of some criteria for ductile fracture to the prediction of the forming limit of sheet metal, J. of mat. Proc. Tech., 95, 116-121, 1999.
60. Shim K.H., Lee S.K., Kang B.S., Hwang S.M., Investigation on blanking of thin sheet metal using the ductile fracture criterion and its experimental verification, Int. J. of Mat. Proc. Tech., 155, 1935–1942, 2004.
61. Bai Y., Wierzbicki T., A new model of metal plasticity and fracture with pressure and Lode dependence, Int. J. of Plasticity, 24, 1071–1096, 2008.
62. Uthaisangskuk V., Prah U., Munstermann S., Bleck W., Experimental and numerical failure criterion for formability prediction in sheet metal forming, Computational Materials Sci., 43, 43–50, 2008.
63. Khelifa M., Oudjene M., Khennane A., Fracture in sheet metal forming: Effect of ductile damage evolution, Computers and Structures, 85, 205–212, 2007.
64. Saanouni K., On the numerical prediction of the ductile fracture in metal forming, Eng. Frac. Mech., 75, 3545–3559, 2008.

65. Stoughton T.B., Yoon J.W., A new approach for failure criterion for sheet metals, *Int. J. of Plasticity*, 27, 440-459, 2011.
66. Hongsheng L., Yuying Y., Zhongqi Y., Zhenzhong S., Yongzhi W., The application of a ductile fracture criterion to the prediction of the forming limit of sheet metals, *J. of Mat. Proc. Tech.*, 209, 5443–5447, 2009.
67. Li Y., Wierzbicki T., Prediction of plane strain fracture of AHSS sheets with post-initiation softening, *Int. J. of Solids and Structures*, 47, 2316–2327, 2010.
68. Li Y., Luo M., Gerlach J., Wierzbicki T., Prediction of shear-induced fracture in sheet metal forming, *J. of Mat. Proc. Tech.*, 210, 1858-1869, 2010.
69. Xue L., Localization conditions and diffused necking for damage plastic solids, *Eng. Frac. Mech.*, 77, 1275–1297, 2010.
70. Kim N., Oh C., Kim Y., Yoon B., Ma Y., Comparison of fracture strain based ductile failure simulation with experimental results, *Int. J. of Pressure Vessels and Piping*, 88, 434-447 , 2011.
71. Vladimirov I.N., Pietryga M.P., Reese S., Anisotropic finite elastoplasticity with nonlinear kinematic and isotropic hardening and application to sheet metal forming, *Int. J. of Plasticity*, 26, 659–687, 2010.
72. Dunne F., Petrinick N., *Introduction to Computational Plasticity* , Oxford university, UK, 2006.
73. Reddy J.N., *An introduction to the finite element method*, McGraw Hill, 2<sup>nd</sup> edition, 1993.
74. Joaquim P., Spencer Sh., *Handbook of Materials Modeling*, Springer, 1, 1–32, 2005.
75. Thomee T., *From finite differences to finite elements, A short history of numerical analysis of partial differential equations*, 128, 1-54, 2001.
76. Reddy J.N., Gartling D.K., *The finite element method in heat transfer and fluid dynamics*, CRC Press, 1994.
77. Rebelo N., Nagtegaal J.C., Taylor L.M., *Numerical Methods in Industrial Forming Processes*, 99–108, 1992.

78. Hibbitt, Karlsson, and Sorenson, ABAQUS Theory Manual, Pawtucket, RI, USA, 1997.
79. Kutt L.M., Pifko A.B., Nardiello J.A., Papazian J.M., Slow-dynamic finite element simulation of manufacturing processes, Computers and Structures, 66, 1–17,1998.





## APPENDIX A

### REQUIRED TOOLS TO WRITE A SUBROUTINE

The snapshots of the software to write, run and process the VUMAT and VUHARD subroutines have been presented in this appendix.

The complete view of the software environments to debug and run a subroutine for numerical simulations with ABAQUS commercial have been shown in the below figures.

- ABAQUS CAE is needed to be installed in the system to produce the model (\*.inp) and present the final results (post processing)

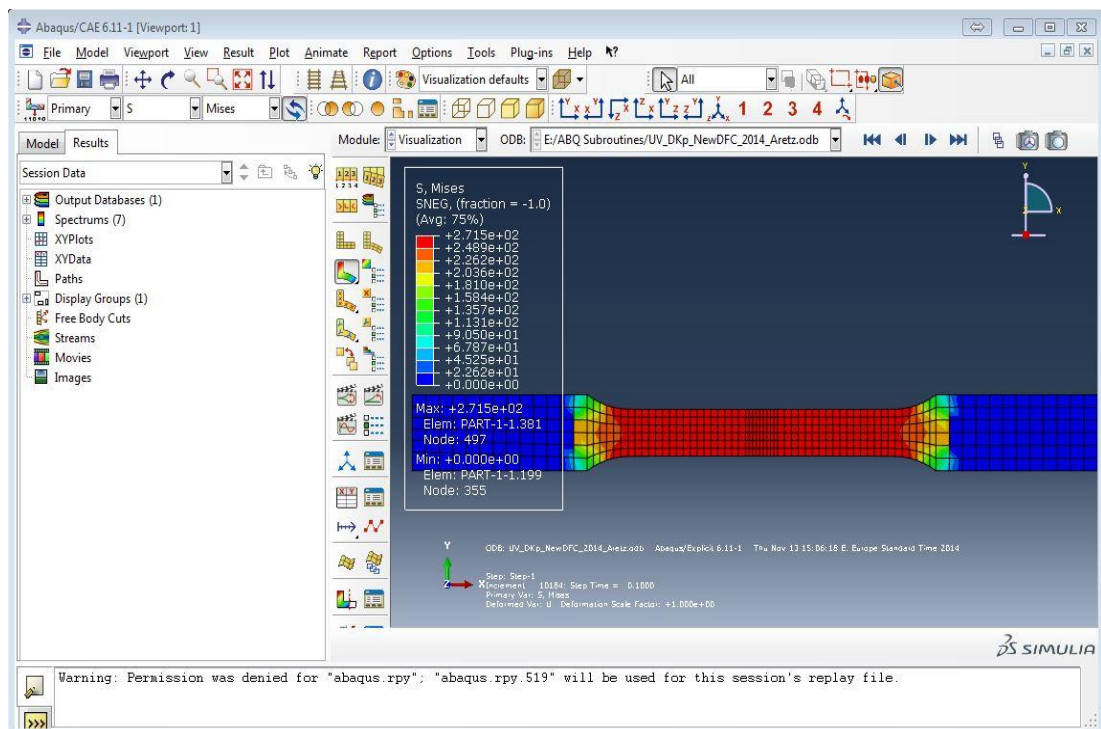


Figure A.1. ABAQUS CAE post processing environment

```

UV_DKp_NewDFC_2014_Aretz.inp - Notepad
File Edit Format View Help
**Heading
** Job name: UV_DKp_NewDFC_2014_BBC Model name: DKP2014_UV_Shell-BBC8p-NewDFC
** Generated by: Abaqus/CAE 6.11-1
** Preprint, echo=NO, model=NO, history=NO, contact=NO
**
** PARTS
**
** Part, name=Part-1
** Node
1, 106.51091, 11.25, 0.
2, 106.51091, -1.25, 0.
3, 139.51091, -1.25, 0.
4, 139.51091, 11.25, 0.
5, 97.51091, 11.25, 0.
6, 97.51091, -1.25, 0.
7, 52.8516846, 15., 0.
8, 52.8516846, -5., 0.
9, 64.51091, -1.25, 0.
10, 64.51091, 11.25, 0.
11, 151.170135, 15., 0.
12, 151.170135, -5., 0.
13, 201.170135, -5., 0.
14, 201.170135, 15., 0.
15, 2.85168409, 0., 0.

```

Figure A.2. An example of the generated model file

- Microsoft Visual Studio is needed to be installed and get linked with Intel Fortran software in which the subroutine files will be generated (\*.for).

```

Console1 - Microsoft Visual Studio
File Edit View Project Build Debug Tools Window Help
Debug Win32 sigeq
Solution Explorer - Aralik
Solution 'Console1' (1 project)
  Aralik
    Header Files
    Resource Files
    Source Files
Solution Explorer Class View
Properties
Uncoupled_Aretz_Planestress.for
Vtest_Aretz_Planestress2.for
Vtest_Aretz_Planestress_NewDFC.for
Uncoupled_DFC_Constants.for
C for UTI tests.
C Material: DKP6112 steel
C Hardening: piecewise linear
C Yield Criterion: Aretz2005
C DFC: Freudenthal
SUBROUTINE VUMAT (NBLOCK, NDIR, NSHR, NSTATEV, NFIELDV, NPROPS,
  LANEAL, STEPTIME, TOTALTIME, DT, CMNAME, COORDMP, CHARLENGTH,
  PROPS, DENSITY, STRAININC, RELSPININC, TEMPOLD, STRETCHOLD,
  DEFGRADOLD, FIELDOLD, STRESSOLD, STATEOLD, ENERINTERNOLD,
  ENERINELASOLD, TEMPNEW, STRETCHNEW, DEFGRADNEW, FIELDNEW,
  STRESSNEW, STATENEW, ENERINTERNNEW, ENERINELASNEW)
INCLUDE 'VABA_PARAM.INC'
DIMENSION PROPS (NPROPS), DENSITY (NBLOCK), COORDMP (NBLOCK),
  CHARLENGTH (NBLOCK), STRAININC (NBLOCK, NDIR+NSHR),
  RELSPININC (NBLOCK, NSHR), TEMPOLD (NBLOCK),
  STRETCHOLD (NBLOCK, NDIR+NSHR), DEFGRADOLD (NBLOCK, NDIR+NSHR+NSHR),
  FIELDOLD (NBLOCK, NFIELDV), STRESSOLD (NBLOCK, NDIR+NSHR),
  STATEOLD (NBLOCK, NSTATEV), ENERINTERNOLD (NBLOCK),
  ENERINELASOLD (NBLOCK), TEMPNEW (NBLOCK),
  STRETCHNEW (NBLOCK, NDIR+NSHR), DEFGRADNEW (NBLOCK, NDIR+NSHR+NSHR),
  FIELDNEW (NBLOCK, NFIELDV), STRESSNEW (NBLOCK, NDIR+NSHR),
  STATENEW (NBLOCK, NSTATEV), ENERINTERNNEW (NBLOCK),

```

Figure A.3. Visual FORTRAN environment linked with Microsoft Visual studio

- The Intel FORTRAN Build environment should be installed to link the model to the related code and run the solution.

```
Intel(R) Visual Fortran Compiler Professional for applications running on IA-32, Version 11.1.072
ODB Field Frame Number      9 of      11 requested time points at 1.930009E+00
168865 1.940E+00 1.940E+00 00:07:35 1.200E-05      136 1.972E+00 -1.127
E+05 1.999E+05
ODB Field Frame Number     10 of      11 requested time points at 1.940002E+00
169696 1.950E+00 1.950E+00 00:07:37 1.199E-05      136 1.956E+00 -1.133
E+05 1.999E+05
ODB Field Frame Number     11 of      11 requested time points at 1.950007E+00
173882 2.000E+00 2.000E+00 00:07:48 1.194E-05      136 2.087E+00 -1.165
E+05 1.999E+05
Restart Number 1 at 2.0000
ODB Field Frame Number     20 of      20 requested intervals at 2.000000E+00
ODB Field Frame Number     12 of      11 requested time points at 2.000000E+00

  THE ANALYSIS HAS COMPLETED SUCCESSFULLY

11/13/2014 3:31:55 PM
End Abaqus/Explicit Analysis
Begin Selected Results Translator
11/13/2014 3:31:55 PM
Run select.exe
11/13/2014 3:31:55 PM
End Selected Results Translator
Abaqus JOB UU_DKp_NewDFC_2014_Aretz COMPLETED

e:\ABQ Subroutines>
```

Figure A.4. Intel Fortran build environment



## APPENDIX B

### DETERMINATION OF THE CRITERION UNKNOWN

The flowchart showing a method used numerically to determine the new ductile fracture criterion unknown by a single experiment test. To determine the criterion unknown ( $B$ ), the other criterion constants should be calculated using empirical formulas and material properties. Then by obtaining the strain at fracture experimentally, the criterion unknown can be attained using the below flowchart.

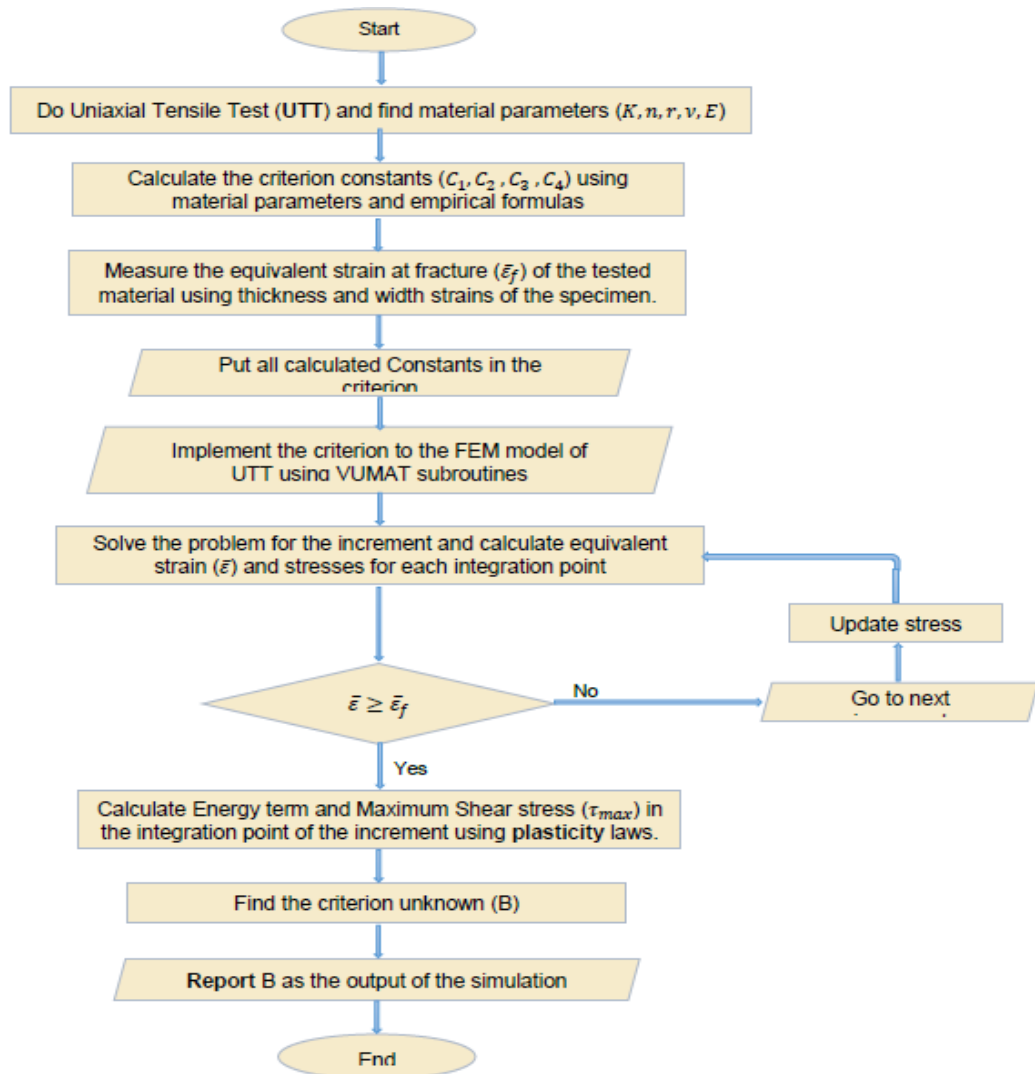


Figure B.1. A flowchart to determine the criterion unknown  $B$



## APPENDIX C

### IMPLEMENTATION OF THE NEW DFC

The below flowchart is showing a method to implement the new DFC to the desired forming process to determine the fracture initiation point. It is assumed that the material parameters and criterion constants have been determined by UTT beforehand.

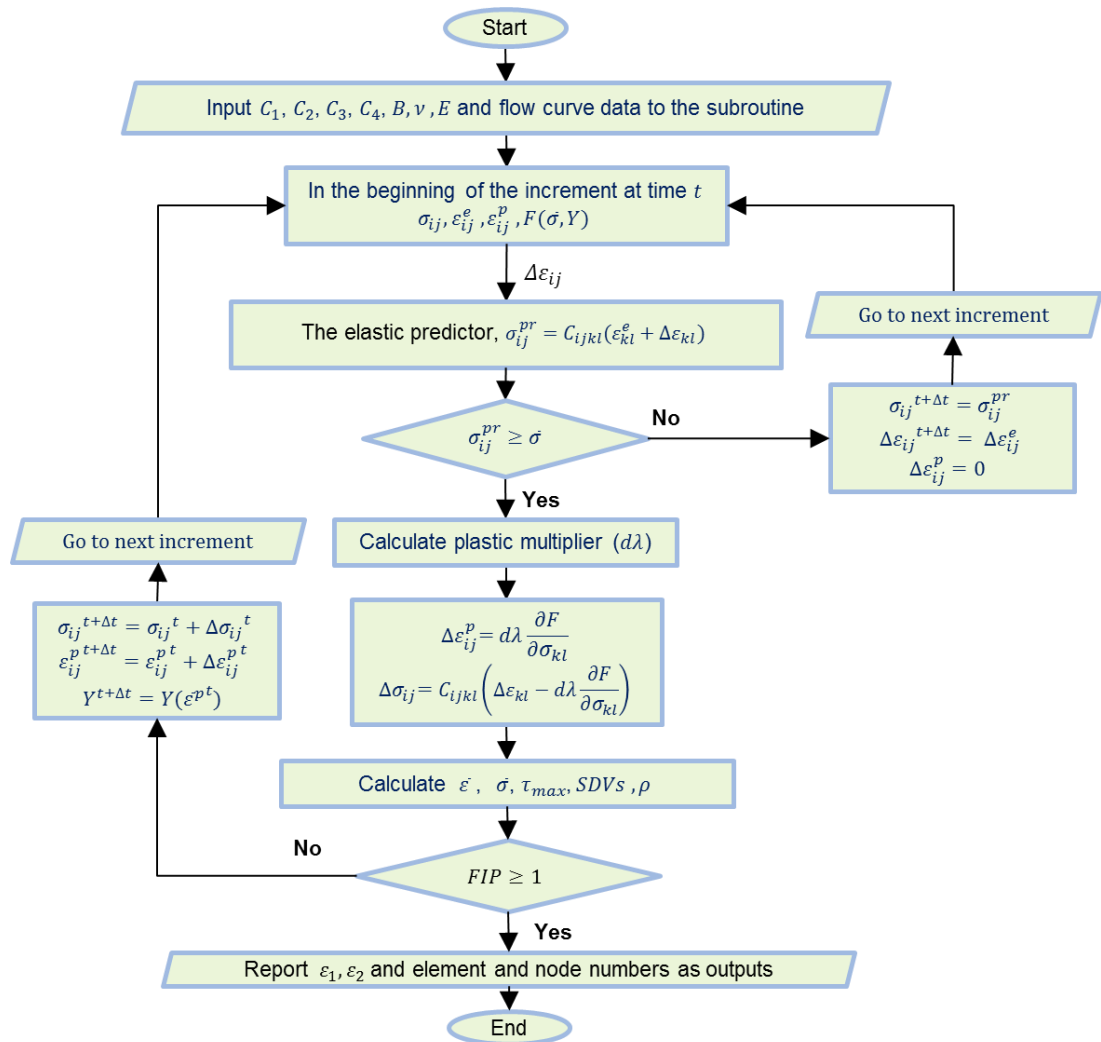


Figure C.1. Flowchart showing the implementation of the new DFC





## VITA

### PERSONAL INFORMATION

Surname, Name: ABBASNEJAD DIZAJI Shahram

Nationality: IRAN

Date and Place of Birth: 1 December 1981, Urmia

Marital Status: Single

Phone: +90 312 210 52 03

Fax: +90 312 210 52 02

Email: abbasnegzad@gmail.com

### EDUCATION

Degree	Institution	Year of Graduation
MS	IRAN University of Science and Technology	2008
BS	Tabriz University	2005
High School	Modarres, Khoy	2001

### WORK EXPERIENCE

Year	Place	Enrollment
2013-present	STC Elektronik, Ankara	R&D Specialist
2008-2009	Urmia University of Technology, Urmia	Lecturer
2002-2003	Machining Industries, Tabriz	Quality Control

### FOREIGN LANGUAGES

Advanced English, Advanced Azerbaijani, Advanced Turkish, Advanced Persian, Basic Arabian

### PUBLICATIONS

1. "Effect of hardening models on different ductile fracture criteria in sheet metal forming", Int. J. Mater. Form. (2014), DOI: 10.1007/s12289-014-1188-5
2. "Effect of anisotropy on the hydroforming of aluminum alloy AA6061-T6 using newly developed method", 5th International Mechanical Engineering Forum, June (2012), Prague, Czech Republic.
3. "Deep drawing of aluminum alloys using a novel hydroforming tooling", Journal of Materials and Manufacturing Processes, Volume 26, Issue 5, (2011), pages 796-801.

4. "Effect of Ambient Pressure on Bubble Growing in Micro-Channel and Its Pumping Effect", ASME, 10th biennial Conference on Engineering Systems Design and Analysis, July (2010), Istanbul, Turkey.
5. "Effect of punch nose radii in the hydroforming of Titanium alloy Ti-6Al-4V", The 14th International Conference on Machine Design and Production, June (2010), Güzelyurt, Turkish Republic of Northern Cyprus.
6. "A New Method of Ti6Al4V Hydroforming, Used in Aerospace Structures" 8th Iranian Aerospace Society Conference Feb. (2009), Malek-e-Ashtar University of Technology, Isfahan, Iran.
7. "Obtaining the flow stress curve of Aluminum alloy sheet, Al7075, from hydraulic bulge test", 5th International Conference and Exhibition on Design and Manufacturing of Machines and Dies/Molds, June (2009), Kusadasi, Turkey.
8. "Experimental and numerical analysis for hydroforming of Ti6Al4V alloy used in aerospace, assisted by floating disk", Journal of Applied Sciences, Vol. 9, Issue 16, (2009), pages 2925-2932.
9. "Experimental and numerical analysis for hydroforming of aluminum alloys, Al7075, assisted by floating disk", The 13th International Conference on Machine Design and Production, October (2008), Istanbul, Turkey.
10. "A new experimental method for hydromechanical deep drawing of titanium alloys, Ti6Al4V", The 13th International Conference on Machine Design and Production, October (2008), Istanbul, Turkey.

## **HOBBIES**

Soccer, Volleyball, Bowling, Swimming